POLYMER DYNAMIC ORGANIC THERANOSTIC SPHERES FOR PHOTOTHERMAL THERAPY AND FLUORESCENT IMAGING OF CANCER

BY

ELIZABETH GRACE GRAHAM

A Dissertation Submitted to the Graduate Faculty of

WAKE FOREST UNIVERSITY GRADUATE SCHOOL

OF ARTS AND SCIENCES

In Partial Fulfillment of the Requirements

For the Degree of

DOCTOR OF PHILOSOPHY

In the program of

Virginia Tech - Wake Forest University School of Biomedical Engineering and Sciences

May 2015

Winston-Salem, North Carolina

Approved By:

Nicole H. Levi-Polyachenko, Ph.D., Advisor, Co-Chair

Aaron M. Mohs, Ph.D., Co-Chair

John H. Stewart IV, M.D.

Ravi N. Singh, Ph.D.

Linda J. Metheny-Barlow, Ph.D.

Lissett R. Bickford, Ph.D.

ACKNOWLEDGEMENTS

Many people have supported me over the past few years and without them this work would not have been possible.

I would like to thank my advisor Dr. Nicole Levi-Polyachenko. Her guidance and support throughout my graduate career have been invaluable. Her enthusiasm for science is infectious and she constantly goes above and beyond for her students. She has been a great mentor and has pushed me to be a better researcher and for that I thank her.

Many thanks to my research committee members Dr. Lissett Bickford, Dr. Linda Metheny-Barlow, Dr. John Stewart IV, Dr. Aaron Mohs, and Dr. Ravi Singh. Their guidance and insight into experiment development and research plan has been instrumental. I would especially like to thank Dr. Singh and Dr. Mohs who have always made time to discuss results and offer direction.

The members of the Plastic and Reconstructive Surgery lab have been a pleasure to work with. Their broad expertise and insight have helped to shape my work. I would specifically like to thank Dr. Christopher MacNeill for both teaching me everything I know about organic polymer chemistry and being a good friend to me throughout these past few years.

I would like to thank my family and friends who have been more than understanding of my hectic schedule and have been amazing, especially my parents who have supported me in all my endeavors. Finally, I would like to thank my best friend Kevin. His love, encouragement, and support have been everything.

TABLE OF CONTENTS

LIST OF FIGURES

LIST OF TABLES

LIST OF ABBREVIATIONS

ANOVA – analysis of variance

AR – aspect ratio

CB – carbon black

D-A – donor-acceptor

DAPI - 4',6-diamidino-2-phenylindole

DEPC - diethylpyrocarbonate

DLS – dynamic light scattering

DSPE - 1,2-distearoyl-sn-glycero-3-phosphoethanolamine

DSPE-PEG - 1,2-distearoyl-sn-glycero-3-phosphoethanolamine-N-[amino(polyethylene glycol)

ECM – extracellular matrix

ECP – electrically conductive polymers

ECPN – electrically conductive polymer nanoparticles

EGFR – epidermal growth factor receptor

EMT – epithelial mesenchymal transition

FA – folic acid

FR – folate receptor

GPC – gel permeation chromatography

HOMO – highest occupied molecular orbital

ICG – indocyanine green

IVIS – in vivo imaging system

LITT – laser interstitial thermal therapy

LUMO – lowest unoccupied molecular orbital

NIR – near infrared

NMR – nuclear magnetic resonance

NP – nanoparticle

MEH-PPV - poly[2-methoxy-5-(2- ethylhexyloxy)-1,4-phenylenevinylene]

MTS - (3-(4,5-dimethylthiazol-2-yl)-5-(3-carboxymethoxyphenyl)-2-(4-sulfophenyl)-2H-tetrazolium)

MW – molecular weight

MWNT-COOH– carboxylated multi-walled carbon nanotubes

P3HT - Poly(3-hexylthiophene-2,5-diyl)

PBS – phosphate buffered saline

PCPDTBSe - Poly[4,4-bis(2-ethylhexyl)-cyclopenta[2,1-b;3,4-b']dithiophene-2,6-diyl-alt-2,1,3-benzoselenadiazole-4,7-diyl]

PCR – polymerase chain reaction

PDT – photodynamic therapy

PEDOT:PSS - poly(ethylenedioxythiophene): poly(styrenesulfonate)

PEG – poly(ethylene glycol)

PFBT – poly[(9,9-dioctylfluorenyl-2,7-diyl)-co-(1,4-benzo- {2,1=,3}-thiadiazole)]

PFBTDBT10 - poly[(9,9-dihexylfluorene)-co-2,1,3-benzothiadiazole-co-4,7-di(thiophen-2-yl)-2,1,3-benzothiadiazole]

PFPV – poly[{9,9-dioctyl-2,7-divinylene-fluorenylene}-alt-co-{2-methoxy- 5-(2-ethylhexyloxy)-1,4-phenylene]

PolyDOTS – polmer dynamic organic theranostic spheres

PPE - Poly(2,5-di(3=,7=-dimethyloctyl)phenylene-1,4- ethynylene

PTT – photothermal therapy

QD – quantum dots

SPR – surface plasmon resonance

SWNT – single walled carbon nanotubes

TEM – transmission electron microscopy

THF – tetrahydrofuran

UVvis – ultraviolet visible

ABSTRACT

Nanoparticle mediated photothermal ablation of cancer is a promising technique that utilizes light energy to destroy cancer cells. Specifically, nanoparticles that absorb in the near infrared (NIR) region of light, 700 - 900 nm, are optimal because these wavelengths are an absorption minimum for water, hemoglobin, and deoxygenated hemoglobin. As these wavelengths are where tissues are most transparent, NIR photothermal therapies allow for efficacious localized hyperthermia. Our lab has recently utilized poly[4,4-bis(2-ethylhexyl)-cyclopenta[2,1-b;3,4-b']dithiophene-2,6-diyl-alt−2,1,3-benzoselenadiazole-4,7-diyl] (PCPDTBSe), a conjugated polymer, to form nanoparticles capable of generating effective photothermal ablation when stimulated by NIR light.

Non-invasive visualization of nanoparticles is invaluable for better understanding nanoparticle behavior both *in vitro* and *in vivo*. Among imaging modalities, fluorescence is one of the most common as it is safe and cost-effective. Conjugated polymer-based probes are attracting significant attention due to their increased Stoke's shifts, improved photostability, and decreased susceptibility to enzymes or pH changes.

Theranostic nanomaterials are becoming increasingly prevalent as they offer the ability to both image and treat cancer. To ensure the safety and efficacy of treatment, it can be advantageous to determine the size, location and heterogeneity of the tumor mass using imaging techniques prior to photothermal therapy. Additionally, theranostic nanoparticles allow for visualization of the therapeutic to ensure an adequate dose has been achieved. Both of these methods allow for optimization in therapeutic planning and parameters, which can help to reduce side effects and guarantee effective treatment.

I hypothesized that by combining a NIR absorbing and NIR fluorescing conjugated polymers together, I could develop a theranostic nanoparticle capable of image-guided photothermal therapy of breast cancer.

CHAPTER 1

Introduction

1.1 Hyperthermia

Hyperthermia is a useful cancer therapy that has been utilized since as early as 1700 BC when a hot firedrill was used to treat breast cancer [1]. Since then, radiofrequency [2, 3], microwaves [4, 5], ultrasound [6, 7], and even fever [8] have been used to generate therapeutic hyperthermia. While hyperthermia is stricly defined as a rise in temperature of body tissues above normal, it can further be classified as clinical hyperthermia or thermal ablation. Thermal ablation is a rise in temperatures high enough to cause immediate cell death (typically >55°C), while clinical hyperthermia refers to a smaller rise in temperature, typically 39 - 45°C [9].

Hyperthermia begins to have cytotoxic effects beyond 42°C [10]. A dose effect curve (Figure 1) shows a 'shoulder' followed by a steep decrease is cell survival. This indicates a two-step process of cell death: a linear growth arrest at temperatures greater than 42°C, followed by exponential cell death [10]. As evident between Figure 1A and Figure 1B, the thermal dose required for cell death can vary by a factor of ten depending on the cell line [10]. However, the thermal dose energy required to induce exponential cell death *in vitro* correlates with the energy required to denature proteins (140 kcal/mol); therefore it is postulated that the mechanism of cell death from hyperthermia is through denaturation of membrane and cytoplasmic proteins [10].

The cell cycle plays a role in cell sensitivity to hyperthermia (the cell cycles listed in decreasing order of sensitivity are: M, S, and G_1 and G_2 phase) [10]. As cancer cells are more mitotically active than normal cells, a greater portion of cancer cells will be sensitive to hyperthermia than normal cells. This is the same principal behind many cytotoxic chemotherapies. Hyperthermia offers an additional therapeutic option for chemotherapy and radiation resistant cells. While cells can develop a tolerance to thermal therapy, through the induction of heat shock proteins and other post-transitional adaptation processes (like cell cycle arrest), this effect is transient (lasting 3-5 days duration) [11].

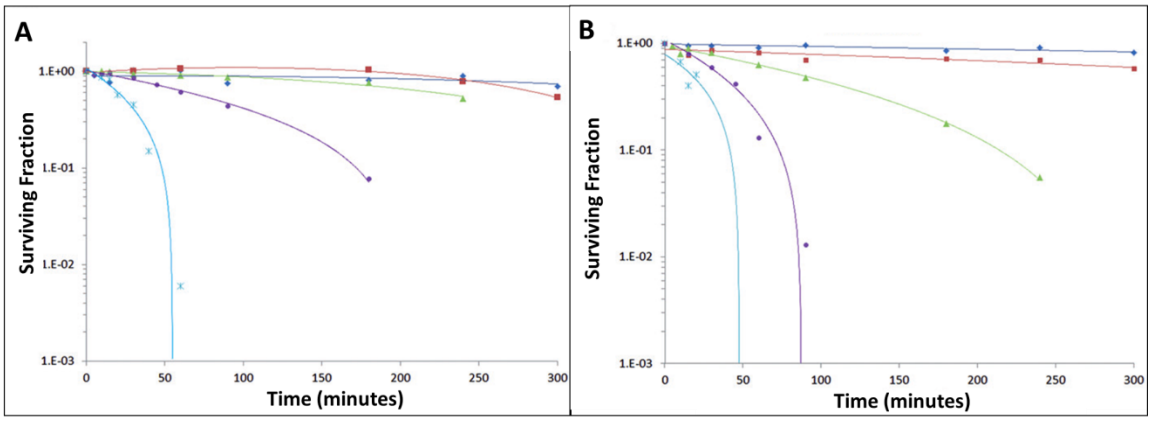

Figure 1. Dose-response relationship of thermal killing. Surviving fraction of breast cancer cell lines MCF7 (a) and MDA-MB231 (b) heated at different temperatures (40°C = blue, 42°C = red, 45°C = green, 47°C = purple, and 50°C = aqua) illustrating cytotoxic effects of temperatures greater than 42°C. Reproduced with permission from Reference [12]

Hyperthermia treatment for cancer was revolutionized by the use of laser light to create controlled and defined thermal damage to the tumor. Laser, the acronym for Light Amplification by the Stimulated Emission of Radiation, is an optical source that emits photons in a monochromatic, coherent, collimated, narrow beam [1, 13-15]. This creates a narrow beam of high intensity energy that is capable of transmitting deep into tissue with precision and little power loss [1]. Proposed in 1959 [1], laser light was first reported for tumor treatment in 1965 [16] and is still used for treatment of melanoma of the eye [17]. Using laser light to generate hyperthermia, termed laser interstitial thermal therapy (LITT), has been utilized clinically to treat liver, cervical, uterine, and brain neoplasms [18-24] with promising results. Unfortunately, one disadvantage of LITT is that cell heating (and thus cell death) is non-selective so it is difficult to control thermal damage to surrounding healthy tissue.

1.2 Nanoparticle Induced Hyperthermia

A way to improve LITT is through the use of photothermal agents with strong absorption at the specific laser light wavelength to improve light absorption and thus increase selective heating of the local environment [1, 25, 26]. Photoabsorbing agents absorb the laser light causing electrons to make transitions from the ground state to the excited state which then relax through

nonradiative decay channels [1]. This results in an increase in kinetic energy which generates heat in the surrounding environment that can be used for local cell or tissue destruction, known as photothermal therapy (PTT) [1, 27, 28].

The considerable recent developments of nanotechnology have provided a range of nanostructures with unique optical properties that can be utilized for PTT. Nanoparticles are advantageous due to their small size, customizable properties, and ability to target predetermined tissues through conjugation of specific ligands to their surface [29-31]. Specifically, nanoparticles that absorb in the near infrared (NIR) region, 700 - 900 nm, are optimal because these wavelengths are an absorption minima for water, hemoglobin, and deoxyheomoglobin (Figure 2) [32]. As these wavelengths are where tissues are most transparent, NIR PTT allows for efficacious localized hyperthermia. Additionally, if the nanoparticle is targeted through ligand functionalization to a predetermined tissue, this can generate selective PTT and result in less thermal damage to the untargeted healthy tissue.

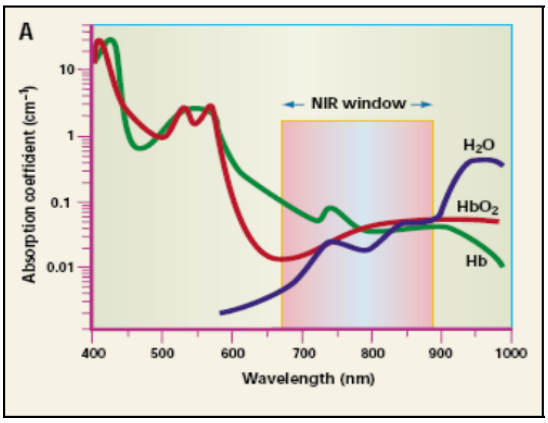

Figure 2. The NIR window is ideally suited for PTT because of minimal light absorption by hemoglobin, deoxyhemoglobin, and water. Reproduced with permission from Reference [32].

1.3 Electrically Conductive Polymer Nanoparticles

There are many nanoparticles capable of absorbing NIR light and generating heat as a photothermal agent, such as gold nanoparticles, silver nanoparticles and carbon nanotubes [33-45]. However, there has been concern in the literature about the long term toxicity of these nanostructures, especially carbon nanotubes [46-53]. Additionally, gold and silver nanoparticles

have been known to exhibit a "melting effect" under prolonged stimulation from NIR radiation, which affects their absorptive properties and can exclude these nanostructures from repeated or fractionated hyperthermic therapies [54-59]. Repeated or fractionated photothermal therapy would be beneficial clinically to allow for additional hyperthermic treatment without the need for additional nanoparticle administration.

For this reason, moving away from the conventional nanostructures to polymer-based nanomaterials could be advantageous. Due to their large pi-conjugated backbones and delocalized electronic structure, conjugated polymers are excellent electron conducting materials that have been extensively applied in optoelectronic devices, such as light-emitting diodes and photovoltaic cells.[60, 61] Recently, conjugated polymers, such as polyaniline [62], polypyrrole [63-65], and poly(ethylenedioxythiophene): poly(styrenesulfonate) (PEDOT:PSS), have been synthesized as nanoparticles and used to photothermally ablate cancer cells with NIR light [66, 67]. Cheng *et al.* [67] used polyethylene glycol (PEG)-coated PEDOT:PSS conducting polymer nanoparticles to photothermally ablate breast cancer cells in an *in vivo* murine model. The PEG-PEDOT:PSS NPs exhibited a long circulation halftime in blood and a high tumor uptake (28% at 48 hours) when administered systemically when exposed to near infrared light survived greater than 45 days compared to the control mice (PEG-PEDOT:PSS only, laser only, or no treatment), which showed average life spans of 16 - 18 days.

Optical absorption properties of an electrically conductive polymer nanoparticle can be fine-tuned by decreasing the width of its absorption peak. Decreasing the width of the absorption peak equates to the same mass absorbing a smaller range of light, and therefore more mass absorbing a specific wavelength of light. As such, increasing the amount of material absorbing a specific wavelength of light could potentially increase the heat generated by the nanoparticles. This would result in a decrease in the number of nanoparticles necessary for effective thermal therapy. The absorption properties of a polymeric nanomaterial can be tuned by using the donor-acceptor (D-A) copolymer approach [68-70]. A D-A copolymer incorporates both an electron

donating monomer and an electron accepting monomer. The absorptive properties of D-A polymers can be tuned by choosing monomers with various affinities for electron accepting and donating to change the band gap [68, 71]. The two monomers copolymerized together create two new highest occupied molecular orbital (HOMO) levels and lowest unoccupied molecular orbital (LUMO) levels, which changes the size of the band gap as seen in Figure 3A. D-A conjugated polymers that have a low band gap (from 1.7 to 1.1 eV) can absorb in the NIR window from 700 to 1100 nm [68], Figure 3B. Our lab has developed a D-A copolymer that strongly absorbs around 800 nm; 4,4-*Bis*(2-ethylhexyl)-2,6-*bis*(trimethylstannyl)-4*H*-cyclopenta-[2,1-b;3,4-b′]dithiophene and 4,7-dibromo-2,1,3-benzoselenadiazole were copolymerized to create Poly[4,4-bis(2-ethylhexyl)-cyclopenta[2,1-b;3,4-b']dithiophene-2,6-diyl-alt-2,1,3-benzoselenadiazole-4,7-diyl] (PCPDTBSe) [68].

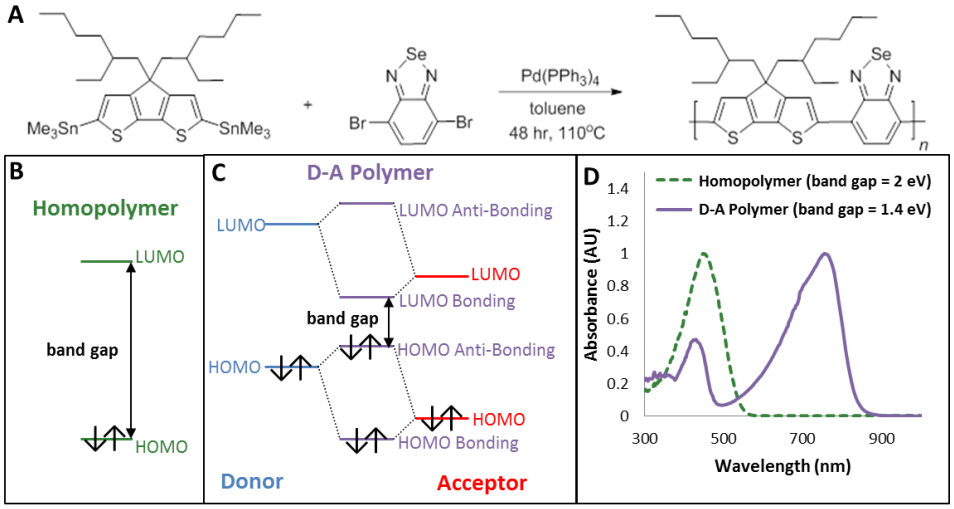

Figure 3. (**A)** Schematic of PCPDTBSe synthesis. **(B)** Schematic of band gap in homopolymer and **(C)** D-A polymer. **D)** Red shift seen with decreased band gap in the absorbance spectroscopy of homopolymer (with a band gap of 2 eV) and D-A polymer (with band gap of 1.4 eV).

The method of heat generation in D-A conjugated polymers is not yet fully understood, however, it is thought to occur through a different process than carbon- and metal-based nanoparticles. It is hypothesized that photoexcitation causes an electron hole pair (exciton) to form. The electron and hole then recombine nonradiatively, producing heat [68] as seen in the schematic in Figure 4.

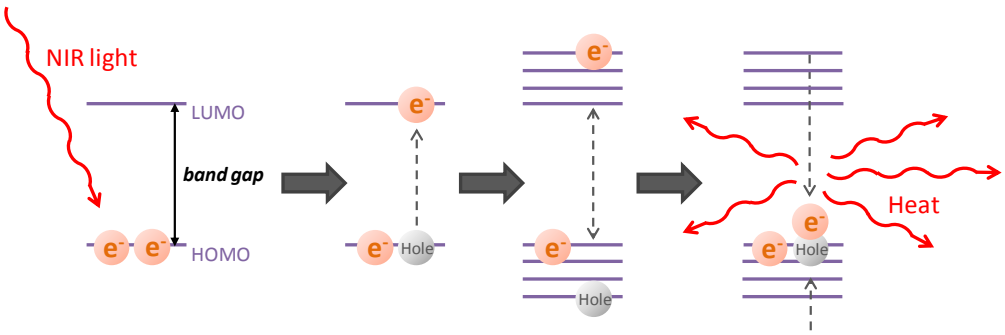

Figure 4. Schematic of hypothesized method of heat generation in D-A polymers. NIR light forms an electron hole pair (exciton) and recombination of the electron and hole causes energy to be released as heat.

Previous studies show that conjugated polymers have been used safely as coating on biological sensors [68, 72], metal-ion detectors [68, 73], neural stimulants [68, 74], and cellular imaging platforms [68, 75]. Since D-A copolymers are hydrophobic, suspension in aqueous media is difficult without attachment of a hydrophilic side chain such as PEG [68, 76] or an ionic pendant group, like those found on conjugated polyelectrolytes [68, 77]. Hydrophobic polymers can also be forced into aqueous media through emulsion or reprecipitation (also known as nanoprecipitation) depending on whether the polymer is dissolved in an organic solvent miscible or not miscible with water respectively [78, 79]. In a typical polymer nanoparticle synthesis, the polymer is dissolved in an organic solvent and then added to an aqueous phase containing a surfactant or amphipathic compound (such sodium dodecyl sulfate or phospholipid respectively) [79]. This is followed by sonication to disperse the organic phase into the aqueous phase and polymer nanoparticles are produced as the organic fraction evaporates [79]. Figure 5 illustrates a hydrophobic polymer nanoparticle formed by reprecipitation using a phospholipid as the amphipathic compound. These phospholipid coated polymer nanoparticles can be easily modified through the conjugation of polyethylene glycol (PEG) to the hydrophilic head group of the phospholipid to decrease protein adsorption. Additionally, a ligand can also be conjugated to either the phospholipid head group or to PEG to target the nanoparticle to a specific cellular receptor. The addition of a targeting ligand allows subsequent treatment to be targeted to a

specific cell or tissue type. These qualities allow D-A copolymer nanoparticles to be targeted to specific cells where they would be inert until exposed to NIR light, which would then induce heating and subsequently targeted cell death.

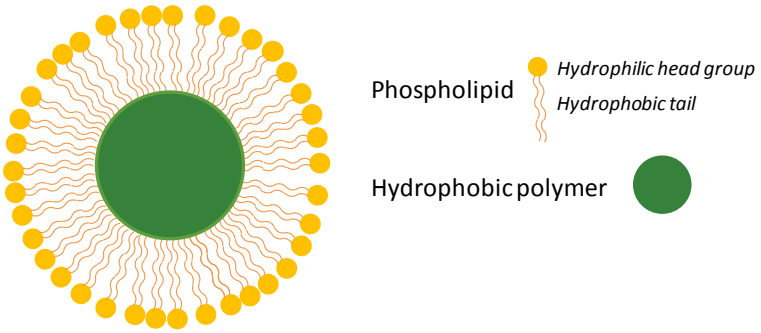

Figure 5. Example of a soluble polymer nanoparticle made through a re-precipitation method with a hydrophobic polymer and phospholipid

1.4 Fluorescence

Non-invasive visualization of nanomaterials is invaluable for determining *in vitro* cellular location and *in vivo* biodistribution. Among imaging modalities in scientific experiements, fluorescence is one of the most common methods because it is safe and cost-effective. Organic fluorophores are incredibly versatile and frequently used for fluorescent imaging; however, intrinsic limitations such as low absorptivity and poor photostability have posed difficulties for further development [80]. As a result, there has been considerable interest in brighter and more stable fluorescent probes. One promising strategy is the development of nanoparticles from conjugated polymers due to their high molar absorptivity, increased Stoke's shifts, better photostability, and low cytotoxicity [60, 78, 79, 81-86]. As a result, conjugated polymer nanoparticles have been utilized by several groups as novel biological imaging agents both *in vitro* [87, 88] and *in vivo*.[89-91] Conjugated polymer nanoparticles have been found to outperform both small molecule organic fluorophores, which have a tendency to photobleach, produce toxic effects and rapidly clear from cells [92, 93]. Studies show that conjugated polymer nanoparticles can efficiently be taken up into cells through macropinocytosis without impacting cellular processes [94]. The ability of cells to take up conjugated polymer nanoparticles coupled

with their high fluorescence brightness and low cytotoxicity make them an ideal candidate for use as nanoparticle-based imaging agents.

A limitation to NIR fluorophores is their lower quantum yields compared to their visible spectrum counterparts. For example, IR800 emits at 800 nm and has ~10% quantum yield, while cyanine5 which emits at 660 nm and fluorescein which emits at 520 nm have much higher quantum yields, 30% and 92% respectively. The same appears to hold true for fluorescent conjugated polymers (Table 1). However, in general, the fluorescence quantum yields of conjugated polymer nanoparticles, are low due to aggregation induced quenching [95].

Conjugated Polymer	Emission	Quantum Yield
PPE	440 nm	12%
PFPV	510 nm	8%
PFBT	545 nm	7%
MEH-PPV	590 nm	1%

Table 1. Conjugated polymer nanoparticles, their emission, and fluorescence quantum yield. Conjugated polymer name abbreviations: Poly(2,5-di(3=,7=-dimethyloctyl)phenylene-1,4-ethynylene (PPE) poly[{9,9-dioctyl-2,7-divinylene-fluorenylene}-alt-co-{2-methoxy- 5-(2-ethylhexyloxy)-1,4-phenylene}] (PFPV) , poly[(9,9-dioctylfluorenyl-2,7-diyl)-co-(1,4-benzo-{2,1=,3}-thiadiazole)] (PFBT), and poly[2-methoxy-5-(2- ethylhexyloxy)-1,4-phenylenevinylene] (MEH-PPV). [82]

1.5 Theranostic Nanoparticles

Many research groups have employed theranostic nanoparticles in order to image and treat cancer [96-98], as well as better understand the *in vitro* and *in vivo* behavior of nanoparticles. To ensure the safety and efficacy of treatment, it can be advantageous to determine the size, location and heterogeneity of the tumor mass using imaging techniques prior to PTT. Additionally, theranostic nanoparticles allow for visualization of the therapeutic to ensure an adequate dose has been achieved. These allow for optimization in therapeutic planning and parameters, which can help to reduce side effects and guarantee effective treatment.

We hypothesize that by combining a NIR absorbing and a NIR fluorescing conjugated polymers together, we can synthesize an optically and aqueously stable theranostic nanoparticle capable of both fluorescent imaging and photothermal therapy of cancer.

The following chapters will describe the optimization of our conjugated polymer, PCPDTBSe, nanoparticle synthesis and the fluorescent conjugated polymers combined with PCPDTBSe to generate a theranostic nanostructure. A murine model of breast cancer is utilized as a proof of concept for photothermal therapy. Although human breast cancer could not be treated in the same way due to the limitations of photothermal therapy for deep seated tumors, nanoparticle-mediated photothermal therapy could be employed in conjunction with surgery. In addition to a breast cancer model, an *in vitro* colorectal cancer model is used as well. The future clinical application for colorectal cancer would be a modified HIPEC (heated intraperitoneal chemotherapy).

CHAPTER 2

PCPDTBSe Polymer Nanoparticles

2.1 Abstract

Donor–acceptor conjugated polymer nanoparticles based on Poly[4,4-*bis*(2-ethylhexyl)-cyclopenta[2,1-*b*;3,4-*b'*]dithiophene-2,6-diyl-*alt*−2,1,3-benzoselenadiazole-4,7-diyl] (PCPDTBSe), were synthesized using Pluronic®F127 and 1,2-distearoyl-sn-glycero-3-phosphoethanolamine-N-[amino(polyethylene glycol) (DSPE-PEG) as a template. The nanomaterials have excellent aqueous stability and photothermal heating efficiency. Under stimulation from 800 nm near infrared light (3 W, 1 min), PCPDTBSe-F127 and PCPDTBSe-DSPE nanoparticles show heat generation ($\Delta T = 47$ °C) and are able to reproducibly generate heat for up to ten cycles. Cytotoxicity studies determined that neither PCPDTBSe-F127 or PCPDTBSe-DSPE nanoparticles display any significant toxicity toward either noncancerous small intestinal cells (FHs 74 Int) or colorectal cancer cells (CT26) in the absence of near infrared light. Photothermal ablation studies confirmed that both PCPDTBSe-F127 and PCPDTBSe-DSPE nanoparticles can be used as localized photothermal agents to eradicate colorectal cancer cells due to their excellent ablation efficiency (>95% cancer cell death at 15 μg/mL concentration).

The data for PCPDTBSe-F127 nanoparticles was published in Journal of Polymer Science Part A: Polymer Chemistry in June 2014 [99].

2.2 Introduction

Nanoparticle-mediated photothermal therapy provides a rapid, efficient, and noninvasive approach to locally treat cancerous tissue while minimizing the negative effects to surrounding healthy tissue [38, 100]. Nanoparticles have the ability to absorb light and convert it to heat, which can eradicate cancer cells [101, 102]. Nanoparticles that absorb light within the near infrared (NIR) spectrum (700–1100 nm) are ideal because body tissue is most transparent within this range, allowing for enhanced tissue penetration with minimal light scattering. Many groups have successfully utilized inorganic-based nanostructures for nanoparticle-mediated photothermal therapy [103, 104]. Among these, the most widely used are gold-based and carbon-based nanomaterials [38, 105-107]. However, very few groups have developed organic-based nanomaterials and tested their capabilities as potential nanoparticle-mediated photothermal therapeutics [62, 66, 108]. Our group has shown that donor–acceptor electrically conducting polymer nanoparticles can photothermally ablate colorectal cancer cells *in vitro*.[68] Some of the challenges we encountered include large size and lack of nanoparticle stability in aqueous solution.

Pluronic®F127 and 1,2-distearoyl-sn-glycero-3-phosphoethanolamine-N-[amino(polyethylene glycol)-COOH (DSPE-PEG-COOH) were used as soft templates to facilitate the synthesis of PCPDTBSe into small, aqueously stable, spherical nanoparticles. The smaller size and biocompatible coating helps decrease chemical instability and aggregative properties that uncoated polymer nanoparticles can face under physiological conditions, which may limit their applicability in preclinical studies. The heating efficacy of each nanoparticle as well as cytotoxicity and photothermal ablation efficiency PCPDTBSe-F127 and PCPDTBSe-DSPE was investigated.

2.3 Materials and Methods

2.3.1 Materials

All reagents were purchased from common commercial sources and used without further purification unless otherwise noted. Pluronic®F127 and phosphate buffered solution tablets were purchased from Sigma Aldrich. 4H-Cyclopenta-[1,2-b:5,4-b0]dithiophene was purchased from Astar Pharma. Tetrahydrofuran (THF) and anhydrous toluene were purchased from Fisher Scientific. DSPE-poly(ethylene glycol)-COOH, molecular weight 3400 was purchased from Nanocs. 4,4-Bis(2-ethylhexyl)-2,6-bis(trimethylstannyl)-4H-cyclopenta-[2,1-b;3,4-b']dithiophene was synthesized according to its published procedure [109-113]. Poly[4,4-bis(2-ethylhexyl)cyclopenta[2,1-b;3,4- b0]dithiophene-2,6-diyl-alt-2,1,3-benzoselenadiazole-4,7-diyl] (PCPDTBSe) was synthesized using a Stille coupling procedure under microwave radiation similar to Coffin et al [114].

2.3.2 Synthesis of PCPDTBSe

4,4-*Bis*(2-ethylhexyl)-2,6-bis(trimethylstannyl)-4H-cyclopenta [2,1-*b*;3,4-*b'*]dithiophene (1.5 mmol) and 4,7-dibromo-2,1,3-benzoselenadiazole (1 mmol) were dissolved in anhydrous toluene and stirred in the presence of $Pd(PPh_3)_4$ (5 mol %) at 110°C for 24 hours. The polymer was precipitated in methanol and collected by vacuum filtration. The solid was then transferred to a Soxhlet thimble and subjected to extraction with MeOH (3 hours)and hexane (6 hours) to remove oligomeric and low molecular weight PCPDTBSe. The remainder was dissolved in chloroform, subjected to rotary evaporation, and precipitated in methanol to yield a dark green powder of high molecular weight PCPDTBSe.

2.3.3 Synthesis of PCPDTBSe NPs

Bare PCPDTBSe nanoparticles (nanoPCPDTBSe): Bare PCPDTBSe nanoparticles were synthesized using a phase separation and sonication method according to a previous procedure [68]. PCPDTBSe is dissolved in 40 mL of toluene, layered on top of 40 mL of deionized water, and water bath sonicated in Branson water bath sonicator until the toluene evaporates (~6 hours).

As the toluene evaporates, PCPDTBSe is forced into the water layer where it collapses into spherical nanoparticles. This solution was then gravity filtered to remove the polymer film floating on water that did not get forced into the aqueous layer as nanoparticles. This yields aqueously dispersed polymer nanoparticles.

Pluronic wrapped PCPDTBSe nanoparticles (PCPDTBSe-F127): Pluronic wrapped PCPDTBSe nanoparticles were synthesized by a reprecipitation method using Pluronic®F127as a soft template. PCPDTBSe dissolved in tetrahydrafuran (1 mL, 2.5 mg/mL) was rapidly injected into Pluronic®F127 (8 mL, 5 mg/mL) under continuous horn sonication on a Branson Digital Sonifier fitted with microtip (1 minute, 20% amplitude).

DSPE-PEG-COOH wrapped PCPDTBSe nanoparticles (PCPDTBSe-DSPE)*:* DSPE-PEG-COOH wrapped PCPDTBSe nanoparticles were synthesized by a reprecipitation method using DSPE-PEG-COOH as a soft template. PCPDTBSe dissolved in tetrahydrafuran (2 mL, 0.25 mg/mL) was rapidly injected into DSPE-PEG-COOH (8 mL, 0.25 mg/mL) under continuous horn sonication on a Branson Digital Sonifier fitted with microtip (2 min, 45% amplitude).

Nanoparticle Collection: All nanoparticle solutions were centrifuged at 7,500 rpm for 30 minutes to pellet larger particles and aggregates. The supernatant was then centrifuged at 14,000 rpm for 4 hours to collect nanoparticles. This process was repeated several times to isolate nanoparticles

2.3.4 Characterization and Quantification of PCPDTBSe NPs

Ultraviolet visible spectrometry was measured on a Beckman Coulter DU® 730 Life Sciences UV-vis spectrophotometer over a range of 200 – 1100 nm with nanoparticles suspended in water in a silica cuvette. Fluorescence spectra were obtained from a TECAN M200 Infinite plate reader. Dynamic light scattering and zeta potential were measured in water using a Malvern Instruments Zetasizer Nano-ZS90 light scattering instrument. To visualize nanoparticles by transmission electron microscopy (TEM), a dilute solution of nanoparticles suspended in water were dropcast onto Formvar coated copper TEM grids. Images were taken on an FEI Technai Bio-Twin 120 keV TEM with digital imaging.

To determine the concentration of aqueous nanoparticle solutions, an absorption concentration calibration curve was created. To ensure that the mass of the absorption-concentration curve is only PCPDTBSe polymer and not optically transparant soft template, nanoPCPDTBSe were utilized. A known volume of concentrated nanoPCPDTBSe nanoparticles was lyophilized to dryness in a pre-weighed microtube to obtain the mass. Once the mass was known, the remaining concentrated solution was serially diluted. The absorbance spectra was obtained for each different concentrations and the absorption at the λ_{max}, 760 nm, for each concentration was recorded and plotted versus the concentration to generate an absorption-concentration calibration curve. This process was repeated three times and calibration curves averaged.

2.3.5 Heating Analysis of PCPDTBSe Nanoparticles

To compare heating capacity of the nanoparticles, 200 µL of PCPDTBSe-F127, or PCPDTBSe-DSPE nanoparticles, and carboxylated multi-walled carbon nanotubes (MWNT-COOH) in water at different concentrations were added to wells of a 96 well plate for temperature testing. A Cube^{TM} continuous wave diode laser from K-laser (800 nm, 2.654 W/cm^2) was used to apply near infrared stimulation to the nanoparticle solutions for 30 seconds per sample. A thermocouple measured the temperature of solutions immediately before and after laser application. The change in temperature was plotted versus the concentration.

To determine the ability of nanoparticles to reproducibly generate heat, heating/cooling cycles of the nanoparticles were completed over ten cycles. Each cycle includes 1 minute of 3 Watt, 800 nm laser exposure to generate heat (first half of the cycle) followed by a cooling time of 30 minutes (second half of the cycle) before the start of the next cycle. Temperatures were recorded immediately before and after exposure to laser light.

2.3.6 Cells and Reagents

FHs Int74 and CT26 were purchased from ATCC. CT26 cells were cultured with RPMI 1640 media supplemented with 10% fetal bovine serum, 1% penicillin/streptomycin, and 1% L-

glutamine. FHs Int 74 cells were cultured with Hybricare media supplemented with 30 ng/mL epidermal growth factor, 10% fetal bovine serum, 1% penicillin/streptomycin, and 1% L-glutamine. All cells were cultured and maintained in the exponential growth phase, incubated at 37°C under 5% CO_2. Cell viability was quantified by MTS assay using Promega's CellTiter 96 Aqueous assay kit.

2.3.7 Cytotoxicity Assay

FHs Int 74 cells and CT26 colorectal cancer cells were seeded at a density of 5,000 cells per well in 96 well tissue culture plates and grown to approximately 50% confluency at 37°C for 24 hours. PCPDTBSe-F127 or PCPDTBSe-DSPE nanoparticles were diluted 1 to 10 in sterile cell medium. The nanoparticle solutions were added (200 µL) at concentrations of 0, 5, 10, 20, 30, 40, 50, and 100 µg/mL. Following a 24 hour incubation, nanoparticle solutions were removed, cells washed twice with ice cold phosphate buffered saline (PBS), and an MTS assay was performed. Absorbance values were normalized to the 0 µg/mL control.

2.3.8 Thermal Ablation Assays

FHs 74 Int and CT26 cells were seeded at 5,000 cells per well in 96 well tissue culture plates and grown to ~50% confluency at 37 °C for 24 hours. PCPDTBSe-F127 or PCPDTBSe-DSPE nanoparticles were sterilized by centrifugation and resuspension in sterile water, followed by dilution 1 to 10 in sterile cell medium. The nanoparticle solutions were added to the well plates (200 µL) at concentrations of 0, 5, 10, 15, 20, and 30 µg/mL solutions (200 µL) of PCPDTBSe-F127 nanoparticles in cell medium were added to the wells. 800 nm near infrared light (2.654 W/cm^2) was applied for 1 minute per well. Following laser exposure, nanoparticle solutions were removed, cells washed twice with PBS followed by fresh cell medium. After a 24 hour incubation, an MTS assay was performed. Absorbance values were normalized to the 0 µg/mL control.

2.3.9 Statistical Analysis

Statistical analysis was performed by one way analysis of variance and post hoc Fisher LSD test.

2.3.10 Fluorescent Microscopy

A two well chamber plates (2 x 2 cm^2) was collagen coated. Type I collagen (50 µg/mL) in 0.02M acetic acid was added to wells for 1 hour before it was removed and wells washed twice with PBS and allowed to dry. Cells were then seeded at a density of 50,000 cells per well and grown to 80% confluency. PCPDTBSe-F127 nanoparticles in cell culture medium (50 µg/mL) were added on top of the cells and allowed to incubate at 37 °C for 30 min. One of the two chambers was subject to NIR stimulation (800 nm, 3 W, 1 minute) while the other was not. Both wells were washed twice with PBS and stained using a Life Technologies live/dead (calcein AM/ethidium homodimer) cell viability kit. The samples were imaged using an Olympus IX70 inverted fluorescent microscope fitted with Image Pro Plus Software.

2.4 Results

2.4.1 Synthesis and Characterization of PCPDTBSe

PCPDTBSe was prepared using a Stille coupling procedure of 4,4-bis(2-ethylhexyl)-2,6-bis(trimethylstannyl)-4Hcyclopenta[2,1-b;3,4-b0]dithiophene with 4,7-dibromo-2,1,3-benzoselenadiazole in the presence of Pd(0) catalyst in chlorobenzene similar to Coffin *et al.* [114]. The polymer was washed via Soxhlet extraction with methanol and hexanes to remove lower molecular weight material. Finally, the polymer was extracted into chloroform and evaporated to yield high molecular weight PCPDTBSe.

2.4.2 Synthesis of PCPDTBSe Nanoparticles

PCPDTBSe was dissolved in THF and rapidly injected into an aqueous solution containing Pluronic®F127 or DSPE-PEG-COOH under horn sonication. Pluronic®F127 and DSPE-PEG-COOH were used as soft templates to shape the PCPDTBSe polymer into aqueous-stable spherical nanoparticles. At low concentration and temperature, the hydrophobic and hydrophilic

components are freely soluble in aqueous solution. When the concentration or temperature of the solution exceeds the critical micelle temperature or critical micelle concentration, the components self-assemble into spherical micelles that contains a hydrophobic inner core (polypropylene oxide or DSPE) and a hydrophilic outer corona (polyethylene oxide or PEG). Upon injection, the hydrophobic PCPDTBSe polymer self-assembles within the hydrophobic core of the spherical micelle.

2.4.3 Particle Size and DLS

TEM images of PCPDTBSe-F127 and PCPDTBSe-DSPE nanoparticles can be seen in Figure 1. Both nanoparticles are electro-dense with average diameters between 30 – 50 nm. The hydrodynamic diameter, measured by dynamic light scattering, was found to be 92 nm, and 100 nm for PCPDTBSe-F127 and PCPDTBSe-DSPE respectively. PCPDTBSe-DSPE has a strongly negative zeta potential, -30 mV, while PCPDTBSe-F127 nanoparticles have close to neutral zeta potential, 1.61 mV, which is indicative of a pluronic wrapping on the surface of the nanomaterials [115-117].

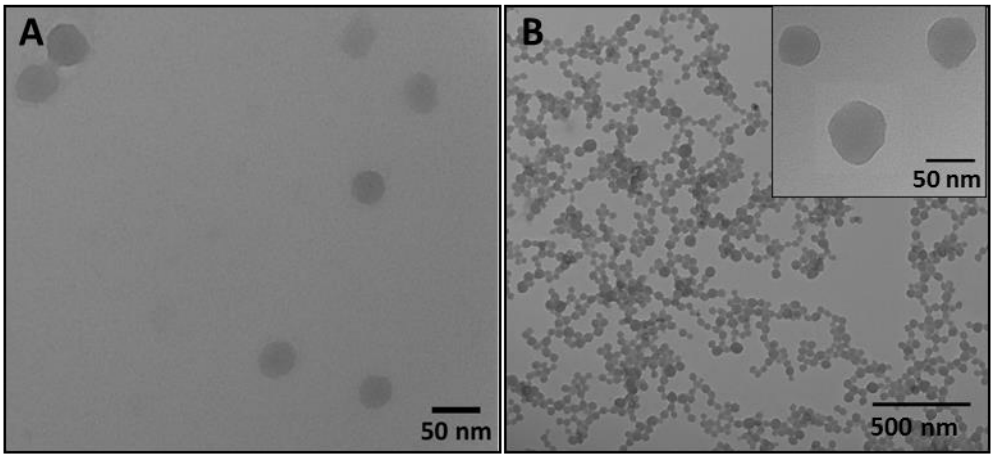

Figure 1. (A) PCPDTBSe-F127 and **(B)** PCPDTBSe-DSPE nanoparticles visualized by TEM

2.4.4 UVvis and Heating Analysis

The UV-visible spectra of the nanoPCPDTBSe, PCPDTBSe-F127, and PCPDTBSe-DSPE can be seen in Figure 2A. The absorption-concentration calibration curve for nanoPCPDTBSe

nanoparticles can be seen in Figure 2B. The heating efficiency curves comparing PCPDTBSe-DSPE nanoparticles and MWNT-COOH can be seen in Figure 2C; both PCPDTBSe nanoparticles generate comparable heat to MWNT-COOH. In addition, it was investigated whether the nanomaterials could reproducibly generate heat over multiple heating/cooling cycles. The results can be seen in Figure 2D and 2E. Over all cycles, it was demonstrated that the polymer nanomaterials were able to generate the same increase in temperature after NIR stimulation. This is important if these nanomaterials might be utilized for multiple near infrared treatments.

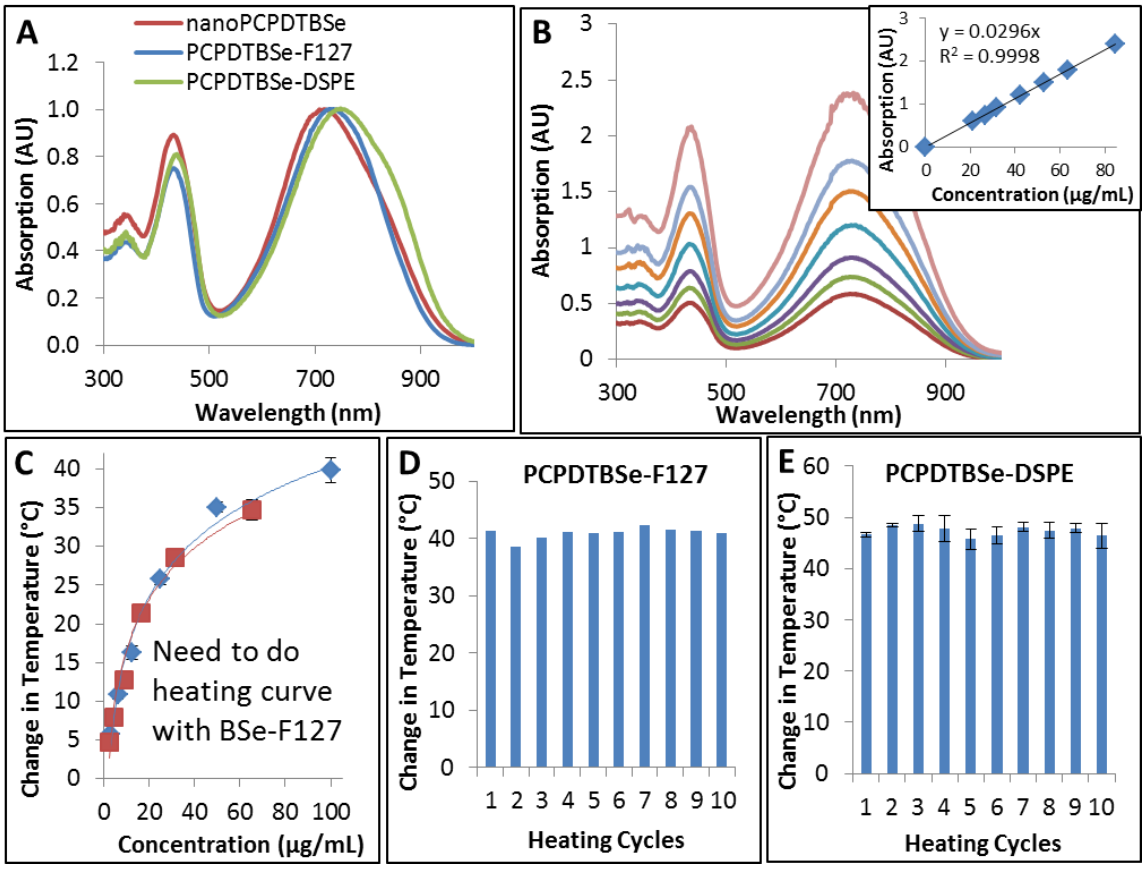

Figure 2. (A) UVvis absorption spectra. **(B)** absorption concentration calibration curve of nanoPCPDTBSe, used to determine concentration of NP in solution. **(C)** heating curve of MWNT-COOH (blue) and PCPDTBSe-DSPE (red). **(D)** and **(E)** Heating cycles of PCPDTBSe-F127 and PCPDTBSe-DSPE. Error bars shown are standard deviation.

2.4.5 Cytotoxicity, Thermal Ablation, and Fluorescent Microscopy

The cytotoxicity of the PCPDTBSe-F127 and PCPDTBSe-DSPE nanoparticles was tested in both noncancerous small intestinal epithelial cells, FHs Int 74, and colorectal cancer cells, CT26. Nanoparticles were incubated with both cell lines for 24 hours. Cell viability was measured using an MTS assay. Nanomaterials showed no inherent cytotoxicity for concentrations up to100 μg/mL in either cell line Figure 3A and 3B.

Photothermal ablation studies were performed using PCPDTBSe-F127 and PCPDTBSe-DSPE nanoparticles with both FHs Int 74 intestinal cells and CT26 colorectal cancer cells in the presence of 1 minute of 2.654 W/cm^2, 800 nm light. The results can be seen in Figure 3C and 3D. The noncancerous CT26 cells, are more susceptible to this nanoparticle-mediated photothermal therapy, only requiring 15 μg/mL to kill >95% of CT26 colorectal cancer cells, possibly due to the intrinsically increased sensitivity to hyperthermia seen in many cancer cells.

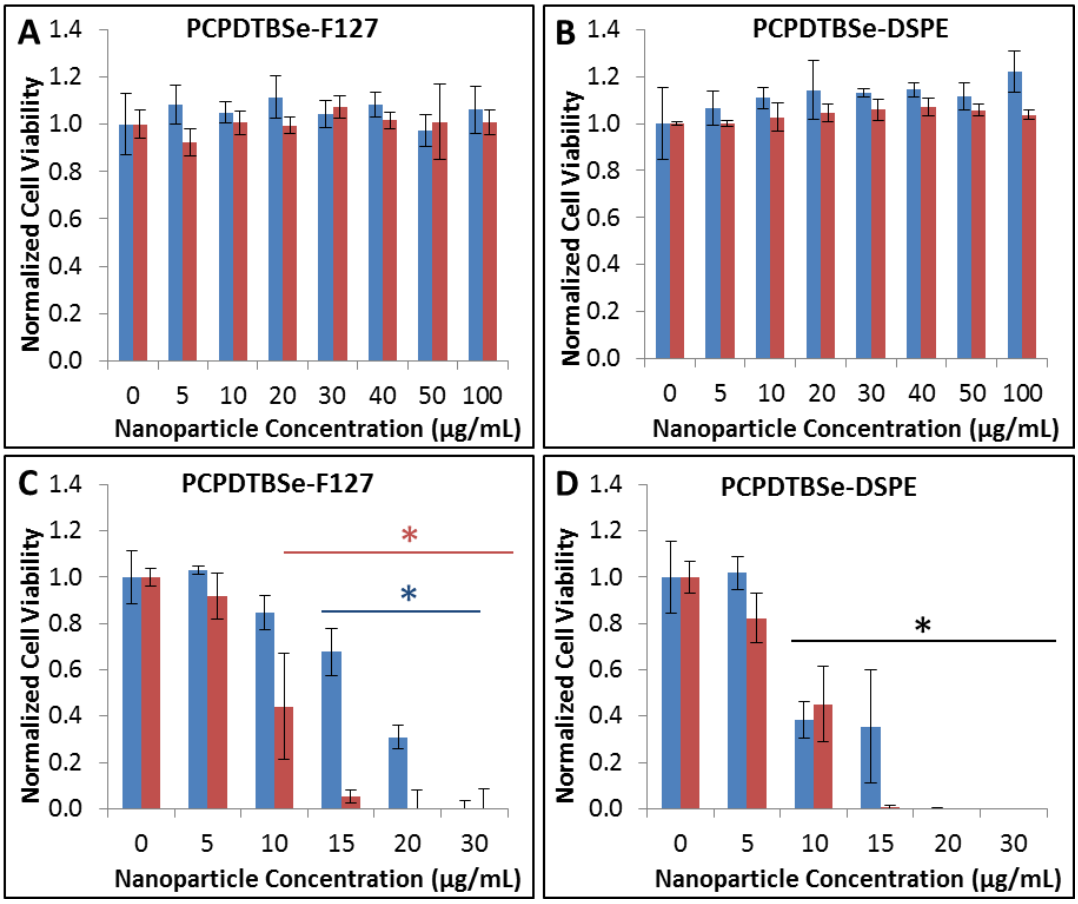

Figure 3. (A) and **(B)** Cytotoxicity of PCPDTBSe-F127 and PCPDTBSe-DSPE respectively in non cancerous FHs Int 74 cells (blue) and cancerous CT26 cells (red). **(C)** and **(D)** Photothermal Ablation of PCPDTBSe-F127 and PCPDTBSe-DSPE respectively in non cancerous FHs Int 74 cells (blue) and cancerous CT26 cells (red) using 1 minute of 2.654 W/cm^2, 800 nm light. Error bars shown are standard deviation. Asterisk denotes significance of $p<0.001$ compared to control.

Fluorescence microscopy was used in order to visualize localized photothermal ablation of the CT26 cell line in the presence of 50 µg/mL PCPDTBSe-F127 nanoparticles, a concentration that is known from the thermal ablation assay to generate complete thermal ablation. The control well, which was not exposed to laser light, shows a plethora of viable cells, as indicated by the green calcein AM staining (Figure 4). The well that experienced NIR stimulation gave a large circular area of cell death, as seen by the red ethidium homodimer stain that corresponds with the location of the NIR light exposure. These results demonstrate that PCPDTBSe-F127 nanoparticles can be used for localized photothermal ablation therapy.

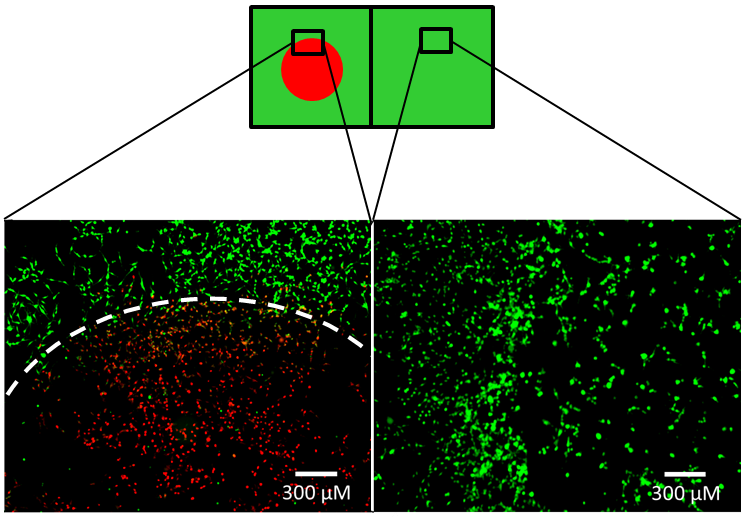

Figure 4. Live/dead (green/red) stain of CT26 cells incubated with 50 µg/mL of PCPDTBSe-F127. The well on the left was exposed to near infrared light, while the well on the right was not. Where cells were exposed to near infrared light, a spot of dead (red) cells can be seen.

2.5 Conclusions

In this proof of concept, we have demonstrated that the low band gap D–A conjugated polymer, PCPDTBSe, can be fabricated into spherical nanoparticles by reprecipitation method using both Pluronic®F127 and DSPE-PEG-COOH as a soft template. The PCPDTBSe-F127 and PCPDTBSe-DSPE nanoparticles are both very stable in aqueous media and generate significant heat when exposed to NIR light. Nanomaterials showed no significant cytoxicity toward either non-cancerous FHs Int 74 cells or CT26 colorectal cancer cells at concentrations of 5 - 100 µg/m, however, in the presence of NIR light, both PCPDTBSe-F127 and PCPDTBSe-DSPE cause effective photothermal ablation at low nanoparticle concentrations.

Acknowledements
Chris MacNeill synthesized PCPDTBSe by microwave radiation method. He developed synthesis of PCPDTBSe and PCPDTBSe-F127 nanoparticles. Chris assisted in cytotoxicity, photothermal ablation, and fluorescent microscopy of CT26 and FHS Int 74 cells used in conjunction with PCPDTBSe-F127 nanoparticles.

CHAPTER 3

PolyDOTS #1 - #6: Oligomeric PCPDTBSe and High Molecular Weight PCPDTBSe

3.1 Abstract

Theranostic nanoparticles, agents capable of both imaging and treatment, are becoming increasingly prevalent. Herein, the synthesis of an all-organic theranostic polymer nanoparticle that can be used for image-guided photothermal cancer therapy is described. The nanoparticle is built upon an oligomeric cyclopentadithiophene-benzoselenadiazole species, which fluoresces in the near infrared, combined with a near infrared absorbing polymer, poly[4,4-bis(2-ethylhexyl)-cyclopenta[2,1-*b*;3,4-*b'*]dithiophene-2,6-diyl-*alt*-2,1,3-benzoselenadiazole-4,7-diyl] (PCPDTBSe), to form a nanoparticle capable of both fluorescent imaging and photothermal therapy. The nanoparticles display no cytotoxicity to either non-cancerous MCF10A breast cells or triple negative MDA-MB-231 breast cancer cells; however, the nanoparticles can generate significant heating under stimulation from near infrared light resulting in efficient photothermal ablation. The nanoparticles can be imaged using fluorescence microscopy and show non-specific uptake in both cell lines. Purification of the oligomeric species increases fluorescence quantum yield. The high photothermal efficacy and fluorescent brightness in the NIR make these nanoparticles ideal candidates for *in vivo* image-guided photothermal therapy of cancer.

Manuscript in preparation.

3.2 Introduction

Nanoparticle mediated photothermal therapy (PTT) is as a unique approach to treat cancer due to its minimally invasive technique with high specificity [38, 100]. Our lab has utilized Poly[4,4-bis(2-ethylhexyl)-cyclopenta[2,1-b;3,4-b']dithiophene-2,6-diyl-alt-2,1,3-benzoselenadiazole-4,7-diyl] (PCPDTBSe) polymer to synthesize nanoparticles that absorb in the near infrared. In this chapter, an all organic theranostic polymer nanoparticle is synthesized using the conjugated polymer, PCPDTBSe. It was found that by increasing or decreasing the polymer chain length, PCPCDTBSe can be synthesized that absorbs anywhere from the visible region into the near infrared. By combining oligomeric PCPDTBSe (which absorbs at 550 nm and emits fluorescence at 800 nm) with high molecular weight PCPDTBSe (absorbs around 760 nm) a hybrid nanoparticle capable of both fluorescence imaging and NIR mediated PTT can be formed. We have termed this hybrid nanoparticle Poly-DOTS (polymer dynamic organic theranostic spheres). The optical properties, fluorescence imaging, *in vitro* cytotoxicity, and photothermal therapy efficiency of Poly-DOTS are discussed herein.

3.3 Materials and Methods

3.3.1 Materials

All reagents were purchased from common commercial sources and used without further purification unless otherwise noted. *4H*-cyclopenta-[1,2-*b*:5,4-*b'*]dithiophene was purchased from Astar Pharma. 4,7-dibromo-2,1,3-benzoselenadiazole was purchased from TCI America. Pluronic®F127 and phosphate buffered saline (PBS) tablets were purchased from Sigma Aldrich. Tetrahydrofuran (THF) was purchased from Fisher Chemical Co. 4,4-*Bis*(2-ethylhexyl)-2,6-*bis*(trimethylstannyl)-4H-cyclopenta-[2,1-*b*;3,4-*b'*]dithiophene was synthesized according to its published procedure.[109-113]. Alexafluor488 phalloidin and 4',6-diamidino-2-phenylimdole (DAPI) were purchased from Life Technologies.

3.3.2 Synthesis of PCPDTBSe

4,4-*Bis*(2-ethylhexyl)-2,6-bis(trimethylstannyl)-4H-cyclopenta [2,1-*b*;3,4-*b'*]dithiophene (1.5 mmol) and 4,7-dibromo-2,1,3-benzoselenadiazole (1 mmol) were dissolved in anhydrous toluene and stirred in the presence of $Pd(PPh_3)_4$ (5 mol %) at 110°C for 24 hours. The polymer was precipitated in methanol and collected by vacuum filtration. The solid was then transferred to a Soxhlet thimble and subjected to extraction with MeOH (3 hours), hexane (6 hours), and finally chloroform. The methanol, hexanes and chloroform extracts were evaporated and collected to give oligomeric, low, and high MW PCPDTBSe respectively. The methanol extract was evaporated and subject to column chromatography (3:1 chloroform to hexanes) in order to isolate oligomers 1 and 2 from oligomeric PCPDTBSe.

3.3.3 Gel Permeation Chromatography

Polymers were characterized using gel permeation chromatography (GPC) to determine the relative weight-average molecular weights (M_W). A calibration curve was developed using polystyrene standards (ReadyCal-kit, Polymer Standards Service-USA Inc.) of molecular weights varying between 500-1200 kDa. HPLC grade THF was used as mobile phase and flow rate was adjusted to 0.5 mL/min. Polymers were dissolved in THF at 2 mg/mL concentration and separated with Styragel® HT 3 column (7.8 x 300 mm, Waters Corporation, USA). This GPC system was equipped with Waters 2998 Photodynamic array, and 2414 refractive index detectors, and Wyatt's miniDAWN TREOS multi-angle light scattering detector. The data was recorded and analyzed using the ASTRA software version 6.1.

3.3.4 Synthesis of PolyDOTS, PCPDTBSe, and Oligomeric Nanoparticles

PolyDOTS #1: Oligomeric PCPDTBSe (λ_{max} = 550 nm) [1mL, 2 mg/mL in THF] and high molecular weight PCPDTBSe (λ_{max} = 754 nm) [1 mL, 1 mg/mL in THF] were premixed and injected under continuous horn sonication (Branson Digital Sonifier fitted with microtip, 20% amplitude, 1 minute) into 8 mL of Pluronic®F127 [5 mg/mL in water].

PCPDTBSe-F127: High molecular weight PCPDTBSe (λ_{max} = 754 nm) [2 mL, 1 mg/mL in THF] was injected under continuous horn sonication (Branson Digital Sonifier fitted with microtip, 20% amplitude, 1 minute) into 8 mL of Pluronic®F127 [5 mg/mL in water].

Oligomeric-F127: Oligomeric PCPDTBSe [2 mL, 2 mg/mL in THF] was injected under continuous horn sonication (Branson Digital Sonifier fitted with microtip, 20% amplitude, 1 minute) into 8 mL of Pluronic®F127 [5 mg/mL in water].

Oligomer 1 and 2 – DSPE Nanoparticles: Oligomer 1 [1mL, 1 mg/mL in THF] or Oligomer 2 [1 mL, 1 mg/mL in THF] were injected under continuous horn sonication (Branson Digital Sonifier fitted with microtip, 20% amplitude, 1 minute) into 8 mL of DSPE-PEG-COOH (0.25 mg/mL in water).

PolyDOTS #2 - #6: Oligomer 1 and high molecular weight PCPDTBSe were mixed in various ratios (3, 5, 7, 9, and 19 to 1) always maintaining 1 mg/mL polymer concentration in THF. 1 mL of the pre-mixed PCPDTBSE was injected under continuous horn sonication (Branson Digital Sonifier fitted with microtip, 20% amplitude, 1 minute) into 8 mL of DSPE-PEG-COOH [0.25 mg/mL in water].

Nanoparticle Collection: Solutions were centrifuged (30 minutes, 7,500 rpm) to remove large nanoparticles and aggregates. The resulting supernatant was centrifuged (4 hours, 14,000 rpm) to collect nanoparticles.

3.3.5 Quantification of PolyDOTS #1

The concentration of Poly-DOTS #1 in water was obtained by lyophilization of a concentrated nanoparticle solution to dryness to measure its mass. Once the mass was known, the remaining nanoparticle solution was serially diluted and absorption spectra were taken on a Beckman Coulter DU® 730 Life Sciences UV-vis spectrophotometer. The absorbance at λ_{max} = 760 nm of Poly-DOTS at different concentrations was recorded and plotted versus the concentration to generate an absorption-concentration calibration curve.

3.3.6 Nanoparticle Characterization: TEM, DLS, fluoresence

To visualize the nanoparticles by TEM, a dilute solution of nanoparticles suspended in water were dropcast from water onto Formvar coated copper transmission electron microscopy grids and images were recorded on FEI Technai Bio-Twin 120 keV TEM with digital imaging. Dynamic light scattering (DLS) with zeta potential was measured in water using a Malvern Instruments Zetasizer Nano-ZS90 light scattering instrument. UVvis spectrometry was taken on a Beckman Coulter DU® 730 Life Sciences UV-vis spectrophotometer. Fluorescence spectra were obtained on TECAN M200 Infinite plate reader.

3.3.7 Fluoresence Quantum Yield

The relative fluorescence quantum yield (φ) of nanoparticle samples was calculated using a comparative method on a TECAN M200 Infinite plate reader.[118] Rhodamine 6G in ethanol ($\eta = 1.36$, $\Phi = 0.95$)[119] and Fluorescein in 0.1M sodium hydroxide ($\eta = 1.36$, $\Phi = 0.92$)[44] were used as reference standards. Absorbance of samples and standards were kept below 0.1 to minimize re-absorption effects.[120] An excitation wavelength of 550 nm was used for both Oligomeric-F127 and Poly-DOTS nanoparticles. Fluorescence spectra were measured from 600 - 850 nm. The fluorescence spectra were baseline corrected, integrated and plotted against the absorbance of the corresponding solutions. The following equation was used to calculate the relative fluorescence quantum yield: $\Phi = \Phi_R(m/m_R)(\eta^2/\eta^2_R)$. Where Φ is the fluorescence quantum yield, m is the slope of the line obtained from the plot of integrated fluorescence intensity vs. absorbance and η is the refractive index of the solvent. The R subscript is representative of the reference fluorophore in which the quantum yield is known.

3.3.8 Heating Analysis

Two hundred microliters of nanomaterial were suspended in water were added to a 96 well plate at different concentrations for temperature testing. A Cube^{TM} continuous wave diode laser from K-laser (800 nm, 2.654 W/cm^2) was used to apply NIR light to the solutions for 1 minute per well. A Fluke 714 thermocouple calibrator type k 80Pk-1 bead probe wire

thermocouple measured the temperature of the solutions immediately before and after laser application. To assess heating reproducibility, heating/cooling curves of Poly-DOTS were completed over 10 cycles. Each cycle included 1 minute of laser time followed by 30 minutes of cooling time before the start of the next cycle. To determine the effect that multiple heating/cooling cycles have on the optical properties of PolyDOTS, UVvis and fluorescent spectra were taken.

3.3.9 Cells and Reagents

Non-tumorigenic human breast epithelial cell line, MCF 10A, and triple negative human breast cancer cell line, MDA-MB-231, were purchased from American Type Culture Collection (ATCC # CRL-10317 and HTB-26 respectively). MDA-MB-231 was cultured in DMEM/F12 medium supplemented with 1% L-glutamine, 1% penicillin/streptomycin and 10% fetal bovine serum. MCF10A was cultured in DMEM/F12 medium supplemented with 10 µg/mL insulin, 20 ng/mL epidermal growth factor, 0.5 µg/mL hydrocortisone, 100 ng/mL of cholera toxin, 5% heat inactivated horse serum, and 1% penicillin/streptomycin. Cells were cultured and maintained in the exponential phase of growth at 37°C under 5% carbon dioxide. Cell viability was quantified by MTS assay (Promega's CellTiter 96 AQueous assay kit).

3.3.10 In Vitro Characterization of PolyDOTS #1, Oligomeric-F127, and PCPDTBSe-F127

Cytotoxicity: MCF10A and MDA-MB-231 were plated at a density of 5,000 cells per well in a 96 well tissue culture plate and cultured for 24 hours. 200 µL of Poly-DOTS, PCPTBSe-F127, and Oligomeric-F127 nanoparticles were added to the well plates at concentrations of 0, 5, 10, 20, 30, 40, 50, and 100 µg/mL and incubated for 24 hours. Nanoparticle solutions were removed and cells were washed twice with PBS before MTS assay was performed. Absorbance values were normalized to the 0 µg/mL control.

Photothermal Ablation: MCF10A and MDA-MB-231 were plated at a density of 5,000 cells per well in a 96 well tissue culture plate and cultured for 24 hours. 200 µL of Poly-DOTS, PCPDTBSe-F127, and Oligomeric-F127 nanoparticles were added to the well plates at

concentrations of 0, 5, 10, 20, 30, 40, 50, and 100 µg/mL. NIR light (800 nm, continuous wavelength, 2.654 W/cm^2) was applied for 1 minute per well. Following NIR light exposure, nanoparticle solutions were removed, wells were washed twice with ice cold PBS, fresh cell medium was added and the cells were incubated at 37°C for 24 hours. Cell viability was then quantified using an MTS assay and absorbance values were normalized to the 0 µg/mL control.

3.3.11 Statistical Analysis

Statistical analysis was performed by one way analysis of variance and post hoc Fisher LSD test.

3.3.12 Fluorescent Microscopy of PolyDOTS #1, Oligomeric-F127, and PCPDTBSe-F127

MCF10A and MDA-MB-231 cells were plated at a density of 100,000 cells/well onto collagen coated, two chamber well plates and allowed to grow to 50% confluence. Poly-DOTS, 30 µg/mL in cell culture medium, were incubated with the cells at 37°C for 24 hours. Poly-DOTS solutions were removed, and cells washed twice with cold PBS solution. Cells were fixed with 4% paraformaldehyde in 1x PBS for 10 minutes, permeabilized by 0.1% Triton-x-100 in 1x PBS for 5 minutes, blocked with 1% bovine serum albumin in 1x PBS for 20 minutes, stained with alexa-fluor-488 phalloidin (5 µL for every 200 µL of 1% bovine serum albumin) and DAPI (300 nM for 5 minutes), and mounted with fluoromount. Cells were visualized by Zeiss Axioplan 2 inverted fluorescent microscope at 63x using fitted with 100 Watt AttoARC light source and Zeiss AxioCam camera and Zen Lite 2012 software. Fluorescent images were merged using Image J. PolyDOTS were visualized with a 650 nm longpass filter.

3.3.13 In Vivo Imaging

To evaluate PolyDOTS #5 and #6 for *in vivo* imaging, 100 µL of the nanoparticle concentration necessary for complete photothermal ablation was injected subcutaneously into a previously euthanized Balb/C mouse. To determine this concentration we looked at previous photothermal ablation data. In Chapter 2, it was determined 15 µg/mL of PCPDTBSe causes complete photothermal ablation. 15 µg/mL of PCPDTBSe has an absorption of 0.57 at 760 nm.

Therefore, it is expected that PolyDOTS #5 and #6 might also cause complete photothermal ablation with an absorption of 0.57 at 760 nm (as PCPDTBSe is the heating component of this nanoparticle. The mouse was then imaged using a Perkin Elmer Lumina LT Series III In Vivo Imaging System (IVIS) exciting at 535 nm and using the Cy5.5 and ICG emission filters (which span 695 nm – 770 nm and 810 nm – 875 nm respectively).

3.4 Results

3.4.1 Synthesis and Characterization of PCPDTBSe

A Stille coupling procedure was employed to polymerize of 4,4-*bis*(2-ethylhexyl)-2,6-*bis*(trimethylstannyl)-4H-cyclopenta-[2,1-*b*;3,4-*b'*]dithiophene with 4,7-dibromo-2,1,3-benzoselenadiazole in the presence of palladium catalyst using a reflux synthesis (Figure 1A) to yield PCPDTBSe that ranged in size from oligomeric to high molecular weight. In order to control the molecular weight of the conjugated polymer, the stoichiometric ratios of the two monomers can be varied. The oligomeric, low, and high molecular weight portions of the PCPDTBSe polymer were isolated through Soxhlet extraction of the bulk polymer with methanol, hexanes and chloroform, respectively. The high and low MW PCPDTBSe polymer fractions were evaporated, precipitated in methanol, and stored as a powder. Methanol extract, oligomeric PCPDTBSe, was evaporated and dissolved in THF. There is a visible color change (Figure 1C) as well as a red shift in absorption spectra (Figure 1B) as the polymer chain length increases, with the lambda max being 546, 668, and 756 nm for the oligomeric, low, and high molecular weight PCPDTBSe in THF respectively. GPC was used to determine the molecular weights of the different oligomeric and polymeric fractions (Figure 1D). The molecular weights of high and low fractions of PCPDTBSe match expected literature values based on their lambda max; however, the molecular weight of oligomeric PCPDTBSe is expected to be closer to 700. The significantly reduced molecular weight may be due to polymer packing.

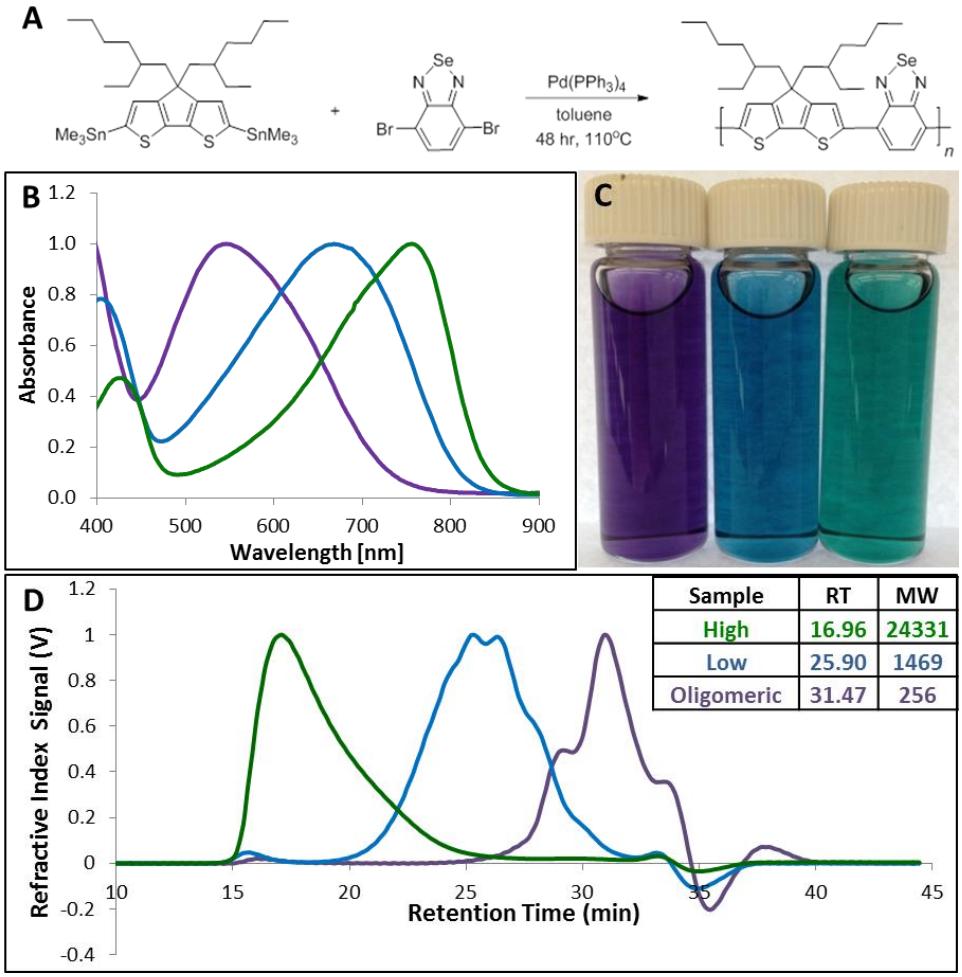

Figure 1. (A) Scheme illustrating synthesis of PCPDTBSe. **(B)** Absorption spectra of oligomeric (purple), low (blue), and high (green) molecular weight PCPDTBSe dissolved in THF. **(C)** Picture of oligomeric (purple), low (blue), and high (green) molecular weight PCPDTBSe dissolved in THF. **(D)** GPC data: the retention time of different molecular weight fractions of PCPDTBSe. (inset) Samples and their associated retention time (RT) and corresponding molecular weight (MW)

3.4.2 Synthesis and Characterization of Poly-DOTS #1, PCPDTBSe-F127, and Oligomeric-F127

PolyDOTS were synthesized using a nanoprecipitation method (Figure 2A). Oligomeric and high molecular weight fractions of PCPDTBSe were dissolved together in THF and rapidly injected into an aqueous solution containing Pluronic®F127 under horn sonication. Pluronic®F127, a biocompatible, non-ionic surfactant FDA approved for use as a drug delivery vehicle,[121-123] was used as a soft template to shape the PCPDTBSe polymer into aqueously stable spherical nanoparticles. Upon injection, the hydrophobic PCPDTBSe self-assembles within

the hydrophobic core of the spherical micelle leading to the formation of a hybrid nanoparticle (PolyDOTS) that contains both oligomeric and high molecular weight PCPDTBSe intermixed. Solely oligomeric and high molecular weight PCPDTBSe nanoparticles were synthesized in the same manner. The absorption spectrum of Poly-DOTS show peaks at 550 nm and 760 nm indicating the presence of both oligomeric and PCPDTBSe (Figure 1B). There is also a peak seen at 650 nm most likely due to the combined absorption at 650 nm for both oligomeric and high molecular weight polymers. Additionally, when excited at 550 nm, Poly-DOTS generate a fluoresence emission peak at 800 nm (Figure 1C). Nanomaterials were visualized using transmission electron microscopy (TEM) and both PolyDOTS and PCPDTBSe nanoparticles were found to be spherical and electro-dense with of diameters 30 - 60 nm (Figure 2C and 2D). However, oligomeric nanoparticles formed rods of approximately 20 nm by 300 – 500 nm (Figure 2E). Additionally, dynamic light scattering (DLS) revealed that PolyDOTS, Oligomeric-F127, and PCPDTBSe-F127 nanoparticles have hydrodynamic diameter of 65, 107, and 94 nm and a zeta potential of 17.5, -7, and 8.4 mV respectively.

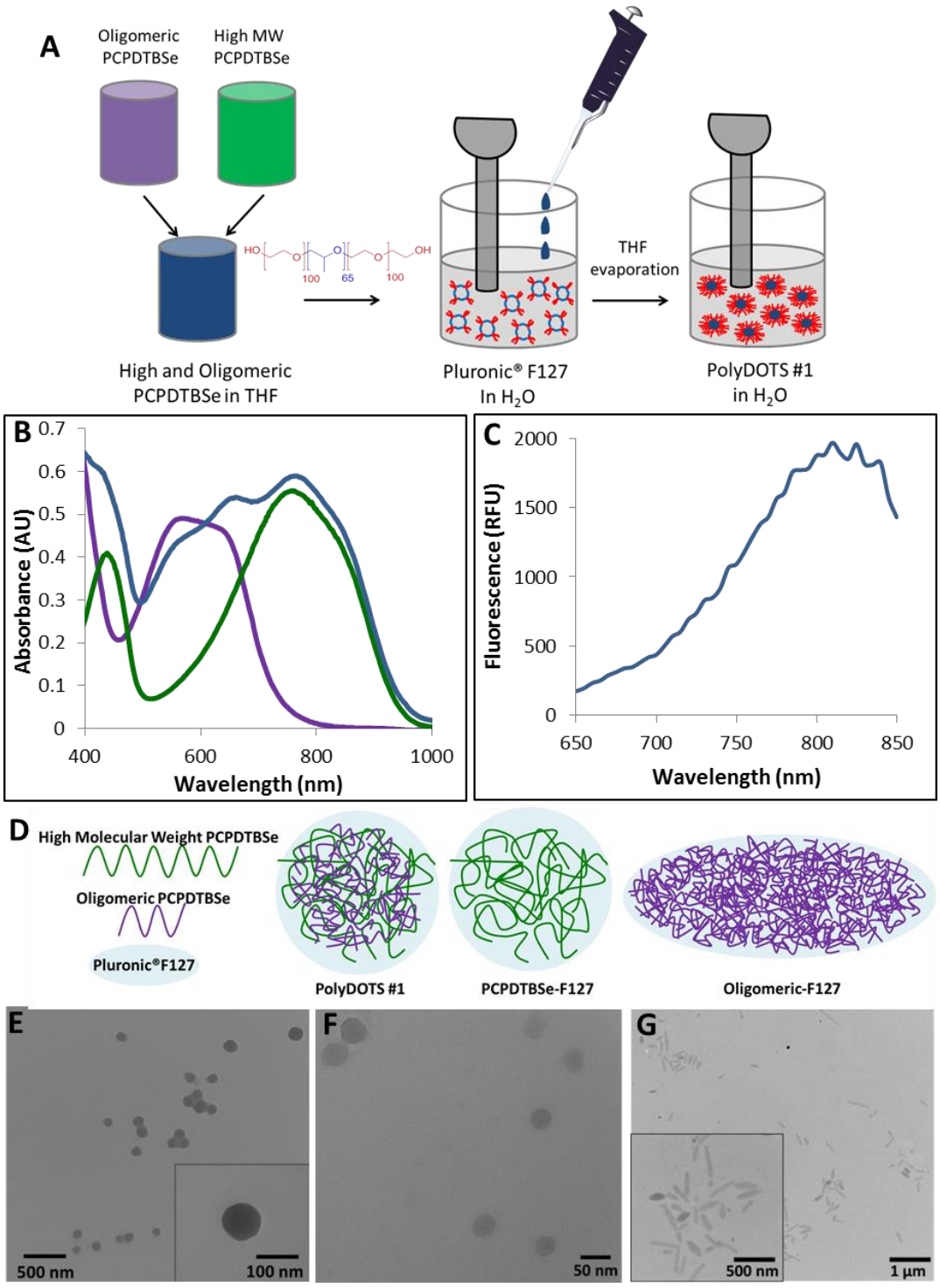

Figure 2. (A) Schematic of PolyDOTS synthesis. Oligomeric and high molecular weight fraction of PCPDTBSe are dissolved in THF and premixed before being rapidly injected into water containing Pluronic®F127 under continuos horn sonication. **(B)** Absorption spectra of PolyDOTS (blue), PCPDTBSe (green), and oligomeric (purple) nanoparticles. **(C)** Fluorescence spectra of PolyDOTS excited at 550 nm. **(D)** Visual representation of nanoparticles**, (E)**, **(F)** and **(G)** are TEM of PolyDOTS, PCPDTBSe, and oligomeric nanoparticles respectively.

Poly-DOTS generate excellent heating when stimulated by 800 nm light, comparable to PCPDTBSe-F127 nanoparticles (Figure 3A). Additionally, Poly-DOTS are able to reproducibly generate heat and maintain approximately 80% of their fluorescence capabilities over 10 cycles of NIR stimulation (Figure 3B); losing ~20% within the first 5 cycles and stabilizing for the 5 subsequent rounds of heating. Due to the varied pH of the cellular microenvironment, the fluorescence intensity of Poly-DOTS was measured after 24 hours of incubation at a range of pHs where they displayed a slight decrease, up to 20%, in fluorescence intensity at pHs above and below 7 (Figure 3C).

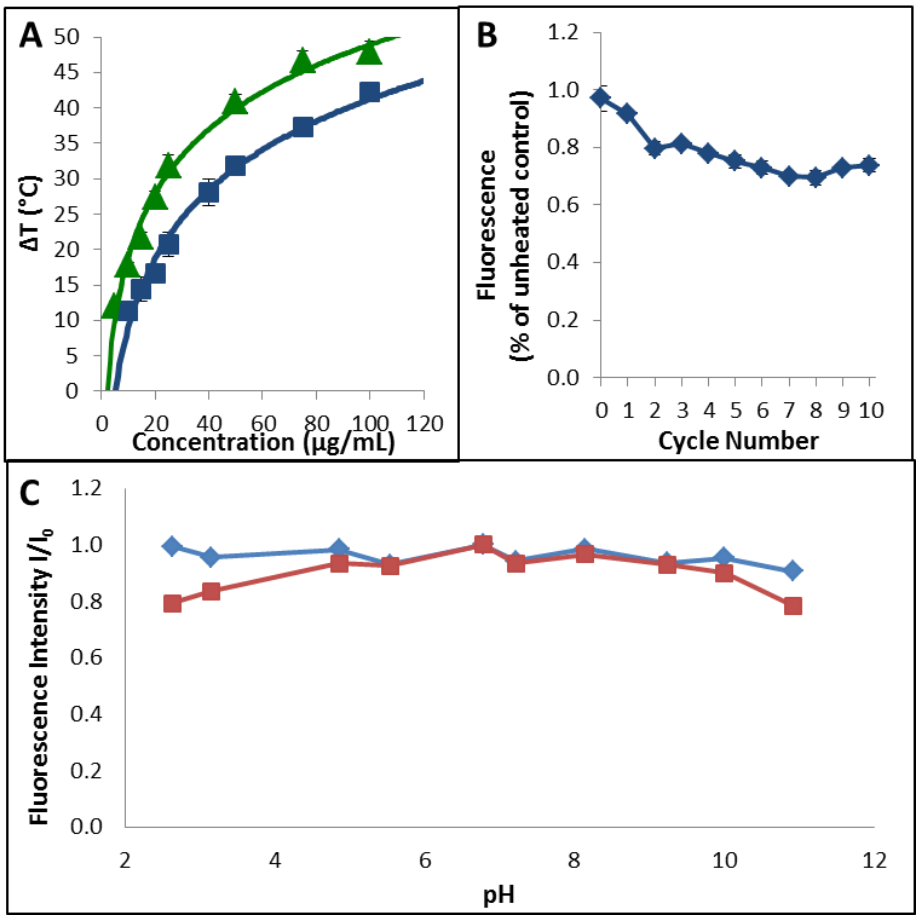

Figure 3. (A) Heating curve of PolyDOTS (blue) compared to high molecular weight PCPDTBSe nanoparticles (green) under 1 minute of 2.654 W/cm^2, 800 nm light. **(B)** Effect of heating on fluorescent intensity. The maximum fluorescence intensity is plotted versus heat cycle number. **(C)** The effect that pH has on the maximum fluorescence intensity of PolyDOTS after 1 (blue) and 24 (red) hour incubations.

The fluorescence quantum yield of oligomeric nanoparticles and Poly-DOTS were found to be 0.27% and 0.077% respectively. To see if the same decrease in quantum yield would occur if PCPDTBSe-F127 and Oligomeric-F127 nanoparticles were mixed, a solution was made to match the absorption spectra of PolyDOTS #1. Interestingly, a decrease in quantum yield does occur, but not quite at the same magnitude as PolyDOTS #1. The quantum yield of PCPDTBSe-F127 and Oligomeric-F127 nanoparticles mixed together was found to be 0.18%. The decrease in quantum yield of Poly-DOTS compared to the oligomeric PCPDTBSe nanoparticles may be due to the close interaction between high molecular weight PCPDTBSe which absorbs NIR light and oligomeric PCPDTBSe which emits NIR light. This quenching indicates a very close interaction between the two PCPDTBSe species.

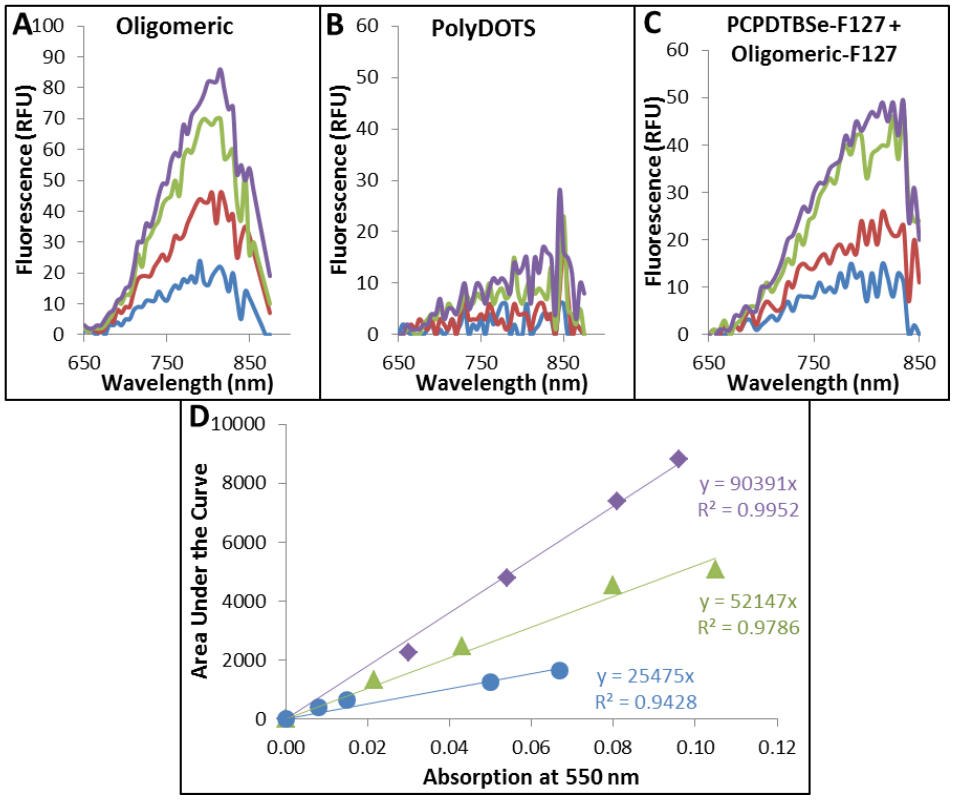

Figure 4. (A) Fluorescent spectra of Oligomeric nanoparticles with absorptions of 0.03, 0.05, 0.08, and 0.10 at 550 nm. **(B)** Fluorescent spectra of PolyDOTS with absorptions of 0.01, 0.015, 0.05, and 0.07 at 550 nm. **(C)** Fluorescent spectra of PCPDTBSe-F127 and Oligomer-F127 nanoparticles mixed with absorptions of 0.02, 0.05, 0.08, and 0.10 at 550 nm. **(D)**The above curves were integrated and plotted versus the absorption at 550 nm. Purple = oligomeric-F127, green = PCPDTBSe-F127 and Oligomeric-F127 nanoparticles mixed, and blue = PolyDOTS #1.

3.4.3 In Vitro Characterization of Poly-DOTS, Oligomeric, and PCPDTBSe Nanoparticles

The acute cytotoxicity of PolyDOTS, Oligomeric-F127 and PCPDTBSe-F127 nanoparticles was assessed using a conventional MTS cell viability assay. After 24 hours of incubation in the absence of 800 nm light, all three nanoparticles showed no substantial effect on cell viability for either the non-cancerous breast epithelial cell line MCF10A or the triple negative breast cancer cell line MDA-MB-231 (Figure 5A and B). However, after exposure to 800 nm light (2.654 W/cm^2, 1 minute), Poly-DOTS and PCPDTBSe-F127 nanoparticles demonstrated excellent photothermal ablation, resulting in complete ablation at 100 µg/mL and 40 µg/mL respectively for both MDA-MB-231 and MCF10A. Oligomeric-F127 nanoparticles, which do not absorb at 800 nm, did not cause any cell death when stimulated with NIR light (Figure 5C and D).

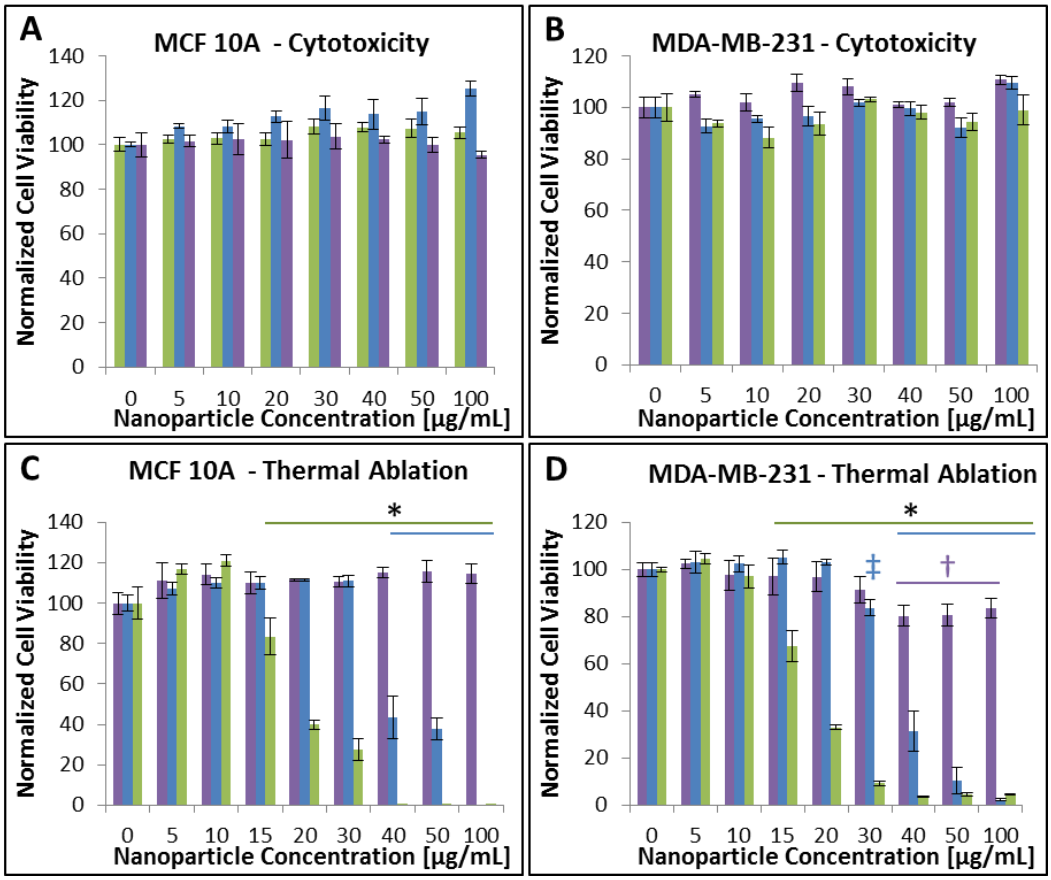

Figure 5. Cytotoxicity and photothermal ablation of MCF10A and MDA-MB231 incubated with PolyDOTS (blue), oligomeric (purple), and PCPDTBSe (green) nanoparticles. For photothermal ablation, cells exposed to 1 minute of 2.654 W/cm^2 800 nm light. Error bars shown are standard deviation. * $p<0.001$, ‡ $p< 0.01$, † $p<0.02$

Fluorescent microscopy was done to investigate *in vitro* cellular uptake of Poly-DOTS in both MCF10A and MDA-MB-231 cell lines. After a 24 hour incubation with Poly-DOTS at 30 µg/mL, the cells were stained with alexa-fluor488-phalloidin to visualize the cytoskeleton and DAPI to visualize the nucleus. Composite fluorescent images (Figure 6), illustrate that Poly-DOTS are clearly visible in the cytoplasm of both cell lines. The absence of a "no nanoparticle" control affects the interpretation of this data, as it is possible that there the fluorescence seen is autofluorescence, and will be investigated in the future.

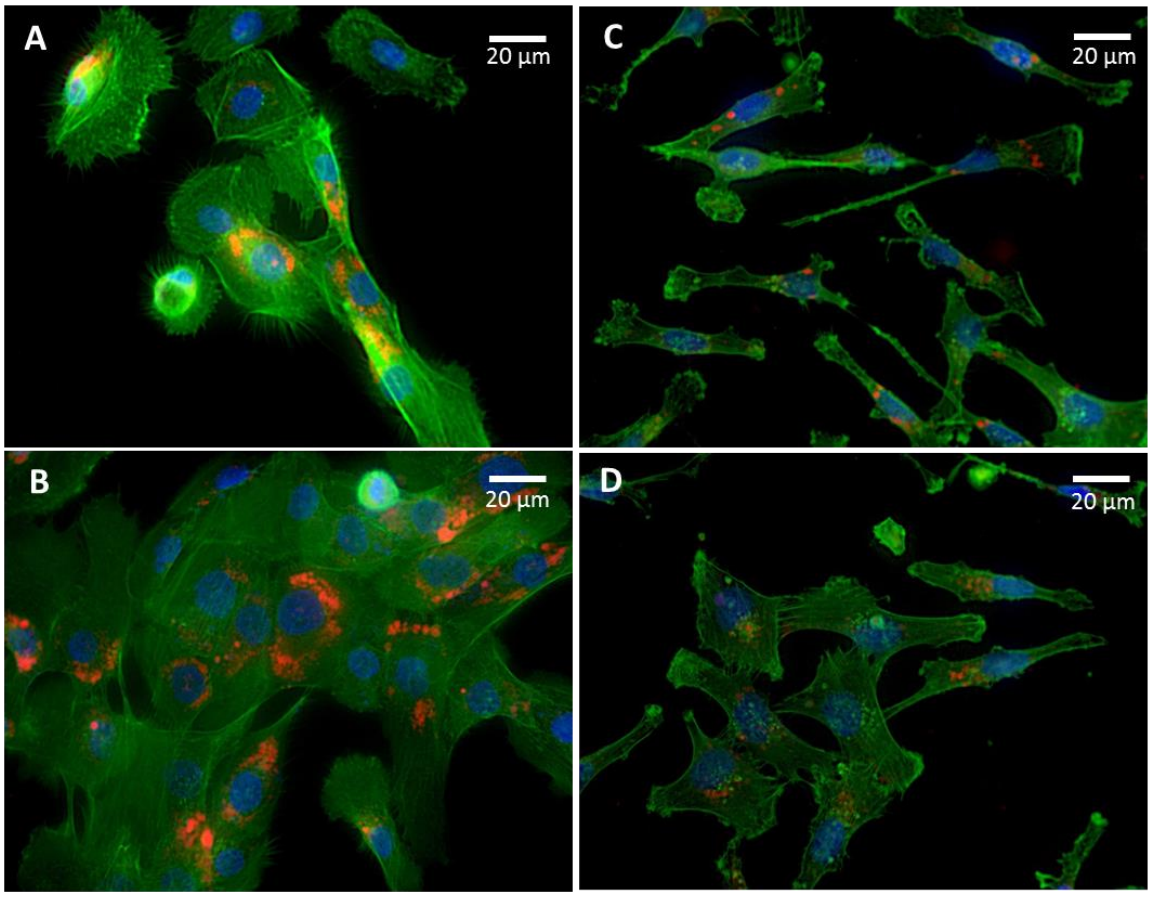

Figure 6. Fluorescent Microscopy of MCF10A **(A & B)** and MDA-MB-231 **(C & D)** cell lines. Actin is stained green with alexafluor488, the cell nuclei are stained blue by DAPI, and PolyDOTS fluoresce red.

3.4.4 Concerns with PolyDOTS #1

PolyDOTS using high and oligomeric PCPDTBSe is a promising start, but unfortunately, during each subsequent PCPDTBSe synthesis, the oligomeric fraction is always slightly different.

This is obvious as the oligomeric fractions are not always the same color, appearing to red and blue shift (Figure 7A). Additionally, there is difficulty reproducibly synthesizing PolyDOTS. As seen in Figure 7B, each "batch" of PolyDOTS has quite varying ratios of oligomeric PCPDTBSe to high molecular weight PCPDTBSe (visualized by the changes in intensity of absorption peak at 550 nm), despite adding the same mass of oligomeric PCPDTBSe (as determined by absorption-concentration calibration curve). Based on the shoulders seen by gel permeation chromatography, it is hypothesized that by purifying the oligomer component, the fluorescent component could be isolated, thus ensuring accuracy for future PolyDOTS synthesis.

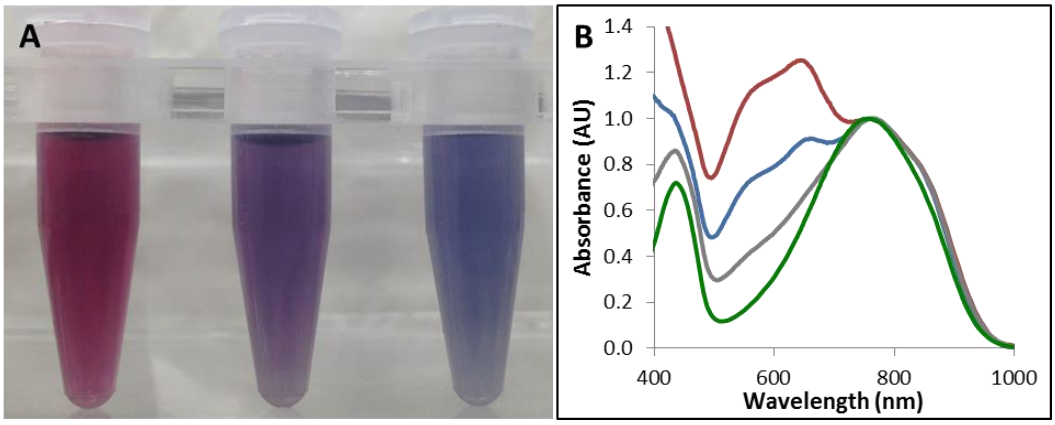

Figure 7. (A) Image of color change seen in oligomeric PCPDTBSe (dissolved in THF) obtained from different PCPDTBSe synthesises. **(B)** Absorption spectra of 3 "batches" (1st = blue, 2nd = red, 3rd = grey) of PolyDOTS compared to PCPDTBSe nanoparticles (green).

3.4.5 Isolation of Oligomer 1 and Oligomer 2

Methanol extract was subjected to column chromatography to isolate Oligomer 1 and Oligomer 2 (Figure 8A). There is a visible color change (Figure 8B) as well as a red shift in absorption spectra (Figure 8C) as the polymer chain length increases, with the lambda max being 518, 600, 668, and 756 nm for the oligomer 1, oligomer 2, low, and high molecular weight PCPDTBSe in THF respectively.

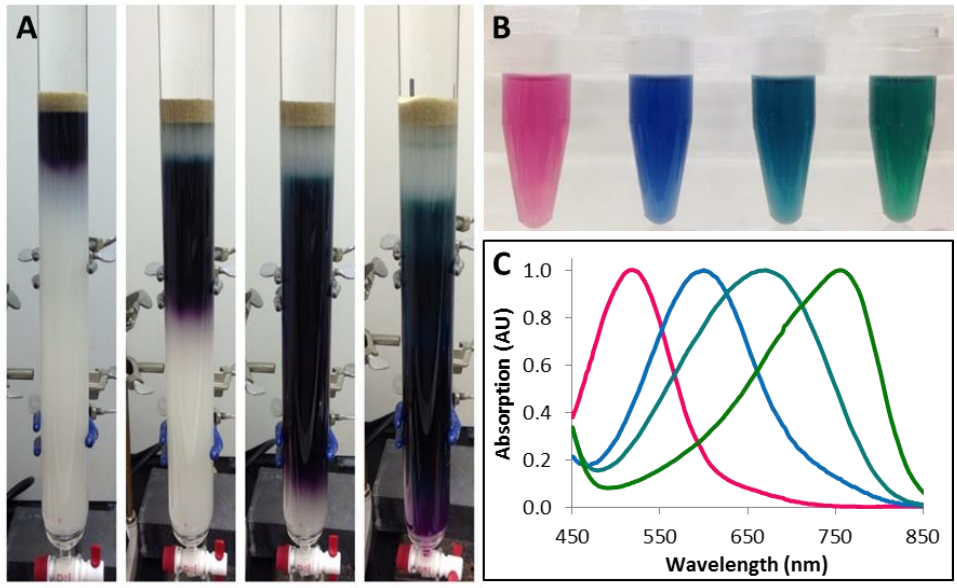

Figure 8. (A) Image of column chromatography used to separate oligomers 1 and 2. **(B)** image of (from left to right) oligomer 1, oligomer 2, low, and high molecular weight PCPDTBSe**. (C)** Absoprtion spectra of oligomer 1 (pink), oligomer 2 (blue), low molecular weight PCPDTBSe (aqua), and high molecular weight PCPDTBSe (green) dissolved in THF.

3.4.6 Evaluation of Oligomer 1 and Oligomer 2 Fluorescence

In order to determine which component of oligomeric PCPDTBSe would be a better fluorescent compound, oligomer 1 and 2 nanoparticles were synthesized by a nanoprecipitation method. The absorption and fluoresence spectra are shown in Figure 9. The fluorescence quantum yield of oligomer 1 and 2 nanoparticles were found to be 10.8% and 1.8%, respectively. As such, oligomer 1 was chosen as the fluorescent component for PolyDOT synthesis.

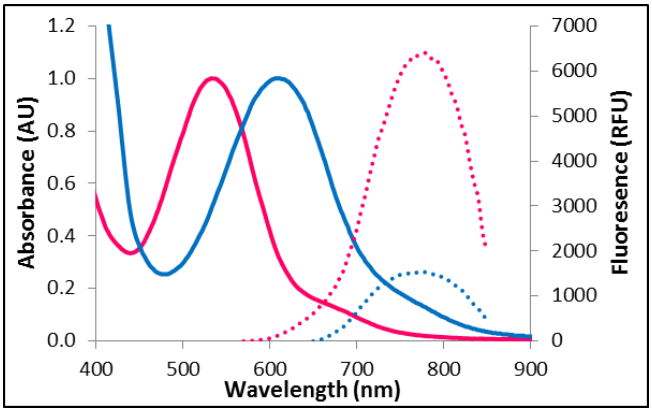

Figure 9. Absorption (solid line) and fluorescent spectra (dotted line) of oligomer 1 and 2 nanoparticles (pink and blue respectively).

3.4.7 Evaluation of PolyDOTS #2 - #6

Several PolyDOTS were synthesized with a range of proportions of oligomer 1 to high molecular weight PCPDTBSe as summarized in Table 1 and their optical absorption spectra are shown in Figure 10.

	Mass of Olig 1 added [µg]	Mass of PCPDTBSe added [µg]	Ratio of Olig 1 to PCPDTBSe added	Ratio of Absorption at 535nm:800nm
PolyDOTS #2	750	250	3:1	0.6
PolyDOTS #3	833	167	5:1	1.0
PolyDOTS #4	875	125	7:1	1.5
PolyDOTS #5	900	100	9:1	1.9
PolyDOTS #6	950	50	19:1	4.0

Table 1. Lists the mass of oligomer 1 and high molecular weight PCPDTBSe added to synthesize PolyDOTS #2 - #6. Additionally Summarizes the ratio of oligomer 1 to PCPDTBSe added versus what is incorporated into the nanoparticles (the ratio of the absorption of 535 nm to 800 nm).

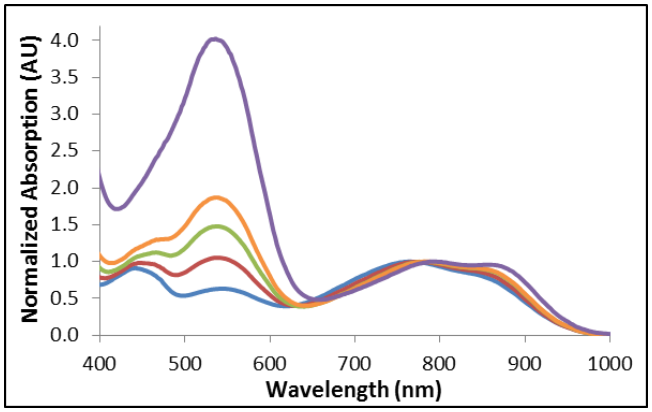

Figure 10. Absorption spectra of PolyDOTS #2 (blue), #3 (red), #4 (green), #5 (orange), #6 (purple) normalized for PCPDTBSe.

The concentration of the two most promising PolyDOTS, #5 and #6, were chosen for further evaluation. To determine whether or not PolyDOTS will be visible *in vivo*, the concentration necessary for photothermal therapy (based on previous photothermal ablation data, need an absorption of 0.57 at 760 nm) was evaluated for fluorescence (Figure 11). The Cy5.5 (695 nm -770 nm) and ICG (810 nm – 875 nm) emission filters for Perkin Elmer's Lumina LT Series III In Vivo Imaging System are highlighted in red and green respectively. Based on the fluorescent spectra, it is expected that Cy5.5 filter will be best.

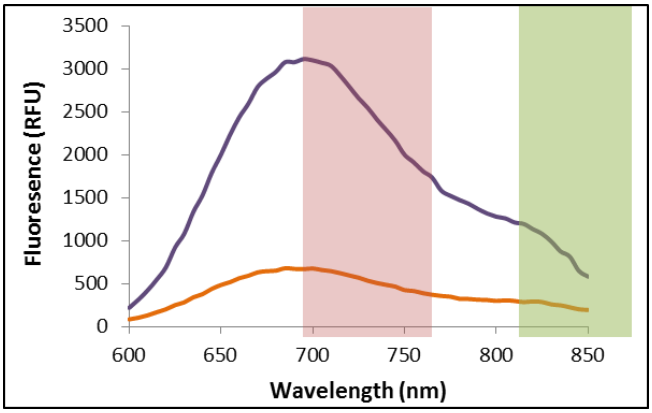

Figure 11. The fluorescent spectra of PolyDOTS #6 (purple) and #5 (orange) at a concentration necessary for photothermal ablation (an absorption of 0.57 at 760 nm). The Cy5.5 and ICG emission filter of the Perkin Elmer IVIS system are highlighted in red and green respectively.

PolyDOTS #5 and #6 (100 µL) were injected subcutaneously into a previously euthanized Balb/C mouse and imaged exciting at 535 nm using emission filters Cy5.5 and ICG. PolyDOTS #5 is not visible using either filter emission. PolyDOTS #6 is visible using both filters, however it is worth noting that the background fluoresence is significantly decreased using the ICG filter (Figure 12).

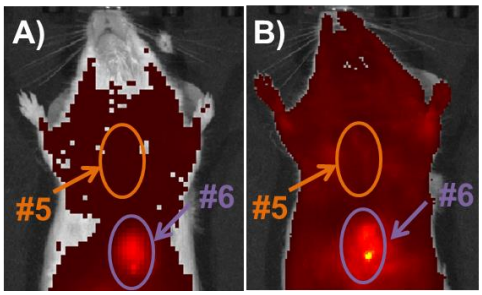

Figure 12. IVIS fluorescent images of PolyDOTS #5 and #6 injected subcutaneously into a Balb/c mouse. Both images were excited aat 535 nm, **(A)** used ICG emission filter and **(B)** used Cy5.5 emission filter.

As PolyDOTS #5 is not visible *in vivo*, further analysis was only performed with PolyDOTS #6. The fluorescence quantum yield of PolyDOTS #6 is 3.36% (Figure 13). As with PolyDOTS #1, there is a significant decrease in quantum yield that is possibly caused by close interaction with high molecular weight PCPDTBSe.

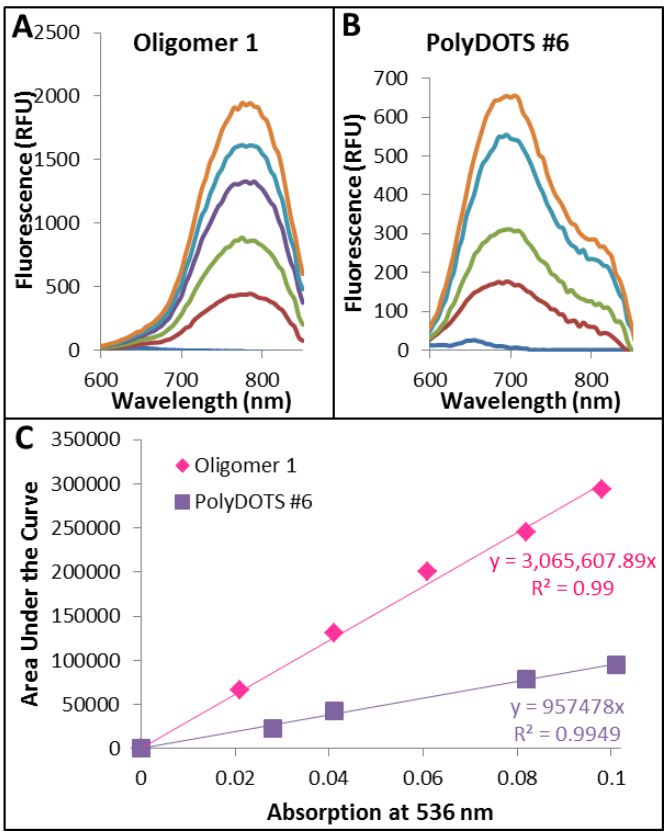

Figure 13. (A) Fluorescent spectra of oligomer 1 nanoparticles with absorption of 0.02, 0.04, 0.06, 0.08, 0.10 at 535 nm. **(B)** Fluorescent spectra of PolyDOTS #6 with absorption of 0.03, 0.04, 0.08, 0.10 at 535 nm. **(C)** Integration of the above curves plotted versus absorption at 535 nm. The slopes of these lines was compared to those of fluorescein and rhodamine 6G on the same machine.

Next, the stability PolyDOTS #6 was assessed. It was determined that PolyDOTS #6 is able to reproducibly generate heat (Figure 14A) and these heating cycles did not have any effect on the absorption spectra (Figure 14B), hydrodynamic diameter, or zeta potential (Figure 14C). Although, there was a 30% decrease in fluorescence intensity after the first heat cycle, no further decrease was seen after subsequent heating cycles (Figure 14D). PolyDOTS #6 are stable in deionized water, PBS, and media; remaining suspended up to 2 weeks (Figure 14E). However, there is a visible color change and shift in nanoparticles which is mirrored in the absorption spectra with the decrease of the 535 nm peak and the inititation and increase of a peak at 446 nm (Figure 14F). Interestingly, when excited at the new 446 nm peak, PolyDOTS #6 generated comparable fluorescence intensity to that at Day 0, albeit slightly blue shifted (Figure 14G).

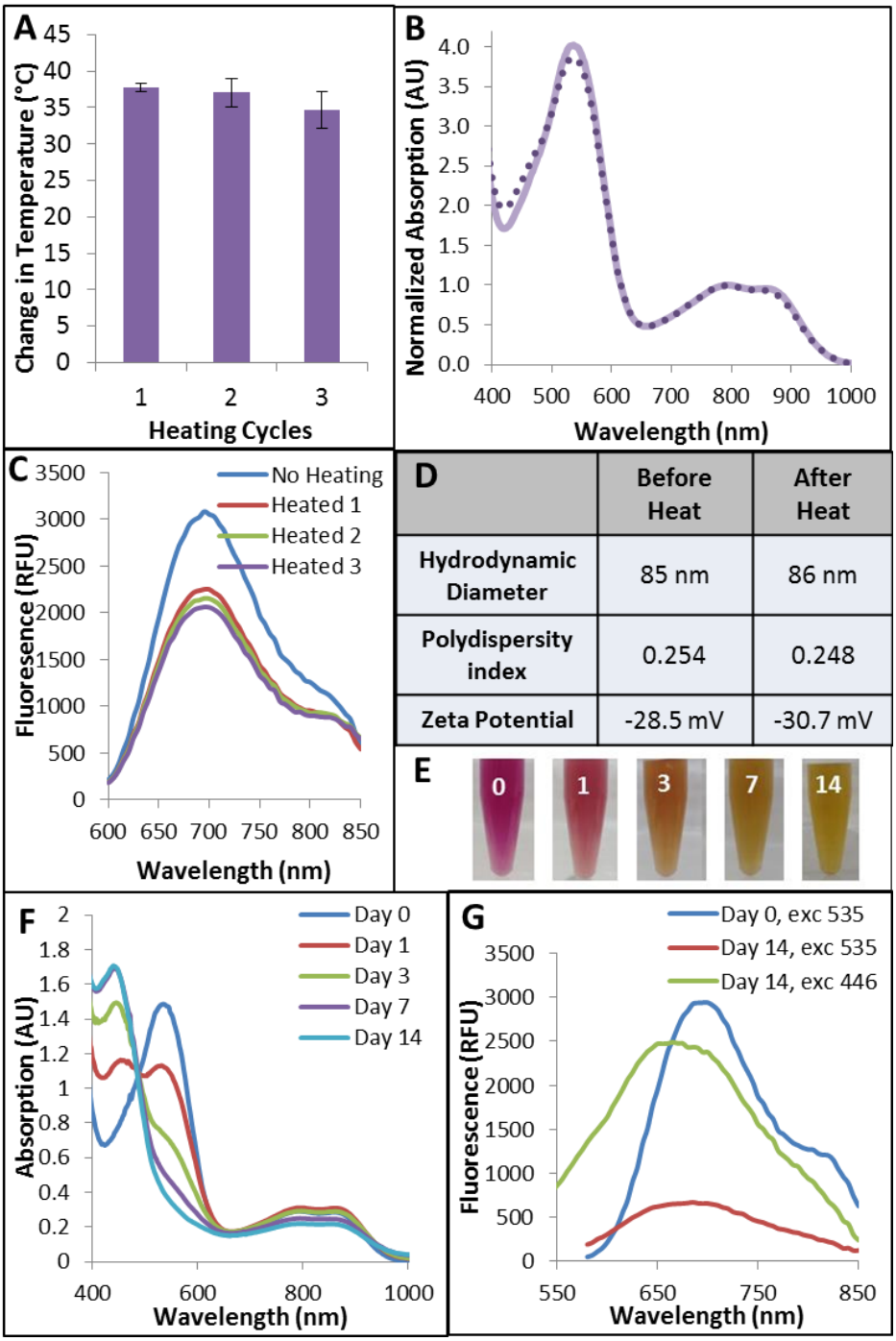

Figure 14. (A) Heating cycles of PolyDOTS #6 show reproducible generation of heat when exposed to 1 minute of 3 Watt, 800 nm light**. (B)** Absorption spectra of PolyDOTS #6 before (solid line) and after (dotted line) heat cycles. **(C)** Fluorescence spectra of PolyDOTS #6 prior to heating and after each heat cycle. **(D)** Dynamic light scattering data of PolyDOTS #6 before and after heat. **(E)** Image of PolyDOTS #6 in water on days 0, 1, 3, 7, and 14 illustrating color change**. (F)** absorption spectra of PolyDOTS #6 in water on days 0, 1, 3, 7, and 14. **(G)** Fluorescent spectra of PolyDOTS #6 in water, excited with 535 nm light on day 0 and 14, and excited with 446 nm light on day 14.

3.5 Conclusion

In conclusion, PolyDOTS #6 is an ideal candidate for *in vitro* and *in vivo* work that is an improvement on PolyDOTS #1. PolyDOTS #6 is an improvement due to the ability to reproducibly synthesize nanoparticles, the significantly increased fluoresence quantum yield, and ability to visualize *in vivo*. However, there are concerns about long term stability of Oligomer 1 due to its low molecular weight. As such, investigations as to whether a higher molecular weight conjugated polymer would be a more stable fluorescent component in a PolyDOTS should be done.

Acknowledgements
Chris MacNeill taught and assisted in the synthesis of CPDT monomer and PCPDTBSe polymer He also taught me and assisted in column chromatography of oligomeric PCPDTBSe to extract oligomers 1 and 2. We equally contributed to PolyDOTS #1 experimentation. I performed all experiments for PolyDOTS #2 - #6. Sneha Kelkar performed GPC experiments and data analysis.

CHAPTER 4

PolyDOTS #7 - #13: P3HT AND PCPDTBSe

4.1 Abstract

Theranostic nanoparticles, agents capable of both imaging and treatment, are becoming increasingly prevalent. Herein, the synthesis of an all-organic theranostic polymer nanoparticle that can be used for image-guided photothermal cancer therapy is described. The nanoparticle is built upon Poly(3-hexylthiophene-2,5-diyl), which fluoresces in the near infrared, combined with a near infrared absorbing polymer, poly[4,4-bis(2-ethylhexyl)-cyclopenta[2,1-*b*;3,4-*b'*]dithiophene-2,6-diyl-*alt*-2,1,3-benzoselenadiazole-4,7-diyl] (PCPDTBSe), to form a nanoparticle capable of both fluorescent imaging and photothermal therapy. The nanoparticles display no cytotoxic or clonogenic effects to either non-cancerous lung or brain, WI-38 and C8-D30, well differentiated liver carcinoma cell line HepG2, murine breast cancer cells EO771, or brain metastasis selected breast cancer cell line EO771 BR. However, the nanoparticles can generate significant heating under stimulation from near infrared light resulting in efficient photothermal ablation. The nanoparticles can be imaged using fluorescence microscopy. This nanoparticle system is both aqueously and optically stable and is ideal candidates for image-guided photothermal therapy of cancer.

Manuscript in preparation.

4.2 Introduction

Brain metastasis occurs in approximately 30% of breast cancer cases [124, 125] and only has an estimated 1 year survival rate of 20% [126]. The proportion of breast cancer patients that acquire brain metastases is increasing [124, 127, 128]. This is thought to be due to progresses in systemic chemotherapy treatments that prolong patient survival, but make the central nervous system a refuge to tumors since commonly used agents such as taxanes, anthracyclines, and trastuzumab cannot effectively cross the blood-brain barrier [124, 127, 128].

Radiation therapy, used as either a primary treatment or in conjunction with chemotherapy or surgery, is currently used for patients with multiple lesions larger than 35mm, inoperable lesions, or patients with a prognosis less than 3 months [124]. Unfortunately, radiotherapy only extends median survival from 1 - 2 months to 4 months [129] and therefore there is a clear need for new and improved treatments.

Recently, MRI guided laser interstitial thermal therapy (LITT) has been used as a minimally invasive surgical method to treat refractory glioblastoma [18] and metastatic brain tumors [19-21]. This procedure involves drilling a 4.37mm burr hole in the cranium through which the laser fiberoptic applicator and cooling catheter is threaded and a treatment dose of 10 - 15 Watts of 1064 nm light is applied for 30 - 180 seconds [21].

A way to improve LITT is through the use of photothermal agents with strong absorption at the specific laser light wavelength to improve light absorption and thus increase selective heating of the local environment [1, 25, 26]. The considerable recent developments of nanotechnology have provided a range of nanostructures with unique optical properties that can be utilized for photothermal therapy. The blood-brain barrier represents a substantial obstacle to treatment of brain metastasis however, nanoparticles have been utilized to permeate this barrier [130]. Nanoparticles are advantageous due to their small size, customizable properties, and ability to target predetermined tissues through conjugation of specific ligands to their surface [29-31]. If the nanoparticle is targeted through ligand functionalization to a predetermined tissue, this can

generate selective photothermal ablation and result in less thermal damage to the untargeted healthy tissue.

Utilizing a theranostic nanoparticle, capable of both fluorescent imaging and photothermal therapy, would allow for both detection and treatment of metastatic lesions. Our lab has developed a theranostic nanoparticle [Chapter 3], however, the lack of optical stability of the fluorescent component, oligomeric PCPDTBSe, needs improvement. Utilizing a higher molecular conjugated polymer such as poly(3-hexylthiophene-2,5 diyl) (P3HT), which absorbs in the visible (510 nm) and emits in the near infrared (700 nm). In this chapter, the development and characterization of a hybrid theranostic nanoparticle composed of P3HT and PCPDTBSe for photothermal therapy of the brain metastasis of breast cancer is discussed.

4.3 Materials and Methods

4.3.1 Materials

All reagents were purchased from common commercial sources and used without further purification unless otherwise noted. *4H*-cyclopenta-[1,2-*b*:5,4-*b'*]dithiophene was purchased from Astar Pharma. 4,7-dibromo-2,1,3-benzoselenadiazole was purchased from TCI America. Poly(3-hexylthiophene-2,5 diyl) region-regular, molecular weight 15,000-45,000 was purchased from Sigma Aldrich. DSPE-PEG-COOH molecular weigh 3400 was purchased from Nanocs. Tetrahydrofuran (THF) was purchased from Fisher Scientific. 4,4-*Bis*(2-ethylhexyl)-2,6-*bis*(trimethylstannyl)-4H-cyclopenta-[2,1-*b*;3,4-*b'*]dithiophene was synthesized according to its published procedure.[109-113]

4.3.2 Quantification of P3HT

Since P3HT does not completely dissolve in THF, P3HT pellets were incubated in THF overnight and then filtered to remove undissolved polymer. To determine the concentration of P3HT dissolved in THF, P3HT was allowed to dissolve in THF before being filtered to remove undissolved P3HT. A portion of this stock solution was serially diluted in THF and the absorption spectra taken. To determine the concentration of the stock solution, a known volume was added

to a pre-weighed glass vial and the solvent was allowed to evaporate. The vial was re-weighed to obtain the mass. The λmax, 444 nm, was then plotted versus the concentration to yield an absorption-concentration calibration curve of P3HT in THF.

4.3.3 Gel Permeation Chromatography

Polymers were characterized using GPC to determine the relative weight-average molecular weights (M_W). A calibration curve was developed using three polystyrene standards (ReadyCal-kit, Polymer Standards Service-USA Inc.) of molecular weights varying between 500-1200 kDa. HPLC grade THF was used as mobile phase and flow rate was adjusted to 0.5 mL per minute. Polymers were dissolved in THF at 2 mg/mL concentration and separated with Styragel® HT 3 column (7.8 x 300 mm, Waters Corporation, USA) on GPC system equipped with Waters 2998 Photodynamic array, 2414 refractive index detectors, and Wyatt's miniDAWN TREOS multi-angle light scattering detector. The data was recorded and analyzed using ASTRA (version 6.1) software.

4.3.4 Synthesis of PolyDOTS #7 - #13 and P3HT Nanoparticles

P3HT-DSPE: P3HT [2 mL, 0.25 mg/mL in THF] was injected under continuous horn sonication (90 seconds, 45% amplitude) into 8 mL of DSPE-PEG-COOH [0.25 mg/mL in water].

PolyDOTS: P3HT and PCPDTBSe were pre-mixed in various mass ratios (1:4, 1:3, 2:3, 1:1, 3:2, 3:1, 4:1) always maintaining 0.25 mg/mL polymer concentration in THF. Two milliliters of the pre-mixed P3HT-PCPDTBSE was injected under continuous horn sonication (90 seconds, 45% amplitude) into 8 mL of DSPE-PEG-COOH [0.25 mg/mL in water].

Nanoparticle Collection: Nanoparticle solutions were stirred at room temperature for 2 hours to help remove excess THF before being centrifuged (30 minutes, 7,500 rpm) to remove large nanoparticles and aggregates. The resulting supernatant was centrifuged (4 hours, 14,000 rpm) to collect nanoparticles.

4.3.5 Nanoparticle Characterization: UVvis, DLS, TEM, fluoresence quantum yield

Dynamic light scattering (DLS) with zeta potential was measured in water using a Malvern Instruments Zetasizer Nano-ZS90 light scattering instrument. UVvis spectrometry was taken on a Beckman Coulter DU® 730 Life Sciences UV-vis spectrophotometer. Fluorescence spectra were obtained on TECAN M200 Infinite plate reader. Fluorescence quantum yield was obtained by comparative method as described previously in Chapter 3.

4.3.6 Quantification of PolyDOTS #10

The concentration of Poly-DOTS #10 in water was obtained by lyophilization of a concentrated nanoparticle solution to dryness to measure its mass. Once the mass was known, the remaining nanoparticle solution was serially diluted and absorption spectra were taken on a Beckman Coulter DU® 730 Life Sciences UV-vis spectrophotometer. The absorbance at λ_{max} = 760 nm of Poly-DOTS at different concentrations was recorded and plotted versus the concentration to generate an absorption-concentration calibration curve.

4.3.7 Heating Methods

Two hundred microliters of Poly-DOTS suspended in water were added to a 96 well plate for temperature testing. A Cube^{TM} continuous wave diode laser from K-laser (800 nm, 1 cm diameter, 3 W) was used to apply NIR light to the solutions for 1 min per well. A Fluke 714 thermocouple calibrator and a type k 80Pk-1 bead probe wire thermocouple measured the temperature of the solutions immediately before and after laser application. To assess heating reproducibility, heating/cooling curves of Poly-DOTS were completed over 10 cycles. Each cycle included 1 min of laser time followed by 30 minutes of cooling time before the start of the next cycle. To determine the effect that multiple heating/cooling cycles have on the optical properties of PolyDOTS, UVvis and fluorescent spectra were taken.

4.3.8 Cell Culture

Murine breast cancer cell line, EO771 parental, and brain metastasis selected breast cancer cell line, EO771 BR5, were generously gifted by Metheny-Barlow lab. As brain metastasis is

being studied, a non-cancerous murine astrocyte cell line, C8-D30 was purchased from ATCC. Due to the fact that nanoparticles often accumulate in organs of the reticuloendothelial system, a non-cancerous lung cell line, WI-38, a well differentiated liver carinoma cell line, HepG2 were obtained from CVVL and also used as controls.

4.3.9 Statistical Analysis

Statistical analysis was performed by one-way analysis of variance and post hoc Fisher LSD test.

4.3.10 In Vitro Characterization

Cytotoxicity Assay: Cells were plated at a density of 5,000 cells per well in a 96 well tissue culture plate and cultured for 24 hours. 200 µL of Poly-DOTS #10 were added to the well plates at concentrations of 0, 5, 10, 20, 30, 40, 50, and 100 µg/mL and incubated for 24 hours. Nanoparticle solutions were removed and cells were washed twice with PBS before MTS assay was performed. Absorbance values were normalized to the 0 µg/mL control.

Photothermal Ablation Assay: Cells were plated at a density of 5,000 cells per well in a 96 well tissue culture plate and cultured for 24 hours. 200 µL of Poly-DOTS #10 were added to the well plates at concentrations of 0, 5, 10, 15, and 25 µg/mL. Near infrared light (800 nm, continuous wavelength, 2.654 W/cm^2) was applied for 1 minute per well. Following 800 nm light exposure, nanoparticle solutions were removed, wells were washed twice with PBS, fresh cell medium was added and the cells were incubated at 37°C for 24 hours. Cell viability was then quantified using an MTS assay and absorbance values were normalized to the 0 µg/mL control.

Confocal Microscopy: EO771 BR5 and C8-D30 cells were plated at a density of 100,000 cells/well onto collagen coated, two chamber well plates. Poly-DOTS #5, 30 µg/mL in cell culture medium, were incubated with the cells at 37°C for 24 hours. The nanoparticle solutions were removed, and cells washed twice with cold PBS solution. Cells were fixed with 4% paraformaldehyde (20 minutes in 1x PBS), permeabilized by 0.1% Triton-x-100 (5 minutes in 1x PBS), blocked with 1% bovine serum albumin, stained with alexa-fluor-488 phalloidin. Cells

were visualized by Zeiss LSM 510 confocal microscope. PolyDOTS were excited with 514 nm light with argon laser and detected using a 650 nm long pass filter.

4.4 Results

4.4.1 Synthesis and Characterization of PCPDTBSe and P3HT

A Stille coupling procedure was employed to polymerize of 4,4-*bis*(2-ethylhexyl)-2,6-*bis*(trimethylstannyl)-4H-cyclopenta-[2,1-*b*;3,4-*b'*]dithiophene with 4,7-dibromo-2,1,3-benzoselenadiazole in the presence of palladium catalyst using a reflux synthesis similar to reference [109].

P3HT was purchased from Sigma. Since P3HT does not completely dissolve in THF, it was necessary to have an alternate method to determine P3HT concentration in THF. As such, P3HT pellets were incubated in THF then filtered to remove undissolved polymer. A portion of this stock solution was serially diluted in THF and the absorption spectra taken. To determine the concentration of the stock solution, a known volume was added to a pre-weighed glass vial and the solvent was allowed to evaporate. The vial was re-weighed to obtain the mass. The λmax, 444 nm, was then plotted versus the concentration to yield an absorption-concentration calibration curve of P3HT in THF (Figure 1A)

GPC was used to determine the molecular weight of the P3HT that would readily dissolve in THF and the synthesized PCPDTBSe. As seen in Figure 1B, both P3HT and PCPDTBSe have a molecular weight of approximately 25,0000.

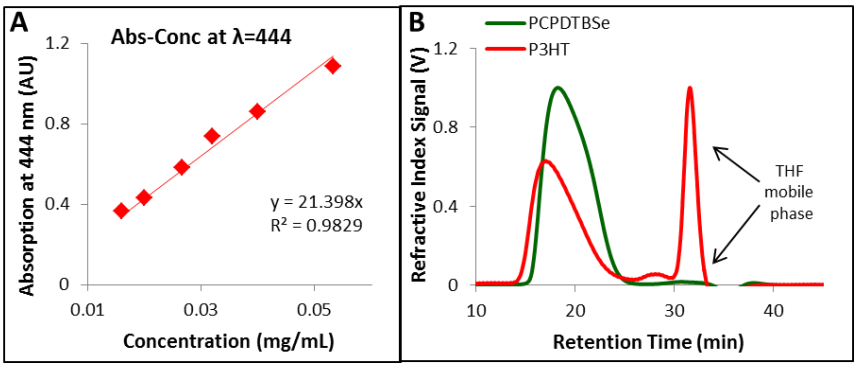

Figure 1. (A) Absorption-concentration calibration curve of P3HT in THF. **(B)** GPC of PCPDTBSe and P3HT using THF as an eluent and polystyrene standards.

4.4.2 Synthesis and Characterization of Poly-DOTS and P3HT Nanoparticles

Poly-DOTS were synthesized using a nanoprecipitation method (Figure 2A). Polymers were dissolved in THF and rapidly injected into an aqueous solution containing DSPE-PEG-COOH under horn sonication. Upon injection, the hydrophobic polymer self-assembles within the hydrophobic core of the DSPE-PEG-COOH micelle leading to the formation of water soluble nanoparticle. Several PolyDOTS were synthesized with a range of proportions of P3HT to PCPDTBSe as summarized in Table 1 and their optical absorption spectra are shown in Figure 2B. The absorption spectrum of Poly-DOTS show peaks at 508 nm and 800 nm indicating the presence of both P3HT and PCPDTBSe. Additionally, when excited at 508 nm, Poly-DOTS generate a fluorescence emission peak at 710 nm (Figure 2C). As the ratio of P3HT and PCPDTBSe changes, there is a visible shift in the color of the nanoparticles (Figure 2D).

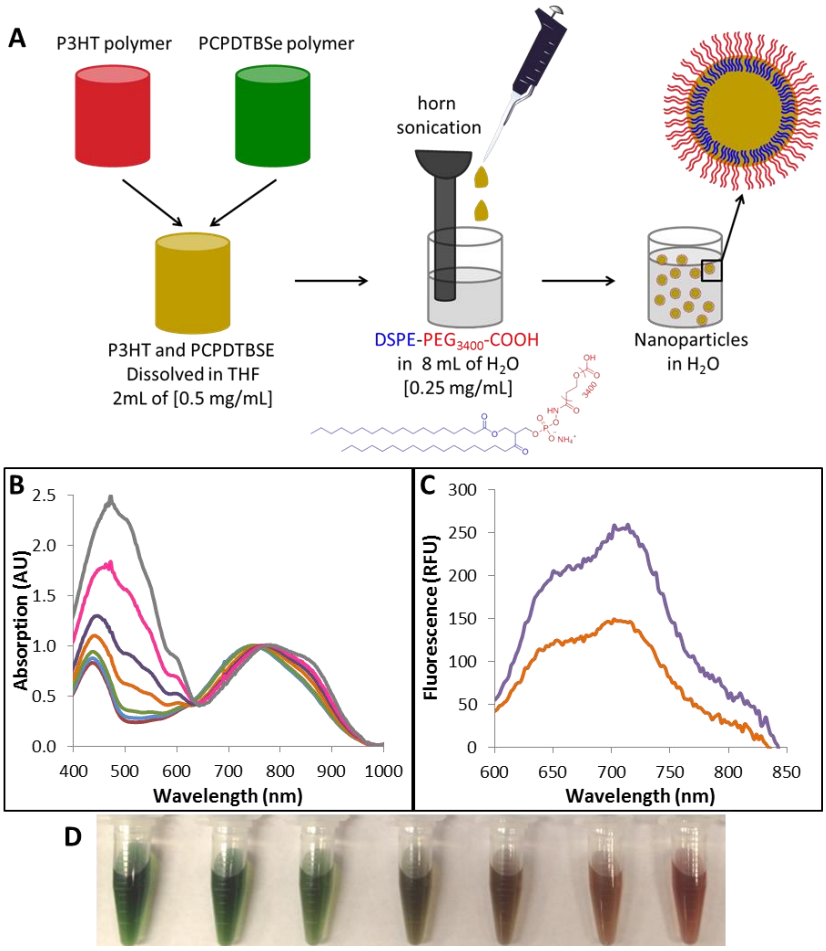

Figure 2. (A) Schematic of PolyDOTS synthesis. **(B)** Absorption spectra of PolyDOTS #7 (red), #8 (blue), #9 (green), #10 (orange), #11 (purple), #12 (pink), and #13 (grey) normalized for PCPDTBSe component (fixed absorption of 1 at wavelength 756 nm). **(C)** Fluorescent spectra of PolyDOTS #5. **(D)** Image of PolyDOTS in ascending order #7 through #13.

	Mass of P3HT added [µg]	Mass of PCPDTBSe added [µg]	Ratio of P3HT to PCPDTBSe added	Ratio of Absorption at 508nm:800nm
PolyDOTS #7	100	400	1:4	0.37
PolyDOTS #8	125	375	1:3	0.40
PolyDOTS #9	200	300	2:3	0.48
PolyDOTS #10	250	250	1:1	0.83
PolyDOTS #11	300	200	3:2	1.2
PolyDOTS #12	375	125	3:1	1.9
PolyDOTS #13	400	100	4:1	2.9

Table 1. Mass of P3HT and PCPDTBSe added to generate PolyDOTS #7 - #13. This ratio of polymers added is compared to the ratio that is incorporated into the nanoparticles (as observed by absorption intensity at 508 nm, P3HT, compared to 800 nm, PCPDTBSe).

Nanomaterials were evaluated by dynamic light scattering (summarized in Table 2 and interestingly it was found that as the ratio of P3HT increased, the polydispersity index decreases. Additionally, the size increases. As expected, the zeta potential stays approximately the same; strongly negative between -30 and -40 mV. P3HT nanoparticles and PolyDOTS #10 and #11 were visualized using transmission electron microscopy (TEM) and all nanoparticles were found to be spherical with an electro-dense polymer core of diameters 30 - 60 nm (Figure 3).

	Hydrodynamic Diameter [nm]	Polydispersity Index	Zeta Potential [mV]
PCPDTBSe	98.5	0.645	-35.4
PolyDOTS #7	91.5	0.624	-27.8
PolyDOTS #8	88.5	0.547	-31.1
PolyDOTS #9	96.2	0.358	-24.4
PolyDOTS #10	105.9	0.201	-29.8
PolyDOTS #11	104.4	0.160	-32.0
PolyDOTS #12	113.3	0.093	-31.8
PolyDOTS #13	110.8	0.087	-32.3
P3HT	144.7	0.099	-38.9

Table 2. Dynamic light scattering data of PCPDTBSe-DSPE, P3HT-DSPE, and PolyDOTS #7 - #13. Hydrodynamic diameter determined using distribution analysis for PCPDTBSe-F127, and PolyDOTS #7 - #11and using cumulant analysis for PolyDOTS #12, #13, and P3HT-DSPE.

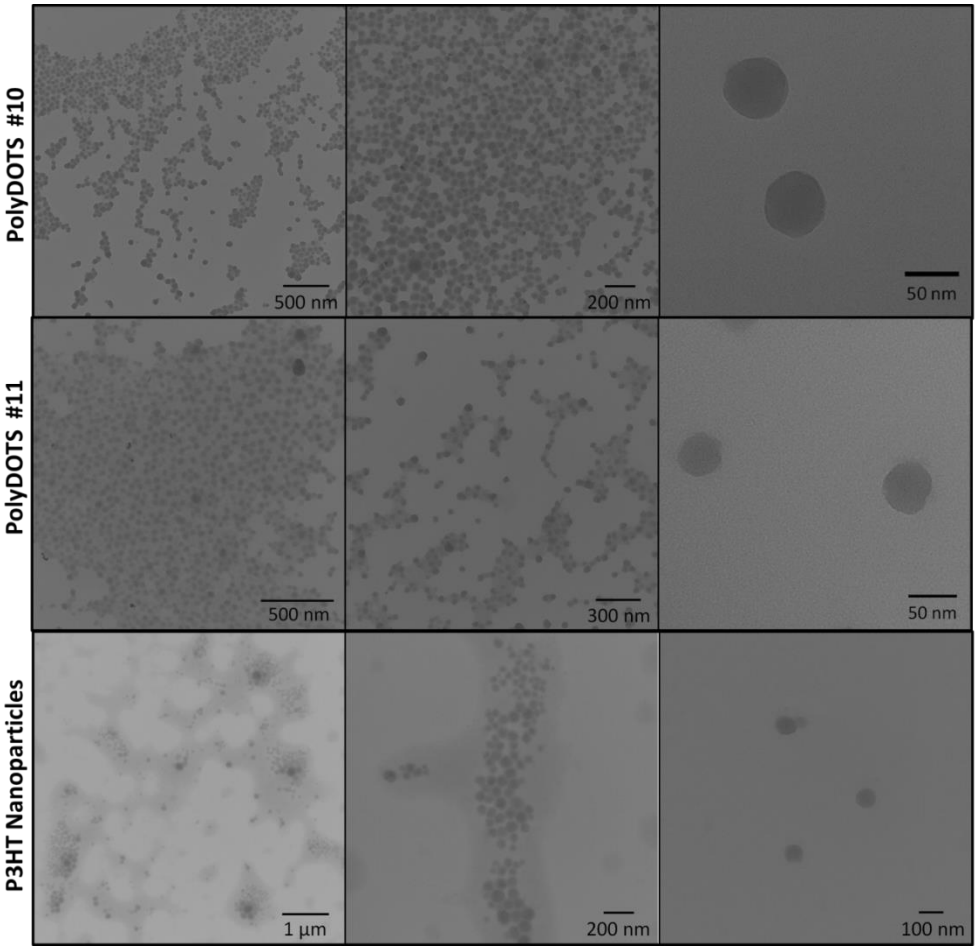

Figure 3. Transmission electron microscopy images of PolyDOTS #10, #11, and P3HT-DSPE nanoparticles. A film appears to be surrounding P3HT-DSPE nanoparticles and PolyDOTS #11. This same film is not seen on PolyDOTS #10.

Based on the improved TEM and polydispersity index, PolyDOTS #10 was selected for further investigation. It was determined that PolyDOTS #10 could be reproducibly synthesized as seen in Figure 4A, generating comparable absorption spectra across 5 different batches. An absorption-concentration and fluorescence-concentration calibration curves were generated for PolyDOTS #10 (Figure 4B and C). Poly-DOTS #10 generates excellent heating when stimulated by 800 nm light, comparable to carboxylated multi-walled carbon nanotubes and PCPDTBSe-F127 (Figure 4D) and maintain their heating and 90% of their fluorescent capabilities over 10 cycles of NIR stimulation (Figure 4E and F).

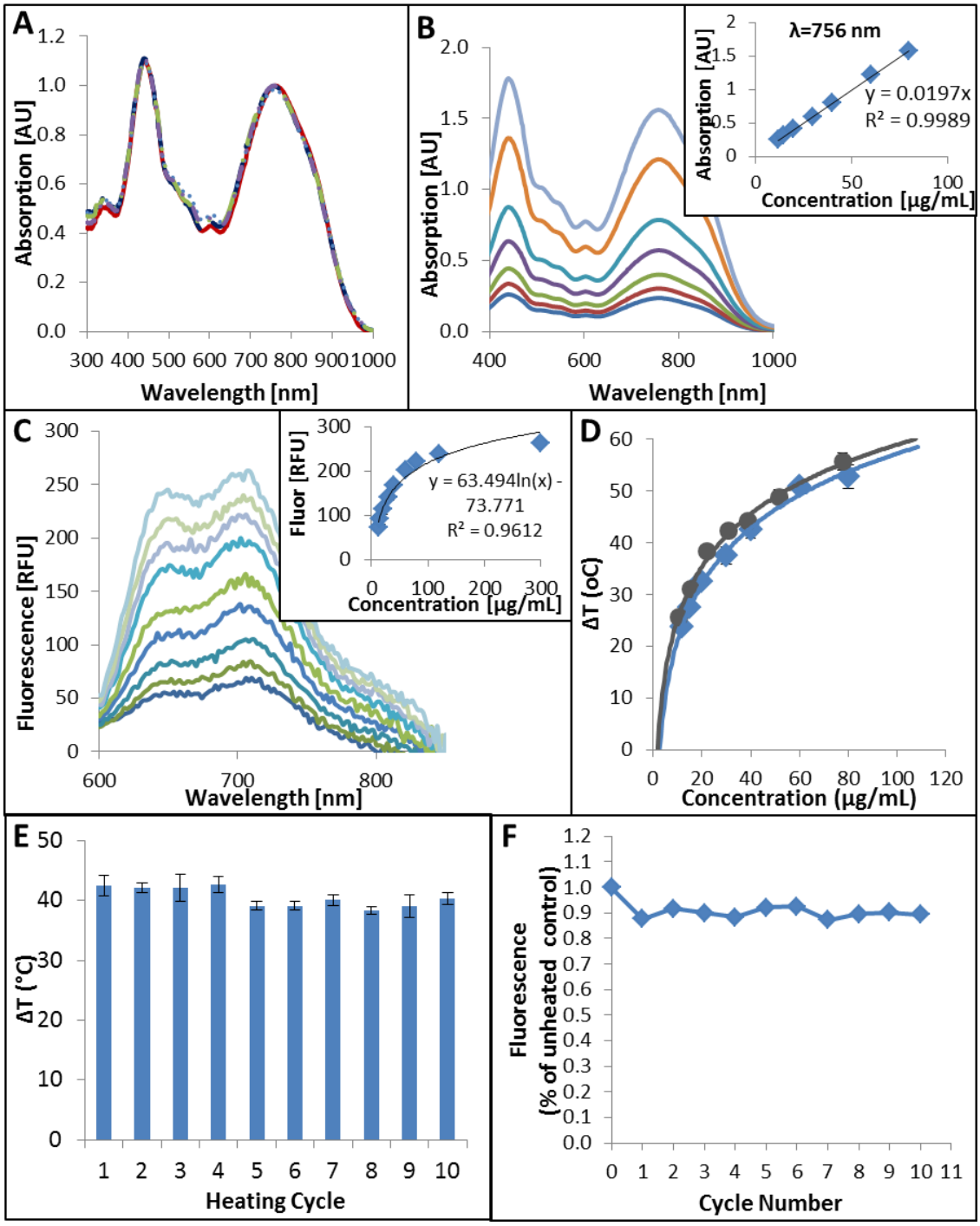

Figure 4. (A) Absorption spectra comparison of multiple "batches" of PolyDOTS #10**. (B)** Absorption and **(C)** fluorescence-concentration calibration curves of PolyDOTS #10**. (D)** Heating curve of PolyDOTS #10 (blue) compared to carboxylated multi-walled carbon nanotubes (grey). Both nanomaterials were exposed to 800 nm light for 1 minute at 2.654 W/cm^2**. (E)** Heat cycles of PolyDOTS #10 illustrating the ability to generate heat over multiple exposures to near infrared stimulation**. (F)** Effect that the heat cycles had on the maximum fluorescent intensity of PolyDOTS #10. Error bars shown are standard deviation.

The photostability of nanoparticles is important for potential long term tracking and other imaging applications. Various tests of the photostability of Poly-DOTS #10 can be seen in Figure 5. Poly-DOTS #10 display strong optical and aqueous stability in water and phosphate buffered solution stored in ambient light over 30 days, with no decrease in fluorescence.

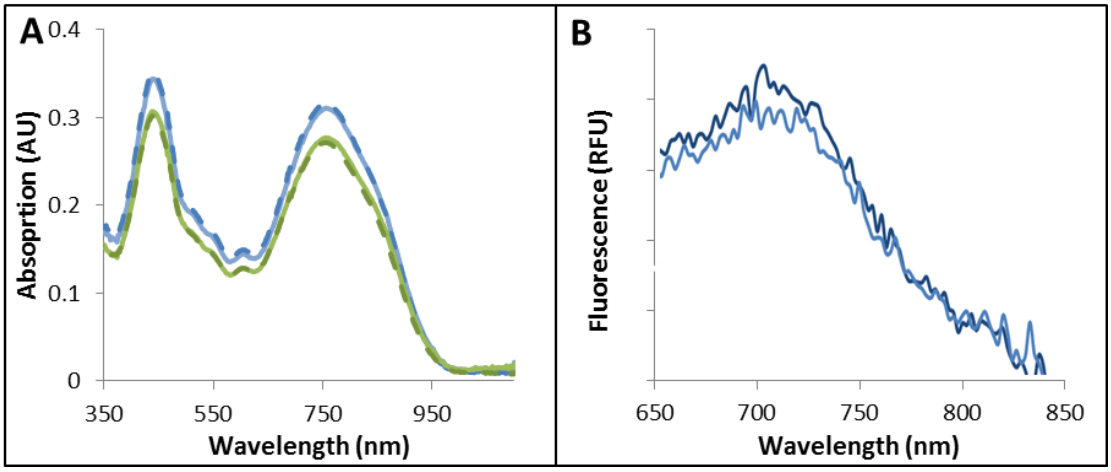

Figure 5. (A) Absorption of PolyDOTS #10 stored in water (blue) and PBS (green) at Day 0 (solid line) and Day 30 (dashed line). **(B)** Fluorescence spectra of PolyDOTS #10 at Day 0 (blue) and Day 30 (grey).

The fluorescence quantum yield of P3HT nanoparticles and Poly-DOTS #10 were found to be 1.54% and 0.22%, respectively. The low fluorescence quantum yield is comparable to other near infrared fluorescing conjugated polymers [82]. The decreased quantum yield for PolyDOTS #10 may be due to quenching by PCPDTBSe, polymer-polymer aggregation induced excited state quenching, large nanoparticle size (affecting exciton coupling) or quenching of excitons.[131, 132]

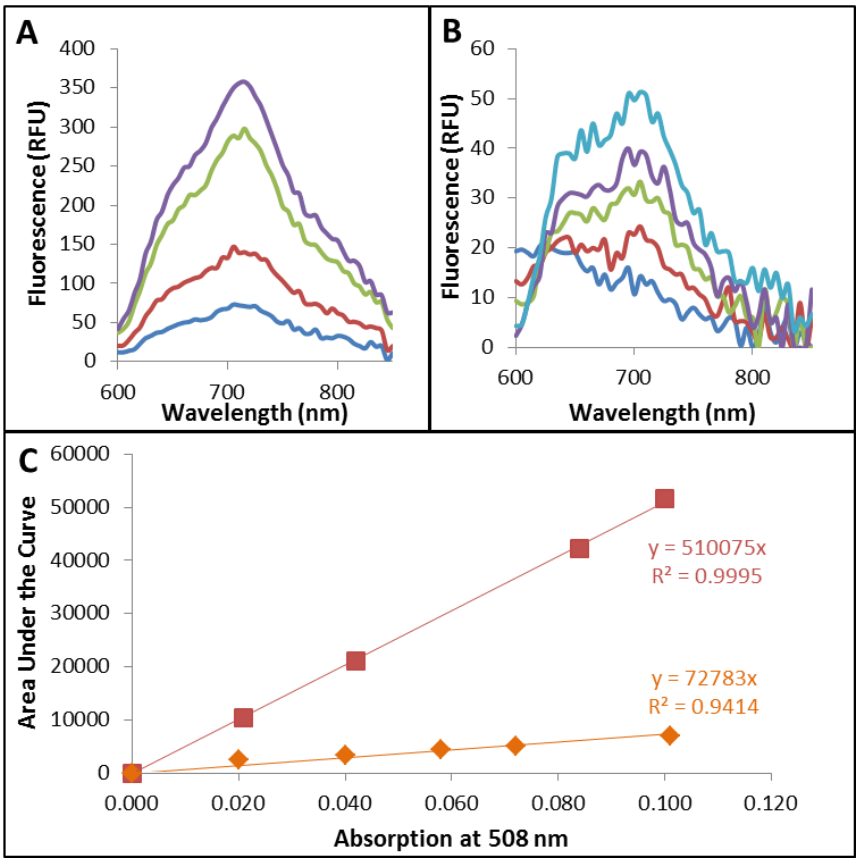

Figure 6. (A) Fluorescent spectra of P3HT nanoparticles with absorptions of 0.02, 0.04, 0.08, and 0.10 at 508 nm. **(B)** Fluorescent spectra of PolyDOTS #10 with absorptions of 0.02, 0.04, 0.058, 0.07, and 0.10 at 508 nm. **(C)** The area of the above curves was integrated and plotted versus the absorption at 508 nm. These slopes were compared to the slopes of fluorescent standards fluorescein and rhodamine 6G.

4.4.3 In Vitro Characterization of Poly-DOTS #10

The acute cytotoxicity of Poly-DOTS #10 was assessed using a conventional MTS cell viability assay. After 24 hours of incubation in the absence of 800 nm light, PolyDOTS #10 showed no substantial effect on cell viability for brain selected breast cancer cell line EO771 BR, non-cancerous lung cell line WI-38, or liver cell ine HepG2 (Figure 7A). However, EO771 parental and astrocyte cell line, C8-D30 show approximately a 20% decrease in cell viability between 40 and 100 µg/mL. After exposure to 800 nm light (2.654 W/cm^2, 1 minute), Poly-DOTS #10 demonstrated excellent photothermal ablation, resulting in complete cell death at 20

µg/mL for breast cancer cell line EO771 parental and EO771 BR and 25 µg/mL for non cancerous astrocyte cell line C8-D30 (Figure 7B).

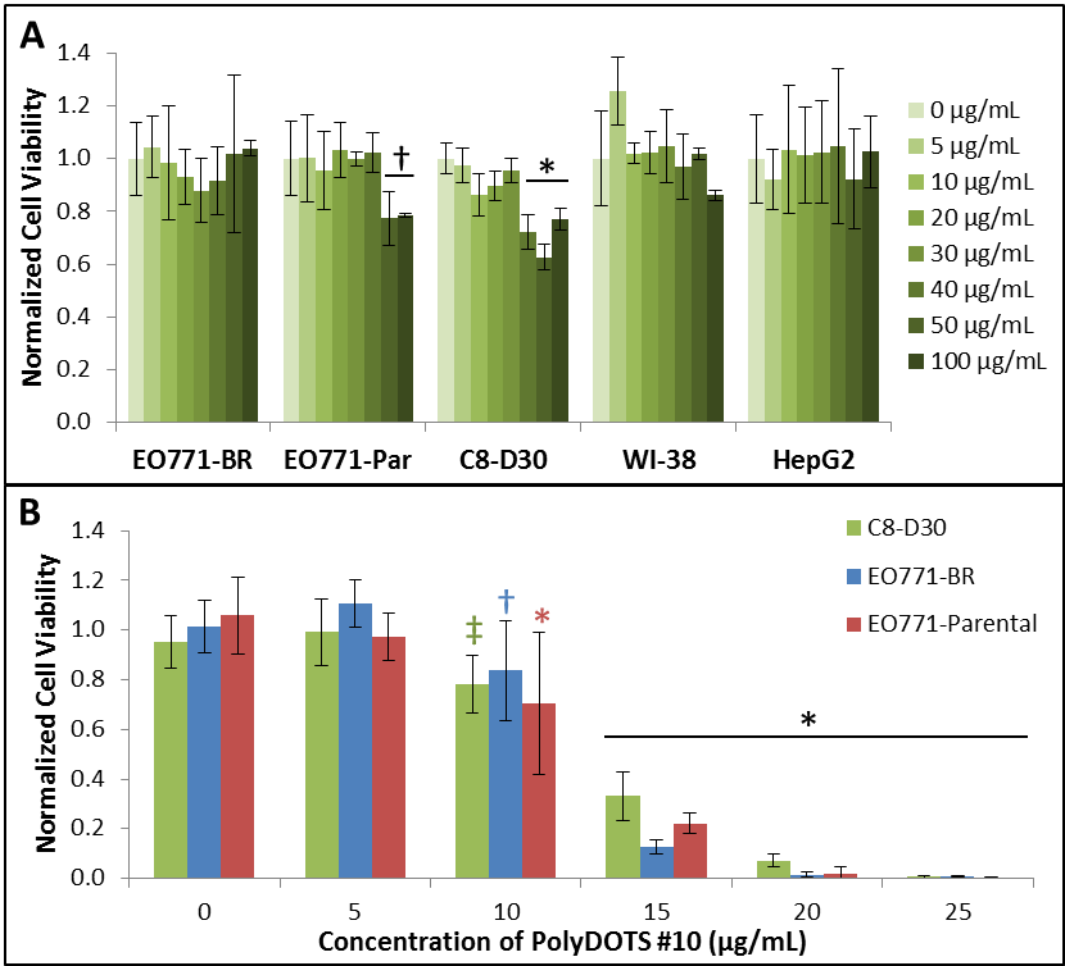

Figure 7. (A) In vitro cytotoxicity of PolyDOTS #10 incubated with cells for 24 hours. **(B)** Photothermal ablation of C8-D30, EO771 BR and EO771 par cell lines incubated with PolyDOTS #10 and exposed to 1 minute of 3 Watt, 800 nm light. Error bars shown are standard deviation. * $p<0.001$, † $p < 0.03$, ‡ $p<0.01$ compared to 0 µg/mL control.

Fluorescent microscopy was done to investigate *in vitro* cellular uptake of Poly-DOTS #10 in both C8-D30 and EO771 BR cell lines. After a 24 hour incubation with Poly-DOTS #10 at 30 µg/mL, the cells were stained with alexa-fluor488-phalloidin to visualize the cytoskeleton imaged by confocal microscopy. Figure 8 illustrates that Poly-DOTS #10 are visible attached to both cell lines. Additionally, the nanoparticles also appear to have bound to the plate as well. This non-selective binding suggests a need for a more targeted therapy, possibly through the

conjugation of a targeting ligand to the DSPE-PEG-COOH. The absence of intracellular nanoparticles suggests that although our nanoparticles were found to be not-cytotoxic, this may be due to lack of uptake rather than actual lack of cytotoxicity. The absence of a "no nanoparticle" control affects the interpretation of this data and will be investigated in the future.

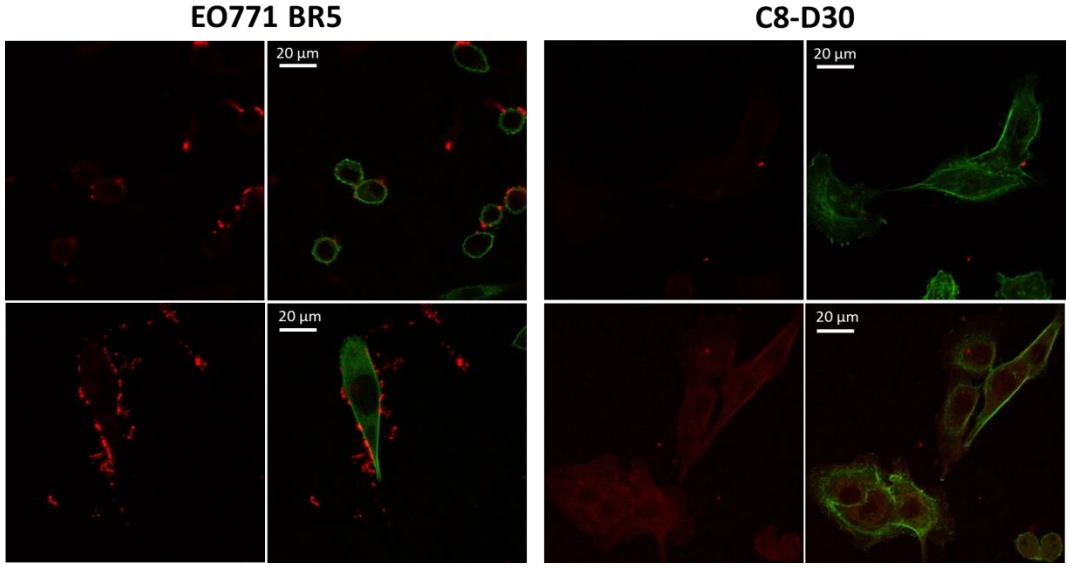

Figure 8. Confocal microscopy imaged of EO771 BR and C8-D30 cells incubated with PolyDOTS #10. The cytoskeleton of cells are stained green with elexafluor488 phalloidin and PolyDOTS #10 are seen as red. Figures on the left show just the fluorescence from PolyDOTS #10, and images on the right are merged with the fluorescence from alexa488phalloidin.

4.5 Conclusions

In conclusion, we have developed a non-cytotoxic hybrid nanoparticle capable of fluorescent imaging and efficient photothermal therapy. PolyDOTS #10 is stable in aqueous solution, and optically stable when exposed to ambient light for 30 days and after repeated stimulation and heating with near infrared light. Additionally, PolyDOTS #10 is an improvement over PolyDOTS #1 and #6 as far as optical stability. Unfortunately, although the nanoparticles are easily visible *in vitro*, the fluorescence quantum yield is too low for *in vivo* imaging. As such, investigation of a conjugated polymer with high brightness in the NIR should be done.

Acknowledgements
Chris MacNeill taught and assisted in CPDT monomer and PCPDTBSe polymer synthesis. Sneha Kelkar performed GPC experiments and did data analysis.

CHAPTER 5

PolyDOTS #14 - #18: PFBTDBT10 AND PCPDTBSe

5.1 Abstract

Theranostic nanoparticles offer many advantages over nanoparticles just capable of treating or imaging. Additionally, they offer key insights into *in vitro* and *in vivo* behavior of nanoparticles. Herein, the synthesis of an all-organic theranostic polymer nanoparticle that can be used for image-guided photothermal therapy of breast cancer is described. The nanoparticle is built upon poly[(9,9-dihexylfluorene)-co-2,1,3-benzothiadiazole-co-4,7-di(thiophen-2-yl)-2,1,3-benzothiadiazole], which fluoresces in the near infrared, combined with a near infrared absorbing polymer, poly[4,4-bis(2-ethylhexyl)-cyclopenta[2,1-*b*;3,4-*b'*]dithiophene-2,6-diyl-*alt*-2,1,3-benzoselenadiazole-4,7-diyl] (PCPDTBSe), to form a nanoparticle capable of both fluorescent imaging and photothermal therapy. This hybrid nanoparticle, termed PolyDOTS (polymer organic theranostic spheres), is both aqueously and optically stable in acidic, basic, and strongly ionic solutions. PolyDOTS display no cytotoxic or clonogenic effects to either non-cancerous murine fibroblast cell line, BALB/c CL.7, or murine breast cancer cell lines EO771 and 4T1. However, they can generate significant heating under stimulation from near infrared light resulting in efficient photothermal ablation. Additionally, PolyDOTS are bright enough to be visible *in vivo* and, as such, are an ideal candidate for image-guided photothermal therapy of cancer.

Manuscript in preparation.

5.2 Introduction

Recently, conjugated polymers are receiving significant attention for biomedical applications. We have previously utilized the conjugated polymer poly[4,4-bis(2-ethylhexyl)cyclopenta[2,1-b;3,4-b']dithiophene-2,6-diyl-alt-2,1,3-benzoselenadiazole-4,7-diyl] (PCPDTBSe) to develop very aqueously stable spherical nanoparticles capable of efficient photothermal ablation [99, 133]. *Ding et al.* [81] recently published synthesis of conjugated polymer poly[(9,9-dihexylfluorene)-co-2,1,3-benzothiadiazole-co-4,7-di(thiophen-2-yl)-2,1,3-benzothiadiazole (PFBTDBT10) which has high quantum yield fluorescence in the near infrared. We hypothesize that by combining PCPDTBSe and PFBTDBT10 we can generate a hybrid theranostic nanoparticle capable of both photothermal ablation and fluorescent imaging of cancer. The optical properties, *in vitro* cytotoxicity, clonogenicity, and photothermal efficacy, as well as *in vivo* studies are discussed herein.

5.3 Materials and Methods

5.3.1 Materials

All reagents were purchased from common commercial sources and used without further purification unless otherwise noted. 4H-cyclopenta-[1,2-b:5,4-b']dithiophene was purchased from Astar Pharma. 4,7-dibromo-2,1,3-benzoselenadiazole and 2,2'-(9,9-dihexyl-9H-fluorene-2,7-diyl)bis(4,4,5,5-tetramethyl-1,3,2-dioxaborolane), CAS #: 254755-24-3, were purchased from TCI America. Pluronic®F127, tetraethylammonium hydroxide, 2,1,3-benzothiadiazole, CAS # 15155-41-6, and 4,7-Bis(2-bromo-5-thienyl)-2,1,3-benzothiadiazole, CAS # 288071-87-4 were purchased from Sigma Aldrich. Tetrahydrofuran (THF) was purchased from Fisher Chemical Co. 4,4-*Bis*(2-ethylhexyl)-2,6-*bis*(trimethylstannyl)-4H-cyclopenta-[2,1-*b*;3,4-*b'*]dithiophene were synthesized according to published procedure.[109-113]

5.3.2 Synthesis of PCPDTBSe

4,4-*Bis*(2-ethylhexyl)-2,6-bis(trimethylstannyl)-4H-cyclopenta [2,1-*b*;3,4-*b'*]dithiophene (1.5 mmol) and 4,7-dibromo-2,1,3-benzoselenadiazole (1 mmol) were dissolved in anhydrous

toluene and stirred in the presence of $Pd(PPh_3)_4$ (5 mol %) at 110°C for 24 hours. The polymer was precipitated in methanol and collected by vacuum filtration. The solid was then transferred to a Soxhlet thimble and subjected to extraction with methanol, hexanes, and finally chloroform. The chloroform extract was evaporated, precipitated in methanol, and collected to yield high molecular weight PCPDTBSe.

5.3.3 Synthesis of PFBTDBT10

2,2'-(9,9-dihexyl-9H-fluorene-2,7-diyl)bis(4,4,5,5-tetramethyl-1,3,2-dioxaborolane) (293 mg, 0.5 mmol), 2,1,3-benzothiadiazole (117.6, 0.4 mmol), and 4,7-Bis(2-bromo-5-thienyl)-2,1,3-benzothiadiazole (45.8 mg, 0.1 mmol) were dissolved in 20 mL of anhydrous toluene and stirred in the presence of $Pd(PPh_3)_4$ (25 mg, 20 mmol) at 80°C for 20 hours. After the mixture was heated, an aqueous solution of Et4NOH (1.7 mL, 35 wt%) was added to initiate the reaction. After 20 hours, the reaction was allowed to cool to room temperature to yield poly[(9,9-dihexylfluorene)-co-2,1,3-benzothiadiazole-co-4,7-di(thiophen-2-yl)-2,1,3-benzothiadiazole] (PFBTDBT10). PFBTDBT10 was dissolved in dichloromethane, washed three times with water and dried over magnesium sulfate. After solvent removal by rotary evaporation, the polymer was dissolved in THF and stored.

5.3.4 Gel Permeation Chromatography

Polymers were characterized using GPC to determine the relative weight-average molecular weights (M_W). A calibration curve was developed using three polystyrene standards (ReadyCal-kit, Polymer Standards Service-USA Inc.) of molecular weights varying between 500-1200 kDa. High performance liquid chromatography grade THF was used as mobile phase and flow rate was adjusted to 0.5 mL/min. Polymers were dissolved in THF at 2 mg/mL concentration and separated with Styragel® HT 3 column (7.8 x 300 mm, Waters Corporation, USA) on a GPC system was equipped with Waters 2998 Photodynamic array, and 2414 refractive index detectors, and Wyatt's miniDAWN TREOS multi-angle light scattering detector. The data was recorded and analyzed using ASTRA (version 6.1) software.

5.3.5 Synthesis of PolyDOTS, PFBTDBT10, and PCPDTBSe Nanoparticles

PFBTDBT10 and PCPDTBSe Nanoparticles: PFBTDBT10 1 (1mL, 2 mg/mL in THF) or PCPDTBSe (1 mL, 2 mg/mL in THF) were injected under continuous horn sonication via Branson Digital Sonifier fitted with a microtip (1 minute, 20% amplitude) into Pluronic®F127 (8 mL, 1 mg/mL in water).

PolyDOTS: PFBTDBT10 and PCPDTBSe were mixed in various ratios (1, 3, 7, 9, 19, and 39 to 1) always maintaining 2 mg/mL polymer concentration in THF. 1 mL of the pre-mixed PFBTDBT10 and PCPDTBSE was injected under continuous horn sonication into Pluronic®F127 (8 mL, 1 mg/mL in water).

Nanoparticle Collection: Nanoparticle solutions were autoclaved to sterilize before being centrifuged (30 minutes, 7,500 rpm) to remove large nanoparticles and aggregates. The resulting supernatant was centrifuged (4 hours, 14,000 rpm) to collect nanoparticles. The centrifugation process was performed using asceptic technique in a tissue culture hood to maintain sterility.

5.3.6 Characterization of Nanoparticles: UVvis, DLS, TEM, Fluoresence Quantum Yield

Dynamic light scattering (DLS) with zeta potential was measured in water using a Malvern Instruments Zetasizer Nano-ZS90 light scattering instrument. UVvis spectrometry was taken on on a Beckman Coulter DU® 730 Life Sciences UV-vis spectrophotometer. Fluorescence spectra were obtained on TECAN M200 Infinite plate reader. Fluorescence quantum yield was obtained on TECAN M200 plate reader using a comparative technique as described previously (Chapter 3).

5.3.7 Quantification of PolyDOTS #17

The concentration of Poly-DOTS #10 in water was obtained by lyophilization of a concentrated nanoparticle solution to dryness to measure its mass. Once the mass was known, the remaining nanoparticle solution was serially diluted and absorption spectra were taken on a Beckman Coulter DU® 730 Life Sciences UV-vis spectrophotometer. The absorbance at λ_{max} =

760 nm of Poly-DOTS at different concentrations was recorded and plotted versus the concentration to generate an absorption-concentration calibration curve.

5.3.8 Heating Analysis

To determine heating potential of PolyDOTS, 200 µL of Poly-DOTS suspended in water were added to a 96 well plate for temperature testing. A Cube^{TM} continuous wave diode laser from K-laser (800 nm, 1 cm diameter spot size) was used to apply near infrared light. A Fluke 714 thermocouple calibrator and a type k 80Pk-1 bead probe wire thermocouple measured the temperature of the solutions immediately before and after laser application. To assess heating reproducibility, heating/cooling curves of PolyDOTS were completed over 3 cycles. Each cycle included 1 min of 3 Watt, 800 nm light exposure followed by 30 minutes of cooling time before the start of the next cycle. To determine the effect that multiple heating/cooling cycles have on the optical properties and size of of PolyDOTS, absorption spectra, fluorescent spectra, dynamic light scattering measurements, and TEM images were taken.

5.3.9 In Vivo Fluorescent Imaging

To evaluate *in vivo* imaging prior to *in vitro* studies, PolyDOTS were injected subcutaneously into previously euthanized BALB/c mouse. PolyDOTS were normalized for heating potential (same mass of heating component, PCPDTBSe) determined by absorption of 0.59 at 760 nm. BALB/c mouse was then imaged using Perkin Elmer In Vivo Imaging System Lumina LT III, exciting at 465 nm and using the ICG filter emission (collects light from 810 – 870 nm).

5.3.10 Cells and Reagents

Non tumorigenic murine epithelial cell line, BALB/c CL.7, and murine breast cancer cell line 4T1 were purchased from American Type Culture Collection (ATCC # TIB-80 and CRL-2539 respectively). Murine breast cancer cell line, EO771, was generously gifted by the Metheny-Barlow lab. 4T1 and EO771 cell lines were cultured in RPMI 1640 medium and BALB/c CL.7 was cultured in DMEM medium. Both medias were supplemented with 1% L-glutamin, 1%

penicillin/streptomycin, and 10% fetal bovine serum. Cells were cultured and maintained in the exponential phase of growth at 37°C under 5% carbon dioxide. Cell viability was quantified by MTS assay using Promega's Cell Titer 96 AQuesous assay kit.

5.3.11 Cytotoxocity Assay

4T1, EO771, and BALB/c CL.7 cells were plated at a density of 5,000 cells per well in a 96 well tissue culture plate and cultured for 24 hours. 200 µL of Poly-DOTS were added to the well plates at concentrations of 0, 25, 50, 75, 100, 125, and 150 µg/mL and incubated for 24 hours. Nanoparticle solutions were removed and cells were washed twice with ice cold phosphate buffered solution before MTS assay was performed. Absorbance values were normalized to the 0 µg/mL control.

5.3.12 Clonogenic Assay

4T1 and EO771 cell lines, were both plated at a density of 150 cells per well, BALB/c CL.7 cell line was plated at a density of 100 cells per well, in a 12 well plate and cultured for 24 hours. 1 mL of Poly-DOTS were added to the well plates at concentrations of 0, 25, 50, 75, 100, 125, and 150 µg/mL and incubated for 24 hours. Nanoparticle solutions were removed and cells were washed twice with cold phosphate buffered solution and fresh media was added. Cells cultured for 7-10 days before being fixed and stained with crystal violet. Colonies with greater than 50 cells well counted and normalized to the 0 µg/mL control.

5.3.13 Photothermal Ablation Assay

4T1, EO771, and BALB/c CL.7 cell lines were plated at a density of 5,000 cells per well in a 96 well tissue culture plate and cultured for 24 hours. 200 µL of Poly-DOTS were added to the well plates at concentrations of 0, 10, 20, 30, 40, 50, 60, 70, 80, 90 and 100 µg/mL. NIR light (800 nm, continuous wavelength) was applied at 2.654 W/cm^2 for 1 minute per well or 1.77 W/cm^2 for 2 minutes per well. Following NIR light exposure, nanoparticle solutions were removed, wells were washed twice with cold phosphate buffered solution, fresh cell medium was

added and the cells were incubated at 37°C for 24 hours. Cell viability was then quantified using an MTS assay and absorbance values were normalized to the 0 µg/mL control.

5.3.14 Statistical Analysis

Statistical analysis for in vitro experiments was performed by one-way analysis of variance and post hoc Fisher LSD test. For in vivo experiments, a two-way repeated measures analysis of variance and post hoc Holm Sidak test.

5.3.15 In Vivo Fluorescence-Concentration Calibration Curve

Various concentrations of PolyDOTS #17 were serially injected subcutaneously into a previously euthanized BALB/c mouse and imaged by Perkin Elmer In Vivo Imaging System Lumina LT Series III, exciting at 465 nm and emission using the ICG filter (collecting fluorescence from 810 nm – 870 nm). The maximum fluorescence intensity was then plotted versus the mass of PolyDOTS #17 injected. A linear trendline was fitted.

5.3.16 In Vivo Photothermal Ablation of 4T1 tumors in Mammary Fat Pad

BALB/c mice were purchased from Charles River Laboratories. They were housed in groups of five in a vivarium maintained on a 12-hour light/dark schedule with a temperature of 30°C and a relative humidity of 50%. Food and water were available ad libitum.

Luciferase transfected 4T1 cells, passage 11, were trypsinized, washed with phosphate buffered solution, and resuspended to a concentration of 8E4 cells/mL. BALB/c mice were anesthetized with 2.5% isoflurane before receiving an injection of 50 µL cell solution (40,000 cells) into the mammary fat pad below the fourth nipple. Tumor growth was monitored by caliper measurements and luminescence. Mice were divided into treatment groups: (1) PBS injection, (2) PBS injection and laser exposure, (3) PolyDOTS#17 injection, (4) PolyDOTS #17 injection and laser exposure. Groups (1) and (2) were treated 11 days after cell injection, group (4) was treated 12 days after injection, and group (3) was treated 14 days after injection. The average volume of tumors, determined by measuring the tumor's length and width and using the calculation for the area of an oval $A = \pi (L/2)(W/2)$, on the day of treatment was 14.4 mm^2 with groups (1), (2), (3),

and (4) having averages of 13.1 ± 3.8, 15.2 ± 1.7, 13.3 ± 2.7, and 15.9 ± 3.3 respectively. Groups (3) and (4) received an intratumoral injection of 50 µL of 0.1 mg/mL of PolyDOTS #17 (total mass of 5 µg) suspended in 1x PBS. Groups (1) and (2) received an intratumoral injection of 50 µL of 1x PBS. Immediately after injection, groups (2) and (4) were exposed to 1 minute of 2.654 W/cm^2, 800 nm light. Fluorescent and luminescent images of mice were taken before and after treatment and for the remainder of the study every 2 to 3 days. Mice were humanely euthanized once tumors got larger than 12 mm in any direction, the tumors began to ulcer, the mice lost more than 20% of their starting body weight, or showed signs of neurological impairment.

Results

5.4.1 Synthesis and Characterization of PCPDTBSe and PFBTDBT10

PCPDTBSe and PFBTDBT10 were both synthesized using a Stille coupling reflux procedure similar to literature procedures [81, 109]. After polymerization, PCPDTBSe was washed by soxhlet extraction using methanol and hexanes to remove oligomeric and low molecular weight fractions, high molecular weight PCPDTBSe. High molecular weight PCPDTBSe dissolved in chloroform was concentrated by rotary evaporation and precipitated in methanol. Following PFTBDBT10 polymerization, the polymer was precipitated in methanol, dissolved in dichloromethane and washed with water. The polymer was then dried over magnesium sulfate, and concentrated by rotary evaporation. In the literature, PFBTDBT10 was then precipitated in methanol and collected as a powder. I had difficulty dissolving the polymer because its clot-like form clogged the filter paper. Therefore, after rotary evaporation to remove the dichloromethane, I instead dissolved the PFBTDBT10 directly into THF to store it.

Gel permeation chromatography using THF eluent and polystyrene standards was used to determine the molecular weight of PCPDTBSe and PFBTDBT10 was 25,840 and 43,115 respectively (Figure 1B). PFBTDBT10 was dissolved in THF and the absorption spectra was obtained. As seen in Figure 1A, PFBTDBT10 has absorption peaks at 465 nm and 550 nm which matched the literature [81]. As PFBTDBT10 could not be resolved as a powder, to accurately

determine concentrations of PFBTDBT10 in THF, a concentrated stock solution was serially diluted in THF and the absorption spectra taken. To determine the concentration of the stock solution, a known volume was added to a pre-weighed glass vial and the solvent was allowed to evaporate. The vial was re-weighed to obtain the mass. The λmax, 452 nm, was then plotted versus the concentration to yield an absorption-concentration calibration curve of P3HT in THF (Figure 1C)

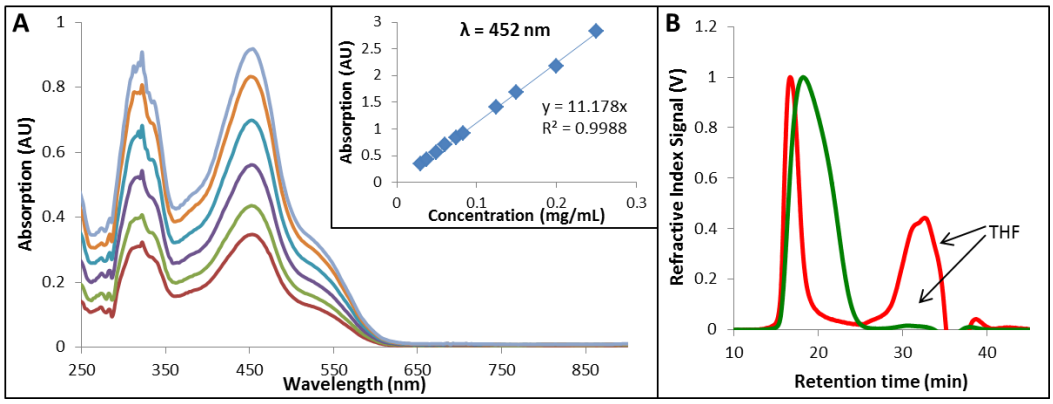

Figure 1. (A) Absorption spectra of PCPDTBSe and PFBTDBT10 polymers in THF. **(A inset)** Absorption-concentration calibration curve of PFBTDBT10 **(B)** Gel Permeation Chromatography plot illustrating retention time of PCPDTBSe (green) and PFBTDBT10 (red).

5.4.2 Synthesis and Characterization of Poly-DOTS and PFBTDBT10 Nanoparticles

Poly-DOTS and PFBTDBT10 nanoparticles were synthesized using a nanoprecipitation method (Figure 2A). Polymers were dissolved in THF (1 mL, 2 mg/mL) and rapidly injected into an aqueous solution containing Pluronic®F127 (8 mL, 1 mg/mL) under horn sonication. Upon injection, the hydrophobic polymer self-assembles within the hydrophobic core of the pluronic micelle leading to the formation of water soluble nanoparticle. The absorption and fluorescence spectra of PFBTDBT10 nanoparticles are seen in Figure 2B. The absorption spectra matches the literature, however, the fluorescent spectra has a λmax of 658 nm whereas the literature is 698 nm. It is possible that this is due to instrument detection limitations in the near infrared. Additionally, the fluorescence quantum yield of PFBTDBT10 nanoparticles, 31.6% is also very similar to literature, 27%.

Several PolyDOTS were synthesized with a range of mass ratios of PFBTDBT10 to PCPDTBSe (1:1, 3:1, 7:1, 19:1, and 39:1) as summarized in Table 1. The absorption spectrum of Poly-DOTS show peaks at 465 nm and 760 nm indicating the presence of both PFBDBT10 and PCPDTBSe (Figure 2C). The fluorescence quantum yield Poly-DOTS #17 and #18 were found to be 0.52% and 1.2%, respectively. There is significant quenching of fluoresence in PolyDOTS, that correlates with absorption of PCPDTBSe. This quenching is not as significant when aliquots of individual PCPDTBSe and PFBTDBT10 nanoparticles were mixed together (Figure 2D). The degree of quenching suggests that a PolyDOTS are in fact a hybrid nanoparticle and that the two polymers do not form separate nanoparticles. As *in vivo* imaging has been a limiting factor in previous nanoparticle systems, the concentration of PolyDOTS #17 and #18 necessary for photothermal ablation (generate $\Delta T = 30°$ with 1 minute of 3 watt 800 nm light) was injected subcutaneously in a BALB/c mouse and imaged with an *in vivo* fluorescent and bioluminescent imaging system. Although there is a significant decrease in quantum yield, PolyDOTS #17 and #18 are still easily visible by IVIS due to low tissue autofluorescence in the near infrared (Figure 2E and F).

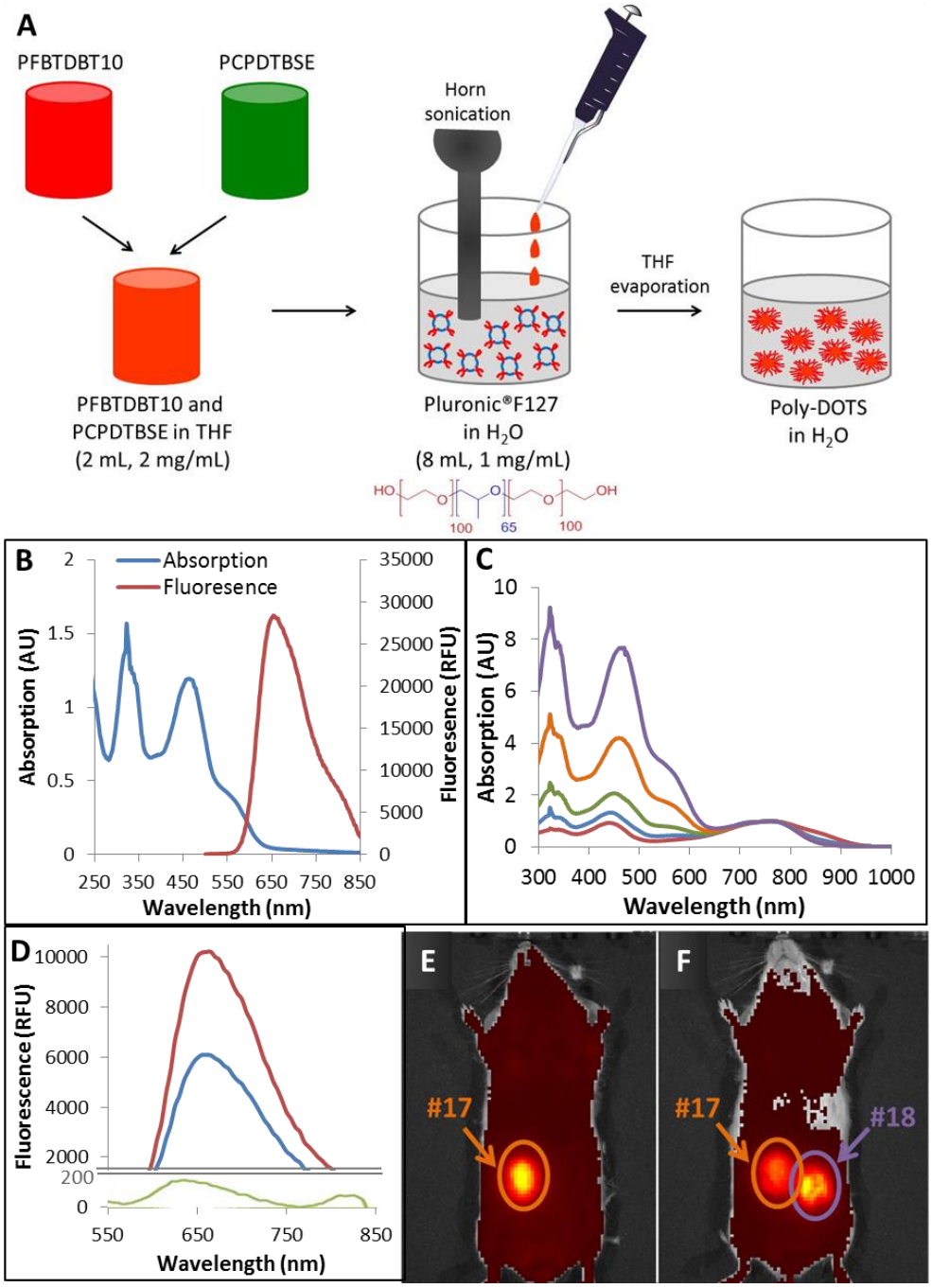

Figure 2. (A) Schematic of PolyDOTS synthesis. **(B)** Absorption and fluorescent spectra of PFBTDBT10 nanoparticles. **(C)** Absorption spectra of PolyDOS #14 (red), #15 (blue), #16 (green), #17 (orange), and #18 (purple). **(D)** Fluorescence spectra of PFBTDBT10 alone, PFBTDBT10 and PCPDTBSe nanoparticles mixed together, and PolyDOTS #17. **(E)** Fluorescent images of PolyDOTS #17 injected subcutaneously into Balb/c mouse excited at 465 nm and using ICG emission filter. (F) Fluorescent images of PolyDOTS #17 and #18 injected subcutaneously into Balb/c mouse excited at 465 nm and using ICG emission filter.

	Mass of PFBTDBT10 added [mg]	Mass of PCPDTBSe added [mg]	Ratio of PFBTDBT10 to PCPDTBSe added	Ratio of Absorption at 465nm:760nm
PolyDOTS #14	1.00	1.00	1:1	0.75
PolyDOTS #15	1.50	0.50	3:1	1.10
PolyDOTS #16	1.75	0.25	7:1	2.00
PolyDOTS #17	1.90	0.10	19:1	4.20
PolyDOTS #18	1.95	0.05	39:1	7.70

Table 1. Mass of P3HT and PCPDTBSe added to generate PolyDOTS #14 - #18. This ratio of polymers added is compared to the ratio that is incorporated into the nanoparticles (as observed by absorption intensity at 465 nm, PFBTDBT10, compared to 760 nm, PCPDTBSe).

Nanomaterials were evaluated by dynamic light scattering (summarized in Table 2) and interestingly, as with P3HT, it was found that as the ratio of PFBTDBT10 increased, the size of the PolyDOTS increase. As expected, the zeta potential stays approximately the same; strongly negative between -20 and -30 mV.

	Hydrodynamic Diameter [nm]	Polydispersity Index	Zeta Potential [mV]
PCPDTBSe	120.0	0.301	-12.3
PolyDOTS #14	103.7	0.117	-26.5
PolyDOTS #15	100.5	0.089	-32.6
PolyDOTS #16	117.5	0.123	-26.9
PolyDOTS #17	148.2	0.172	-17.4
PolyDOTS #18	170.4	0.176	-29.7
PFBTDBT10	115.3	0.158	-27.9

Table 2. Hydrodynamic diameter and zeta potential of PolyDOTS, PCPDTBSe, and PFBTDBT10 nanoparticles.

Based on the encouraging dynamic light scattering and IVIS data, and to minimize the mass of nanoparticles needed for photothermal ablation, PolyDOTS #17 was chosen for further investigation. An absorption-concentration calibration curves were generated for PolyDOTS #17 (Figure 3A). Poly-DOTS #17 generates excellent heating when stimulated by 800 nm light (Figure 3B), and reproducibly generate heat over multiple cycles (Figure 3C). Additionally, Poly-DOTS #17 maintain their fluorescence capabilities over several cycles of near infrared stimulation (Figure 3D). Additionally, heat cycles do not affect the absorption spectra of PolyDOTS #17 (Figure 3E)

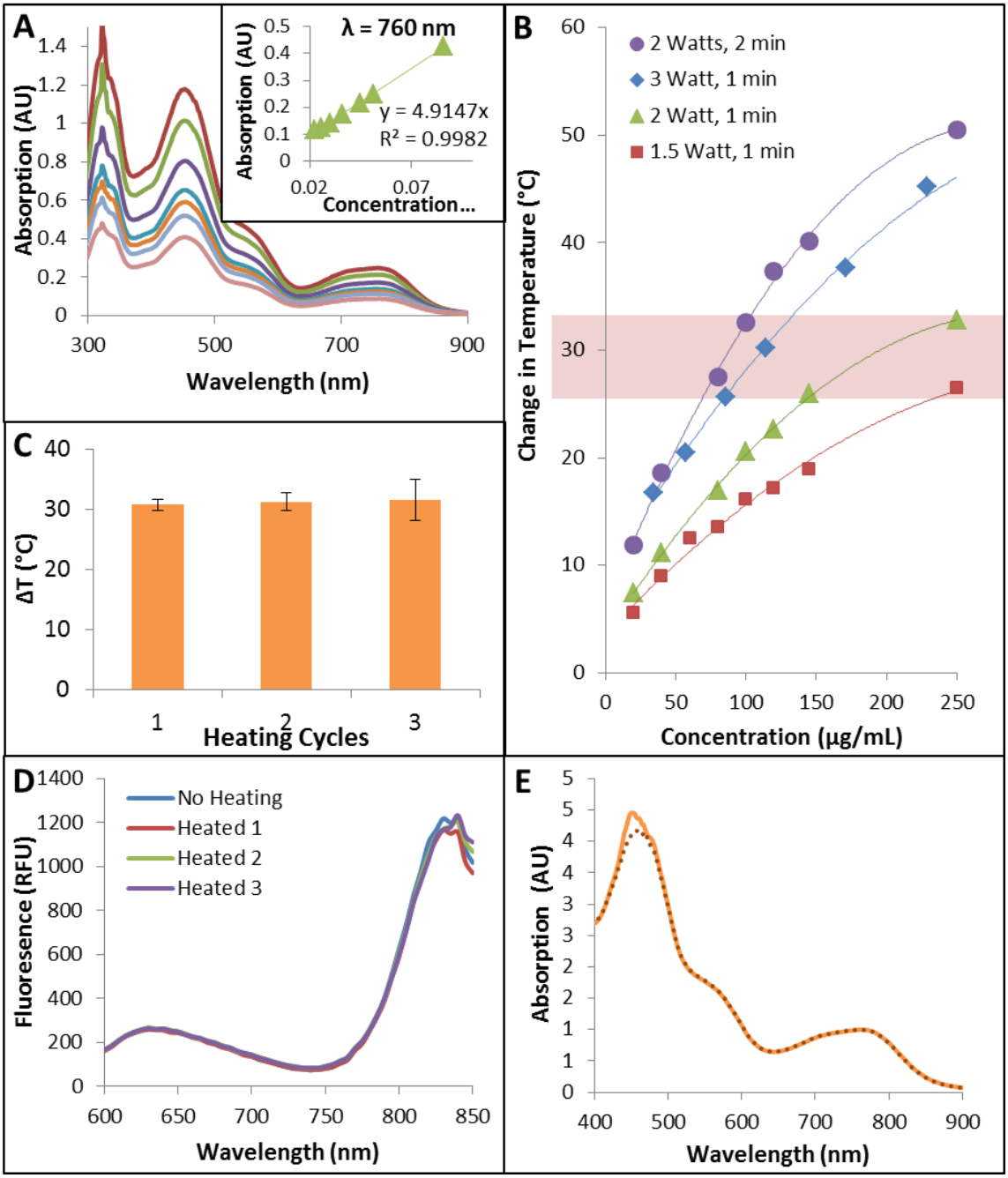

Figure 3. (A) Absorption-concentration calibration curve of PolyDOTS #17 using the absorption at 760 nm. **(B)** Heating curves of PolyDOTS #17 exposed to various laser powers and times. The thermal ablation threshold is highlighted in red, and to minimize nanoparticle mass, laser parameter 2.654 W/cm^2 for 1 minute or 1.77 W/cm^2 for 2 minutes are ideal. **(C)** Heat cycles illustrate that PolyDOTS #17 are capable of reproducibly generating heat when repeatedly exposed to 2.654 W/cm^2 of 800 nm light for 1 minute. **(D)** The effect that heat cycles have on fluorescence. **(E)** The effect that heat cycles have on absorption spectra (before heating = solid, after 3 cycles = dotted). Error bars shown are standard deviation.

To ensure nanoparticle sterility for *in vivo* experiments, PolyDOTS #17 were sterilized by autoclaving. To ensure that autoclaving does not affect nanoparticles, the absorption spectra, fluorescence specta, hydrodynamic diameter, zeta potential, and morphology were evaluated before and after autoclaving (Figure 4 and Table 3). PolyDOTS #17 morphology, zeta potential, and absorption and fluorescent spectra remain fairly unchanged. However, the hydrodynamic diameter is decreased by about 25 nm. It is expected that during the nanoparticle synthesis, some THF gets trapped within the hydrophobic polymer and that autoclaving releases this solvent.

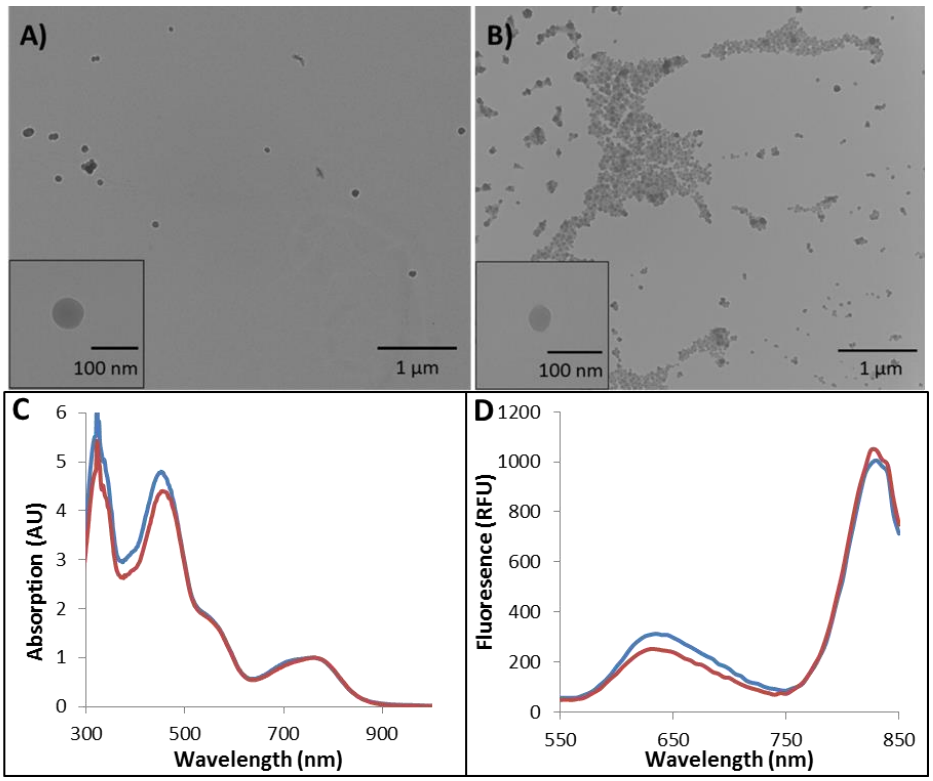

Figure 4. TEM of PolyDOTS #17 before **(A)** and after **(B)** autoclaving. Absorption **(C)** and fluorescent **(D)** spectra of PolyDOTS #17 before (red) and after (blue) autoclaving.

	Hydrodynamic Diameter (nm)	**Poly-dispersity Index**	**Zeta Potential [mV]**
PolyDOTS #17 before	148.1	0.172	-17.5
PolyDOTS #17 after	121.1	0.218	-16.8

Table 3. Hydrodynamic diameter and zeta potential of PolyDOTS #17 before and after autoclaving.

The aqueous and optical stability of nanoparticles is important for potential long term tracking and other imaging applications. Poly-DOTS #17 display strong aqueous stability in various solutions. As seen in Figure 5A, PolyDOTS #17 remain suspended in water, phosphate buffered solution, pHs of 4 and 10, and serum for 30 days in ambient light. Some white sedimentation is present in the PolyDOTS suspended in 10% fetal bovine serum, but this is also seen in 10% fetal bovine serum without nanoparticles. PolyDOTS #17 not only remained aqueously stable, but the fluorescent and absorption spectra also remained constant. After 30 days, an aliquot of nanoparticles was diluted in water and centrifuged to remove excess salts or proteins before being evaluated by dynamic light scattering (Table 4). Phosphate buffered solution resulted in a more positive zeta potential and fetal bovine serum caused a negative shift in zeta potential and a slight (5 nm) increase in hydrodynamic diameter, however, there was no change to the nanoparticles when stored in water, acid, or base.

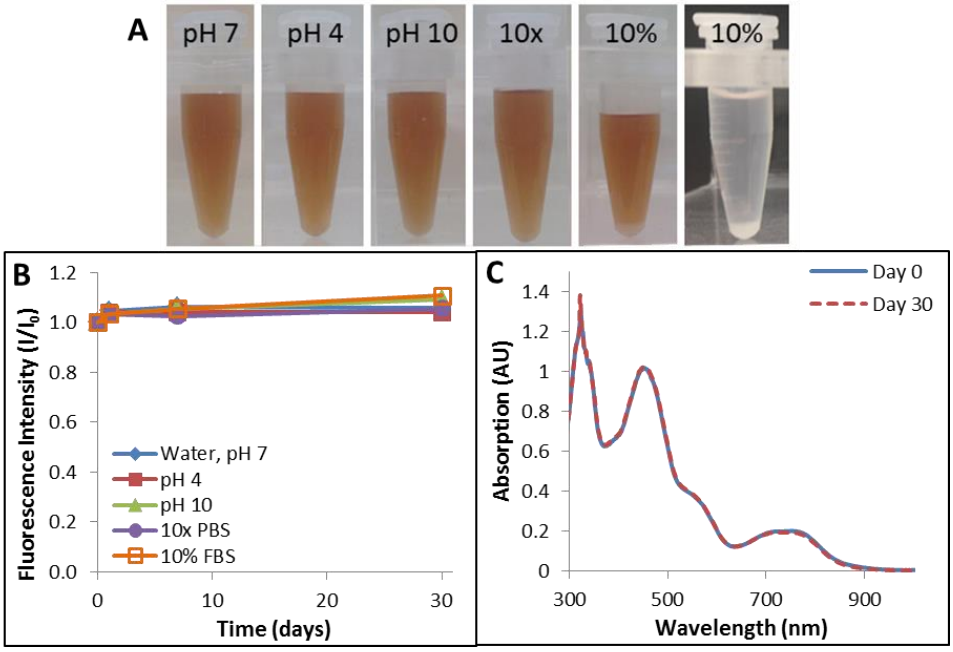

Figure 5. (A) Image of PolyDOTS #17 in suspension for 30 days in various solutions (from left to right: water with a pH of 7, water titrated to a pH of 4, water titrated to a pH of 10, 10x phosphate buffered solution, 10% fetal bovine serum, 10% fetal bovine serum without PolyDOTS). **(B)** Maximum fluorescent intensity of PolyDOTS #17 in various solutions at Day 1, 7, and 30 normalized to the intensity at Day 0. **(C)** Absorption spectra of PolyDOTS #17 in water at Day 0 and Day 30

	Hydrodynamic Diameter (nm)	Poly-dispersity Index	Zeta Potential [mV]
Water, pH 7	135.8	0.088	-15.4
pH 4	136.4	0.089	-17.2
pH 10	135.7	0.102	-16.4
10X PBS	135.5	0.095	-3.8
10% FBS	140.8	0.114	-35.6

Table 4. Hydrodynamic diameter and zeta potential of PolyDOTS #17 after 30 day incubation in water (pH of 7), water with a pH of 4, 10x phosphate buffered solution, and 10% fetal bovine serum.

5.4.3 In Vitro Characterization of Poly-DOTS #17

The acute cytotoxicity of Poly-DOTS #17 was assessed using a conventional MTS cell viability assay. After 24 hours of incubation in the absence of 800 nm light, PolyDOTS #17 showed no substantial effect on cell viability for either the non-cancerous breast epithelial cell line BALB/c CL.7 or murine breast cancer cell lines EO771 and 4T1 (Figure 6A). To evaluate for more chronic toxicity, a clonogenic assay was performed. As visualized in Figure 6B, PolyDOTS #17 do not display any significant clonogenic effects. However, after exposure to 800 nm light at 2.654 W/cm^2, 1 minute or 1.77 W/cm^2 for 2 minutes Poly-DOTS #17 demonstrated excellent photothermal ablation, resulting in complete cell death for cancerous cell lines at 100 µg/mL (Figure 6C) or 80 µg/mL (Figure 6D) respectively.

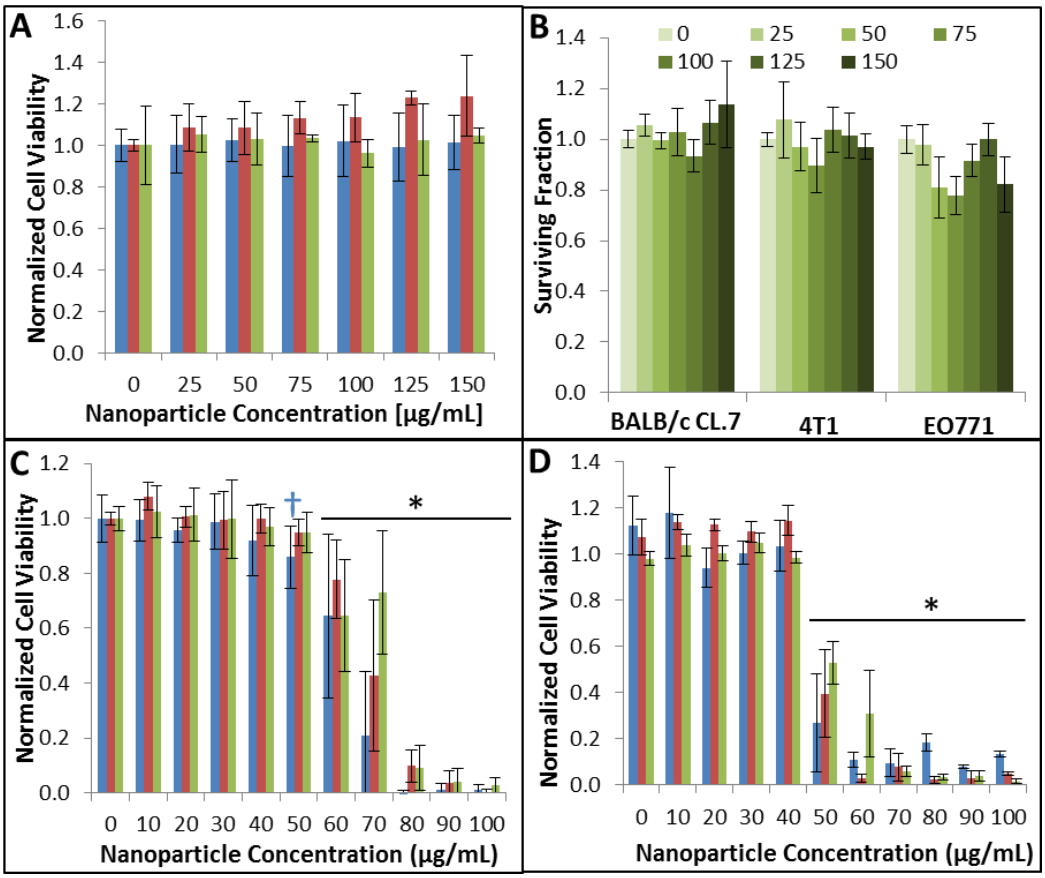

Figure 6. (A) Cytotoxicity and **(B)** Clonogenic assay of PolyDOTS #17 in BALB/c CL.7 (blue), 4T1 (red), and EO771 par (green). **(C)** and **(D)** Photothermal ablation of cells incubated with PolyDOTS #17 and exposed to 1 minute of 2.654 W/cm^2 or 2 minute of 1.77 W/cm^2, 800 nm light respectively. Error bars shown are standard deviation. * $p<0.001$, † $p<0.05$.

5.4.4 In Vivo Characterization – Direct Injection, Mammary Fat Pad

An orthotopic mammary fat pad tumor was developed in immune competent BALB/c mice using luciferase transfected 4T1 murine breast cancer cells. Tumors developed within the first 7 days and mice were treated 11 – 14 days after injection depending on tumor size. Tumor size was assessed directly by caliper measurements. There were 4 treatment groups (1) PBS injection, (2) PBS injection and laser, (3) PolyDOTS #17 injection, and (4) PolyDOTS #17 injection and laser with 5 mice within each group. Treatment occurred on Day 0. A response was only expected in Group (4), however, there were 2 complete responses seen in Group (2). These two complete responses were excluded from the study to reduce standard deviation within Group (2). This is thought to be due to the fact that the PBS injection may have disrupted the vasculature, compromising the ability of the tumor to regulate temperature and thus causing thermal damage from the laser exposure. Although group (4) appeared to have good intratumoral injections (Figure 7C) and the laser exposure resulted in dermal burns (Figure 7D), only a partial response was seen (Figure 7A). A possible explanation for this is seen in Figure 7E; as the laser excited the nanoparticles and they began to generate heat very quickly, changing the optical properties of the tissue, thus making it less permeable to light. As such, the deep portion of the tumor did not reach full thermal ablation temperatures and tumors were able to regrow. A hypothesized way to reduce this risk is to adjust the laser parameters heat the tissue at a slower rate, such as using 1.77 W/cm^2 for 2 minutes. This can be done by reducing the power of the laser and increasing the length of exposure.

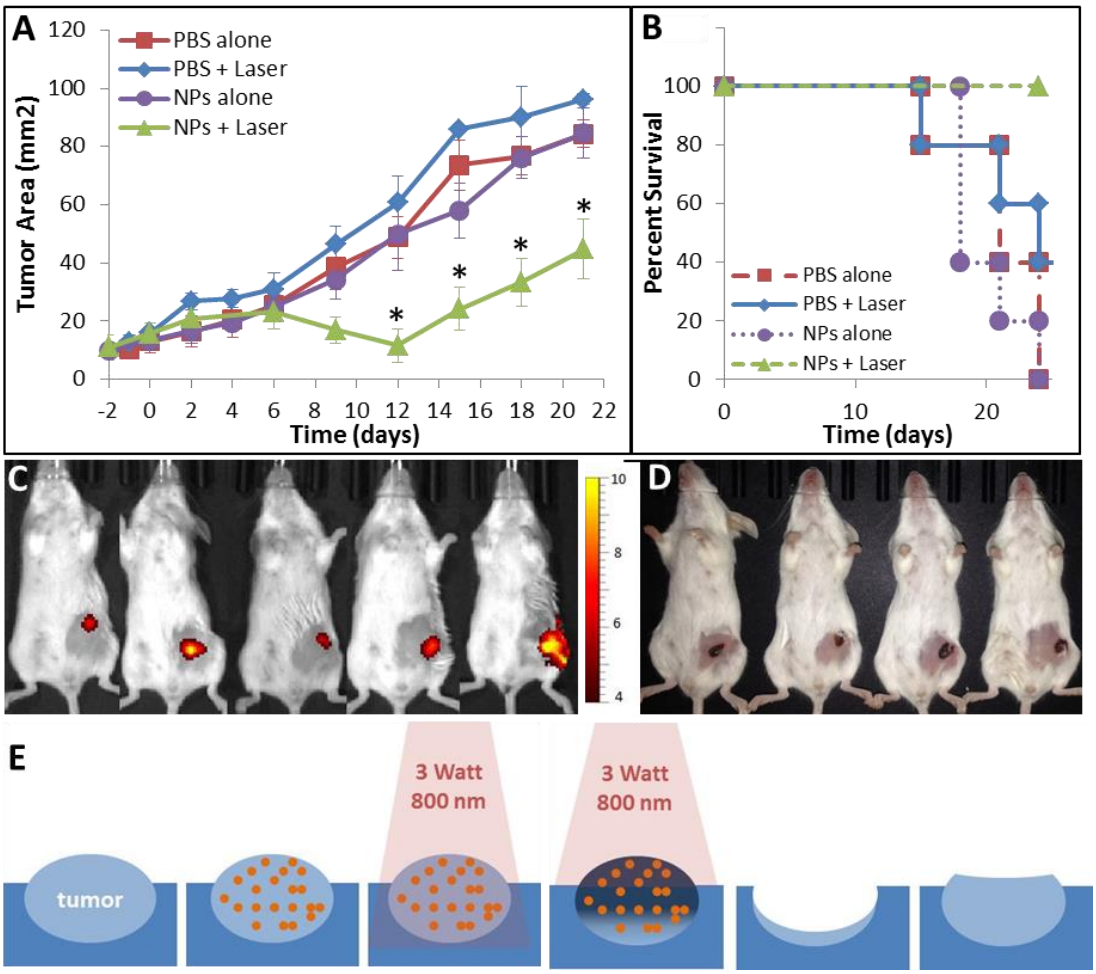

Figure 7. (A) Tumor area plotted versus time. Treatment occurred on Day 0. To keep standard deviation low, the two complete responses seen from Group 2, PBS + Laser, were not included **(B)** Kaplan Meier survival curve. **(C)** Group 4 immediately after injection. **(D)** Group 4 four days after treatment showing dermal burns from photothermal treatment. **(E)** Schematic illustrating mechanism for partial response. PolyDOTS #17 are orange spheres. As NIR light is shone on the tumor with PolyDOTS, the NPs rapidly begin to heat resulting in changes in the optical properties of the tissue. As a result, near infrared light cannot penetrate deep enough to fully eradicate tumor. Error bars shown are standard deviation. * $p<0.0001$

PolyDOTS #17 were readily visible after intratumoral injection and remained visible by fluorescence for up to 15 days (Figure 8A). Post mortem dissection of the mice was performed and the organs were imaged for fluorescence. As seen in Figure 8B, fluorescence is only seen in the tumor. This suggests that the decrease in fluorescence seen over time might not be an actual decrease in mass of PolyDOTS #17 at the tumor, but rather, an increasing depth of tissue as the tumors continue to grow.

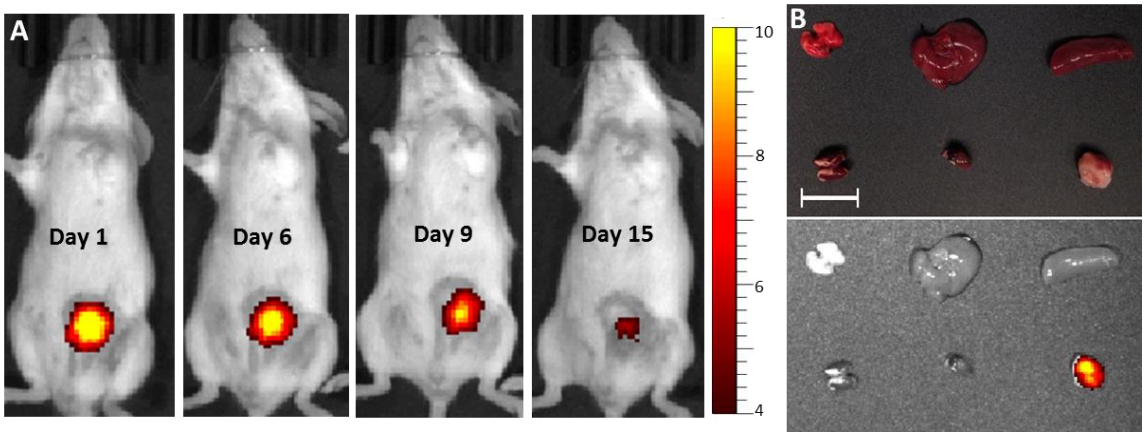

Figure 8. (A) Fluorescent images taken on IVIS on mouse from Group 3 (PolyDOTS #17 alone). Treatment occurred Day 0. **(B)** Picture and fluorescent images of organs from Groups 3. Organs top row: lungs, liver, spleen. Organs bottom row: kidneys, heart, tumor. Scale bar is 2 cm.

5.4.5 Evaluation of PolyDOTS #17 In Vivo Fluoresence

To determine if the mass of PolyDOTS #17 can be quantified by *in vivo* fluorescence and bioluminescent imaging system, serial subcutaneous injections (50 µL) were made into a previously euthanized BALB/c mouse using various concentrations of PolyDOTS #17 (0, 10, 20, 30, 40, 50, 60, 70, 80, 90, and 100 µg/mL). The maximum fluorescent intensity was plotted versus the concentration (Figure 9) and a linear trend line was fitted. The 50 µg/mL injection leaked, so it was not included. This is important should PolyDOTS #17 be administered systemically, the mass of nanoparticles that accumulate in the tumor could be approximated, thus allowing tailoring of laser parameters. Additionally, this could be utilized to determine mass of nanoparticles still in a location if re-treatment is necessary.

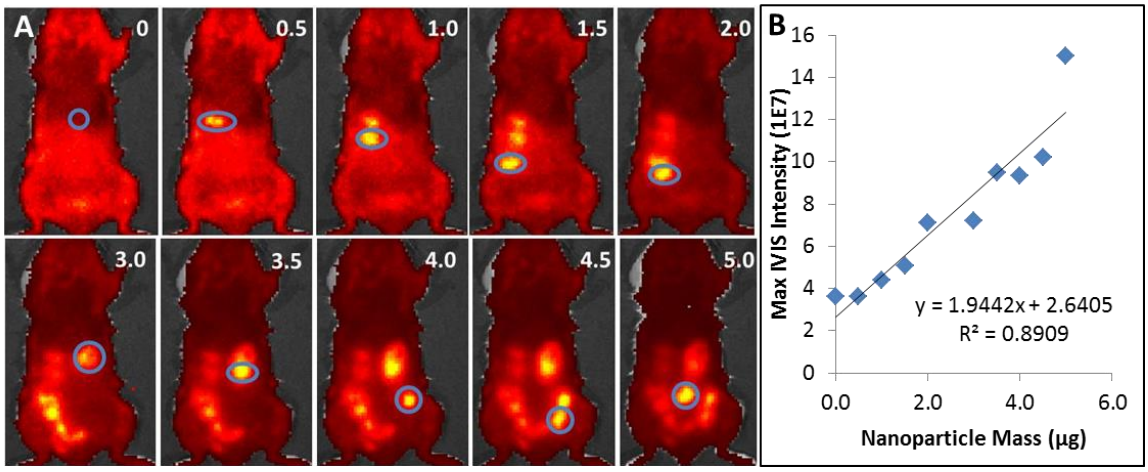

Figure 9. (A) Fluorescent images of mouse after serial subcutaneous injections of PolyDOTS #17. Locations of injections are circled in blue. Mass of PolyDOTS #17 is stated in top right corner of each image (B) Graph displaying the linear relationship between mass of nanoparticles and maximum fluorescent intensity.

5.5 Conclusions

PolyDOTS #17 have bright enough fluorescence to be visualized *in vivo.* They are aqueously stable, remaining in solution in acidic, basic, strongly ionic (10x PBS), and serum conditions for more than 30 days. PolyDOTS #17 are also optically stable, retaining 100% of their fluorescence through autoclaving, multiple laser excitations, and over 30 days in ambient light (in all aqueous conditions listed previously). PolyDOTS #17 was found to have no cytotoxic or clonogenic effects and to generate efficient photothermal ablation. PolyDOTS #17 were utilized in an orthotopic breast cancer model and in combination with laser exhibited a delay in tumor growth. PolyDOTS #17 are a promising theranostic nanoparticle for *in vivo* photothermal ablation and fluorescent imaging of cancer.

Acknowledgements
Chris MacNeill taught and assisted in CPDT monomer and PCPDTBSe polymer synthesis. Sneha Kelkar performed GPC experiments and data analysis. Rong Ma embedded, sectioned, and stained tissue samples. Nancy Kock did pathological analysis of tissues.

CHAPTER 6

Conclusions and Future Directions

Throughout the preceding chapters the development and characterization of multiple theranostic nanoparticles were discussed. The primary goal of this research was to create a completely organic theranostic nanoparticle in which the core of the nanoparticle contained both the heating and fluorescent components, leaving the surface free for modification. All nanoparticles developed have many similar characteristics. They all are spherical and electrondense with diameters of approximately 30 – 60 nm as visualized by TEM with hydrodynamic diameters of 90 – 150 nm. The zeta potential depends on which soft template was utilized during the synthesis; Pluronic®F127 typically leading to a more neutral zeta potential while DSPE-PEG-COOH or nanoparticles without wrapping have strongly negative zeta potentials (approximately -25 mV to -40 mV).

First, the synthesis of conjugated polymer, polycyclopentadithiophene benzoselenadiazole (PCPDTBSe), nanoparticles was optimized using both Pluronic®F127 and DPSE-PEG-COOH as soft templates. The addition of amphipathic compounds to the synthesis of PCPDTBSe nanoparticles resulted in small, aqueously stable nanoparticles that generate efficient photothermal ablation. Next, Oligomeric PCPDTBSe was combined with high molecular weight PCPDTBSe to form a hybrid nanoparticle, PolyDOTS #1, using Pluronic®F127 as a soft template. PolyDOTS #1 was found to be a non-cytotoxic, efficient photothermal agent that is readily taken up by cells and easily imaged by fluorescent microscopy. However, Oligomeric PCPDTBSe was not a pure product, and as such, PolyDOTS #1 varied drastically with each preparation. Two components of oligomeric PCPDTBSe were purified through column chromatography, termed Oligomer 1 and Oligomer 2. Nanoparticles of each oligomer were made using DSPE-PEG-COOH as a soft template and their fluorescent capabilities were analyzed. Oligomer 1 was found to have significantly higher quantum yield, and therefore was utilized in

combination with PCPDTBSe to generate improved PolyDOTS. Various mass ratios of Oligomer 1 to PCPDTBSe were combined to optimize the fluorescent properties. PolyDOTS #6, synthesized with a 20 to 1 mass ratio of Oligomer 1 to PCPDTBSe, was be bright enough to be seen *in vivo.* Although aqueously stable for more than 2 weeks, PolyDOTS #6 are not completely optically stable. Within 2 days of exposure to ambient light, PolyDOTS #6 exhibit a visible color shift (from pink to orange to yellow) which is matched with a blue shift in absorption peak from 535 nm to 446 nm. This lack of optical stability drove the search for a more stable fluorescent polymer.

Poly(3-hexylthiophene-2,5-diyl) was chosen for investigation based on its absorption and fluorescent spectra; absorbing in the visible and fluorescing in the near infrared. Additionally, it is commercially available and already known to be non-cytotoxic [133]. Similar to Oligomer 1, P3HT was combined in various mass ratios with PCPDTBSe. PolyDOTS #10, a 1 to 1 mass ratio of P3HT and PCPDTBSe, was chosen for further characterization. PolyDOTS #10 was found to be aqueously and optically stable, remaining in solution and not losing any fluorescence after 30 days in ambient light. Additionally, PolyDOTS #10 retain their heating efficiency and 90% of fluorescence over numerous exposures to near infrared light. Although easily visible *in vitro* by confocal microscopy, the fluorescence quantum yield of PolyDOTS #10 is too low for *in vivo* applications.

Recently, Dr. Bin Liu's group developed a conjugated polymer, poly[(9,9-dihexylfluorene)-co-2,1,3-benzothiadiazole-co-4,7-di(thiophen-2-yl)-2,1,3-benzothiadiazole] (PFBTDBT10), which high quantum yield that fluoresces in the near infrared [81]. Since, PFBTDBT10 has a similar synthesis technique to that of PCPDTBSe and the monomers are commercially available, it was synthesized. Absorption spectra of the polymer in THF and of the PFBTDBT10 nanoparticles matched that of the literature. Although the λmax of the fluorescence was slightly different (660 nm as opposed to 698 nm), the quantum yield, 31.7%, was comparable. As such, PFBTDBT10 was combined in different mass ratios with PCPDTBSe and

utilized to form PolyDOTS. PolyDOTS #17, a 20 to 1 ratio of PFBTDBT10 and PCPDTBSe, was found to be ideal. PolyDOTS #17 have bright enough fluorescence to be visualized *in vivo*. Additionally, they are very aqueously stable, remaining in solution in acidic, basic, strongly ionic (10x PBS), and serum conditions for more than 30 days. PolyDOTS #17 are also optically stable, retaining 100% of their fluorescence through autoclaving, multiple laser excitations, and over 30 days in ambient light (in all aqueous conditions listed previously). PolyDOTS #17 was found to have no cytotoxic or clonogenic effects and to generate efficient photothermal ablation. PolyDOTS #17 were utilized in an orthotopic breast cancer model and in combination with laser exhibited a delay in tumor growth. PolyDOTS #17 offer the most promising theranostic nanoparticle for *in vivo* use from this body of work. Figure 1 summarizes

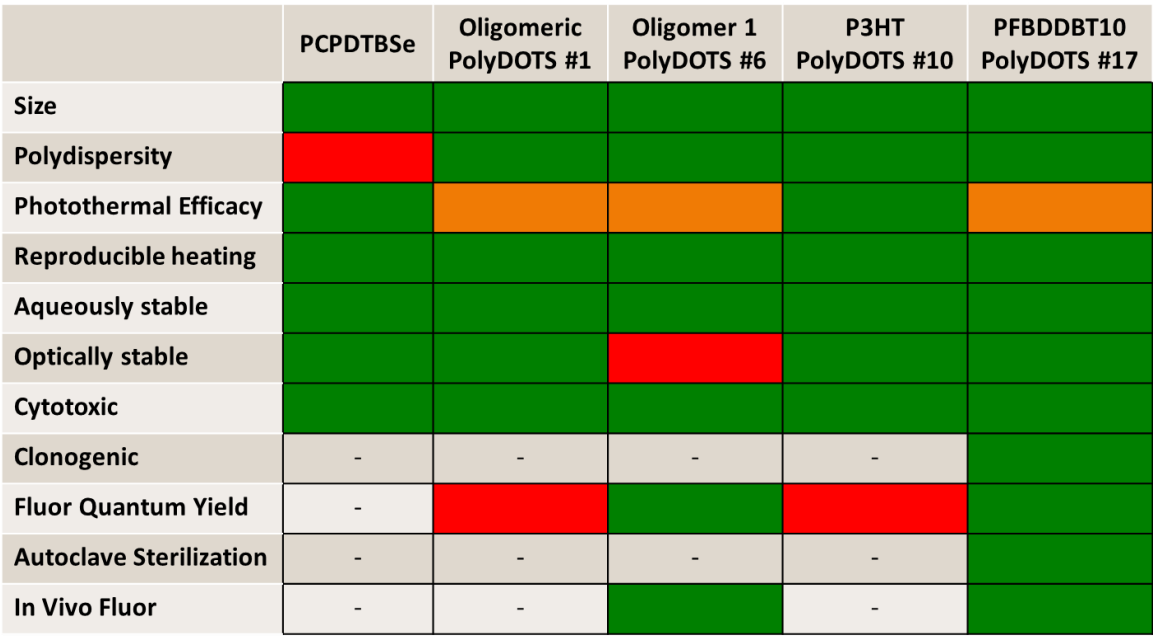

Figure 1. Comparison of PolyDOTS performance. Green = good, Orange = okay, Red = poor

For *in vivo* imaging, far red fluorescence is most ideal due to low background from mice themselves. Therefore, overall the highest overall quantum yield does not necessarily translate into the best *in vivo* imaging agent. The farthest red emission filter in Perkin Elmer's Lumina LT Series III In Vivo Imaging System (IVIS) is for indocyanine green (ICG) and collect emissions

from 810 nm to 870 nm. To better compare fluorescent polymer components and their associated POlyDOTS for *in vivo* imaging, their quantum yield over these wavelengths was determined (Table 1).

	Excitation (nm)	Emission Peaks (nm)	Quantum Yield	Quantum Yield limits of ICG Filter
Oligomeric	550	800	0.32	0.123
PolyDOTS #1	550	800	0.089	0.042
Oligomer 1	535	775	10.76	1.92
PolyDOTS #5	535	700	1.798	0.13
PolyDOTS #6	535	700	3.36	0.26
P3HT	508	710	1.54	0.16
PolyDOTS #10	508	710	0.22	0.014
PFBTDBT10	465	660	31.6	1.49
PolyDOTS #17	465	620, 825	0.52	0.28
PolyDOTS #18	465	620, 825	1.20	0.44

Table 1. Fluorescent quantum yield comparison of PolyDOTS using complete fluorescent emission and the limits of Perkin Elmer's Lumina LT Series III In Vivo Imaging System's ICG filter emission parameters.

Although Oligomer 1 nanoparticles have the highest quantum yield using ICG filter parameters, this doesn't translate to PolyDOTS #6. This is most likely due to the red shift in the absorption spectra of PolyDOTS #6 in the near infrared. The increased breadth of the near infrared absorption peak past 800 nm results in increased fluorescence quenching, specifically from the far red fluorescence (Figure 2B) shifting λmax of fluorescence from 775 nm to 700 nm. Interestingly, this red shift does not occur with P3HT or PFBTDBT10 PolyDOTS (Figure 2A) and PFBTDBT10 PolyDOTS fluorescence is instead quenched at its λmax, 660 nm, leaving fluorescence peaks at 620 nm and 825 nm (Figure 2C).

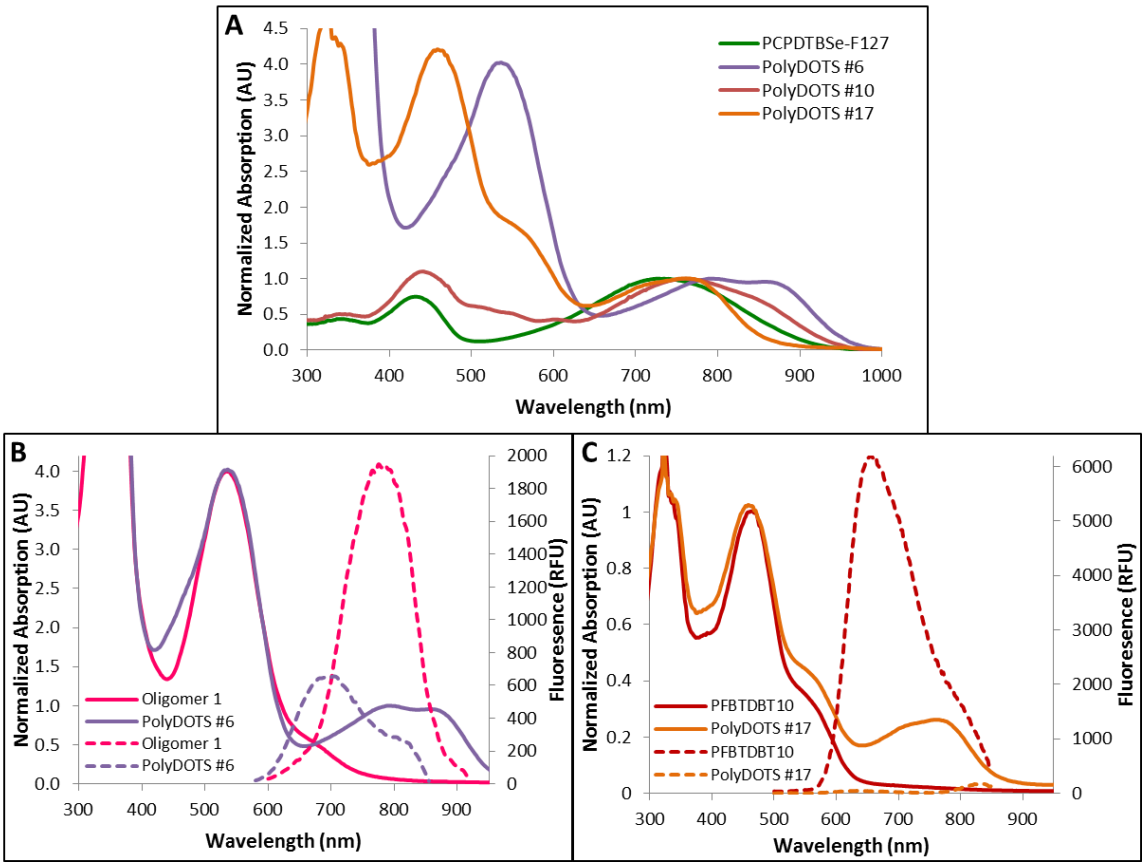

Figure 2. (A) Normalized absorption spectra of PolyDOTS and PCPDTBSe-F127 illustrating large red shift seen in PolyDOTS #6. **(B)** Absorption (solid line) and fluorescent (dashed) spectra of Oligomer 1 (pink) and PolyDOTS #6 (purple). Fluorescent spectra are of samples with 0.10 absorption at 535 nm. **(C)** Absorption (solid line) and fluorescent (dashed) spectra of PFBTDBT10 (red) and PolyDOTS #17 (orange). Fluorescent spectra are of samples with 0.10 absorption at 465 nm.

For more immediate future work, further evaluation into *in vitro* interactions of PolyDOTS with cells should be investigated to determine method of cell uptake, intracellular location, cause of cytotoxicity with photothermal therapy (necrosis, apoptosis, reactive oxygen species). Another animal model for photothermal ablation should be performed with modified laser parameters, such as reduced laser power with a longer treatment time or fractionated laser exposure, in an effort to ensure full tumor ablation and temper any response from laser light alone. PolyDOTS #17 should be evaluated for biodistribution and toxicity after systemic administration in an animal model. Additionally, it would be interesting to investigate if photothermal therapy can elicit an immune response and have an abscopal effect.

For future directions, PolyDOTS #17 can be further improved through the addition of targeting ligands to its surface, such an antagonist to chemokine receptor, CXCR4. CXCR4 is a G-coupled protein receptor [134] that is a key mediator in tumor metastasis [134-136], cancer stem cell maintenance, and therapeutic resistance [137-139]. CXCR4 is overexpressed in a subset of all breast cancer subtypes [140-145] and is correlated with decreased disease free survival [141-144, 146, 147] and overall survival [142-144]. Targeting the nanoparticle could improve tumor uptake and retention time to allow for more selective photothermal ablation. Additionally, CXCR4 antagonists have been shown to reduce tumor size on their own, and combination with hyperthermia may have a beneficial effect.

The fluorescent imaging potential of PolyDOTS could be improved through the use of a fluorescent conjugated polymer that absorbs further in the red (600 – 650) and emits fluorescence in the infrared. This would allow deeper penetration of the excitation light and also improve the fluorescence quantum yield (as the fluorescence should not directly overlap with the absorption of PCPDTBSe). Finally, a direct comparison between PolyDOTS and gold nanoparticles should be performed.

APPENDIX

A1. Review of Metal, Carbon, and Polymer Nanoparticles for Infrared Photothermal Therapy

A1.1 Abstract

The aim of this review is to provide an up-to-date overview of nanoparticles developed for use as photothermal therapy agents (PTT) over the past five years. The main emphasis is on nanoparticles that absorb near infrared (NIR) light for PTT of cancer. Mild hyperthermia, including drug delivery, versus thermal ablation is also discussed. Recent advances in the synthesis of highly anisotropic novel metal nanoparticles for PTT are described. New metals and metal oxide complexes, as well as the use of quantum dots for PTT and as imaging agents are newer areas of development that are explained. This review also highlights current progress in the development of carbon nanoparticles, including reduced graphene oxide for both thermal ablation as well as drug delivery. The review culminates in the recent use electrically conductive polymer nanoparticles for hyperthermia. The advantages and unique features of these contemporary nanoparticles being used for PTT are highlighted. The goal of the present work is to describe the recent evolution of nanoparticles for NIR stimulated PTT, and highlight the innovations and future directions.

This is an electronic version of an article published in Nano LIFE, Vol. 3, No. 3 (2013), 1330002 DOI: 10.1142/S1793984413300021© copyright World Scientific Publishing Company http://www.worldscientific.com/worldscinet/nl.

A1.2 Background

Hyperthermia and infrared light use in medicine

Elevated body temperature, also called hyperthermia, is an inherent physiological response to diseases such as viral and bacterial infections. Hyperthermia has been applied to medicine for millennia, as evidenced by the ancient Greek physician and philosopher Parmenides who said, "Give me the power to produce fever and I will cure all disease." In current medical practice hyperthermia is routinely used for analgesia, facilitation of wound healing, drug delivery, or for tissue removal via ablation. Hyperthermia may be divided into two distinct categories: 1) mild hyperthermia, where temperatures are often below 44˚C and tissue necrosis is not desired and 2) thermal ablation, where cell death is desired using temperatures above 45˚C. Mild hyperthermia can be applied locally, regionally, or to the whole body, whereas thermal ablation is a localized procedure. Current modalities for generating hyperthermia include radiofrequency, ultrasound, or application of near infrared (NIR) light. The focus of this review will be on application of NIR to stimulate nanoparticles for local hyperthermia, termed photothermal therapy (PTT). NIR is advantageous since there are specific wavelengths in the infrared region where water, melanin, and hemoglobin have absorption minima. This means that light between 700-900nm, or near 1050nm, as shown in Figure 1, is most likely to pass directly through tissues without significant absorption and heat generation.[32, 148] Therefore, nanoparticles located in tissue can act as strong absorbers of infrared light to generate localized heat when the tissue is exposed to infrared light.

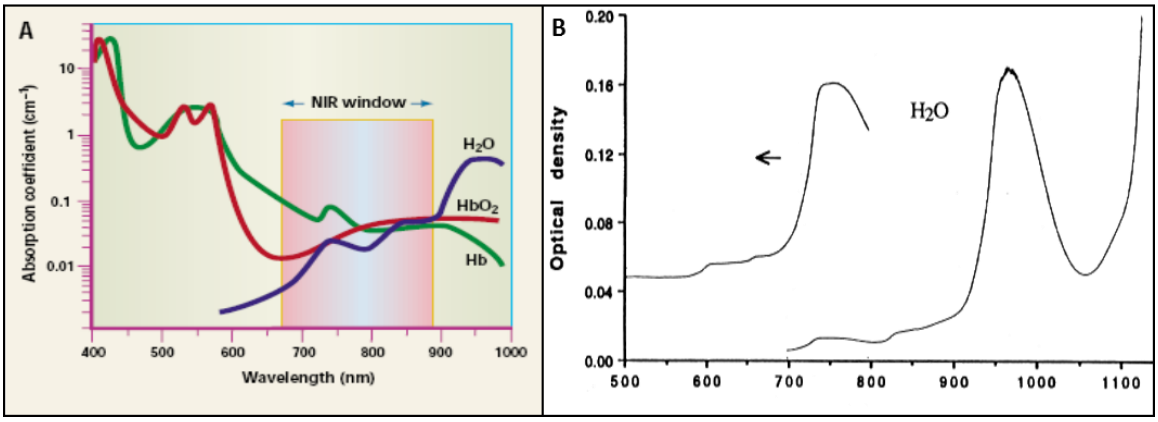

Figure 1. **(A)** Absorption minima of water and hemoglobin from 700-900nm and **(B)** absorption minima of water to show the range from 1000-1100nm. Reproduced from Ref [32, 148].

According to the International Agency for Research on Cancer there are 10.9 million cases of cancer diagnosed every year. Mortality rates vary from 40% in developed countries to as high as 77.9% in impoverished nations.[149] The most frequently occurring cancers are prostate, breast, lung, stomach, cervical/uterine, liver, and skin.[149] Radiofrequency ablation and focused ultrasound can be used to deliver intense hyperthermia (temperatures above 45ºC) to eliminate solid tumors in localized regions.[10, 150, 151] Hyperthermia between 40-43ºC is routinely used to help maximize chemotherapeutic delivery or radiation sensitization.[152-154] For example, Figure 2 shows how different hyperthermic temperatures affect colorectal carcinoma cell survival.[10] Chemotherapeutic agents can be localized to a specific region to aid in cancer cell destruction of micrometastasis. Chemotherapeutic agents that act synergistically with hyperthermia include doxorubicin, melphalan, mitomycin C (MMC), mitoxantrone, gemcitabine, etoposide, cisplatin, carboplatin and oxaliplatin.[153, 154] Hyperthermic chemotherapy aids in drug delivery by increasing blood flow and permeability of cell membranes to increase intracellular drug delivery, cellular metabolism and reducing drug efflux out of the cell.

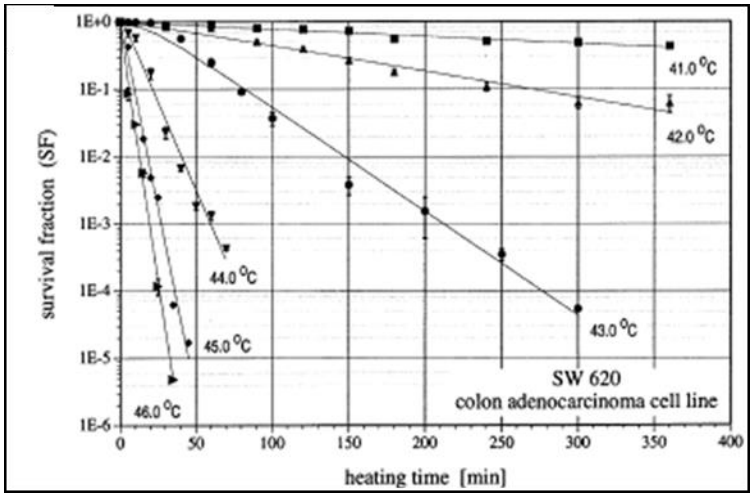

Figure. 2. Effect of various hyperthermic temperatures on colorectal cancer cells. Temperatures above 42ºC are the most effective for cell killing. Reproduced from Ref [10].

Nanoparticles

Nanometer- sized materials have different properties from their macroscopic counterparts, even when they are composed of the same elemental composition. That is why nano-systems are important and unique, and hence why they might be beneficial for medicinal applications. An important characteristic of tumors caused by the combination of fenestrated vasculature and compromised lymphatic drainage is the enhanced permeability and retention (EPR) effect. This is often exploited in nanoparticle based therapeutics because the small size of nanoparticles allows them to pass through fenestrae and the compromised lymphatic drainage causes them to accumulate, thereby passively targeting tumors.[155-157] Nano-sized particles have been shown to avoid immune system detection and clearance and therefore become more localized in tumors.[158-162] The number of publications in the area of nanoparticle mediated photothermally induced hyperthermia has been exponentially increasing for the past decade, as shown in Figure 3. In this time, many new nanoparticle types have been developed for use in medicinal applications.

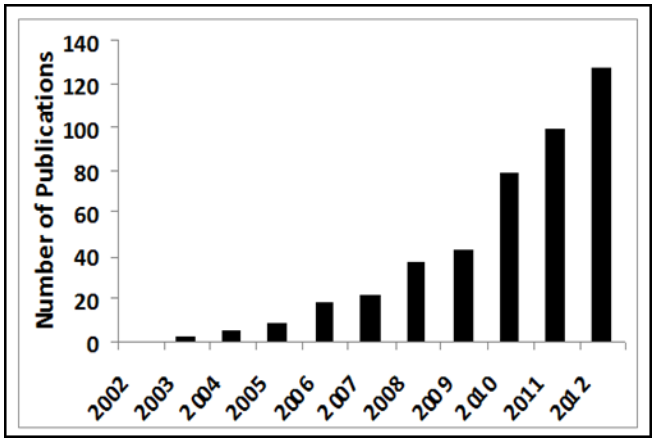

Figure. 3. The exponential increase of publications matching a Pubmed search for "nanoparticle photothermal"

A1.3 Metal Nanoparticles

Mechanism of heat generation

Noble metal nanoparticles are useful photothermal agents due to their enhanced absorption cross sections, which are 4-5 fold greater than conventional photoabsorbing dyes, have strong photostability, and do not incur photobleaching.[1] For some materials, absorption of light induces a resonance in the propagation of conducting electrons and this is called surface plasmon resonance (SPR). SPR can generate heat as the excited electrons lose excess energy in the form of phonons (collective oscillations of elastic waves that propagate through the material).[163, 164] Many metals (such as gold, silver, nickel, aluminum, lithium, palladium and platinum) have a strong SPR depending upon the wavelength of incident light.[165, 166] The strength of the surface plasmons is directly proportional to the quality factor, which is plotted in Figure 4.[167]

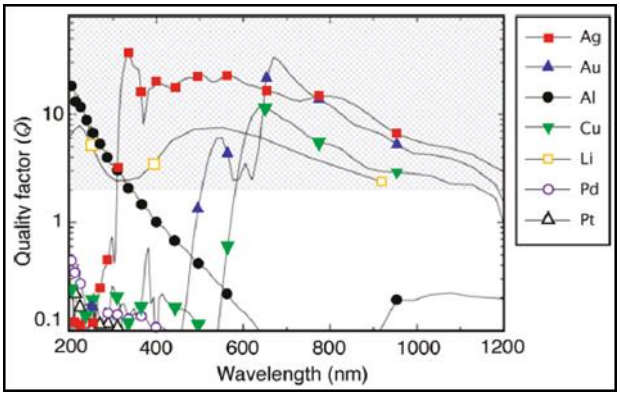

Figure. 4. Quality factor (Q) of localized surface plasmon resonance for metal air interfaces. A higher Q means a strong plasmon resonance. Reproduced from Ref [167].

As it is known that the NIR region is ideal for PTT, based on the quality factor, lithium, copper, silver, and gold should be ideal photothermal agents. However, plasmonic properties alone do not suffice for practical biomedical applications. Lithium is highly reactive and copper has issues with instability and toxicity; as such, they are rarely used for biomedical photothermal applications.[166] While silver has the highest electrical and thermal conductivity among all metals,[166] silver nanostructures are considered toxic due to the release of Ag^+ ions,[168] although passivation of the nanoparticle surface can greatly increase stability and reduce toxicity.[169] By process of elimination, and because gold is relatively bioinert, it has been extensively used for both *in vitro* and *in vivo* photothermal applications.[170]

Small gold and silver nanoparticles, often called 'seed particles' in synthesis procedures, have a strong SPR about 520 nm for Au and 390-420 nm for Ag. But, their size and shape is routinely modified to shift their SPR towards the NIR. Shifting of the absorption towards the NIR (red-shifting) occurs as the size or aggregation of the nanoparticles increases, as shown in Figure 5a.[164] It is also possible to shift the SPR of anisotropic nanoparticles, such as nanorods to the NIR (Figure 5b).[171] Nanorods have both transverse and longitudinal modes of optical absorption corresponding to the diameter and length of the rod respectively, as shown in Figure 5c.[171] Altering the aspect ratio (length / diameter) of the rod causes the longitudinal mode to dominate the optical absorption and simultaneously red-shifts the peak.[172] Silver nanoplates, as

shown in Figure 5d, represent an example of increased anisotropy as the particles develop well defined edges and triangular and hexagonal shapes.[173] An alternate technique for creating metal nanoparticles with strong SPR is through the use of nanoshells. Nanoshells were originally developed by deposition of a thin (between 5-20 nm) layer of gold onto a silica sphere, as shown in Figure 5e.[174] The ratio of shell thickness to core diameter can be adjusted to tune the nanoshell absorption into the NIR. Although solid core nanoshells are still routinely synthesized and evaluated for biomedical applications, the production of hollow metal nanoshells and nanocages has recently come to the forefront. Hollow metal nanoparticles are produced by developing a shell on top of a solid metal core and then selectively dissolving away the core to leave a hollow metal shell. Figure 5f demonstrates that, like solid core nanoshells, the SPR of hollow gold nanoshells can be tuned by changing shell to core thickness ratio, with thinner shells resulting in a larger red-shift.[175] One complication in making a thinner shell is ensuring the integrity of the shell as thinner shells tend to be more unstable and generate a lower yield of useable nanoparticles. Another method to tune SPR is through incorporation of other metals either though alloying (Ag-Au [176-178], Ag-Pt[179, 180], Ag-Pd[179]) or bimetallic core shell nanoparticles (Ag-Au [181-184], Au-Ag[185-190], Ag-Pt[191], Pt-Pd[192]).

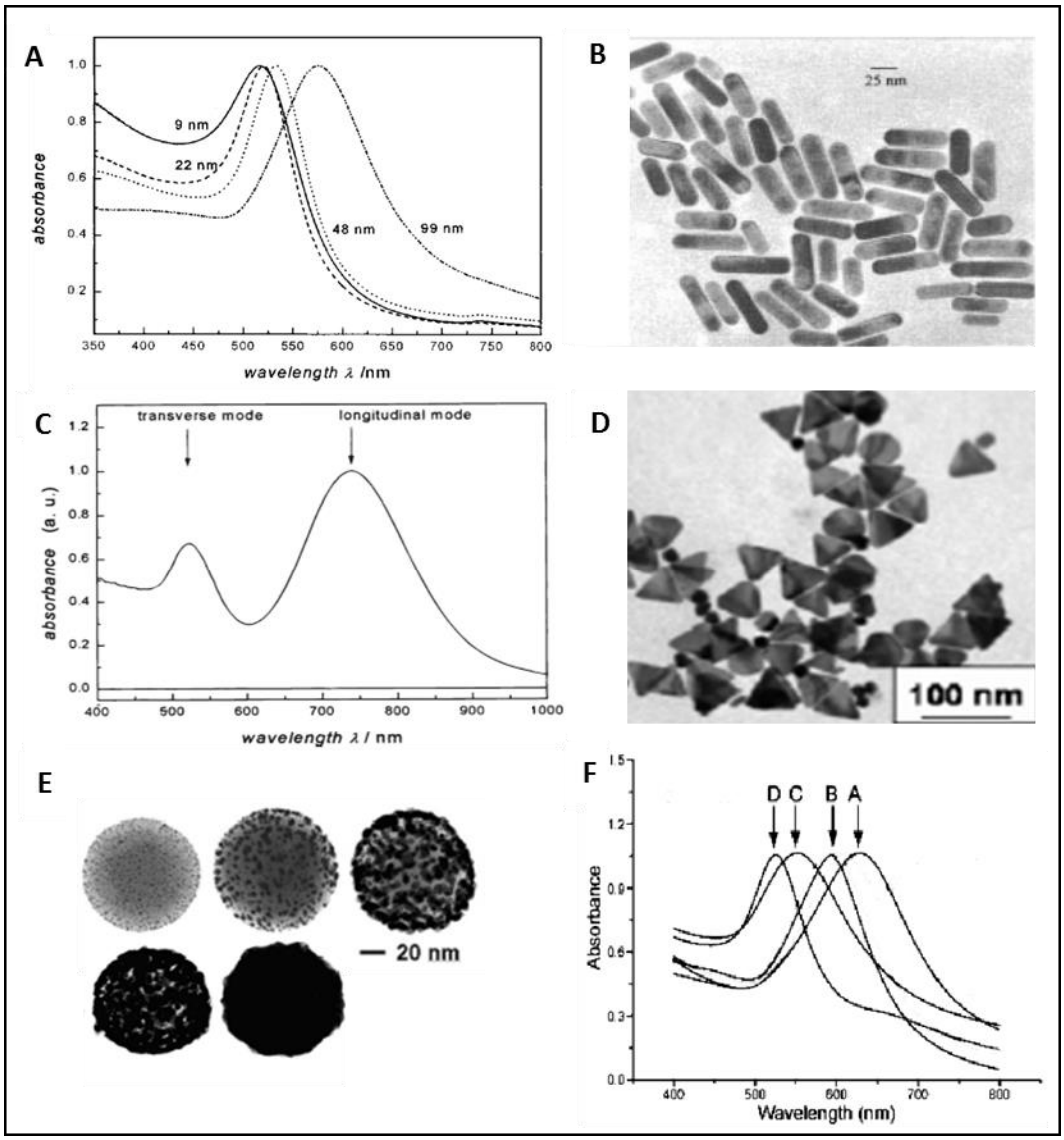

Figure 5. (A) Red-shift in the absorption spectra of 9, 22, 48, and 99 nm gold nanospheres in water. Reproduced from [164]. **(B)** TEM of gold nanorods. Reproduced from [171]. **(C)** Extinction spectrum of gold nanorods illustrating the transverse and longitudinal modes corresponding to the diameter and length of the gold nanorod. Reproduced from [171]. **(D)** TEM of silver nanoplates. Reproduced from [173]. **(E)** TEM images of gold growth (dark dots) on silica core particles. Reproduced from [174]. **(F)** Absorption spectra of hollow gold nanoshells with increasing shell thickness (A: 9.6 ± 4.3nm, B: 15.0 ± 2.0nm, C: 22.1 ± 3.0nm, D: 30.0 ± 2.8nm. Reproduced from [175].

During modification to enhance plasmonic properties of nanoparticles (NP), consideration should be taken as to how geometrical changes will affect transportation and toxicity of the NP. Size, shape and surface chemistry greatly affect NP biological interaction, circulation time, and *in vivo* biodistribution. The field of metal nanoparticles for plasmon induced

hyperthermia is so broad, that to date, it has not been possible for a comprehensive review on circulation and biodistrubution to be prepared. Increased blood circulation time is beneficial to increase the chances that the particles will interact with the tumor. It has been shown that increased nanoparticle size leads to increased half life in the blood; however, particles with a hydrodynamic diameter greater than 60 nm do not effectively diffuse through the dense tumor matrix.[29, 193-195] Although smaller NPs have better transport, due to decreased steric hindrance, smaller particles tend to extravasate into normal tissues more easily and cause adverse effects.[29] Cellular internalization has been shown to be more rapid for spherical particles.[196] Specifically, for Au and Ag NPs in a size range of 2-100 nm, particles with a diameter 40-50 nm had the greatest cellular uptake by receptor mediated endocytosis.[197, 198] However, in a thermodynamic model of receptor mediated endocytosis, *Zhang et al.* found the optimal radius for maximum internalization of a ligand coated NP to be 25-30 nm.[199] This correlates well with *Wang et al's* findings that 30 nm Ag-Au nanocages have better *in vivo* biodistribution and tumor targeting capabilities than 55 nm nanocages.[200]

An interesting *in vitro* study was performed by *Chithrani et al.,* who compared the cellular uptake of transferrin targeted gold nanospheres of diameters 14, 30, 50, 74, and 100 nm and nanorods with aspect ratios of 1.5 (20 x 30 nm), 3.6 (14 x 50 nm), and 6 (7 x 42 nm).[198] They established that for spherical NPs, 50 nm (followed by 74 nm) were the most readily internalized and that 14 nm (followed by 100 nm) had the lowest cell uptake. They then compared 50 nm nanospheres with the nanorods and found that 50 nm nanospheres exhibited the greatest cell uptake and that nanorods with lower aspect ratios were more readily internalized. Additionally, it was determined that the rate of exocytosis is inversely proportional to rate of uptake (the slowest uptake led to the fastest exocytosis). However, data from *Adriani et al*., suggest that for *in vivo* delivery, thin disk-like shaped nanoparticles are the most effective, followed by nanorods, with nanospheres being the least effective.[201] Determining the optimum

shape of nanoparticles is challenging as evidenced by the contradictory results for cellular uptake *in vitro* and *in vivo*, but shape is a very important feature when designing a nanotherapeutic.

Surface charge strongly influences NP transport and cellular uptake. Positively charged particles have the highest rate of cellular uptake, followed by neutrally charged particles, while negatively charged particles have the lowest.[202] Additionally, charge may also affect intracellular particle localization, with data suggesting that positively charged particles exhibit perinuclear localization, while negatively charged particles remain localized in lysosomes.[202] Increasing the magnitude of surface charge, both positive or negative, leads to increased clearance by the reticuloendothelial system.[29] Strongly charged particles also develop electrostatic interactions (to positively charged collagen or negatively charged sulfated glycosaminoglycans) that can inhibit homogenous distribution of NPs throughout the tumor matrix.[29] To combat these diffusion issues and increase circulation time, many nanoparticles are coated with polyethylene glycol (PEG). PEGylation sterically stabilizes NPs and imparts a near neutral surface charge, which helps to reduce unwanted electrostatic interactions, protein adsorption, and clearance by the reticuloendothelial system.[203-205]

Silver Nanoparticles

Traditionally, silver has been used for healing and antibacterial purposes and is still used today for treatment of burns.[206-211] With the introduction of antibiotics, the use of silver has declined, but is currently receiving renewed attention as a treatment avenue for antibiotic resistant pathogenic bacteria.[207] Unfortunately, Ag NP toxicity to mammalian cells has limited their investigation as therapeutic agents despite the fact that passivation of the NP surface has been shown to greatly decrease cytotoxicity. For example, *Jena et al.* has shown that chitosan coated Ag NPs retain their antibacterial properties while exhibiting minimal toxicity to mammalian cells at bacteriocidal concentrations.[169] As previously described earlier, Ag has as high a quality factor as Au in the infrared, and is proving to be an interesting new material for photothermal therapies.[166] A major benefit for using Ag NP as PTT agents for treating localized bacterial

infections is silver's inherent antibacterial nature, even for passivated Ag NP, through the slow release of Ag^+ ions.[212] For PTT applications in cancer, Ag has a few extra benefits that Au does not possess: 1) it has been shown to be anti-angiogenic,[213] and 2) it has recently been demonstrated that tumor cells are more susceptible to Ag NP induced toxicity than non-tumorigenic cells.[214, 215]

Recently, *Boca et al.* synthesized chitosan coated triangular Ag NPs and investigated their capability for PTT compared to PEGylated Au nanorods.[215] Interestingly, it was found that the Ag NPs were more cytotoxic to the lung cancer line (NCI-H460) than the non-cancerous cell line (HEK) and that Ag NPs experienced greater cell uptake than Au nanorods. Exposure of NCI-H460 cells to NIR light after incubation with Ag NPs or Au nanorods revealed that Ag NPs exhibited more effective PTT than Au nanorods (Figure 6) despite incubation at a much lower concentration (0.39 μg/mL and 7.21 μg/mL respectively).[215] The authors hypothesize that the improved PTT is a result of the higher cellular uptake of Ag NP due to their positive surface charge compared to the neutrally charged Au nanorods.

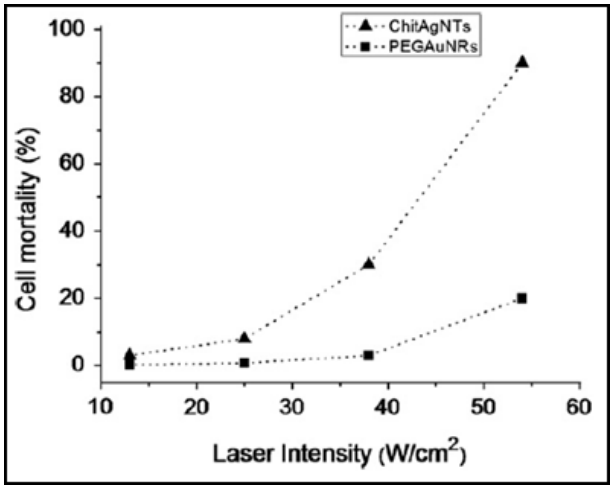

Figure 6. Cell mortality of lung cancer, NCI-H460, cells incubated with chitosan-coated silver nanotriangles (ChitAgNTs, triangle) or PEGylated gold nanorods (PEGAuNRs, square) after irradiation with multiple laser powers of 800 nm light. Reproduced from Ref [215].

Bimetallic and Alloy NPs

More commonly, Ag has been used in conjunction with Au; being incorporated into Ag-Au nanoshells, nanorods, nanocages, and bimetallic particles.[176-178, 216-218] For example, *Cheng et al.* investigated the relative photothermal therapeutic efficiencies of three Au-based nanomaterials with absorption near 800 nm (silica-Au nanoshells, hollow Au/Ag nanospheres and Au nanorods).[216] They determined silica-Au nanoshells to be the most efficient, as shown in Figure 7, closely followed by hollow Au/Ag nanospheres with Au nanorods being least efficient.[216]

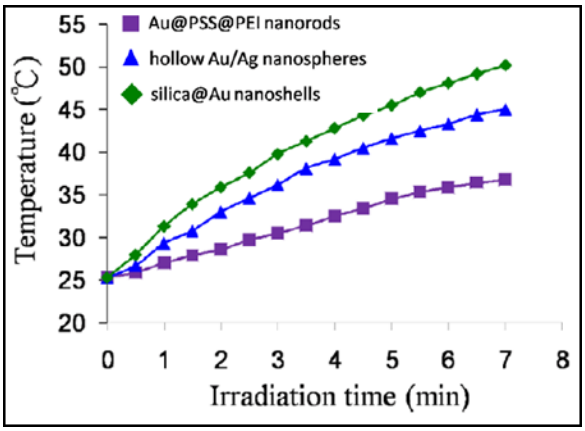

Figure 7. Heating profiles of polyethylenimine-poly(styrenesulfonate) coated gold nanorods (Au@PSS@PEI nanorods), hollow gold-silver nanospheres (hollow Au/Ag nanospheres), and gold coated silica nanoshells (silica@Au nanoshells) at a concentration of 8.36 x 108 particles per 100 µL generated from exposure to 808 nm, 30 W/cm2, continuous wave light. Reproduced from [216].

Huang et al. investigated aptamer conjugated Au-Ag nanorods for PTT because of the sharper and stronger longitudinal SPR compared to Au nanorods, as shown in Figure 8.[217] It was found that under 5 minute irradiation with 808 nm light (at 0.6 W/cm^2), aptamer conjugated Au-Ag nanorods exhibited cell specific targeting, leading to 90% cell death of targeted T-cell acute lymphoblastic leukemia cancer cells (CCRF-CEM) and negligible cell death of untargeted acute promyelocytic leukemia cells (NB 4).[217]

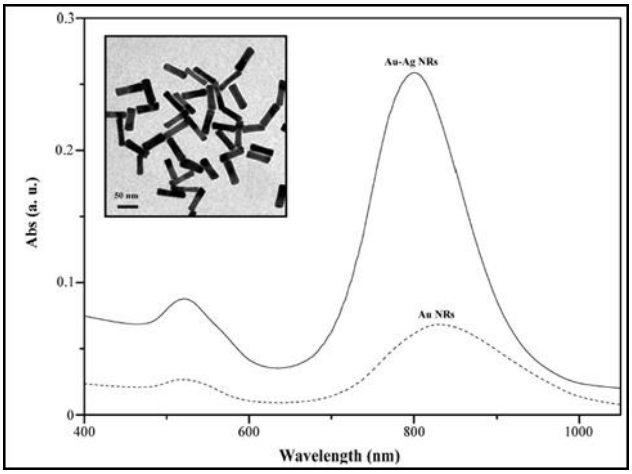

Figure 8. Absorption spectra comparing gold nanorods (Au NRs) to gold-silver nanorods (Au-Ag NRs) and TEM of Au-Ag NRs (inset). Reproduced from [217].

Another Ag-Au bimetallic nanoparticle for infrared PTT is Ag-Au nanocages. Ag-Au nanocages are hollow nanostructures with porous walls that can be prepared by galvanic replacement reaction between silver nanocubes and chloroauric acid creating an Ag-Au alloy primarily comprised of Au (Figure 9 a,b).[177] This nanoparticle is ideal for cancer therapy as its optical resonance peak can be tuned to the NIR. Gold surface chemistry allows for simple surface functionalization, and their hollow nature allows for drug loading. Ag-Au nanocages can be further modified by dealloying to completely remove Ag^{+} ions and create Au nanoframes.[219]

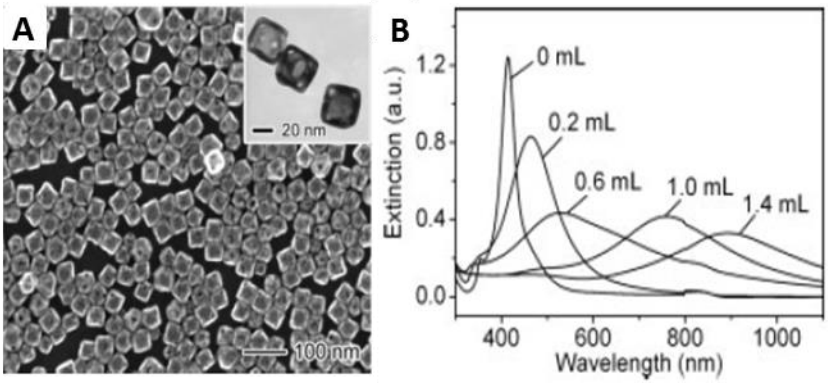

Figure 9. (A) SEM, and **(inset)** corresponding TEM of AgAu Nca with 30 nm edge length. **(B)** Absorption spectra of Ag-Au Nca illustrating the red-shift caused by adding more chloroauric acid to the starting subtrate of Ag nanocubes. Reproduced from [177].

Younan Xia's group investigated *in vitro* PTT using Ag-Au nanocages (75% Au, 25% Ag) and achieved effective killing of SKBR3 breast cancer cells using 5 minutes of 810 nm light

at a power of 1.5 - 4.7 W/cm^2.[178, 220] Next, they investigated *in vivo* efficacy demonstrating that 400 nm PEGylated Ag-Au nanocages can be used as effective photothermal agents to treat glioblastoma.[221] *Gao et al*. combined PTT and photodynamic therapy (PDT) by loading the photosensitizer hypocrellin B onto Ag-Au nanocages.[222] Dose-dependent cell viability was seen *in vitro* with a 94% cell kill of HeLa cells cultured with 35 pM Ag-Au nanocages (equivalent to 7.0 μM HB) for 6 hr and subsequent irradiated with a 790 nm two-photon laser at 85.5 pJ per pulse for 300 seconds. *Shi et al.* has developed a complex nanostructure which integrates magnetic targeting, PTT, and a pH sensitive release of the chemotherapy drug.[223] This was done using iron oxide-calcium phosphate capped, doxorubicin loaded, Ag-Au nanocages. The calcium phosphate linkage of the drug to the particle is acid-decomposable creating pH sensitive drug release. The iron oxide allows for magnetic targeting and MRI contrast, while the Ag-Au nanocages confer PTT ability. In addition to a pH driven drug release of ~28% over 3 hours, it was shown that NIR stimulation resulted in a burst release of an additional 20% of loaded doxorubicin within 1 hr of irradiation (Figure 10).[223] This nanostructure resulted in 20% cell viability with a particle concentration of 30 μg/mL and NIR stimulation (808 nm, 1 W, 5 min), thereby demonstrating a new effective multi-modal bimetallic NP for PTT, imaging and drug release.

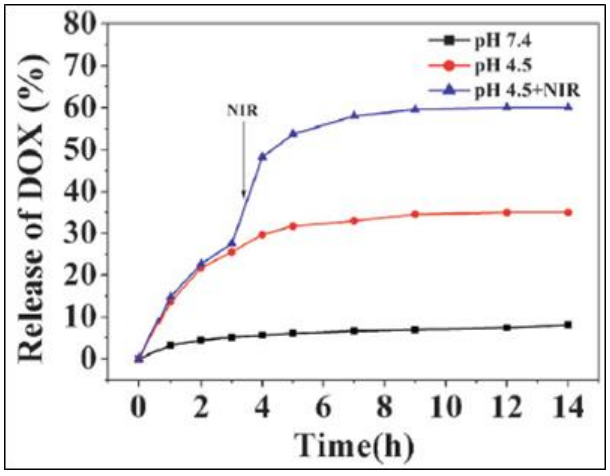

Figure 10. Release kinetics of doxorubicin from iron oxide-calcium phosphate capped AgAu nanocages at pH of 7.4 and 4.5 and with 1 W of 808 nm. Reproduced from [223].

Gold Nanoparticles

Gold nanoparticles are by far the most extensively studied metallic nanoparticle for PTT.[1, 224-227] Gold nanoparticles have taken many shapes beginning with spherical particles such as nanospheres,[42, 228-232] solid and hollow nanoshells,[233-243] and eventually moving into anisotropic particles such as nanorods,[33-43, 244] nanostars,[245-250] nano-popcorn,[251, 252] nanocubes,[253] nanoprisms,[254] and nanohexapods.[255]

Gold nanospheres are solid spherical nanoparticles typically produced by citrate reduction of chloroauric acid in water to Au(0), with a tunable plasmon resonance based on the size of the spheres. First synthesized by Faraday in 1857, gold nanoparticles began being widely studied in the 1950s.[1] Recently, investigation into the mechanism of death in Au nanosphere mediated PTT has revealed that the method of cell death varies depending on location within the cell and whether a pulsed or continuous wave laser stimulation is applied.[228] *Huang et al.* found that utilizing continuous wave laser light resulted in apoptosis, while pulsed laser resulted in necrosis.[228] The authors hypothesize that the higher energy nanosecond laser pulse results in strong and rapid heating that could produce shock waves and damage the cell rapidly, thus resulting in necrosis while continuous wave light more slowly heats the cell allowing for apoptosis. Additionally, it was determined that cytoplasm targeted Au nanospheres resulted in more efficient PTT under continuous wave irradiation, while nuclear targeted Au nanospheres were more efficient under pulsed irradiation.[231] Gold nanospheres have also been used in conjuction with other materials to form multimodal NPs. *Kirui et al.* developed A33scFv conjugated, PEGylated, iron oxide – gold hybrid nanoparticles (HNPs) for combined magnetic resonance imaging and PTT (Figure 11a**)**.[231] They investigated *in vivo* photothermal efficacy of the A33 targeted and untargeted HNPs in subcutaneous SW1222 colorectal cancer mouse xenografts and demonstrated that 200 µL of systemically injected 1 mg/mL particles and repeated exposure (7 times, every 2 days) to 808 nm light (5 W/cm^2 for 30 min) resulted in significant suppression of tumor growth (Figure 11b).[229]

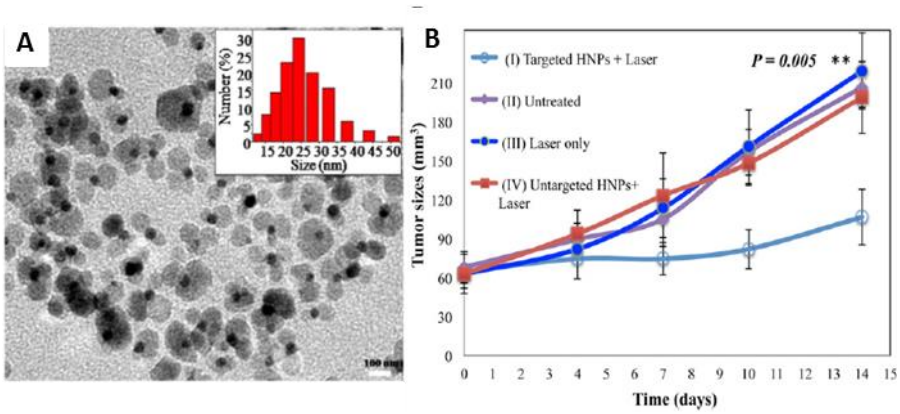

Figure 11. (A) TEM and DLS (inset) of iron oxide – gold nanoparticles with an average size of 25 nm Reproduced from [231]. **(B)** PTT of subcutaneous tumor xenografts measured 24 hrs after irradiation (808 nm, 5 W/cm2, 30 min) demonstrating the improved efficacy of targeted HNPs. Reproduced from [229].

Gold nanoshells are attractive for biomedical applications because of the ability to tune their SPR to the NIR without making gross adjustments to the particle size, simply by modifying the thickness of the shell. Due to their ease of functionalization, gold nanoshells are often conjugated with ligands for targeted PTT both *in vitro* and *in vivo*, recently: HER2, VEGF, EGFR, and integrin αvβ3.[234-237] Gold nanoshells have also been incorporated into drug loaded polymer nanoparticles to create multimodal therapies.[256] *Lu et al.* showed that intravenous injection of hollow gold nanoshells (HAuNS) targeted to RGD integrin, overexpressed in both glioma and angiogenic blood vessels, allowed photoacoustic tomography and selective PTT of an orthotopic mouse xenograft model of glioma.[240] When exposed to NIR light (16 W/cm^2, 3 minutes, 808 nm), RGD integrin targeted HAuNS increased the median survival time of mice from 19 days to 28 days ($p > 0.001$), compared to untargeted particles. *Lu et al.* also investigated *in vivo* targeting of PEGylated HAuNS targeted with a melanocyte-stimulating analog (MSH-PEG-HAuNS) in murine melanomas.*[241]*

In addition to targeted PTT, hollow gold nanoshells have also been loaded with chemotherapeutic drugs for effective drug delivery upon NIR exposure [236, 238, 239]. *You et al.* [242] synthesized doxorubicin (DOX) loaded PEGylated-HAuNS (DOX@PEG-HAuNS) and achieved drug loading as high as 63% DOX by weight (1.7 μg DOX/μg Au).[242] Irradiation

with NIR light (3 minutes of 2 W/cm^2 808 nm light, repeated 4 times over 2 hours) triggered rapid DOX release and significantly greater killing of MDA-MB-231 breast cancer cells *in vitro*. *You et al.* investigated the *in vivo* behavior of several formulations of DOX@PEG-HAuNS and determined that laser irradiation of 1.5 W/cm^2, for 5 min significantly enhanced therapeutic efficacy, while reducing cardiotoxicity compared to clinically used free DOX and liposomal DOX.[239] *You et al.* expanded upon these results and targeted the DOX@PEG-HAuNS to EphB4 receptors and found that targeted DOX@PEG-HAuNS achieved 1.6 - 3 fold higher intratumoral concentrations than untargeted particles.[243] Additionally, 3 minutes of 2 W/cm^2 NIR light exposure resulted in complete tumor regression in 6 out of 8 mice treated with EphB4 targeted DOX@PEG-HAuNS.

Choi et al. synthesized Au nanorods encapsulated in a pluronic chitosan composite (Chit-NC-GNR) which greatly improved intravenous *in vivo* targeting ability while maintaining comparable healthy tissue biodistribution (Figure 12a) in athymic nude mice with subcutaneous squamous cell carcinoma, SC77, tumors.[244] They found that under NIR radiation (4 min, 808 nm, 4 W/cm^2) Chit-NC-GNRs demonstrated improved photothermal efficacy compared to saline, Au nanorods, and pluronic coated Au nanorods (NC-GNRs) as seen in Figure 12b).[244]

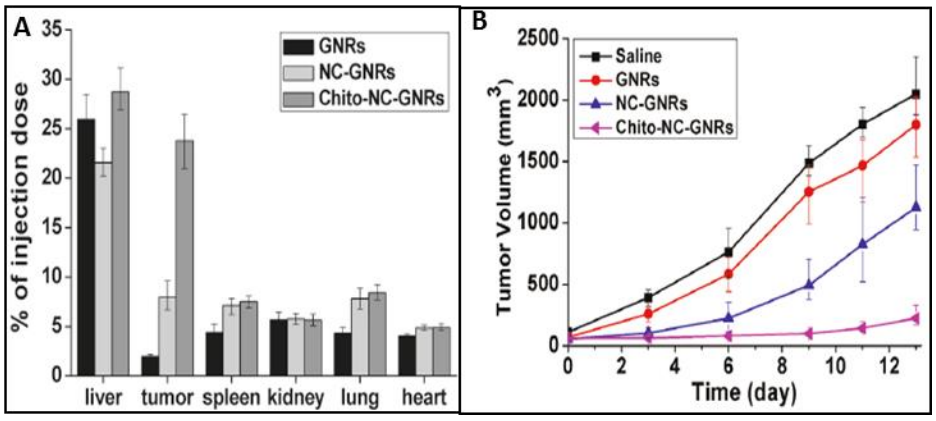

Figure 12. (A) Biodistribution 24 hrs after tail vein injection of gold nanorods (GNRs), gold nanorod loaded nanocarriers (NC-GNRs), and chitosan coated gold nanorod loaded nanocarriers (Chito-NC-GNRs). **(B)** Changes in tumor volume after onetime NIR irradiation (4 min, 808 nm, 4 W/cm2) 24 hrs after treatment with nanomaterials or saline control. Reproduced from [244].

Chen et al. synthesized a nano-sea urchin structure in which gold nanorods are grown inside mesoporous silica nanoparticles (Figure 13), creating a multifunctional nanoprobe capable of photoacoustic imaging and PTT with a tunable plasmon resonance achieved by varying the aspect ratio of the Au nanorods.[35] These particles demonstrated efficacious PTT *in vivo,* in subcutaneous MDA-MB-231 breast cancer cell tumor- bearing nude mice, achieving a 68.4°C intratumoral temperature with 2 minutes of 2 W/cm^2 808 nm light that resulted in tumor-free animal survival 14 days after treatment.[35]

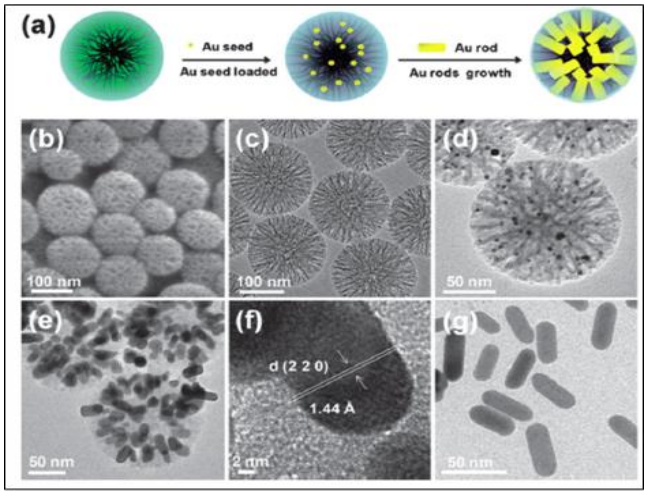

Figure 13. (A) schematic of the synthesis and structure of gold nanorod filled mesoporous silica nanobeads (AuRNBs). **(B)** SEM and **(C)** TEM of mesoporous silica nanobeads. **(D)** TEM of gold seeds formed within silica nanobeads. **(E)** TEM image of gold nanorod pore-filled structure (AuRNBs). **(F)** high resolution TEM illustrating a lattice spaciing of 1.44 A for Au NRs (2 2 0) plane. **(G)** TEM image of Au NRs after removing the silica matrix by NaOH etching. Reproduced from [35].

Gold nanorods have also been incorporated into nanoplatforms with chemotherapeutics for the development of a multimodal therapy. *Shen et al.* developed a nanoparticle for combined chemotherapy and PTT by synthesizing an RGD targeted, PEGylated, doxorubicin loaded, mesoporous silica coated, gold nanorod (DOX-pGNR@mSiO_2-RGD) (Figure 14a**).**[33] They found that both NIR radiation and decreased pH triggered release of doxorubicin (Figure 14b).[33] *In vivo* evaluation was performed in A549 tumor-bearing Balb/c nude mice and resulted in a statistically significant decrease in tumor volume.

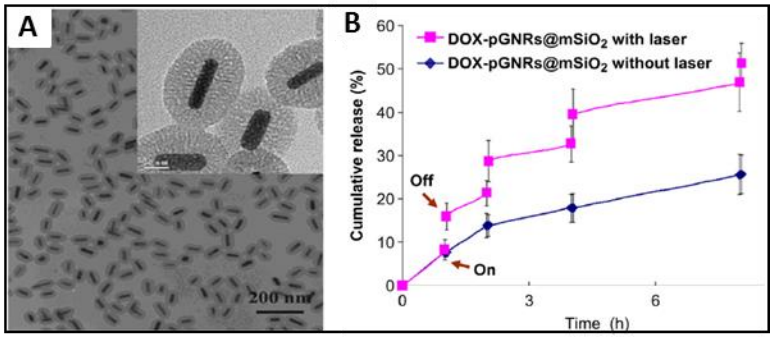

Figure 14. (A) TEM image of mesoporous silica coated gold nanorod. **(B)** Doxorubicin release profile from DOX-pGNR@mSiO2 at pH of 5 with and without NIR irradiation (performed at 1 hr, 2 hr, 4hr, and 8hr mark, 808 nm, 3 W/cm2, 3 min). Reproduced from [33].

Another gold nanoparticle utilized for PTT are Au nanostars, which are spherical NPs with arm-like projections which impart a high surface to volume ratio (Figure 15).[246, 250] The presence of multiple branches on the nanostars creates a structure that simulates a collection of small rods, achieving comparable absorption but lower scattering than larger rods. *Wang et al*. investigated chlorin e6 (Ce6), a fluorescent photosensitizer, functionalized PEGylated gold nanostars (GNSt-PEG-Ce6) for combined PDT and PTT.[248] They tuned the gold nanostars absorption peak to match that of Ce6, ~670 nm, for simultaneous PDT and PTT. The particles were readily internalized by MDA-MB-435 breast cancer cells, and under 671 nm light (10 W/cm^2 for 2 min) caused greater cell death than Au nanostars and Ce6 alone or delivered simultaneously. Compared to the controls, a statistically significant reduction in tumor size resulted after irradiation (1 W/cm^2 for 6 min) of the GNSt-PEG-Ce6 with the cancer cells *in vivo*. *Yuan et al.*, showed that TAT-peptide functionalized Au nanostars have increased uptake by BT549 breast cancer cells compared to bare or PEGylated Au nanostars.[249] Photothermal ablation of BT549 cells was accomplished by 3 min of 850 nm pulsed laser irradiation (12.5 pJ/pulse, 0.4 W/cm^2) after 4 hr incubation with TAT-Au nanostars. In a separate study, *Yuan et al.*, investigated the *in vitro* and *in vivo* photothermal response of the Au nanostars and achieved thermal ablation of SKBR3 breast cancer cells *in vitro* with 3 and 5 minutes of 980 nm light at 15 W/cm^2 and *in vivo* with 10 minutes of 785 nm light at 1.1 W/cm^2.[250]

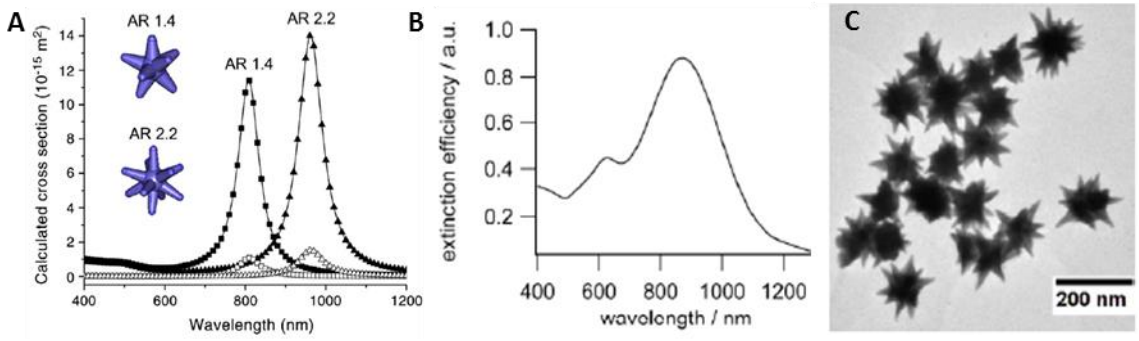

Figure 15. (A) Calculated absorption (solid symbols) and scattering (open symbols) cross-sections of gold nanostars with different aspect. Reproduced from [250]. **(B)** Absorption spectra and **(C)** TEM of gold nanostars. Reproduced from [246].

Lu et al. synthesized prostate specific membrane antigen (PSMA) targeted nanopopcorn, which is similar to nanostars, but with shorter branches.[251] They demonstrated efficacious PSMA targeted PTT by showing that PSMA positive LNCap had significantly decreased cell viability compared to PSMA negative HaCaT and PC-3 cell lines. They determined that Au nanopopcorn resulted in increased cell death compared to Au nanorods at 12.5 W/cm^2. *Beqa et al.* developed a novel hybrid nanomaterial using gold nanopopcorn decorated single wall carbon nanotube (GNPOP-SWNT) that absorb in the NIR.[252] Conjugation of the S6 aptamer to the nanomaterial targeted HER2 positive SKBR3 breast cancer cells exclusively and resulted in effective photothermal therapy, while not binding HER2 negative MDA-MB and HaCaT cell lines.

Gold nanoprisms (Au NPr) are triangular shaped gold discs that have tunable optical properties in the NIR, from 750 to 1075 nm.[254] *Pelaz et al*. demonstrated that Au NPr can effectively thermally ablate Vero cells after 2 minutes at 30 W/cm^2 of 1064nm light.[254] *Wang et al.* synthesized and characterized Au nanohexapods and compared them to Au nanorods and nanocages (Figure 16 a-f).[255] Au hexapods were found to generate comparable heat to nanorods and nanocages, display the highest cell uptake *in vitro* with MDA-MB-435 cells, and exhibited the greatest tumor uptake *in vivo*. As a result, Au nanohexapods created the highest

intratumoral temperature while nanocages generated the lowest (Figure 16g). *In vivo* treatment efficacy indicates that Au nanohexapods are a viable nanomaterial for PTT of cancer.

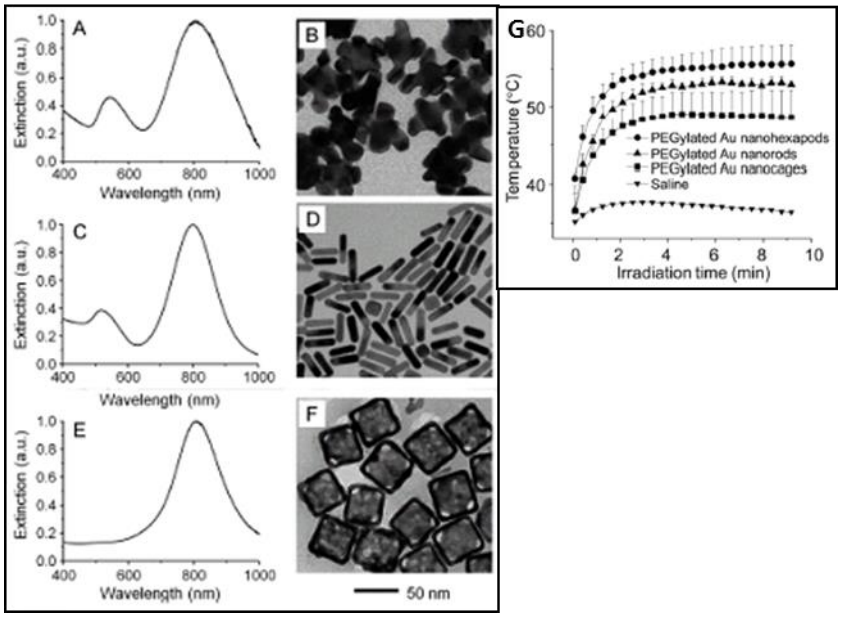

Figure 16. (A, C, E) absorption spectra and **(B, D, F)** TEM of gold nanohexapods, nanorods, and nanocages respectively. **(G)** Average intratumoral temperature generation as a function of irradiation time with a laser power density of 1.2 W/cm2 Reproduced from [255].

Other metals and metal oxides

Researchers have begun to employ other inorganic nanoparticles, besides silver and gold, for PTT because of their diagnostic capabilities, better overall photothermal stability and excellent photothermal conversion efficiency. Nanostructures made up of gold and silver have been known to exhibit a "melting effect" under prolonged stimulation from NIR radiation, which inhibits their SPR in the NIR.[54-58] This same effect is not seen with other inorganic metals such as palladium (Pd).

Due to its higher bulk melting point compared to Au and Ag, Pd has greater photothermal stability compared to Au and Ag.[257-259] However, most Pd-based nanomaterials have absorbances in the UV/visible region and not in the NIR.[260] Recently, *Huang et al.* synthesized hexagonal Pd nanosheets in order to tune the size of the Pd nanosheets (edge length = 20-160 nm) to tune their SPR into the NIR.[257] This allowed them to use the Pd nanosheets as PTT agents,

as shown in Figure 17. Their group demonstrated that the Pd nanosheets can efficiently photothermally ablate QGY-7703 liver cancer cells. They also confirmed that the shape integrity of the nanosheets was retained after irradiation with an 808 nm laser (2W, 30 min). One limitation in the use of hexagonal Pd nanosheets is their inability to enter cancer cells due to their ultrathin nature. This was resolved by using silica-coated Pd (Si@Pd) nanosheets.[258] Coating the palladium nanosheets allowed the authors to increase the thickness of the nanosheets up to 32 nm, with Si@Pd nanosheets having a 13 times greater increase in cell uptake compared to polyvinyl pyrrolidine (PVP)-coated Pd nanosheets. The photothermal efficiency of the Si@Pd nanosheets (55 μg/mL) was also tested in QGY-7703 cells. Cell death was confirmed to be 100% after NIR illumination with an 808 nm laser for 2 min (1.4 W/cm^2). Their group has also fabricated silver-coated Pd (Ag@Pd) nanosheets in order to increase SPR and photothermal efficiency which resulted in cell death under NIR stimulation at a much lower concentration and (20 μg/mL) and 5 min of 1.4W/cm^2 808nm light.[258]

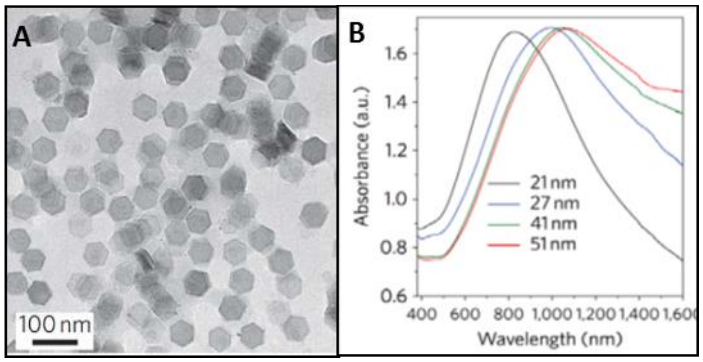

Figure 17. (A) TEM image of Pd nanosheets and **(B)** their corresponding optical absorption spectrum, depending upon their edge length. Reproduced from [257].

Photothermal studies using FePt nanoparticles were undertaken by *Chen et al.*[261] Folic acid was attached to the surface of the FePt nanoparticles to increase uptake in EMT-6 breast cancer cells. Using real time capabilities, their group was able to observe the localized photothermal ablation effects within the cancer cells by visualizing plasma membrane integrity in response to hyperthermia. During laser application, a series of confocal images were taken every 60 seconds to show photothermolysis. They determined that cell death can occur at low energy

fluence (70 mJ/cm^2) if there are enough FePt nanoparticles within the cell to trigger a considerable intracellular explosion and disrupt plasma membrane integrity.

Nanomaterials, based on other inorganic metals such as titanium, have been used for PTT, and have been discussed in a recent review article.[262-264] *Lee at al.* demonstrated that titanium dioxide nanotubes (TiO2 NTs) can be used as photothermal therapeutics *in vitro*.[262] The photothermal effects were studied with CT-26 colorectal cancer cells. Cells incubated with TiO2 NTs (25 μg/mL) and exposed to 808 nm NIR light (0.3 W/cm^2, 20 min) showed greater than 95% cell kill. *Lee et al.* confirmed their *in vitro* results by utilizing TiO2 NTs for photothermal ablation *in vivo*.[263] CT-26 colorectal cancer cells were used to establish tumors in Balb/C mice and were then subjected to two different concentrations of TiO_2 NTs (27.5 or 52.5 mg/mL, 100 μL). Two different laser parameters were used (0.3 W/cm^2 and 0.4 W/cm^2, 20 min). The mice showed insufficient tumor destruction at these parameters; however, when the laser time was increased to 60 minutes, complete tumor destruction was apparent.

Quantum Dots

Quantum dots (QDs) have garnered increasing interest from scientists owing to their small size, excellent photostability, high brightness and narrow absorption and emission bands, which can be tuned based on core size and composition.[265-267] Quantum yields of these semiconductors can also be increased through coating the inner core of the quantum dot with an outer shell made up of a higher band gap material.[265-268] QDs are generally made up of a metal, such as copper, cadmium or zinc and a chalcogen atom, such as sulfur, selenium or tellurium. Smaller sized QDs (2 nm) generally absorb in the UV/Visible region, while larger dots (10 nm) absorb in the NIR. Generally, QDs that absorb in the UV/visible region are used in PDT because they can produce reactive oxygen species (ROS); however, by protecting the core with a material such as zinc sulfide (ZnS), one can prevent ROS production.[269, 270] Recently, QDs have been used for PTT applications. QDs also have the ability to generate free charge carriers, so the mechanism for heat generation is due to the SPR, similar to gold and silver

nanomaterials.[271] *Chu et al.* synthesized silica-coated cadmium telluride (Si@CdTe) QDs for photothermal therapeutic application.[272] The average diameter for the Si@CdTe QDs was 10 nm. Irradiation of 400 μg/ml CdTe QDs, with 671 nm light for 20 min (1.97 W/cm^2) generated a 30 degree chenage in temperature. Mice bearing melanoma tumors were treated with Si@CdTe nanoparticles and NIR radiation for 20 minutes each day over the course of five days. Eighteen days after treatment, all tumors were eradicated with no recurrence found 24 days post treatment.

Recently, copper chalcogenide (CuS or CuSe) based nanomaterials have been pursued as a more biocompatible and cost effective alternative to cadmium-based QDs for cancer cell imaging and PTT.[273, 274] Copper selenide nanocrystals ($Cu_{2-x}Se$) can be synthesized and capped with amphiphilic polymers to increase aqueous stability and biocompatibility.[275-277] *Hessel et al.* synthesized $Cu_{2-x}Se$ nanocrystals that had an average diameter of 16 nm, which allowed them to be removed from the body through the renal system, like larger nanoparticles.[275] The $Cu_{2-x}Se$ nanocrystals showed no cytotoxicity when incubated with HCT-116 colorectal cancer cells for 6 hours. The $Cu_{2-x}Se$ nanocrystals (39 μg/mL) were incubated with HCT-116 colorectal cancer cells and subject to NIR stimulation (30 W/cm^2, 5 min), and bright field images of cells stained with trypan blue confirmed 100% cell death.

Other copper chalcogenide-based nanomaterials that are showing promise as new, low toxicity photothermal therapeutics are copper sulfide (CuS) nanocrystals. These materials are similar to $Cu_{2-x}Se$ nanocrystals, however, they have lower photothermal conversion efficiencies.[273, 278] This is due to the small size (~3 nm) of the CuS nanoparticles. To circumvent this, CuS nanoflowers with sizes around 1 μm were synthesized.[279] Under 980 nm illumination, the CuS nanoflowers showed almost complete cell kill (<95%) at a low power density (0.5 W/cm^2) when incubated with HeLa cells. However, due to the very large size of the CuS nanoflowers, the biological application of these nanomaterials may be limited. Recently, *Tian et al.* developed a Cu_9S_5 nanocrystal with an average size of 70 nm.[279] In order to increase the hydrophilicity of the Cu_9S_5 nanocrystals, the oleylamine capping groups were exchanged with

6-amino caproic acid (ACA). The photothermal conversion efficiency of these newly synthesized Cu_9S_5 nanocrystals was determined to be 25.7%, which is on the order of gold nanorods (23.7%) and $Cu_{2-x}Se$ nanocrystals (22%).[171, 275] The cytotoxic response of the HeLa cancer cells to Cu_9S_5 nanocrystals was measured and showed greater than 80% viability after incubation for 24 hours. PC-3 prostate cancer cells were inoculated in the hind flanks of severe combined immunodeficient (SCID) mice. The Cu_9S_5 nanocrystals (100 µL, 40µg/ml) were intratumorally injected and the mice were treated with 980 nm NIR light (0.5W/cm^2, 10 min). and histological analysis of the tumors displayed shrinking of malignant cells, loss of contact, and nuclear damage were clearly visible in the histology images.

A1.4 Carbon Nanoparticles

Carbon was known to exist in two allotropes, graphite and diamond, prior to the discovery of the fullerene in 1985 by Smalley, Curl and Kroto.[280] Carbon is now found in three forms: graphite, diamond, and fullerene. Fullerenes have unique electrical, optical, and thermal characteristics based on the specific arrangement of the carbon atoms.[280-285] Fullerenes are now classified into two forms: the more spherically shaped molecules are called fullerenes or bucky balls and the more tubular shaped molecules called carbon nanotubes (CNTs). CNTs began being widely studied after S. Ijima's famous publication describing them in 1991.[286]

Nanotubes

Carbon nanotubes can have one, two, or many sidewalls and are referred to as single-walled, double-walled, or multi-walled nanotubes (SWNT, DWNT, or MWNT). SWNT are about 1 nm in diameter, and tens to hundreds of nanometers long, whereas MWNT are like nested SWNTs with increasing diameters up to about 20 – 30 nm and micron lengths. Nanotubes can be metallic or semiconducting, depending on their chirality, and therefore have improved electrical and thermal properties compared to bulk graphitic carbon.[282] Carbon nanotubes can be doped with alternative atoms distributed throughout the tube lattice; for example with nitrogen or

boron.[287, 288] Doped nanotubes have been shown to have reduced toxicological potential and therefore may be advantageous for medical use.[289]

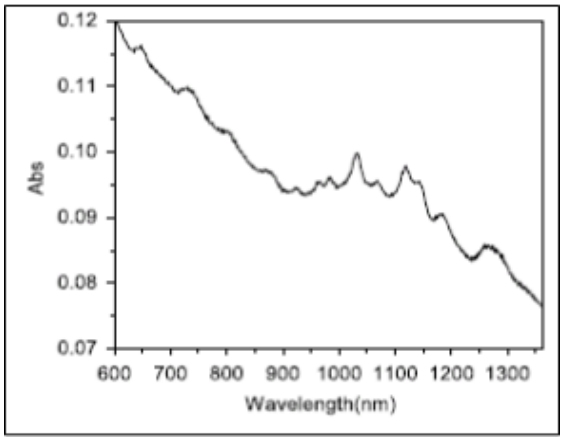

Figure 18. Absorption spectrum of SWNT in sodium cholate aqueous suspension. Reproduced from [290]

Carbon nanotubes strongly absorb electromagnetic radiation throughout the infrared due to transitions between the first and second van Hove singularities, as shown in the absorption spectra in Figure 18.[290-294] Nanotubes generate heat by absorbing incident light which induces phonon resonances along the tube length.[283, 295, 296] It has been theoretically predicted and experimentally shown that nanotubes behave as antenna in response to infrared light absorption.[297] The length of nanotubes can be chosen to match a specific incident frequency of light and will be most efficient when the nanotubes have lengths that are multiples of half the wavelength of the incident light.[298-300] The differences in heat generation of an aqueous suspension of MWNT or SWNT exposed to 3 W/cm^2 1064 nm light for 30 seconds is shown in Figure 19.[106] The authors hypothesize that MWNT are able to generate more heat than SWNT primarily due to length of the nanotubes as the mass concentrations were equal, but also possibly due to the interaction of the multiple sidewalls in MWNT.[106]

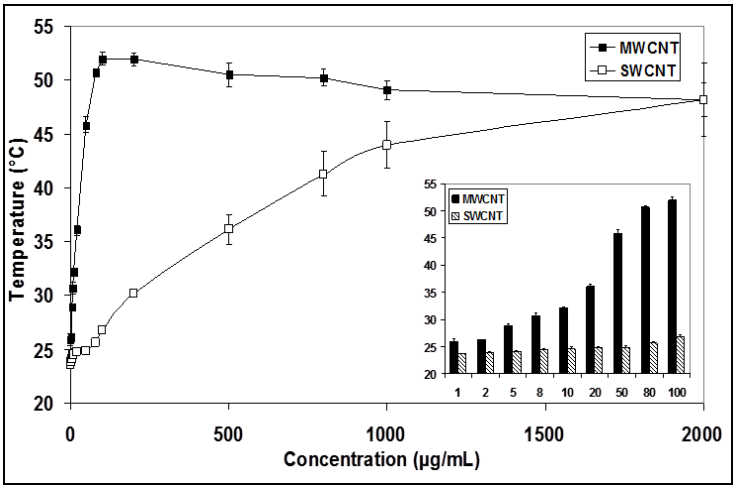

Figure 19. Well- dispersed MWNT generate a greater temperature than well-dispersed SWNT for all concentrations up to 2 mg/ml. Reproduced from [106].

Nanotube bundling can decrease infrared coupling efficiency and nanotube heating so good dispersion of the tubes is important, hence the need for adequate functionalization and solubility of the nanotubes. Nanotubes are commonly functionalized to make them water soluble although they can also be non-covalently wrapped to aid in solubilization.[301-304] Functionalization usually begins through oxidation of the nanotubes to form carboxylic and hydroxyl groups on the exterior of the nanotubes. Secondary chemical reactions attach functional molecules to the carboxyl groups. Many different types of functional molecules have been attached to nanotube, including targeting agents like folic acid and antibodies, as well as DNA, siRNA, and chemotherapeutic agents.[302, 305-315] Drug delivery using hyperthermia generated by nanotubes can occur when the functional molecules are released due to bond breakage between the molecule and nanotube sidewall.[307, 309, 310] 'Nanobombs,' tight bundles of carbon nanotubes that generate such localized and rapid energy under NIR that a microscopic explosion occurs, have been found to have even more powerful anti-tumor effects.[316]

Similar to metal nanoparticles, both SWNT and MWNT have been used for photothermal ablation. *Burke et al.* chose to use 100 µg of MWNT directly injected into xenograft kidney tumors in mice. [106] Only mice treated with MWNT and exposure to 3W/cm^2 of 1064nm light for 30 seconds had complete eradication of the tumors, and no tumor recurrence in 80% of the

mice (Figure 20). *Ghosh et al.* used 50 µg of DNA-wrapped MWNT injected directly into prostate xenograft tumors, and upon exposure to 1064 nm light there was a reduction in tumor volume similar to that in *Burke et al*.[317] Additionally, they showed that encasing MWNT with DNA can further enhance nanotube dispersion leading to better heating, and as a result, a lower concentration of MWNT was needed.

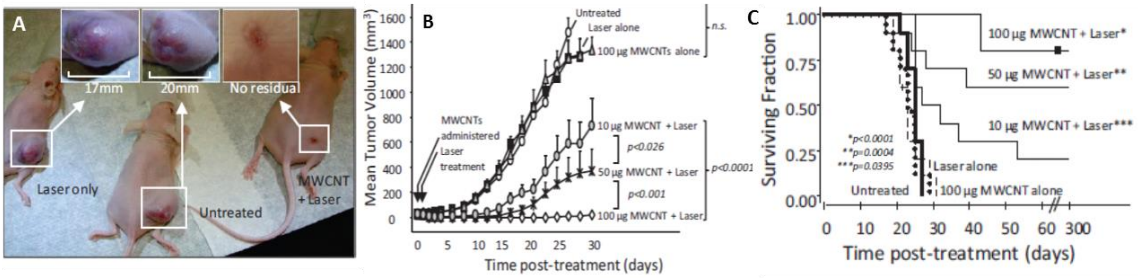

Figure 20. MWCNT-based photothermal therapy reduces subcutaneous kidney tumor volume in nu/nu mice treated with the combination of intratumorally injected MWCNT and laser. **(A)** Photographs at day 21 of representative mice from groups treated with laser only, untreated controls, or mice treated with 100µg of MWCNT plus laser. **(B)** Control groups (untreated, treated with MWCNTs alone, or treated with laser alone) were statistically identical. There was a dose-dependent attenuation in tumor growth after 30 sec of NIR laser treatment of MWCNT-loaded tumors. **(C)** Kaplan–Meier curves demonstrate a significant increase in survival time for mice treated with all doses of MWCNTs plus NIR, with 100µg of MWCNT plus laser offering the greatest benefit. Reproduced from [106].

A number of other researchers have used SWNT for photothermal ablation of cancer, and the focus of research has often been on enhancing the solubility of the SWNT and targeting them to tumors using cell-specific modalities.[306, 310, 318] SWNT have also been explored as dual-purpose agents for imaging as well as therapeutics by utilizing the inherent photoluminescence of semi-conducting SWNT or by attaching fluorescent polymers or quantum dots to the nanotube sidewall. For example, *Robinson et al.*, intravenously injected 0.35 mg/mL of SWNT functionalized with 50% 1,2-distearoyl-phosphatidylethanolamine-methyl-polyethyleneglycol (DSPE-mPEG) and 50% C_{18}-(poly(maleic anhydride-alt-1-octadecene)-poly(ethylene glycol).[319] As shown in Figure 21a SWNT were in the blood for up to 48 hours at which time they were found in high quantities in the liver, spleen, small intestine and tumor, Figure 21b.[320] The signature photoluminescence of SWNT accumulated in the tumor was easily detectable as

shown in Figure 21d.[320] Subsequent PTT using 0.6 W/cm^2 of 808 nm light for 5 minutes resulted in complete tumor regression and survival of all animals treated SWNT, as shown in Figure 21e and f.[320] The above examples demonstrate the potential for both SWNT and MWNT to act as strong infrared absorbers capable of generating significant hyperthermia for eradication of tumor tissue. In addition, SWNT have also been used as photothermal agents to eradicate bacteria.[321]

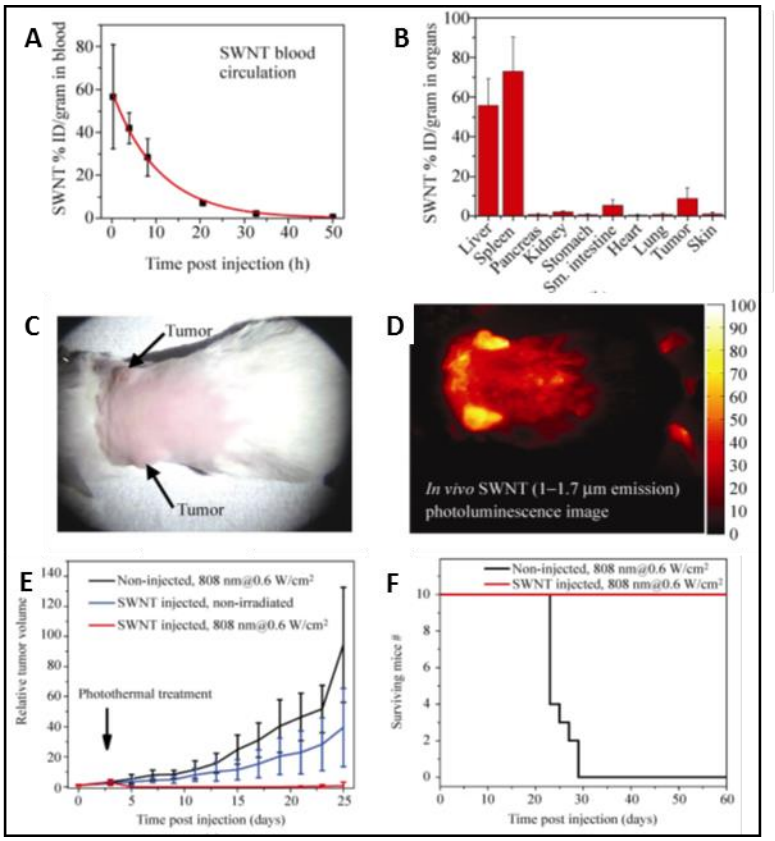

Figure 21. (A) SWNT blood circulation data obtained by Raman spectroscopy. After 48 h, the SWNT signal had dropped below the detection limit. Error bars are based on three mice per group. **(B)** Biodistribution of SWNTs in various organs of three mice 48 h after injection, as determined from Rama spectroscopy. **(C)** Optical image of a BALB/c mouse with two 4T1 tumors (indicated by arrows). **(D)** An NIR photoluminescence image taken 48 h post-injection. High tumor contrast is seen as the SWNTs are cleared from blood circulation, leaving SWNTs passively taken up in the tumors through the enhanced EPR effect. **(E)** Plot of relative tumor volume vs. time for control group not injected with SWNTs but laser irradiated at 808 nm with 0.6 W/cm2 power for 5 min, control group that were injected with SWNTs but received no NIR laser irradiation, and treatment group injected with 3.6 mg/kg of SWNTs and laser irradiated at 808 nm with 0.6 W/cm2 power three days after injection. **(F)** Survival curve of control vs. treated (SWNT injection and NIR irradiation) mice. Reproduced from [320].

Mild hyperthermia, defined as temperatures between 39- 42˚C, is often used to enhance delivery of chemotherapy agents in tumor tissue. It has been hypothesized that nanoparticles can localize mild hyperthermia to more specifically target drug delivery to tumor cells. As shown by *Levi-Polyachenko et. al.,* in Figure 22, MWNT can be used to generate a rapid temperature increase to 42˚C and can enhance cellular uptake of oxaliplatin by colorectal cancer cells leading to a reduction in cell population comparable two hour hyperthermia treatment at 42˚C.[322] Laser stimulation without MWNT had similar results to control cells treated at 37˚C.

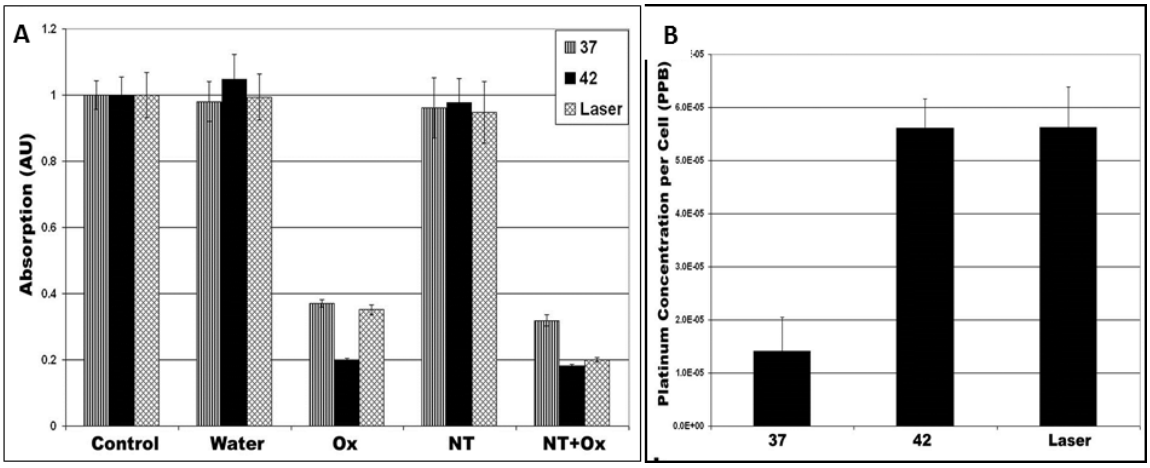

Figure 22. (A) RKO colorectal cancer cell lines cell viability in response to nanotubes (NT), NIR and oxaliplatin (Ox). **(B)** The amount of platinum per RKO cell treated at 37, 42, or 42°C rapidly by NIR laser stimulation of nanotubes. Reproduced from [322].

One potential problem with using carbon nanotubes as infrared photothermal agents is their unknown toxicity, which seems to be dependent upon the length of nanotube, surface charge and mechanism of exposure. Both dermal exposure and inhalation studies using high doses of nanotubes have shown that nanotubes can induce an inflammatory response and tissue damage.[53, 323, 324] *Cheng et al.,* have further shown, by high resolution TEM, that MWNT pierce the cytoplasm of mammalian cells and may also penetrate the nucleus, leading to a 20-25% decrease in cell viability.[325]

In an effort to understand how carbon nanotubes behave *in vivo*, researchers have discovered they can be enzymatically degraded. The first benchtop research showed that horseradish peroxidase can degrade SWNT.[326] *Kagan et al.* further pursued this line of

research by questioning whether immune cells could enzymatically degrade carbon nanotubes.[327] Their research definitively showed that in the presence of hydrogen peroxide, human myeloperoxidase, an enzyme released by macrophages and neutrophils, can cause degradation of SWNT. Furthermore, their finding showed that neutrophils incubated with SWNT could completely degrade the nanotubes, and the degradation by-products do not elicit an immune response when provided to mice via inhalation or pharyngeal aspiration. In a novel *in vitro* assay, *Russier et al*. showed that oxidized SWNT and MWNT can be degraded upon exposure to phagolysosomal simulant fluid and hydrogen peroxide, but that MWNT are more resistant to degradation than SWNT.[328] They confirmed degradation using Raman spectroscopy, finding that the characteristic G and D bands of the SWNT were reduced over time compared to the MWNT samples.

Graphene Oxide

Graphene is a relatively new carbon nanomaterial being explored for PTT. Graphene is a planar sheet that is one carbon atom thick, and it has been evaluated in reduced or oxidized forms for medical applications. One manner of synthesis is simply the unzipping of carbon nanotubes to form the planar sheet, while another synthesis method uses graphite oxide as the starting reagent. Both the optical absorbance of graphene and its ability to generate increased temperatures in aqueous media are similar to carbon nanotubes. A number of research groups have demonstrated that graphene oxide can be used *in vivo* for targeting and eradication of tumors and the results correlate well with PTT using carbon nanotubes. For example, *Yang et al.* demonstrated a complete reduction of 4T1 murine breast tumors and 100% survival of mice treated with 20 mg/kg of PEGylated conjugated nanographene sheets after exposure to 2 W/cm^2 of 808 nm light.[329] The authors demonstrated very high tumor uptake (higher than any organ, including the liver and spleen) of the graphene oxide nanosheets 24 hours after injection, and thus hypothesize that the two- dimensional nature of the graphene nanosheets is superior to the one-dimensional nature of SWNT for accumulated in the tumor by the EPR effect. Other authors

have demonstrated the potential of graphene oxide to target the leaky tumor vasculature, thereby allowing for photothermal ablation of a tumor's blood supply, as an alternative method to eradicate cancer.[330]

A1.5 Polymer Nanoparticles

Photothermal Therapy using Small Organic Molecules

Organic chromophores have been primarily utilized for PDT more than for PTT. This is due to the ability of the chromophore to generate reactive oxygen species (ROS), which can be used to destroy cancer cells. However, if the organic chromophores can be fabricated into a nanostructure, where the packing density of the chromophores is very high, the material will lose its ability to generate ROS.[331, 332] This high packing density allows the absorbed energy to dissipate as heat and for the chromophore to be used for PTT. Few NIR absorbing organic chromophores have been utilized for PTT applications because most chromophores absorb in the visible region. Among those that can absorb in the NIR, indocyanine green (IcG) is an FDA approved imaging agent; however, not many groups have studied IcG for PTT.[26-28, 333-338] IcG has limited potential *in vivo* due to poor specificity, lack of solubility, fast degradation in aqueous media, short half life and aggregative properties.[334, 339-342] IcG binds to plasma proteins, such as lipoproteins, in the blood very efficiently (98%) and as such, is quickly cleared by the liver.[339, 343] In order to circumvent this, colloidal carriers such as poly(lactic-*co*-glycolic acid) (PLGA), dextran, and nanoparticle assembled capsules have been used to stabilize and increase the circulation time of IcG.[344-347] Y*u et al.* assembled a nanoparticle capsule filled with IcG and coated it with anti-EGFR in order to target and induce photothermal ablation of 1483 squamous cell carcinoma cells *in vitro*.[348] The IcG nanocapsules showed efficient cell kill (>95%) under 808 nm light. *Zheng et al.* also actively targeted IcG to tumor cells by incorporating it in a phospholipid-PEG (PL-PEG) polymer matrix attached to a monoclonal antibody.[349] The organic heterostructure had an average diameter of 17.6 nm. They showed that the IcG-PL-PEG-mAb conjugate could photothermally ablate 75% of U87-MG human

glioblastoma cells *in vitro* under NIR stimulation for 5 minutes at 2.25 W/cm^2. They attribute this to the nanoconjugates ability to achieve endocytosis through the integrin receptor on the surface of the U87-MG cells. When the nanoconjugate was incubated with MCF-7 breast cancer cells, which have fewer integrin receptors, the cells showed less cell death compared to the U87-MG cells. Further *in vivo* studies determined that ICG-PL-PEG-mAb systemically administered into the tail vein of nude mice demonstrated more efficient photothermal ablation of U87-MG hind flank tumors after treatment with 808 nm NIR light (2 W/cm^2, 10 min) compared to intravenous injection of IcG alone.[337] With FDA approval and scientists determining new ways to stabilize it for intravenous delivery, IcG has found more widespread use in PTT. However, IcG still suffers from poor solubility, insufficient heating and relatively low photostability.[336, 340, 344, 345]

With a similar structure to IcG, IR-780 iodide has also been used as a NIR imaging probe.[350, 351] *Peng et al.* synthesized a multifunctional micelle containing a ^{188}Re labeled radionucleotide for imaging and IR-780 iodide for PTT.[352] Their group showed that these ^{188}Re-labeled IR-780 loaded micelles can photothermally ablate HCT-116 colorectal cancer cells *in vitro* and *in vivo*. Biodistribution studies using micro-SPECT/CT imaging capabilities showed micelle accumulation in many organs including the liver, spleen and kindey. After 96 hours, micelle accumulation decreased in all organs except the spleen. Photothermal ablation studies demonstrated that ^{188}Re-labeled IR-780 (1.25 mg/kg) injected into HCT116 colorectal tumor xenografts and treated with NIR light (1.8 W/cm^2, 5 min) resulted in 82.6% inhibition of tumor growth 27 days after treatment.[352]

Phthalocyanines are another class of organic-based nanoparticles that have been used for PTT due to their increased photostability over IcG. Phthalocyanines are macrocyclic dyes that have pyrrole containing subunits similar to porphyrin molecules. *Lim et al.* devised a nanoconjugate containing tetra-t-butylphthalocyanine wrapped in a Pluronic F68 surfactant shell and coated with chitosan and heparin for tumor targeting ability.[331] Their group showed that the heparin conjugated phthalocyanine nanoconjugates had sizes around 75 nm and could absorb

efficiently around 700 nm. They determined that SCC7 squamous cell carcinoma cells could be photothermally ablated (~60% cell death) under 671 nm light (6.4 W, 20 min). The lower photothermal efficiency is a major limiting factor for the use of phthalocyanine nanoconjugates. *Gutwein et al.* synthesized a mesoporous silica nanostructure that incorporated two NIR dyes (IR-780 and 2,3-napthalocyanine) within its pores for PTT.[353] Their group used a 4T1 tumor xenograft mouse model and after injection of the multi dye nanoparticles (15 mg/mL, 20 μL) and NIR exposure of the tumor (0.625 W/cm^2, 5 min), the nanoparticles were followed *in vivo* using fluorescence imaging (710 nm excitation/820 nm emission). They found that the nanoparticles remained in the tumor for days follow PTT. This finding would allow researchers to use multiple treatments of NIR for PTT without injecting more nanomaterial.

Similar to Phthalocyanines, porphyrin-lipid nanovesicles (or porphysomes) have been recently used for PTT. A porphysome is a porphyrin containing lipid molecule that can self assemble into a liposomal nano-archtiecture, with pores sizes on the order of 100 nm. This liposomal structure allows for the nanoparticle to have both biocompatibility and biodegradability.[354] Porphysomes have been shown to have increased molar absorptivity compared to other organic dyes used for PTT, with longer half life and greater degradation capability.[354, 355] *Jin et al.* determined the activation mechanism of PDT vs. PTT using a porphyrin-lipid nanovesicle in a hypoxic tumor model, and investigated the advantages to using PTT over PDT.[332] Their group demonstrated complete photothermal ablation (0.75W, 85 s) of KB cervical cancer xenograft tumors without recurrence after 50 days.

Researchers have also developed organic nanomaterials based on naturally occurring substances in an effort to avoid potential long term side effects and increase metabolic degradation. There are few materials known to naturally occur in the body and have absorbance in the NIR region, such as melanin. Melanin is a pigment that occurs naturally and is responsible for protecting an organism from harmful UV radiation. *Liu et al.* developed colloidal polymer nanospheres based on a dopamine/melanin structure.[356] The dopamine/melanin colloidal

nanospheres were very stable in aqueous solution, showed good biocompatibility and excellent photothermal efficiency (40%). The photothermal ablation efficiency of the nanospheres was first measured *in vitro*. The nanospheres (0.1 mg/mL) were incubated with 4T1 cells and exposed to an 808 nm laser (2 W/cm^2, 5 min) resulting in 30% cell viability. The *in vivo* photothermal efficiency (2 W/cm^2, 5 min) was measured in Balb/c mice containing 4T1 xenograft tumors and the nanospheres (200 μg/mL, 100 μL). They showed complete tumor eradication without recurrence for 10 days post treatment.

4.2 Photothermal Therapy using Conjugated Polymer Nanoparticles

Polymer nanoparticle composites are nanomaterials that combine metal or carbon nanoparticles with polymers coated on their surface.[357-360] These composites have been utilized for photothermal ablation of many different cancers; however, the polymer does not generate the heat. The polymer coating is often utilized for a variety of reasons such as facilitating controlled drug delivery, increased biodistribution and ease of functionalization of antibodies and other small molecular for targeted delivery. For the sake of this review, the authors will only discuss polymeric nanomaterials, where the polymer backbone is responsible for the heat generation under NIR stimulation.

Conjugated polymers are a class of polymers exhibiting electrical conduction due to alternating single and double bonds along the polymer backbone, where electrons are delocalized. Photothermal ablation using conjugated polymers is a relatively new field of study. The first report of a conjugated polymer used for photothermal ablation of cancer cells was polyaniline in 2011.[62] *Yang et al.* coated polyaniline (emeraldine base) with a PEGylated fatty acid to enhance the nanoparticles solubility in aqueous media.[62] Emeraldine base absorbs in the visible region, however, upon addition of the nanoparticles to an oxidative/acidic environment, they became doped (emeraldine salt) and their optical absorbance red-shifts into the NIR. The photothermal efficiency of the emeraldine salt nanoparticles was evaluated under NIR stimulation with epithelial A431 squamous cell carcinoma cells using an 808 nm laser (2.45 W/cm^2, 5 min)

and demonstrated photothermal ablation both *in vitro* and *in vivo*. Xenograft flank tumors on nude treated with emeraldine salt and NIR light were histologically evaluated and showed an increase in cellular and blood vessel damage compared to the control.

Polypyrrole (PPy) has also been utilized as an efficient photothermal therapeutic nanomaterial against HeLa cells *in vitro*.[63] To determine potential cytotoxic effect, the authors incubated the PPy nanoparticles (average diameter = 46 nm) with human umbilical vein endothelial cells (HUVEC) at a variety of concentrations, and demonstrated that the particles have low toxicity. HeLa cells were incubated with 2 mg/kg of PPy nanoparticles and after exposure to NIR light (808 nm, 6W/cm^2, 0.2 mg/mL), cell death was determined to be 60%-85% for 5 or 10 minutes of exposure. Two more exhaustive studies have recently been published using polypyrrole nanoparticles in a 4T1 tumor xenograft mouse model.[64, 65] *Chen et al.* showed that after injecting PPy nanoparticles (10 mg/kg, 100 μL) into the tumors and exposing them to 808 nm NIR light (1 W/cm^2, 5 min), the internal temperature of the tumors was able to reach 60^{o}C.[65] Complete eradication of the tumor was observed on day 2 post treatment. In all mice groups that were treated with PPy nanoparticles and NIR radiation, there was no sign of tumor recurrence for up to 60 days. *Yang et al.* used the same 4T1 breast cancer tumor xenograft model and upon exposure of the PPy nanoparticles (2 mg/kg) and 808 nm NIR light (0.5 W/cm^2, 5 min), tumor destruction was seen in all mice without recurrence for two weeks.[64] Their group also wanted to determine the extent of toxicity *in vivo*. After NIR treatment, both liver and kidney function markers were determined to be normal, and histological evaluation of the organs showed no obvious signs of damage compared to the control in the liver, spleen, kidney, heart and lung. A complete blood panel was carried out and all parameters were found to be normal with the exception of a higher white blood cell count. It was hypothesized that this could have been an immune response to the increase in dead cancer cells in the mouse after treatment giving rise to inflammation.

Poly(ethylenedioxythiophene):poly(4-styrenesulfonate) (PEDOT:PSS) nanoparticles are another polymeric nanoparticle utilized for photothermal ablation of cancer cells.[108] *Cheng et al.* synthesized PEG-coated PEDOT:PSS (PEDOT:PSS-PEG) nanoparticles that had diameters of 80 nm, that strongly absorb in the NIR, as shown in Figure 23a. Cytotoxicity studies revealed that the PEDOT:PSS-PEG showed no toxicity up to 0.2 mg/mL for both 4T1 murine breast cancer cells and 293T human embryonic kidney cells. The PEDOT:PSS-PEG nanoparticles (0.1 mg/mL) generated significant heat ($\Delta T = \sim 35^{o}C$) under NIR stimulation (1 W/cm^2, 5 min). The nanoparticles also exhibited a long blood circulation half life (21 hr.) and a high tumor uptake (28%) when administered systemically. Photothermal therapy was carried out in mice bearing 4T1 tumors. Forty-eight hours after intravenous injection of PEDOT:PSS-PEG nanoparticles (1 mg/mL, 200 μL), the mice were treated with NIR light (0.5 W/cm^2, 5 min). Tumors that contained PEDOT:PSS-PEG nanoparticles were completely eradicated one day post treatment. The PEDOT:PSS-PEG treated mice survived greater than 45 days compared to the control mice, which showed average life spans of 16-18 days, as shown in Figure 23b-d.

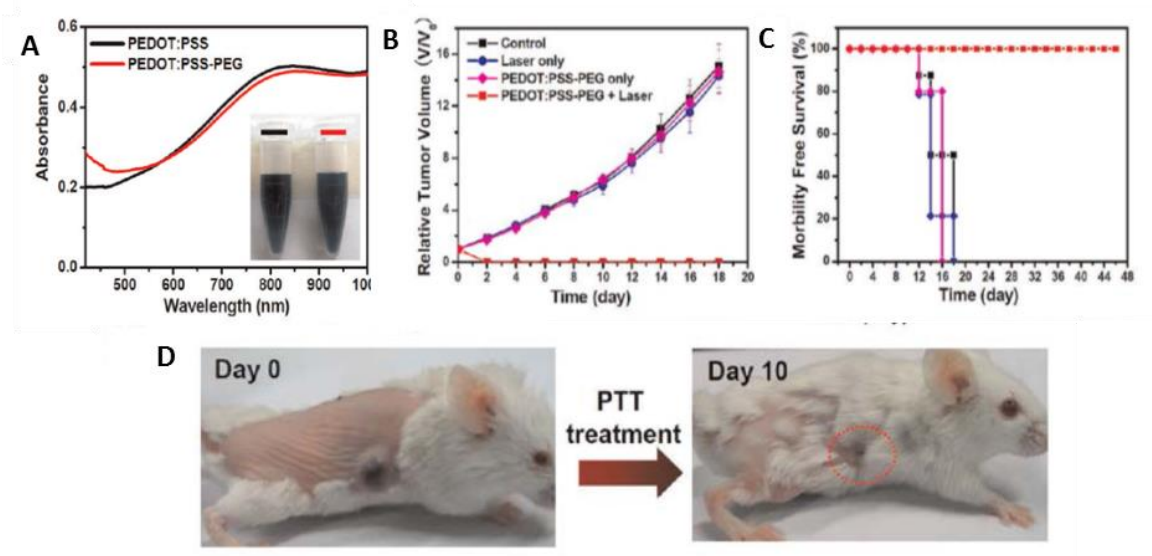

Figure 23. (A) UV_vis_NIR spectra of PEDOT:PSS and PEDOT:PSS-PEG solutions at a concentration of 0.02 mg/mL. Inset: Photo of PEDOT:PSS (left) and PEDOT:PSSPEG solutions at a concentration of 0.1mg/mL in water. **(B)** Growth of 4T1 tumors in different groups of mice demonstrate the effectiveness of PEDOT:PSS-PEG nanoparticles for photothrermal therapy leading to tumor eradication. For the treatment group, mice were injected with PEDOT:PSS-PEG 48 hr prior to 808 nm laser (0.5 W/cm2, 5 min). The other three groups of mice were used as controls: untreated; laser only without PEDOT:PSS-PEG injection; or injected with PEDOT:PSS-PEG but without laser irradiation. **(C)** Survival curves of mice after various treatments as indicated in B. PEDOT:PSS-PEG-injected mice after PTT treatment showed 100% survival ratio over 45 days. **(D)** Representative photos of a PEDOT:PSS-PEG-injected mouse at day 0 before PTT treatment and at day 10 after treatment. The tumor color turned obviously darker after PEDOT:PSS-PEG injection. Complete tumor elimination was achieved after PTT treatment. Reproduced from [108].

One drawback to using polymer nanoparticles for PTT is their relatively broad absorbance in the NIR. Recently, our group has explored using low band gap donor-acceptor (D-A) electrically conducting polymers (ECPs) for PTT.[133] Low band gap D-A ECPs are copolymers that incorporate both an electron donating monomer and an electron accepting monomer into their backbone. The extent of electron donation and electron accepting ability of the individual monomers has an overall effect on the absorption properties of the polymer. Through judicious choice of co-monomers used, D-A ECPs can be tuned to have excellent absorption properties in the NIR window.[71] For example, we have also synthesized two new donor-acceptor (D-A) electrically conductive polymers that are similar to PEDOT: a

cyclopentadithiophene donor monomer co-polymerized with either a 2,1,3-benzothiadiazole acceptor monomer (PCPDTBT) or a 2,1,3-benzoselenadiazole acceptor monomer (PCPDTBSe). These monomers were chosen because both of corresponding D-A ECPs absorb around 800 nm (band gap = 1.46 and 1.37 eV). Heat generation in D-A ECPs is not yet fully understood, however, it occurs through a slightly different process than carbon- and gold-based nanoparticles. It is hypothesized that, upon photoexcitation, a bipolaron is formed within the polymer.[361] The bipolaron can then decay to a phonon band through lattice coupling with subsequent internal conversion generating heat.[362] We have recently shown that we can fabricate D-A ECPs into D-A electrically conducting polymer nanoparticles (ECPNs) through a simple sonication method.[133] The average size of the nanoparticles is either 154 nm or 298 nm depending on the polymer. The D-A ECPNs have excellent absorbance properties in the NIR and can generate significant heating upon stimulation from NIR light, and may be used repeatedly for hyperthermia, as shown in Figure 24a-d. The D-A ECPNs are not cytotoxic and can photothermally ablate colorectal cancer cells under NIR stimulation *in vitro*, as shown in Figure 24e-f. For concentrations above 100 µg/mL (125 and 250 µg/mL), of the D-A ECPNs, cell survival for HCT116 and RKO colorectal cancer cells was less than 20% at a low laser fluence (0.75 W/cm^2). Due to the high photothermal efficiency of the D-A ECPNs, we predict that they will be useful for medical applications where hyperthermia is desired.

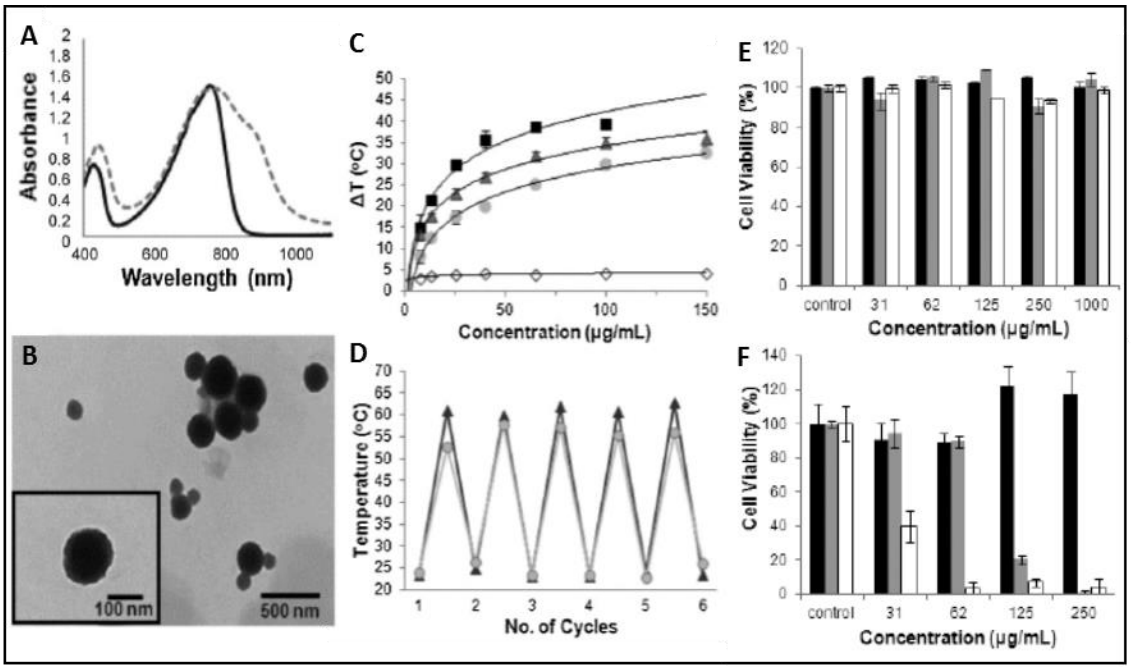

Figure 24. (A) The UV-visible spectrum of PCPDTBSe in toluene (black) and nano-PCPDTBSe in water (dashed). **(B)** TEM images of aqueous nano-PCPDTBSe. **(C)** Change in temperature vs. concentration for MWNTCOOH (squares), nano-P3HT (diamonds), nano-PCPDTBSe (circles) and nano-PCPDTBT (triangles) in cell culture medium (200mL) under 808nm (600mW) laser irradiation for 5 min. **(D)** A heating and cooling curve of 100μg /mL nano-PCPDTBT (triangles) and nano-PCPDTBSe (circles) in cell culture medium (1 cycle is 5 min of laser irradiation followed by 30 min with no laser irradiation). **(E)** Cell viability (as measured by MTS assay) of HCT116 cells with nano-P3HT (black), nano-PCPDTBSe (grey) and nano-PCPDTBT (white) in cell culture medium. **(F)** Cell viability studies of HCT116 colorectal cancer cells with nano-P3HT (black), nano-PCPDTBSe (grey) and nano-PCPDTBT (white) in cell culture medium after treatment with an 808nm (600mW, 5 min) NIR laser. Error bars are shown as standard deviation of the mean. Reproduced from [133].

A1.6 Conclusion

In summary, this report highlights the recent advances in nanoparticles being developed for photothermal therapies via stimulation with NIR. While gold nanoparticles remain at the forefront of research, the advent of other metals such as silver and palladium as PTT agents is eminent. In a similar pursuit, the next generation of carbon nanoparticles, graphene, is being explored as a potential alternative to carbon nanotubes, for photothermal therapies. Polymers represent another class of materials that have been developed to compete in the PTT nanoparticle arena. This field is quite young, but has great potential once the toxicity and tenability

parameters are better characterized. Overall, within the past five years, substantial advances have been made for developing new nanoparticles for PTT that branch away from the classic gold nanoparticles that were developed over a decade ago. Exciting advances are sure to follow, with greater applicability for PTT in fields outside of cancer therapy.

Acknowledgements
I wrote metal the nanoparticle section, Chris MacNeill wrote the polymer nanoparticle section, and Nicole Levi-Polyachenko wrote the carbon nanoparticle section.

CHAPTER A2

Quantifying Folic Acid-Functionalized Multi-Walled Carbon Nanotubes Bound to Colorectal Cancer Cells for Improved Photothermal Ablation

A2.1 Abstract

Peritoneal metastases of colorectal cancer are a significant challenge in the field of medicine today due to poor results of systemic chemotherapy caused by the blood-peritoneal barrier. Multi-walled carbon nanotubes (MWNTs) are a biocompatible material that strongly absorbs near infrared light to locally heat the surrounding area. Colorectal cancer is known to over-express folate receptor; therefore folic acid (FA) was covalently attached to MWNTs to target colorectal cancer cells. Real time polymerase chain reaction found differing expression of folate receptor α in two colorectal cancer cell lines, RKO and HCT116, as well as a healthy epithelial cell line, HEPM. A spectrophotometric method was developed to quantify the mass of MWNTs bound to cells and it was determined that FA targeted MWNTs resulted in a 400-500% greater affinity for colorectal cancer cells than untargeted MWNTs. The non-cancerous cell line, HEPM had higher non-specific MWNT interaction and similar MWNT-FA affinity. Stimulated by 1064 nm light, FA functionalized MWNTs caused a 50 - 60% decrease in colorectal cancer cell viability compared to a 4 - 10% decrease caused by untargeted MWNTs. Our results indicates that FA targeted MWNTs may increase the therapeutic index of MWNT ablation.

This is an electronic version of an article published in Journal of Nanoparticle Research, Vol. 15, No.5, (2013), 1649 DOI: 10.1007/s11051-013-1649-7 © copyright Springer *http://www.springer.com/materials/nanotechnology/journal/11051*.

A2.2 Introduction

Colorectal cancer is the third leading cause of cancer deaths in the United States with an estimated 50,000 deaths in 2011 alone [363]. Unfortunately, 60% of colorectal cancer cases are diagnosed at a late stage, so many cases are diagnosed after the disease has already metastasized. Peritoneal micrometastases (pervasive tumor nodules in the abdomen less than 2 cm in diameter) represent a significant burden to surgical oncologists, as they are often too numerous for complete surgical resection. In this work, we have explored the response of photothermal therapy using carbon nanotubes on two colorectal cancer cell lines, as well as a benign cell line, to serve as a control for how non-tumor cells might respond to folic acid targeted nanotube- induced photothermal therapy.

Multi-walled carbon nanotubes (MWNTs) are a unique biocompatible material with interesting electronic and mechanical properties due to their high aspect ratios. MWNTs have been used as drug transporters [364, 365], imaging agents [314, 366], and cancer therapeutics [45, 302, 367]. Photothermal therapy (PTT) [105, 322, 368] takes advantage of MWNT's ability to absorb near infrared (NIR) light between 700-1100 nm, where body tissue is most transparent. Absorption of NIR light causes lattice vibrations leading to heating of the surrounding environment [284]. PTT utilizing unfunctionalized carbon nanotubes has been shown to reduce tumor size *in-vivo* [45]; however, this method is not cancer cell-specific. New methods have been developed to actively and more selectively target MWNTs to tumor cells. This may be accomplished by attaching drug molecules [305, 369] or antibodies [370, 371] to the MWNT that selectively bind to receptors on the cancer cell surface. Once MWNTs are targeted to the surface of a specific cell, then PTT can be used to selectively thermally damage the cell, leading to apoptosis or necrosis.

The folate receptor α (FRα) is known to be up-regulated on epithelial tumors, such as colorectal, uterine, kidney, and ovarian, compared to normal epithelium [372], and as such, folic acid is an ideal ligand to target MWNTs to colorectal cancer cells. Other groups have employed

folic acid (FA) coupled to MWNTs for selective cancer cell targeting; in most cases utilizing a phospholipid polyethylene glycol (PEG) linker to attach the FA to the MWNT [302, 373]. In this work, we have covalently bound folic acid functionalized PEG to the MWNT. This technique circumvents the more common practice of simply adsorbing phospholipid PEG to the surface of the nanotube, and allows for a much shorter link between the folic acid and carbon nanotubes. It is well known that many cancer cell types over-express folic acid receptors on their cell surface. Unfortunately though, most publications stimulate the cancer cell lines to over-express folic acid receptors by serum-starving the cells prior to their interaction with folic acid functionalized nanotubes. We have chosen to evaluate the inherent over expression of colorectal cancer cell lines without serum-starving in order to better understand how more aggressive phenotypes bind MWNT-FA.

A significant advancement is the development of a spectrophotometric technique to quantify mass of MWNTs bound to cells. Previous literature has observed fluorescently labeled nanotubes within cells to confirm binding and internalization. [374] The results clearly demonstrated that nanotubes can be internalized by cancer cells, and upon exposure to infrared light the cells can be killed. However, information on how many nanotubes must be bound in order to achieve cell kill has not been able to be elucidated to date; therefore we developed a technique that quantifies either the amount of nanotubes internalized or bound to the cells. By determining the mass of MWNTs bound to cells, we are able to quantitatively examine the increase in binding affinity of MWNT-FA compared to untargeted MWNTs. Additionally, the same spectrophotometric technique used to quantify MWNT binding *in-vitro* could be adapted to study and quantify MWNT binding *in-vivo*.

A2.3 Materials and Methods

A2.3.1 Materials

MWNTs (>99% purity; outer diameter, 13-18 nm; length, 3-30 μM) were purchased from Cheap Tubes Inc. Concentrated nitric acid (70%), concentrated sulfuric acid (98%), Triethylamine, dichloromethane, di-*tert*-butyl dicarbonate, ethanol, isopropanol, and pyridine were purchased from Fisher Scientific. Dicyclohexylcarbodiimide, dimethylsulfoxide, 4,7,10-trioxa-1,13-tridecaneamine, folic acid, trifluoroacetic acid and *n*-hydroxysuccinimide were purchased from Aldrich Chemical Co. 1-bromo-3-chloropropane, TriReagent, and polyacryl carrier were purchased from Molecular Research Inc. CellTiter 96® AQueous One Solution Cell Proliferation Assay, RQ1 DNase 10x buffer, RQ1 RNase-free DNase, and RQ1 DNase Stop Reaction were purchased from Promega. TaqMan Universal PCR Master Mix, TaqMan Gene Expression Assays FOLR1 and GAPDH, MuLV Reverse Transcriptase, and RNase Inhibitor were purchased from Applied Biosystems. All reagents were used as received without further purification. Infrared spectra were recorded either on a Mattson Genesis II FT-IR spectrometer or on a Perkin–Elmer Spectrum 10 spectrometer with an attenuated total reflectance sampling accessory equipped with a diamond anvil. Raman spectra were recorded on a DeltaNu Advantage 532 Raman spectrometer at 532nm. Ultraviolet-visible spectroscopy (UV/Vis) was done on a Beckman Coulter DU®730 Life Science UV/Vis Spectrophotometer. Low resolution electrospray ionization mass spectrometry (ESI-MS) experiments were performed on an Agilent Technologies 1100 LC/MSD Trap Instrument. The ion trap mass spectrometer was operated in smart mode. Nebulization was achieved with N_2 pressure of 50 psi. Mass spectra were obtained in positive ion mode. 300 MHz ^{1}H- and ^{13}C-NMR spectra were recorded on Bruker Avance DPX-300 NMR spectrometer. DNase treatment was performed on a Perkin Elmer Gene Amp PCR System with a heating profile of 38°C for 30 minutes, 25°C for 1 minute, and 65°C for 10 minutes. PCR was performed using a Stratagene Mx3000P. An Olympus IX70 inverted microscope with Image Pro Plus software was used for fluorescent microscopy.

A2.3.2 Synthesis of FA-PEG-NH_2

Synthesis of FA-PEG-NH_2 was performed as described in Sideratou *et al.* [375] and Dhar *et al.* [376]. Folic acid (FA, 299 mg) and dimethylsulfoxide (DMSO, 10 mL) were added to a 50 mL round bottom flask under nitrogen. N-hydroxysuccinimide (NHS, 81 mg) was dissolved in DMSO (2 mL) and added to the folic acid solution. Dicyclohexylcarbodiimide (DCC, 147 mg) was dissolved in DMSO (2 mL) and subsequently added to the solution. The solution was allowed to stir at room temperature in the dark for 24 hours. The white solid was vacuum filtered and washed with DMSO. The filtrate was added to a beaker containing 30% acetone in ethyl ether and under stirring yielded a precipitate. The solution was stirred for 30 minutes and vacuum filtered and washed first with acetone/ethyl ether and then with ethyl ether giving a yellow solid. Yield (340.9 mg, 93%).

FA-NHS (2) (340.9 mg) and pyridine (30 mL) were added to a 50 mL round bottom flask. The mixture was allowed to stir for 30 minutes and NH2-PEG-NHBOC (1) (307.6 mg) was added drop-wise over 10 minutes. The mixture was allowed to stir in the dark overnight under nitrogen. The pyridine was evaporated leaving a yellow sludge. Trifluoroacetic acid (TFA, 10mL) was added and the mixture was stirred for 2 hours at room temperature. After stirring, sodium bicarbonate in water was slowly added to neutralize the pH. The water was then evaporated and the remaining oil was added to a 1:1 CH3CN:ether solution yielding a yellow precipitate which was collected by filtration and washed with ether. Yield (1.78g).

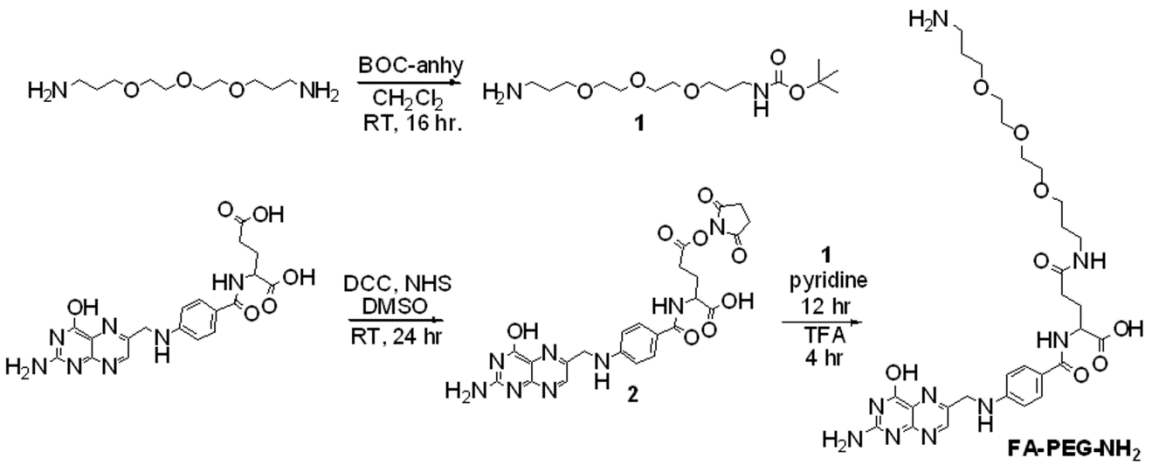

Figure 1. Schematic of synthesis of FA-PEG-NH2. Compound (1) is NH_2-PEG-NHBOC and compound (2) is FA-NHS.

A2.3.3 Synthesis of MWNT-FA

MWNTs were first oxidized by suspending 100 mg of pristine MWNTs in a 3:1 mixture of concentrated sulfuric acid to concentrated nitric acid (40 mL total) followed by heating this mixture to 80oC for 2 hours. The suspension was then filtered through a 0.2 µM filter and washed with copious amounts of water until the pH of the filtrate solution was neutral. The MWNTs were then washed with ethanol and allowed to dry at room temperature in air overnight to yield oxidized MWNTs (MWNT-COOH). This purification helped remove trace impurities and shortened the tubes for better dispersivity in solution. MWNT-COOH (1 mg/mL in DMSO, 12mL) was added to a 20 mL scintillation vial and horn sonicated for 5 minutes using a microtip horn sonicator (20% amplitude, pulsed 2 seconds ON/OFF) to ensure the MWNT-COOH were well suspended. 100 mg of dicyclohexylcarbodiimide (DCC) was then added to the solution and stirred at room temperature for 48 hours. The dicyclohexylurea precipitate was visible after incubation indicates covalent attachment of the DCC to the MWNT-COOH. The mixture was transferred to a 100 mL round bottom flask equipped with a reflux condenser and nitrogen inlet. FA-PEG-NH_2 (70 mg) was added along with triethylamine (500 µL) and the mixture was heated at 120°C for 72 hours. Water was added to the solution after cooling and the tubes were vacuum filtered through a 0.2µM filter paper. Carbon nanotubes were re-dispersed in water and filtered

again before being washed with ethanol. MWNT-FA were allowed to dry in air overnight. Yield (8.3 mg, 69%).

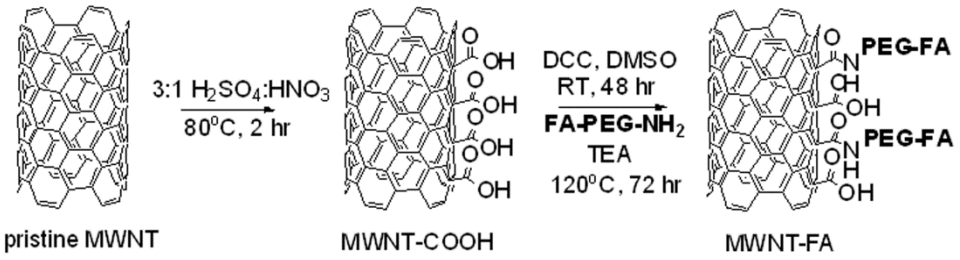

Figure 2. Schematic of folic acid functionalization of MWNTs incorporating a polyethylene glycol spacer *Abbreviations: H_2SO_4 – concentrated sulfuric acid, HNO_3 – concentrated nitric acid, DCC – dicyclohexylcarbodiimide, DMSO – dimethylsulfoxide, PEG – polyethylene glycol, RT – room temperature, TEA – triethylamine.* The schematic shows the steps of the synthesis, starting with pristine MWNT that are oxidized in acids to yield carboxylated MWNT, and the reaction of the MWNT-COOH with folic acid conjugated PEG-amine to yield MWNT-FA.

A2.3.4 Sterilization of MWNT

Dry nanotube suspensions were sterilized by suspending MWNT-FA or MWNT-COOH (1 mg/mL) in ethanol. The MWNTs were then centrifuged to a pellet and the supernatant was removed in a sterile tissue culture hood where the MWNTs were re-suspended in sterile dH_2O at a concentration of 1 mg/mL. This solution was then diluted 1:10 in media to yield a final concentration of 0.1 mg/mL. The final concentration was confirmed using the absorption of the MWNT solution at 1064 nm and comparing it to a known absorption-concentration calibration curve.

A2.3.5 Cells and Reagents

RKO and HCT116 colorectal cancer cell lines were purchased from American Type Culture Collection (ATCC # CRL-2577 and CCL-247 respectively) and cultured in McCoy's 5A medium. HEPM human embryonic palatal mesenchyme cells were purchased from ATCC (ATCC # CRL-1486) and cultured in Hyclone DME/High Modified Medium. Both media were supplemented with 1% L-glutamine, 1% penicillin/streptomycin and 10% fetal bovine serum. Cell viability was quantified by 3-(4,5-dimethyl-2-yl)-5-(3-carboxymethoxyphenyl)-2-(4-sulfophenyl)-2H-tetrazolium (MTS) assay using 96Aqueous One Solution.

A2.3.6 Cytotoxicity Assay

500 µL of MWNT-FA and MWNT-COOH at varying concentrations [0.1, 0.01, and 0 mg/mL] in ethanol was added to a 48 well plate and left uncovered overnight in a tissue culture hood allowing the ethanol to evaporate off and leaving the MWNTs in the well. RKO and HCT116 cells were then plated at a density of 5000 cells/ well, and HEPM cells were plated at a density of 10,000 cells per well and allowed to grow for 48 hours. Cells were in the exponential phase when used to evaluate cytotoxic response. The doubling time for each cell line is: RKO, approximately 12 hours; HCT116, 10 hours; and HEPM, 24 hours. Plating cell density differed because of the differences in cell doubling time, so that the maximum confluency would be approximately 80% of the well surface area after the 48 hour incubation period. Cell viability was quantified by MTS assay.

A2.3.7 Real Time PCR

Folate receptor expression was examined by real time PCR in HEPM, RKO, and HCT116 cell lines. RNA was isolated from cell lines using TriReagent, 1-Bromo-3-Chloropropane, isopropanol, polyacryl carrier, and 75% ethanol. Extracted RNA was suspended in diethylpyrocarbonate (DEPC) treated water and RNA concentration was determined using optical density by UV/Vis at 260 nm and 280 nm. The ratio of A_{260} to A_{280} for all samples was above 1.8. DNA was removed from RNA extract by suspending 2 µg in 2 µL RQ1 DNase 10x buffer and 2 µL RQ1 RNase-free DNase, bringing the volume up to 20 µL with DEPC water and yielding a final concentration of 100 ng/µL of RNA stock. This sample was DNase treated, adding 1 µL of RQ1 DNase Stop Reaction (Promega) immediately prior to the 65°C heating phase. The real time PCR mixture consisted of 5 µL of RNA stock diluted 1:50 in DEPC water, 12.5 µL of TaqMan Universal PCR Master Mix, 0.25 µL of primer (either TaqMan Gene Expression Assays FOLR1 or GAPDH), 0.125 µL MuLV Reverse Transcriptase, and 0.125 µL RNase Inhibitor. The PCR conditions were as follows: initial denaturation at 95°C for 10 minutes; 40 cycles of 30s at 95°C (denaturation), 1 minute at 55°C, and 1 minute at 72°C (annealing and extension). Experiments

were performed in triplicate for each sample and each primer. Folate expression was obtained by normalizing the amount of cDNA to that of GAPDH, with relative gene expression levels calculated by the $2^{-\Delta CT}$ method [377, 378].

A2.3.8 Quantification of bound MWNT-FA

Cells were cultured and grown to approximately 80% confluency in a 96 well plate, corresponding to 10,000 RKO, 13,000 HCT116, and 5000 HEPM cells/ well were used. The media was removed and 200µL of the sterilized solutions of MWNT-COOH or MWNT-FA (0.1 mg/mL in media) or media were added to 12 designated wells. The plates were incubated at 4°C for 4 hours under gentle agitation. Solutions were then removed and cells were washed once with phosphate buffer solution (PBS) to remove unbound MWNTs. Cells were detached using 50 µL of trypsin. PBS (150 µL) was added to all wells to bring the volume up to 200 µL and the solution from each well was combined into a glass vial for each group (media, MWNT-COOH and MWNT-FA). This solution was horn sonicated for 5 minutes and the fixed wavelength absorption at 1064 nm was taken using the "media" group as the blank. This value was compared to a 1064 nm absorption calibration curve to quantify the mass of MWNTs per mL.

A2.3.9 Thermal Ablation

Cells were plated in 96 well plates and grown to approximately 80% confluency. The media was removed and 200 µL of the sterilized solutions of MWNT-COOH or MWNT-FA [0.1 mg/mL in media] or media were added to designated wells and the plates were incubated at 4°C for 4 hours under gentle agitation. MWNT solutions and media were then removed and unbound MWNTs were removed by washing once with PBS. Cell culture media (200 µL) was added to each well and the cells were allowed to warm to 37°C, and were kept warm by placing them on a warm water bottle, to ensure that the starting temperature of the cells most closely matches physiological temperature prior to infrared light exposure. Cells were exposed to 15 cycles (triple pulse, 10 ms duration, 20 ms lag) at 30 J/cm^2 of a Vasculight Photoderm Nd:YAG pulsed 1064 nm laser. After laser exposure, the cells remained in the incubator at 37°C overnight. The next

day, cell viability was quantified by MTS assay and normalized for the "media" control. Statistical analysis was done using the Student's t-test for samples with unequal variance.

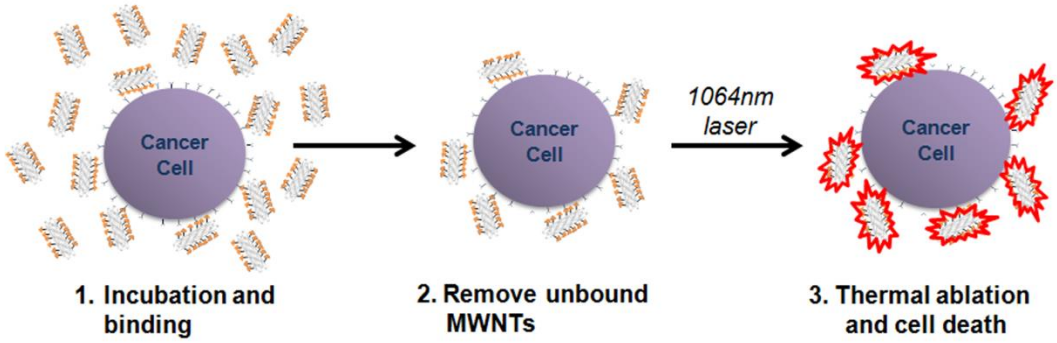

Figure 3. Schematic of the required steps for MWNT- induced photothermal ablation. First, nanotubes are incubated with the cells and allowed to bind. Second, any unbound MWNT are removed by washing the cells with PBS. Finally, cell/ MWNT complex is exposed to infrared light which causes heating of the nanotubes above the 50°C threshold and subsequent cell death.

A2.3.10 Fluorescent Microscopy

Cells were plated in 96 well plates and grown to approximately 80% confluency. The media was removed and 200 µL of the sterilized solutions of MWNT-COOH or MWNT-FA [0.1 mg/mL in media] or media were added to designated wells and the plates were incubated at 4°C for 4 hours under gentle agitation. MWNT solutions and media were then removed and unbound MWNTs were removed by washing once with PBS. Cell culture media (200 µL) was added to each well and the cells were allowed to warm to 37°C prior to infrared light exposure. Cells were exposed to 15 cycles (triple pulse, 10 ms duration, 20 ms lag) at 30 J/cm^2 of a Vasculight Photoderm Nd:YAG pulsed 1064 nm laser. After laser exposure, the cells remained in the incubator at 37°C overnight. The next day, cells were stained with 5µM calcein AM, and 2 µM ethidium homodimer solution (Live/Dead Assay from Invitrogen) in PBS for 30 minutes before being imaged by inverted fluorescent microscopy in fresh PBS. A representative image of the live population for each group was chosen.

A2.4 Results

A2.4.1 Synthesis and Characterization of MWNT-FA

The synthesis of NH_2-PEG-FA incorporated two known procedures [375, 376]. 4,7,10-trioxa-1,13-tridecaneamine was BOC-protected at one end, to ensure that FA functionalization would only occur at one end of the polyethylene glycol (PEG) chain. The γ-carboxylic acid group on FA was then attached to PEG using a DCC-coupling procedure. The ratio of attachment of the PEG to the γ-carboxylic acid group on FA compared to α-carboxylic acid is approximately 90:10 because the γ-carboxylic acid group is a more reactive position [376]. This is important as only attachment through the γ-carboxylic acid group to the PEG will allow the moiety to bind to the folate receptor on the cancer cell [379, 380]. ^{1}H-NMR and ^{13}C-NMR of reaction constituents, NH_2-PEG-NHBOC and FA-NHS, were consistent with values from the literature (data not shown). FA-PEG-NH_2 was characterized ESI-MS, which showed a parent peak $[M+H]^+$ at 644.3 indicating the pure FA-PEG-NH_2 product (Figure 4).

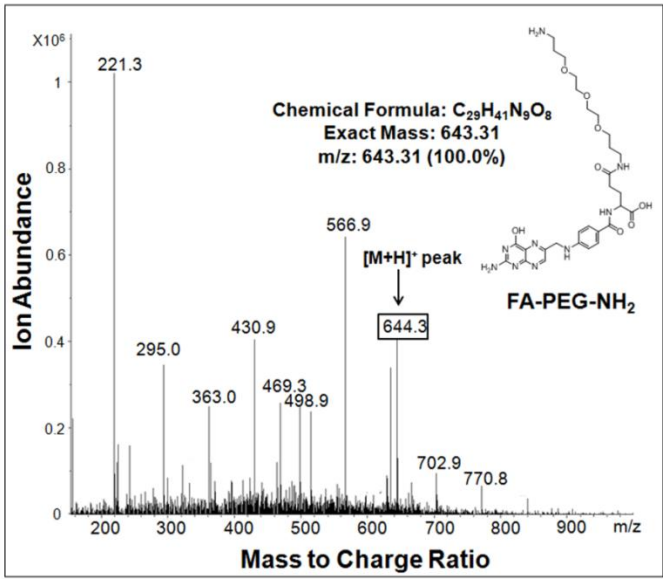

Figure 4. Mass spectroscopy results of FA-PEG-NH_2 show a parent peak at 644.3, which indicates the reaction produced folic acid conjugated to polyethylene glycol without any additional side chains.

Pristine MWNTs were first oxidized to MWNT-COOH. This purification helped remove trace impurities and shortened the tubes for better dispersivity in solution [381]. The FA-PEG-NH_2 moiety was then covalently attached to the MWNT through a simple DCC-coupling procedure.

Characterization of the MWNT-FA was carried out using FT-IR spectroscopy and Raman spectroscopy. The IR spectrum of the MWNT-FA compared to pristine MWNTs and pure folic acid can be seen in Figure 5. Pristine MWNTs showed no peaks in the IR due to low transmittance. The FA-PEG-NH_2 trace shows the two primary amine N-H stretches (3452cm^{-1} and 3360cm^{-1}) and one O-H stretch (3200cm^{-1}). The O-H stretch is known to be the dominant feature in this area, and it swamps the primary amine bands, making resolution difficult; however, this broadening has been observed for other folic acid conjugated materials as well [382]. The C=O stretch of the amides can be seen at 1675 cm^{-1} and at 1369 cm^{-1}. The bridge C-O stretch and the regular C-O stretch are visible at 1198 cm^{-1} and 1056 cm^{-1}. The C=C-H bend on folic acid can be a seen at 846 cm^{-1}. The N-H stretches and one O-H stretch between 3000-3500 cm^{-1} are missing in the MWNT-FA spectra possibly due to a combination of low transmittance and the loss of primary amines and carboxylate groups due to the amide bond formed between FA-PEG-NH_2 and the MWNT. The C=C-H bend on folic acid (846 cm^{-1}) as well as the C=O stretch of the amides (1369 cm^{-1} and 1675 cm^{-1}) from the FA-PEG-NH_2 are seen in the MWNT-FA spectra; however, they have shifted to higher wavenumber (850, 1417, and 1706 cm^{-1} respectively), which is indicative of attachment to the carbon nanotube [311].

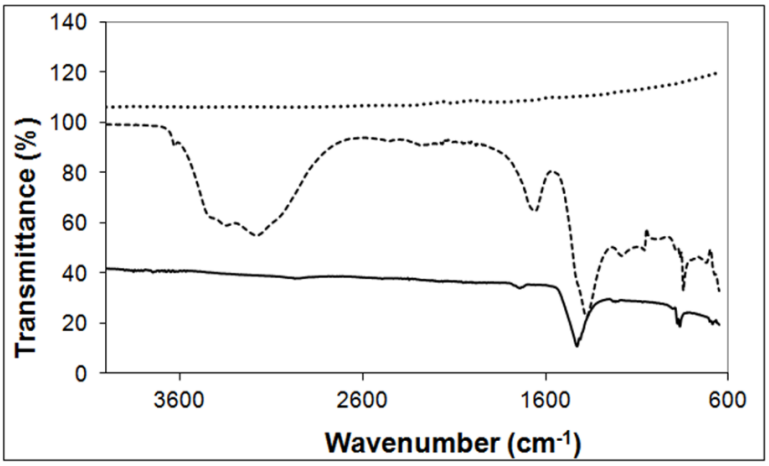

Figure 5. Fourier transform infrared spectra of pristine MWNTs (dotted line), FA-PEG-NH_2 (dashed line) and MWNT-FA (black line) indicates that folic acid is conjugated to MWNT by observation of the folic acid associated peaks near 1400 and 900cm^{-1} in the MWNT-FA line.

Raman spectroscopy was also used to determine whether FA-PEG-NH_2 bound to the MWNT. A comparison of the Raman spectra of MWNT-COOH and MWNT-FA can be seen in Figure 6. The characteristic D- and G-bands for MWNTs are shown at 1341 cm^{-1} and 1575 cm^{-1} respectively. For MWNTs, the D-band is derived from the defects along the walls of the tube [383]. The ratio of the intensity of the D-band to the G-band (I_D/I_G) indicates the degree of disorder on the nanotube, with an increase in the I_D/I_G ratio signifying an increase in the degree of chemical functionalization along the wall of the carbon nanotube [384-386]. The intensity of the D-band for the MWNT-FA is stronger compared to the D-band for MWNT-COOH, indicating that the sidewalls of the nanotube are functionalized with the FA-PEG-NH_2 moiety. However, the intensity of the G-bands for both the MWNT-FA and MWNT-COOH are the same. This is due to the fact that G-band intensity correlates with the vibrations of the sp^2 carbon atoms in the graphitic plane and chemical functionalization of the MWNT does not affect this.

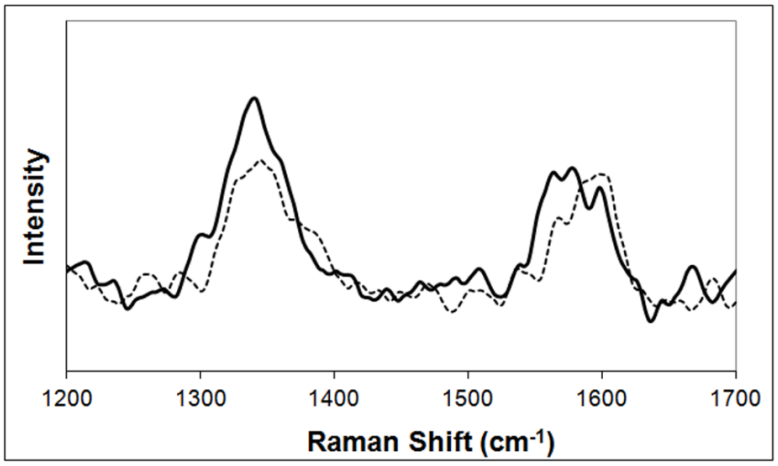

Figure 6. Raman spectra of MWNT-COOH (dashed line) and FA-MWNTs (black line) confirm that folic acid is conjugated to MWNT. This is observed by the increase in signal intensity in the FA-MWNT complex near 1350cm^{-1}, and the frequency shift of folic acid compared to MWNT-FA between 1550 and 1600cm^{-1}.

A2.4.2 Cytotoxicity Assay

In order to determine that MWNT-FA are not intrinsically lethal to cells, *in vitro* cytotoxicity assays were performed in the absence of NIR light. Both MWNT-COOH and MWNT-FA were incubated with colorectal cancer cell lines, RKO and HCT116, and a non-cancerous cell line, HEPM, at a concentration of 0.1 mg/mL, 0.01 mg/mL and 0 mg/mL for 48 hours at 37°C. Initial cell plating densities were 5000 cells for RKO and HCT116 and 10,000 cells for HEPM cells to allow for no greater than 80% cell confluency at the end of the 48 hour incubation period. Following incubation, an MTS assay was carried out to determine the cell viability. Cell viability was normalized for cells incubated with 0 mg/mL control. MTS results demonstrate that HEPM, RKO and HCT116 cell lines all had a greater than 93% cell viability when incubated with 0.01 or 0.1mg/ml of either MWNT-COOH or MWNT-FA in the absence of NIR light, which is expected as MWNTs are inert without NIR stimulation, since it is this stimulation that leads to molecular vibrations of the nanotubes that generate heat (Figure 7).

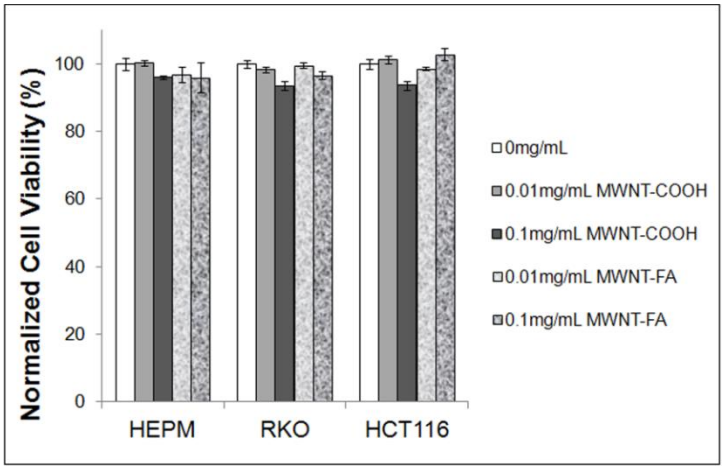

Figure 7. MTS assay results illustrate that MWNT-COOH and MWNT-FA treated RKO, HCT116 or HEPM cells have similar cell viability compared to cells not treated with nanotubes. All cell lines have viability greater than 93%, indicating a lack of cytotoxic response of the cells to either MWNT-COOH or MWNT-FA. RKO and HCT116 cells were then plated at a density of 5000 cells/ well, and HEPM cells were plated at a density of 10,000 cells per well and allowed to grow for 48 hours, so that the maximum confluency would be approximately 80% of the well surface area after the 48 hour incubation period.

A2.4.3 Real Time PCR and Quantification of MWNTs by Absorbance

RNA was extracted and DNase purified in RKO, HCT116, and HEPM in an effort to quantify folate receptor α (FRα) expression in colorectal cancer cell lines by real time PCR. The counts were normalized for housekeeping genes, Glyceraldehyde 3-phosphate dehydrogenase (GAPDH) using the $2^{-\Delta Ct}$ method to quantify folate receptor expression and then these values were averaged. The averaged values were then normalized for the cell line with the lowest expression, HEPM, to give relative expression of the folate receptor between the cell lines. Real time quantitative PCR found that RKO had the highest expression of folate receptor, followed by HCT116 and then HEPM (Table 1).

	Relative Expression of Folate Receptor
HEPM	1
RKO	3,324
HCT116	174

Table 1. Real-time Quantitative PCR was performed to assess folate receptor expression among HEPM, RKO, and HCT116 cell lines. Folate receptor counts were normalized for internal housekeeping gene, GAPDH, and then averaged. The averaged values were then normalized for the cell line with the lowest expression, HEPM, for comparison.

The mass of MWNT-COOH and MWNT-FA bound to cells was determined in order to examine targeting ability and optimal NIR light exposure. Incubation was done at 4°C to decrease non-specific interactions [387]. As seen in Table 2, MWNT-COOH demonstrated fairly equal affinity for cancerous cell lines, indicating negligible binding with an average mass of 11.7pg per cell (± 8.2 pg) determined by fixed wavelength absorption at 1064nm and a MWNT absorption-concentration calibration curve (Figure 8). Both colorectal cancer cell lines, RKO and HCT116, demonstrated a marked increase in affinity for MWNT-FA compared to MWNT-COOH. RKO demonstrated the highest increased affinity with 517% followed by HCT116 with 436%. The non-cancerous cell line, HEPM, had higher affinity for MWNT-COOH and similar affinity for MWNT-FA as RKO and HCT116 which resulted in only a 171% increase in affinity. These studies indicate that untargeted MWNTs may actually bind more readily to non-cancerous cells, and that folic acid functionalization of MWNTs will improve the therapeutic index of the treatment. It is interesting that HEPM has similar affinity for MWNT-FA as RKO and HCT116 despite having the lowest expression of FRα. This indicates that HEPM may express another receptor that FA may bind to, such as folate receptor β (FRβ). This is supported by Ross *et al.* [372] which found that healthy tissue generally expresses moderate amounts of FRβ and that immunotargeting of tumors will benefit from folate receptor isoform specificity.

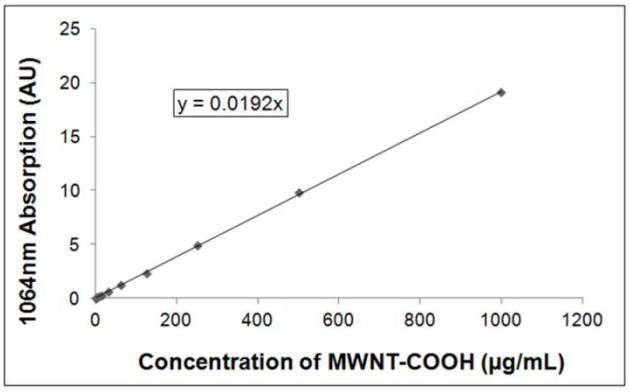

Figure 8. The optical absorption of MWNT-COOH versus concentration in cell culture media at 1064nm. The slope of the line is valuable for determining the number of MWNT in a cell population by measuring the optical absorption of the homogenized cell suspension and calculating the concentration using this plot.

	MWNT-COOH [pg/cell]	MWNT-FA [pg/cell]	Percent Increase
HEPM	21 (0.28)	36 (2.91)*	171%
RKO	8.7 (0.61)	45 (10.95)***	517%
HCT116	5.5 (0.08)	24 (4.73)*	436%

Table 2. The mass of bound MWNT-COOH and MWNT-FA was calculated using the MWNT-COOH absorption-concentration calibration curve (Figure 7) for HEPM, RKO, HCT116 cell lines with the standard error in parentheses. Percent increase is used to measure the magnitude of increased affinity the cell lines have for MWNT-FA over MWNT-COOH. *$p<0.05$, ***$p<0.01$ by student's t test for unequal variance.

A2.4.4 Thermal Ablation

Since RKO and HCT116 were shown to over-express folate receptor by real time PCR and display an increased affinity for MWNT-FA over MWNT-COOH, they were an ideal candidate for a thermal ablation assay. Due to the wide absorption peak (700-1100nm) of MWNTs, 1064nm light can produce thermal ablation and cell death, dependent upon the total energy fluence of the infrared source. In this work a pulsed 1064nm Nd:YAG laser was used at 30J/cm^2, with a pulse duration of 10ms and an application of 15 pulses. Starting at physiological temperature of 37°C, we know that a temperature change of 13°C is needed to reach the thermal ablation temperature of 50°C. But, since it was not possible to determine the temperature change at the cell surface an approximation was made to determine the laser parameters to achieve cell killing. For a 10μg/ml solution of MWNT-COOH, 30J/cm^2, with a pulse duration of 10ms and an application of 15 pulses gave a temperature change of a 200μl volume of 20°C. Therefore, since the temperature change of the bulk volume was sufficient, the same laser parameters were used in the cell photothermal ablation experiment. The laser parameters used in the experiments demonstrated no greater than a 50% cell kill, which could be further refined by increasing the laser fluence, and shortening the pulse duration to apply more energy in a shorter time period and decreasing the number of applied pulses is the optimal method for enhancing cell kill. Prior to laser exposure, each cell line was incubated with either: no MWNT, MWNT-COOH or MWNT-FA at the concentrations and using the procedures as described in the methods section, but no laser was applied, and the cell viability was assessed 48 hours later. This experiment served as a control for

verifying that the results observed once the laser was applied were not simply due to incubation with the nanotubes. There was no significant decrease in cell viability compared to cells incubated with either MWNT-COOH or MWNT-FA; cell viability was 100% ± 4%. As seen in Figure 9, in colorectal cancer cell lines, RKO and HCT116, MWNT-COOH incubation and near infrared light exposure only decrease cell viability by about 4-10% while MWNT-FA decreased cell viability by approximately 50-60%. In the non-cancerous epithelial cell line, HEPM, MWNT-COOH caused a negligible decrease in cell viability while MWNT-FA caused a 27% decrease. Cell viability after ablation with MWNT-FA compared to MWNT-COOH was found to be statistically significant in RKO and HCT116 ($p<0.001$) but not in HEPM. The cell viability between HEPM and RKO after ablation with MWNT-FA was also found to be statistically significant ($p<0.05$). The decreased cell viability seen in colorectal cancer cells incubated with MWNT-FA compared to MWNT-COOH is expected based on the binding assays which indicated targeting ability of the MWNT-FA. Additionally, the increased cell death seen in RKO and HCT116 bound to MWNT-FA compared to HEPM, despite similar MWNT binding, is expected as cancer cells are known to be more sensitive to hyperthermia than non-cancerous cells [10]. There was no observed difference in cell viability between the "media" control cells that were exposed to near infrared light and those that were not (data not shown).

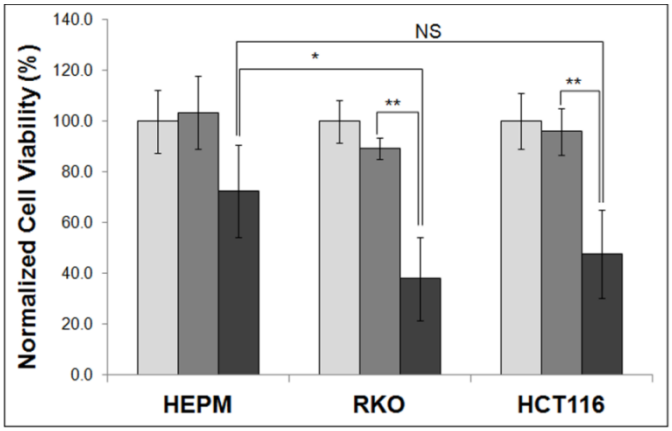

Figure 9. Cell viability measured by MTS assay 16 hours after laser ablation for cells incubated with media only (light grey), MWNT-COOH (grey), MWNT-FA (dark grey). The error bars represent standard error of the mean. *$p<0.05$, **$p < 0.001$, NS=not significant.

A2.4.5 Fluorescence Microscopy

Both the live and dead cell populations were stained using calcein for the live cell fraction and ethidium homodimer for the dead cell fraction. As is common in other thermal ablation procedures, the dead cell population was removed when the cells were washed after photothermal treatment and only the live cells were imaged by fluorescence microscopy, as shown in Figure 10A. Compared to the control cells treated with laser alone and no nanotubes, the number of live colorectal cells per area drastically decreases between populations treated with MWNT-COOH (39% and 28% reduction for RKO and HCT116 respectively) compared to treatment with MWNT-FA (reductions of 92% for RKO and 81% for HCT116), as shown in Figure 10B. In contrast, the HEPM cells do not display such a decline in the number of viable cells with a 20% reduction when treated with MWNT-COOH and laser and a 42% decrease with MWNT-FA and laser. The fluorescence microscopy results further corroborate the findings of the MTS assay of cell viability after photothermal therapy using MWNT-COOH or MWNT-FA. HEPM cells have a higher live cell population, most likely due to the more limited extent of bound MWNT-FA as compared to the RKO and HCT116 cells. Fluorescence microscopy also confirms that HCT116 cells have a higher live cell population after treatment with MWNT-FA and laser compared to RKO. This result could be attributed to either the reduced number of bound MWNT due to the lower expression of folate receptors compared to RKO cells, or else it may be due to the inherent resistance of the HCT116 cell line to hyperthermia.

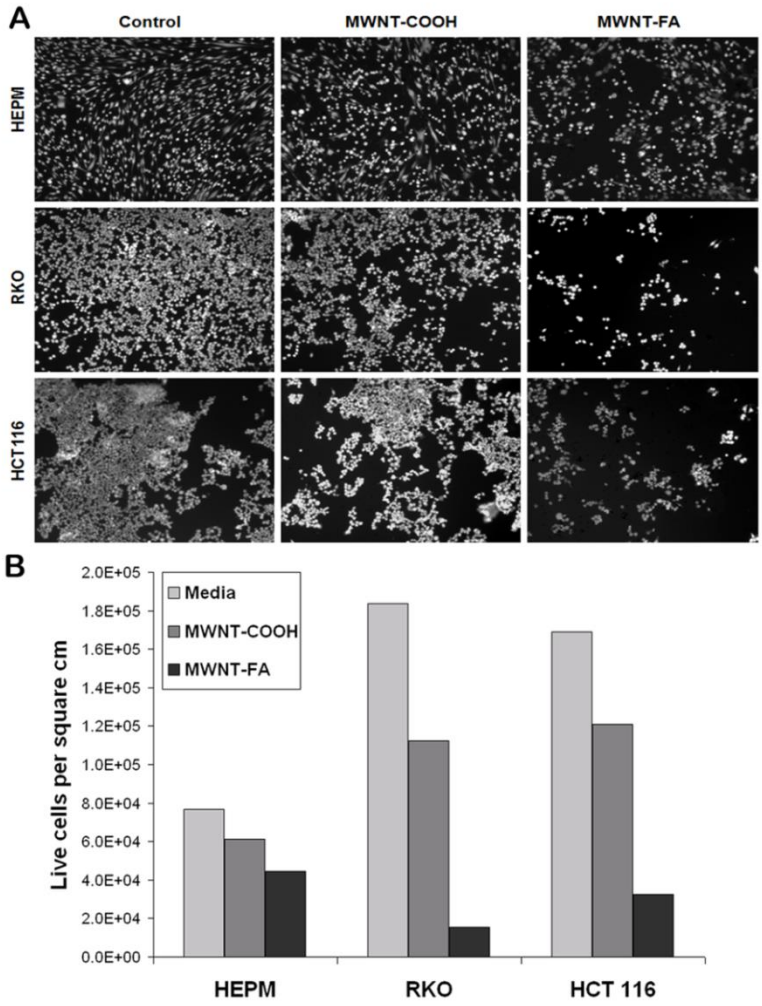

Figure 10.(A) The live populations of cells after exposure to 1064nm infrared laser light were stained using calcein and imaged on an inverted fluorescent microscope. All images are at 10x magnification. The micrographs corroborate the results of the MTS cell viability assay, and demonstrate slight reductions in cell populations treated with MWNT-COOH and infrared light, but significant reductions in RKO and HCT116 cells treated with MWNT-FA and exposed to infrared light as compared to controls without carbon nanotubes. (**B)** The plot of live cells per square centimeter shows an 20, 39, or 28% reduction in the number of cells treated with MWNT-COOH and infrared light for HEPM, RKO, and HCT116 cell lines respectively. HEPM cells treated with MWNT-FA and infrared light had a decrease of 42%, which is only about half of the 92 and 81% reduction observed for RKO and HCT116 cells treated with MWNT-FA and infrared light.

A2.5 Conclusions

Folic acid was chosen as a ligand for MWNTs to target colorectal cancer cells because they are known to over-express the folate receptor. The FRα expression in RKO, HCT116, and HEPM cell lines was quantified by real time PCR and it was found that the colorectal cancer cells have 200-3000% higher expression than HEPM, a non-cancerous epithelial cell line. A method to quantify mass of MWNT bound to cells *in vitro* was developed utilizing spectrophotometric absorption. This straightforward technique is beneficial for determining the number of nanotubes bound for specific cell types and correlating this value with the associated decrease in viable cell populations upon exposure to infrared light. It was shown that folic acid targeted MWNT demonstrated a 400-500% increased affinity for colorectal cancer cells over untargeted MWNTs; which translated to more efficient photothermal ablation and an increased therapeutic index over untargeted MWNTs. Notably, although the two colorectal cancer cell lines had a 10-20% cell survival rate 24 hours after photothermal therapy, there was 47% less MWNT-FA bound to HCT116 compared to RKO cells. In comparison to HEPM cells, HCT116 cells had a 33% reduction in the mass of bound MWNT-FA, yet there was not a significant difference in cell viability after photothermal treatment. The results highlight the value of considering not only the cell type's expression of folate receptors for targeting nanoparticles for photothermal ablation, but also the chosen cell line's resistance to hyperthermia. The disparity between the increased FRα expression and increased affinity MWNT-FA for HEPM may be due to alternate binding mechanism, such as FRβ. Future studies will investigate expression of both folate receptor isoforms to develop specific folate receptor targeting to decrease non-cancerous cell interactions. However, this non-isoform specific targeting may prove beneficial as tumors are composed of heterogeneous cell types and folic acid conjugation could prove valuable for targeting other tumor cell types, such as cancer associated fibroblasts.

Acknowledgements

Chris MacNeill synthesized FA-PEG-NH_2 and optimized attachment to MWNT-COOH. He also performed ESI-MS, FTIR, and Raman experiments and data analysis.

CHAPTER A3

Multi-Walled Carbon Nanotubes Inhibit Breast Cancer Cell Migration

A3.1 Abstract

According to the American Cancer Society, breast cancer is the second leading cause of cancer death in the US. Cancerous cells may have inadequate adhesions to the extracellular matrix and adjacent cells. Previous work has suggested that restoring these contacts may negate the cancer phenotype. This work aims to restore those contacts using multi-walled carbon nanotubes (MWNTs). Varying concentrations of carboxylated MWNTs in water, with or without type I collagen, were dried to create a thin film upon which one of three breast cell lines were seeded: cancerous and metastatic MDA-MB-231 cells, cancerous but non-metastatic MCF7 cells, or non-cancerous MCF10A cells. Proliferation, adhesion, scratch and autophagy assays, western blots, and immunochemical staining were used to assess adhesion and E-cadherin expression. Breast cancer cells grown on a MWNT-collagen coated surface displayed increased adhesion and decreased migration which correlated with an increase in E-cadherin. This work suggests an alternative approach to cancer treatment by physically mediating the cells' microenvironment.

A3.2 Introduction

According to the American Cancer Society, breast cancer is the second leading cause of cancer death for women in the US.[388] One of the hallmarks of cancer is altered contact-dependent inhibition, resulting in decreased adhesion, increased migration, and metastasis.[389] Intercellular adhesion determines the polarity of cells and allows maintenance of normal tissue architecture. Consequently, cell adhesion molecules play a significant role in cancer progression. It has been extensively documented that downregulation or loss of E-cadherin, a cell-cell adhesion protein, is correlated with cancer progression and invasiveness.[390-393] A change in the protein's ability to function is required for invasion and its decreased expression causes more aggressive tumors.[391]

Like many biological pathways, the downstream effects of E-cadherin are multifaceted. However, only one critical component in the E-cadherin adhesion pathway would need to fail in order to cause breast cancer.[391] Tyrosine kinases such as the epidermal growth factor receptor (EGFR) control E-cadherin through its interaction with the actin cytoskeleton.[390] The TGF-β/Smad and NF-κB pathways both suppress E-cadherin formation and TGF-β promotes an epithelial-mesenchymal transition (EMT).[394-396] NF-κB also controls cancer stemness and highly invasive tumor types by inhibiting the effects of integrin complex $\alpha_v\beta_3$, which is associated with receptor tyrosine kinases, more invasive tumor types, and contact independence.[397, 398] Previous work has attacked these tumors biochemically, but it has also been shown that cells can be controlled by forcing them to attach to matrix as $\alpha_v\beta_3$ is not harmful in its ligated state.[399]

An alternative pathway by which physical methods of control can affect the cells is through autophagy.[400] This process causes the cells to recycle their components and has been implicated in both protection from cancer and its improvement once established.[401-404] It is mediated by Beclin-1, which can function as a tumor suppressor gene.[405, 406] It is possible that increasing autophagy may increase Beclin-1 and suppress the cancer. For instance, inhibition of EGFR increases autophagy and halts proliferation.[403, 404] Increasing autophagy can be

beneficial for many types of cells as it promotes cellular fitness and genomic integrity.[407] However, its role in cancer is controversial; sometimes autophagy actually increases a tumor's aggressiveness and resistance to treatment.[404, 407]

While biochemical and physical inputs may seem like separate domains, their interrelation can be understood through the EMT process. EMT is required for cancerous cells to form, and E-cadherin is a strong effector of the epithelial phenotype.[392] Cells that lose E-cadherin lose their normal polarity and cell-cell adhesions which triggers cytoskeletal remodeling that favors migration and intravasation.[408] Such motility requires a relaxation of the actin cytoskeleton in order to form flexible protrusions.[408] However, the close association of actin with E-cadherin coupled with the binding to adjacent cells props the cell structure open when E-cadherin is present, forcing the cytoskeleton to remain rigid and inhibiting cell rounding while blocking the EMT. Helping the cells to maintain their E-cadherin levels blocks the EMT and can even revert them to more-normal epithelial cells.[409, 410]

Breast cancer treatment is uncommonly approached from a more mechanical perspective, even though it has been shown that the microenvironment of cells dominates their gene expression.[411] An extension of this concept was uncovered by Venugopalan *et al.*, who showed that compressing breast cancer cells causes them to return to their normal phenotype including not just their architecture and polarity but also their coherent rotation.[412] This effect was reversed when E-cadherin was blocked. While this is groundbreaking research, compression is not a viable option *in vivo*. The work described herein is aimed at finding something more translatable.

It is known that nanomaterials can affect adhesion, migration, and development of cells.[413-417] Any scaffold attempting to replicate normal extracellular matrix (ECM) must have a large number of highly connected pores smaller than the cells and a high surface to volume ratio.[418, 419] Surface roughness such as porosity or anodization on the nanoscale significantly increases cell attachment, growth and protein adsorption[419, 420] and the porosity

of ECM is an important consideration for tissue integration with the matrix.[421] Different physical features in a substrate also affect cell attachment and spreading.[422-425] Taken together, the various properties of nanomaterials can significantly alter cells' environment and cells clearly respond to these changes. Tailoring the nanomaterial to the intended application will strongly affect the outcome. Given these requirements and our own findings that aspect ratio has a significant effect, we chose to investigate multi-walled carbon nanotubes (MWNTs) with a control group of carbon black. These two particle types are made of the same material with roughly the same diameter, but have different aspect ratios (AR). The MWNTs used in this work have ARs of roughly 20 to 60 while carbon black, which is spherical, has an AR of 1.

MWNTs comprise a unique type of nanomaterial that is exceptionally strong and electrically conductive due to the chemistry and high aspect ratio of the particles.[426, 427] MWNTs are relatively long, cylindrical nanoparticles whose honeycomb structure yields high porosity and high surface area relative to their volume. These pores vary between 4 and 30 nm in diameter.[419, 428-430] The particles' hydrocarbon content and large size makes them normally insoluble in aqueous solutions, which impedes their biological use. However, they can be made soluble through the addition of hydroxyl groups. When carbon nanotubes have been used with cells, they have been shown to facilitate adsorption of proteins such as fibronectin and collagen to encourage cell adhesion[420, 431] and result in decreased migration.[432] The particles have both strength and flexibility,[419, 433] similar to the ECM. Due to the importance of cells' physical microenvironment, the ability of MWNT to emulate the normal ECM might be able to alter cancer cell behavior in a manner that is potentially clinically applicable.

A3.3 Materials and Methods

A3.3.1 Materials

MWNTs (>99% purity; outer diameter, 13-18 nm; length, 3-30 μM) were purchased from Cheap Tubes Inc. Carbon black (17 nm diameter) was purchased from Cabot. Concentrated nitric acid (70%), concentrated sulfuric acid (98%), acetic acid, triton X-100, and ethanol were

purchased from Fisher Scientific. Rat tail collagen type I was purchased from BD Biosciences. CellTiter 96® AQueous One Solution Cell Proliferation Assay was purchased from Promega. Pierce®RIPA Buffer, HALT Protease Inhibitor, and Pierce®BCA Assay Reagents A and B were purchased from Thermo Scientific. Whatman PROTRAN nitrocellulose transfer and immobilization membrane (0.2 µm pore size) and Western Lightning®*Plus*-ECL Enhanced Chemiluminescence substrate was purchased from Perkin Elmer. Anti E-Cadherin antibody (catalog number ab53033), anti β-tubulin antibody (ab6046) and goat polyclonal secondary antibody to rabbit IgG – H&L conjugated to Alexa Fluor®488 (ab150077) were purchased from Abcam. Rhodamine phalloidin conjugated antibody (R415) was purchased from Life Technologies. Goat secondary antibody to anti-rabbit IgG (H&L) conjugated to horseradish peroxidase (#7074S) was purchased from Cell Signaling Technology, Inc. Metal rods (1/8 inch x 1/8 inch x 1 ¼ inch) were purchased from Ace Hardware (item number 2157, made by the Hillman Group) and coated with methacrylate (Sally Hansen Super Shine Top Coat.) Leupeptin hemisulfate was purchased from Life Technologies. A lactate dehydrogenase (LDH) assay kit was purchased from Sigma.

A3.3.2 Oxidation of MWNTs

To aid their dispersion in aqueous media, MWNTs were oxidized by suspending 100 mg of pristine MWNTs in a 3:1 mixture of concentrated sulfuric acid to concentrated nitric acid (40 mL total) followed by heating this mixture to 80^{o}C for 2 hours. Our team has previously demonstrated that MWNT oxidized in these concentrated acids under intense sonication were resistent to shortening and were, on average, still longer than 1 micron even after 7 hours' ultrasonication.[368] The suspension was then filtered through a 0.2 µM polytetrafluoroethylene (PTFE) filter and washed with copious amounts of water until the pH of the filtrate solution was neutral. The MWNTs were then washed with ethanol and allowed to dry at room temperature in air overnight to yield oxidized MWNTs (MWNT-COOH.) Particles treated similarly from the

same manufacturer yielded roughly 3.5% oxygen in OH or COOH groups as measured by chemical derivatization and X-ray photoelectron spectroscopy (CD-XPS).[434]

A3.3.3 Sterilization of MWNT-COOH and Carbon Black

MWNT-COOH and carbon black (CB) were suspended in water and sterilized by autoclaving.

A3.3.4 Nanoparticle Coatings

All solutions used were sterile. Rat tail collagen type I was diluted in 0.02 M acetic acid to a concentration of 2 mg/mL. Collagen was then diluted 1:5 with sterile MWNT or CB in water solutions to achieve final concentrations of 0, 5, 10, 20, 25, 30, 50, and 100 µg/mL. 200 µL of the collagen-nanoparticle mixture was added to each well used in a 48 well plate (40 µL of 2 mg/mL collagen and 160 µL of MWNT or CB in water, used for all experiments except for the scratch assay) or 1.5 mL of the collagen-nanoparticle solution was added for a 6 well plate (0.3 mL collagen and 1.2 mL of the nanoparticle solution for the scratch assay.) For the proliferation, adhesion, and autophagy assays, another set of experimental groups was created by using an equal volume of water in place of the collagen for nanoparticle-only coatings. All plates were air dried in a sterile environment to create nanoparticle-laden coatings. All experiments were done in triplicate except for the western blot. Coatings were examined with a Philips 400 transmission electron microscope (TEM) at 80 keV after adding 10 µL of each solution to a formvar-coated copper grid and allowing the solution to dry.

A3.3.5 Cell and Reagent

MCF7 and MDA-MB-231 breast cancer cell lines were purchased from American Type Culture Collection (ATCC # HTB-22 and HTB-26 respectively) and cultured in DMEM/F12 medium. Both media were supplemented with 1% L-glutamine, 1% penicillin/streptomycin and 10% fetal bovine serum and MCF7 was also supplemented with 10 µg/mL of insulin. MCF10A human breast epithelial cell line was purchased from ATCC (ATCC # CRL-10317) and cultured in DMEM/F12 medium supplemented with 10 µg/mL insulin, 20 ng/mL epidermal growth factor,

0.5 µg/mL hydrocortisone, 100 ng/mL of cholera toxin, 5% heat inactivated horse serum, and 1% penicillin/streptomycin. Cell viability was quantified by 3-(4,5-dimethylthiazol-2-yl)-5-(3-carboxymethoxyphenyl)-2-(4-sulfophenyl)-2H-tetrazolium (MTS) assay using 96®Aqueous One Solution.

A3.3.6 Proliferation Assay

MCF7, MDA-MB-231, and MCF10A cells were plated in 48 well plates at densities of 20,000, 10,000, and 8,000 cells/well respectively and allowed to grow for 2 days until about 80% confluent. An MTS assay was performed using a Tecan Infinite M200 plate reader to quantify cell viability. Absorbance values were normalized for the 0 µg/mL control for each type of coating and cell line after subtracting the values of MTS-only blanks.

A3.3.7 Adhesion Assay

MCF7, MDA-MB-231, and MCF10A cells were plated in 48 well plates at densities of 20,000, 10,000, and 8,000 cells/well respectively and allowed to grow for 2 days until about 80% confluent. The media was removed, and cold 1X PBS was added to the wells. Plates were then sealed and centrifuged upside down for 5 minutes at 50 Gs in a Harrier 18/80 centrifuge in a manner similar to the procedure described by Reyes *et al.*[435] The PBS was removed and cell viability was then quantified by MTS assay as in the proliferation assay. In addition to normalizing for the 0 µg/mL control, each result was normalized by the corresponding viability measured in the proliferation assay to account for any change in viability due to incubation with the nanoparticles.

A3.3.8 Timed Binding Assay

MCF7, MDA-MB-231, and MCF10A cells suspended in appropriate media were added onto MWNT-collagen coatings at a density of 30,000 cells/well and allowed to bind for 0, 15, 30, 45, or 90 minutes at 37°C. After incubation, media was removed and cell viability was assessed by MTS assay as in the proliferation and adhesion assays.

A3.3.9 Scratch Assay

MWNT-collagen coatings were made in 6 well tissue culture plates. To permit a scratch assay without disturbing the coating, rods with a square cross section were put on top of each of the coatings after the coating dried but before cells were added. Rectangular metal rods were painted with methacrylate to prevent the release of cytotoxic metal ions and then ethanol sterilized. MCF7, MDA-MB-231, and MCF10A cells were added to plates at densities of 100,000, 50,000, and 40,000 cells/well respectively and incubated until a confluent monolayer developed. The rods were then carefully removed, wells were washed twice with PBS, and fresh media was added.

The 1/8 inch wide rods are significantly wider than the common scratch method, which leaves a roughly 100-200 μm gap.[436] To account for this increase in distance between the sides of the scratch, the assay was followed for 5 days until the fastest gaps began to close instead of the more common 24-48 hours alloted for the smaller scratches.

Pictures were taken immediately following the removal of the rod (day 0) and every 24 hours until day 5. Every 48 hours the media was removed, wells were washed twice with PBS, and fresh media was added. Because some cells migrated as individuals instead of as a sheet, ImageJ was used to measure the average pixel intensity in each scratch area and the data were normalized by taking the difference between the intensities at days 0 and 5. These results were then divided by the average for the 0 μg/mL concentration at day 5 for each cell line to make the cell lines more easily comparable.

A3.3.10 Statistical Analysis

Statistical analysis was performed using SigmaStat 3.5 for analysis of variance (ANOVA) and T tests. Holm-Sidak post-hoc testing was used as needed for the ANOVA results.

A3.3.11 Cell Lysate Collection for Western Blot

All lysates were generated from the same experiment. Cell lines were plated onto 6 well tissue culture plates coated with MWNT-collagen at the same concentrations evaluated by

adhesion assay. Cells were cultured until approximately 80% confluent before RIPA lysis buffer and HALT protease inhibitor (at a ratio of 100:1) were added and cells were collected by sterile cell scraper. Solutions were briefly homogenized by horn sonication using a Branson digital sonifier with 1/8" tapered microtip attachment and amplitude of 20%. Solutions were then centrifuged using an Eppendorf 5418 centrifuge for 20 minutes at 12,600 Gs to pellet cell debris. The supernatant was collected and evaluated by bicinchoninic acid (BCA) assay to determine protein concentration.

A3.3.12 Western Blot

Equal amounts of protein were resolved on a 10% polyacrylimide gel and transferred onto a nitrocellulose membrane. Non-specific binding was blocked by 2 hour incubation with 5% nonfat dry milk in 1x TBS-T (999 mL water, 1 mL Tween 20, 8.76 g NaCl, 1.21 g Tris Base at a pH of 7.5) at room temperature. The membrane was incubated with primary antibodies: anti E-cadherin (at a dilution of 1:4000 for MCF7 , 1:1000 for MDA-MB-231, and 1:5000 for MCF10A) in blocking solution overnight at 4°C and 1 hour at room temperature. After washing three times for 5 minutes with TBS-T, the membrane was incubated with goat anti-rabbit IgG peroxidase conjugated secondary antibody (at a dilution of 1:8000 for MCF7, 1:2000 for MDA-MB-231, and 1:10,000 for MCF10A) at room temperature for 2 hours. The nitrocellulose membrane was again washed three times with TBS-T for 5 minutes. Detection was assessed by ECL chemiluminescence using Western Lightning®*Plus*-ECL. Anti-β-tubulin (at a dilution of 1:10,000) with secondary antibody at a dilution of 1:15,000 was used as a loading control in all blots. Western blots have been cropped to show the proteins of interest, but have no other alterations. ImageJ was used to measure the area of each band.

A3.3.13 Immunochemical Staining:

Cells were plated onto MWNT-collagen coated 48 well tissue culture plates in triplicate. MCF7, MDA-MB-231, and MCF10A cells were plated at densities of 15,000, 10,000, and 10,000 cells/well respectively and grown for 2 days. The media was removed and the following steps

were performed with 2 washes of PBS between each one: cells were fixed in 4% paraformaldehyde for 10 minutes, permeabilized in 0.1% triton X-100 in PBS for 5 minutes, and blocked in 1% BSA in PBS for 30 minutes. The anti E-cadherin antibody (rabbit-based) was added at 1:375 dilution with 100 µL/well. The plates were then covered and left in a 4°C cold room overnight. The next morning, 100 µL/well of the goat anti rabbit IgG labeled with Alexa Fluor®488 secondary antibody was added at a 1:500 dilution in 1% BSA in PBS for 30 minutes. Then, 100 µL of rhodamine phallodin was added at a 1:40 dilution in 1% BSA in PBS for 30 minutes. The samples were imaged in PBS with an Olympus IX70 inverted fluorescent microscope with Image Pro Plus software.

A3.3.14 Autophagy Assay:

MCF7, MDA-MB-231, and MCF10A cells were plated in 48 well plates at densities of 20,000, 10,000, and 8,000 cells/well respectively and allowed to grow for 2 days until about 80% confluent. Based on previous protocols, the media was then changed and replaced with a solution of leupeptin hemisulfate in media at a concentration of 0.3 mM.[401, 402] The cells were incubated in this solution for 2 hours. Afterward, an LDH assay was performed as directed in the kit. Media was removed and assay buffer was added to each well before the plates were placed on a Lab-Line Instruments, Inc. titer plate shaker at speed 10 for 5 minutes to release LDH from the cells. The contents of each well were then centrifuged at 10,000 G for 15 minutes and 20 µL of each supernatant was added to a 96-well plate. Each well then received 30 µL of assay buffer and 50 µL of the LDH assay master mix. The absorbance of the reaction solution was measured at 450 nm with the same plate reader as for the adhesion and proliferation assays. The results were normalized by those of the 0 µg/mL concentration for each cell line and coating type.

A3.4 Results

A3.4.1 Carbon nanoparticle coatings are more organized with collagen

As shown in **Figure 1**, MWNTs in MWNT-collagen coatings are distributed in a more homogenous manner than MWNTs without collagen. **Figure 1A** shows that MWNTs without collagen aggregate more easily and are distributed heterogenously, with some areas of aggregation and other areas with very few MWNT. In contrast, **Figure 1B** shows that suspending the MWNT in collagen results in a homogenous coating. It also staves off aggregation until higher concentrations of MWNT are used and minimizes the aggregation that occurs even then.

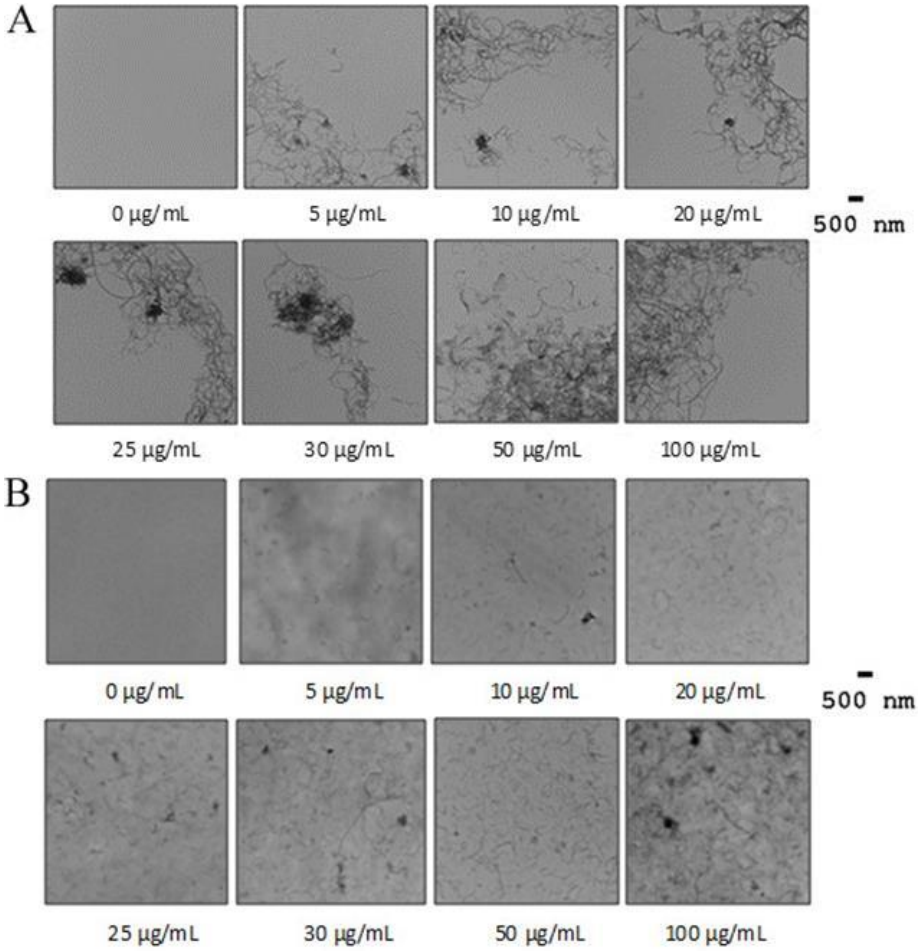

Figure 1 TEM of MWNT and MWNT-collagen coatings. All pictures are shown at a magnification of 13,000x. **A:** When the MWNT are dried in water alone, the vast majority of the particles exist within agglomerations. This leaves very few particles in between these clumps. **B:** When collagen is added to the coating solution, the nanoparticles become more homogenously distributed, though higher concentrations are still prone to agglomeration.

A3.4.2 Carbon nanoparticle coatings are not cytotoxic

After 48 hours of culture on carbon black or MWNT coatings, with or without collagen, the MCF10A cells showed no change in viability at any of the nanoparticle concentrations, as shown in **Figure 2**. The MCF7 cells showed only a few small changes in viability, but the MDA-MB-231 cells displayed greater sensitivity to both nanoparticle types. This sensitivity resulted in a slight decrease in viability of the MDA-MB-231 cells at the higher concentrations, but also an increase in viability at the 5 μg/mL concentration for MWNT alone. However, even where changes were observed, cell viability was always at least 70% of the control viability, so a large percentage of the cells persisted in every condition. In addition, the small decrease in viability was mostly resolved with the addition of collagen to the MWNT but not the carbon black.

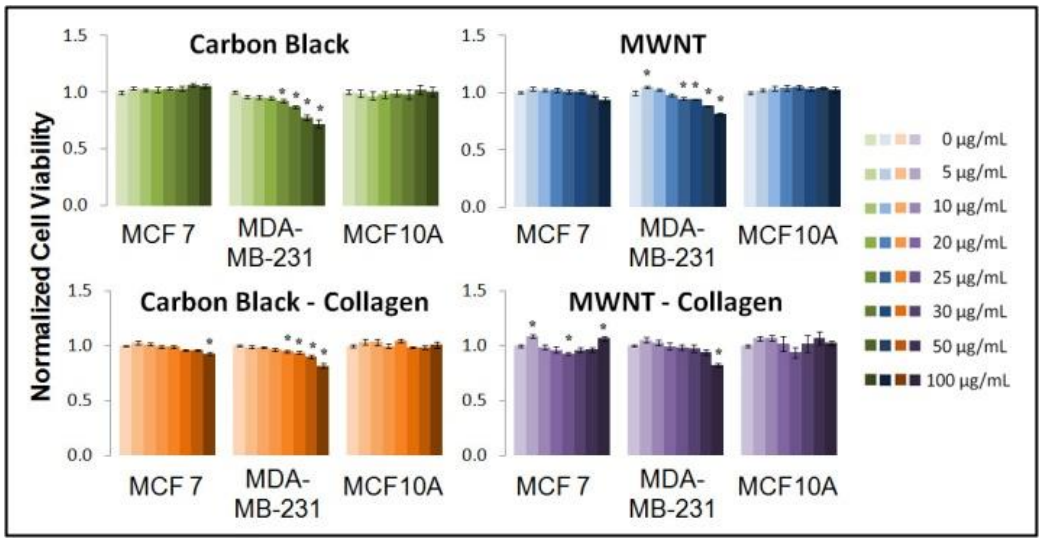

Figure 2 Cell viability as measured by MTS assay to assess the effect of MWNT concentration on cell proliferation in breast cancer cell lines MCF 7 and MDA-MB-231 and non-cancerous breast cell line MCF 10A. Results for each group are normalized to the 0 μg/mL control for that cell line and coating. An asterisk denotes significance on the $p<0.05$ level. Error bars show SEM.

A3.4.3 MWNT-collagen coatings increase adhesion strength of breast cancer cells but not non-cancerous cells

The adhesion strength of cells on each coating type was tested by applying force via centrifugation. As shown in **Figure 3**, trends for cells remaining after that force was applied were flat across the concentrations for the carbon black, MWNT and carbon black-collagen coatings.

The slightly increasing trend observed with these coatings are due to normalization by proliferation data, where small decreases are observed and so register here as small increases. The MWNT-collagen coatings were quite different and with increasing concentrations of MWNT showed a parabolic increase in adhesion for the cancerous cells but no change in the non-cancerous cells.

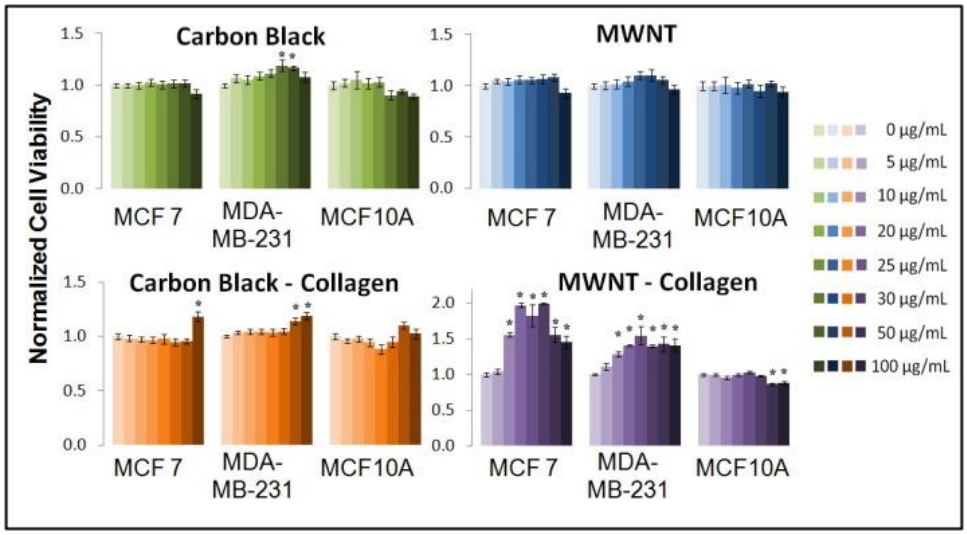

Figure 3 Cell viability as measured by MTS after the adhesion assay. The results for each group are normalized to the 0 µg/mL control for that cell line and coating as well as the viability measured in the proliferation assay. For the carbon black-only, MWNT-only and carbon black-collagen coatings there are only very small changes in cell viability on the different concentrations of each coating and no larger trend emerges. Increased nanoparticle concentration of the MWNT-collagen coating shows a parabolic increase in adhesion for the MCF7 and MDA-MB-231 cancerous cells but not the non-cancerous MCF10A cells. An asterisk denotes significance on the $p<0.05$ level. Error bars show SEM.

A3.4.4 The increase in adhesion strength is not immediate

Different cell lines adhere at different rates and this is very clear in the 15 and 30 minute data shown in **Figure 4**. After giving the cells 15 minutes to adhere, MDA-MD-231 cells had the most cells adhered at most of the concentrations, followed by the MCF7 cells, and MCF10A cells had the fewest adherent cells. At the 30 minute mark, however, the cancerous cells had adhered more uniformly across concentrations and between the two cell lines while the MCF10A cells had

increased their adhesion. By 90 minutes, all cell types and concentrations were fairly similar in their adhesion.

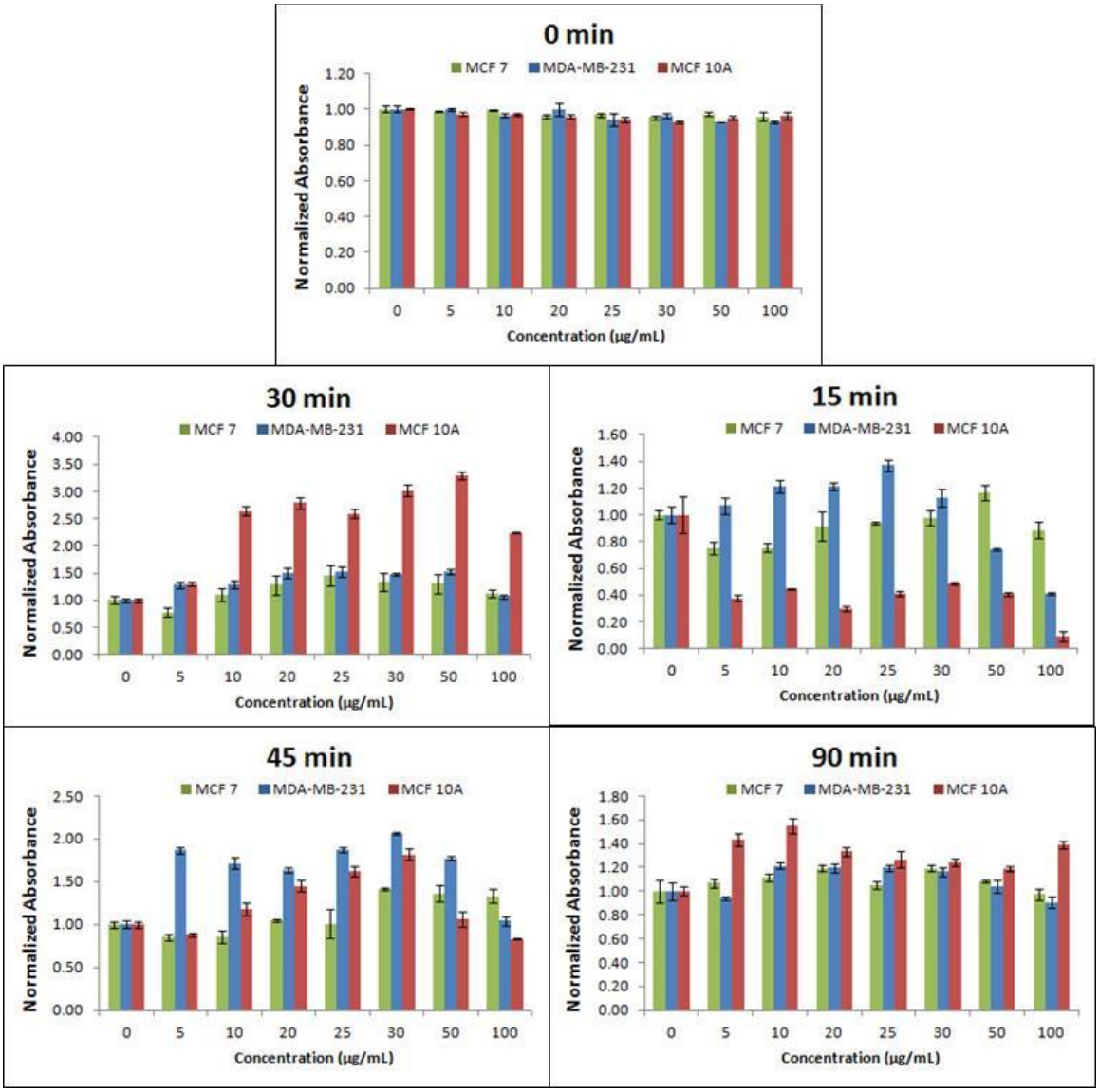

Figure 4 Cell viability as measured by MTS during the timed binding assay. The observed trends are generally a result of differences between cell type, not coating, and any differences are almost completely resolved after allowing the cells to adhere for 90 minutes. Error bars show SEM.

A3.4.5 Increased adhesion strength correlates with increased E-cadherin

As shown in **Figure 5**, western blots indicated an increase in E-cadherin in a pattern of expression similar to the trend in adhesion seen in the adhesion assay performed after 48 hours of culture. Both data sets show an increase in the middle range of tested MWNT concentrations for

the cancerous cell types but no change for the non-cancerous cell type. The density of the bands in **Figure 5A** shows that this change is increasing the E-cadherin from a deficient level in the cancerous cell lines MCF7 and MDA-MB-231 towards the level of expression seen in the non-cancerous MCF10A cells. **Figure 5B** quantifies the change in expression within each cell line and MWNT concentration.

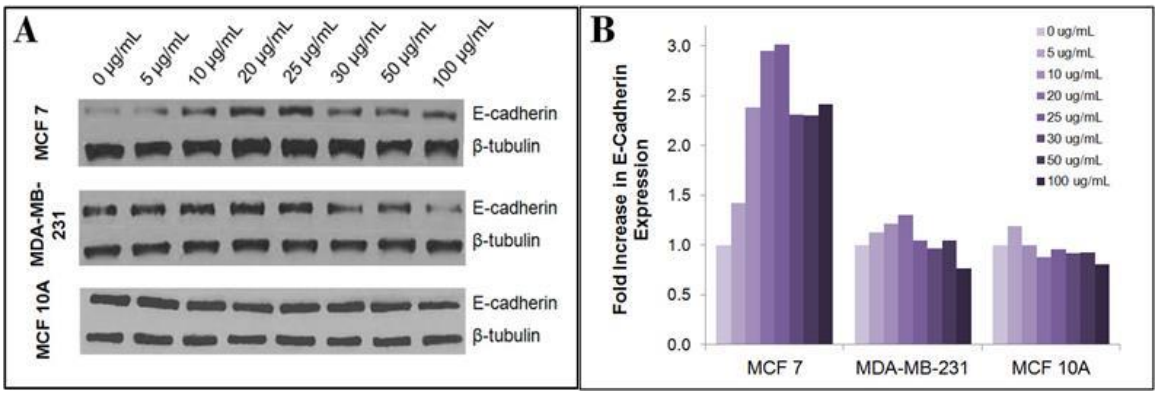

Figure 5 Western blots and their quantitative representation via ImageJ both echo the parabolic increase in adhesion seen in the adhesion assay. **A:** Western blots indicate increased expression of E-cadherin at MWNT-collagen concentrations that displayed increased adhesion, again showing increases in the cancerous cells but not the non-cancerous cells. MCF 10A displayed consistent E-cadherin expression across MWNT concentrations. **B**: ImageJ analysis of western blot images quantifying the area of the band, normalized for the 0 µg/mL control for each cell type to quantitatively visualize E-cadherin expression and its change across the concentrations.

A3.4.6 MWNT-collagen coatings promote co-localization of E-cadherin and F-actin in cancer cells

To better understand how the cells' architecture may be affected by the MWNT-collagen coating, both E-cadherin and the actin cytoskeleton were visualized. As seen in **Figure 6,** all cell lines expressed both proteins at every concentration. However, their distributions were different. There was no co-localization of the two proteins (seen in yellow) at the 0 µg/mL concentration of the MDA-MB-231 cells, but it was widespread in the 5-50 µg/mL concentrations and tapered off at 100 µg/mL. Co-localization was weakly present in the 0 µg/mL concentration of the MCF7 cells, but it became common from 5 µg/mL up to an including the 30 µg/mL concentration, after which it returns to a low level. Co-localization was more common in clustering cells and more

cell clusters were observed at the affected concentrations. The MCF10A cells remained fairly constant at each concentration.

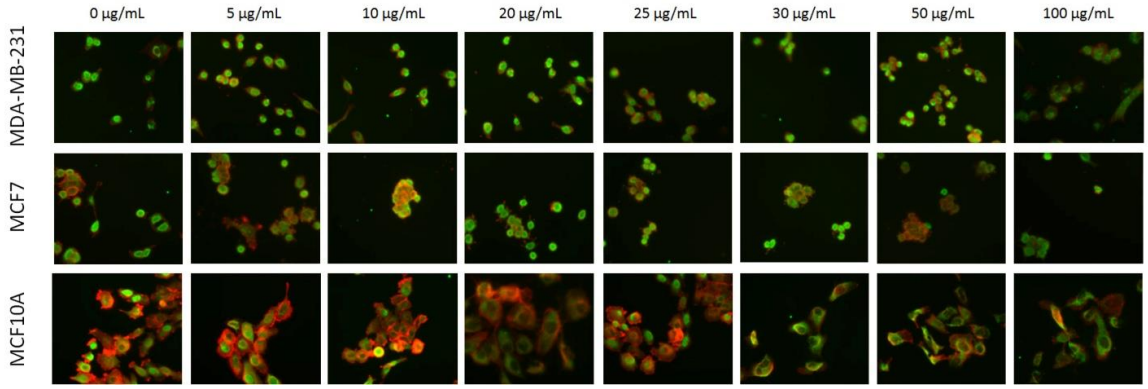

Figure 6 E-cadherin (green) and F-actin (red) expression for each cell line and concentration. For the cancerous cells there is an increase in E-cadherin and F-actin co-localization when MWNT are present and this effect appears to be particularly strong where the cells cluster. MCF10A cells are consistent regardless of MWNT presence or concentration.

A3.4.7 Cells exhibit decreased motility where adhesion strength and E-cadherin expression are higher

In **Figure 7A** the MDA-MB-231 cells, which are observed to migrate individually instead of as a sheet, have a scratch area that is more opaque at the 0 and 5 µg/mL concentrations by day 5, while it is darker at the remaining concentrations. The MCF7 and MCF10A cells migrate more as a sheet and while all cell lines were measured using the same method, the differences are sometimes more apparent to a viewer when considering the width of the unclosed scratch. The MCF7 scratches are wider at 25 and 30 µg/mL than the other concentrations. The MCF10As are almost completely closed and appear uniform across concentrations.

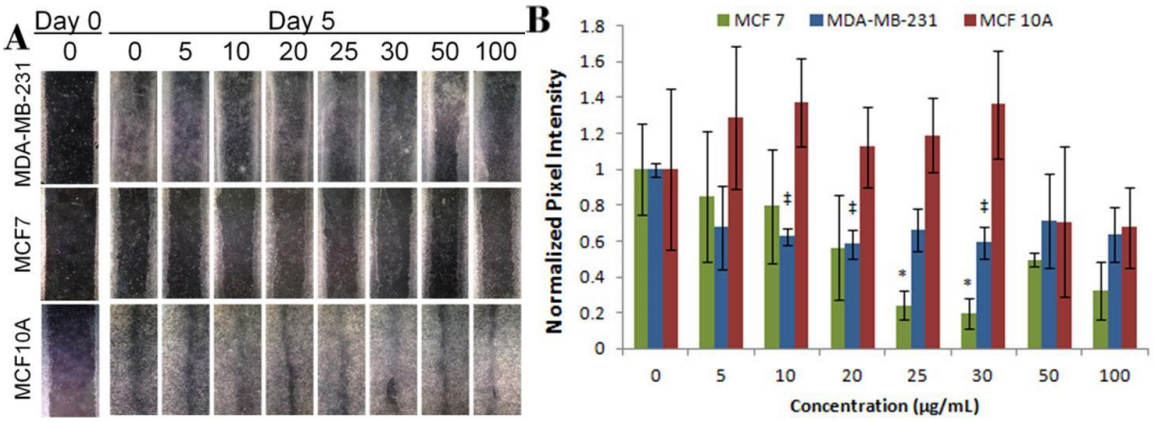

Figure 7 Scratch assay results for each concentration (µg/mL) and cell line. **A:** No difference is observed in the MCF10A normal cells, but closure is inhibited in some concentrations for the MDA-MB-231 and MCF7 cells. Pictures are at 4x magnification. **B:** The values shown are normalized by taking the difference in pixel intensities at days 0 and 5 for the same scratch, then dividing by the average 0 µg/mL intensity at day 5 for that cell line to aid comparison between the cell types. An asterisk denotes significance relative to the control on the $p \leq 0.05$ level, double dagger denotes significance on the $p \leq 0.01$ level. Error bars show SEM.

The results shown in **Figure 7B** were measured with ImageJ and indicate that the addition of MWNT decreases closure in the cancerous cells MDA-MB-231 and MCF7 but has no effect on the non-cancerous MCF10A cells. As is also evident in **Figure 7B**, there was sometimes rather large variability using this method. T tests were used to manage this variability. MCF7 cells were significantly inhibited ($p \leq 0.05$) at 25 and 30 µg/mL and MDA-MB-231 cells were inhibited with high significance ($p \leq 0.01$) at 10, 20, and 30 µg/mL.

A3.4.8 MWNT-collagen coatings greatly increase autophagy in MDA-MB-231 cells

In **Figure 8** it is evident that the MDA-MB-231 cells have an extremely high rate of autophagy when grown on MWNT-collagen (MW+) coatings of 10 µg/mL or higher. The overall p values, whether from an ANOVA across all the groups (each concentration, cell line, and coating type) or within each concentration, were generally less than 0.001. However, the individual comparisons of any one group to the MDA-MB-231 MW+ cells were usually $p<10^{-12}$ to $p<10^{-10}$. Exceptions to this were the 0 µg/mL concentration, which had no differences since all the values were normalized to 1, and the 5 µg/mL concentration, which was also not significant.

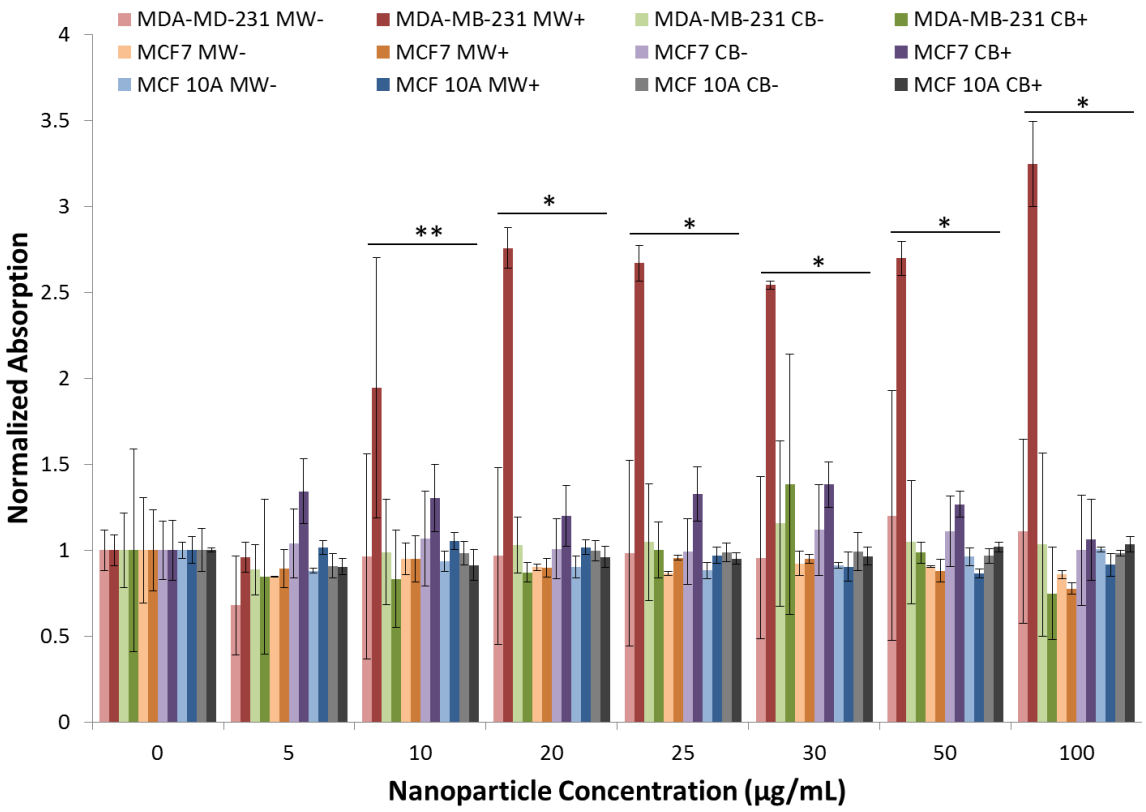

Figure 8 Autophagy results for each concentration (µg/mL), cell line, and coating type. MW refers to the MWNT and CB is carbon black; plus or minus refers to the presence or absence of collagen in the coating. Autophagy is drastically increased for the MDA-MB-231 cells on MWNT-collagen coatings at MWNT concentrations of 10 µg/mL or higher, but no other experimental group displays significant change. When every group is analysed together, the treatments were significantly different with $p<0.001$. An asterisk shows significance on a $p\leq0.0001$ level relative to the other treatments for the same concentration. Two asterisks indicate significance at a $p=0.028$ level.

A3.5 Discussion

E-cadherin loss is a known signal of many cancers,[392] but its return can also restore the epithelial phenotype.[437] The loss of E-cadherin has been shown to decrease cells' adherence to one another and promote motility, leading to invasion and metastasis.[438] Reinstating E-cadherin's functionality should promote cell-cell adhesion and decrease motility. Based on the data presented here, this appears to be the case, as cell adhesion increases in a time-delayed manner that follows a pattern of increased E-cadherin expression. Correspondingly, the same treatment increases the time to close a scratch assay, indicating decreased cell migration.

Cells prefer to adhere to collagen, and MWNTs have been shown to sequester it as a coating.[439] This is an important functional aspect for the effect described in this work, and the disparity is evident in the differences between the MWNT and MWNT-collagen coatings. MWNT-induced reductions in cell viability are prevented by adding collagen, and a change in adhesion is only observed when MWNT and collagen are used together. However, this effect is not observed with the carbon black-collagen coatings. The fiber-shaped MWNTs have been shown to generate an optimized 3D arrangement on the nanoscale which allows greater cell-scaffold interaction.[419, 440] This stable and harmonious ECM substitute allows cells to adhere and appears to help the cells maintain their epithelial origin.

The adhesion assay shows a peak for cells adhered between the concentrations of 10-30 μg/mL MWNT. Since the proliferation assay showed little to no changes in cell viability, this increased number of adhesive cells is not caused simply by increased proliferation. The adhesion data are shown as a fraction of cells remaining after incubation with the MWNT, thereby indicating that the coatings appear to be strengthening the cells' connections so that a larger fraction of the population can resist an applied force. This pattern also takes time to develop, as it is not yet evident after 90 minutes when the cells should have completed the majority of their attachment process. This result is consistent with the behavior of E-cadherin, which is known to take 48 hours to fully downregulate even when using E-cadherin siRNA.[392]

One of the ways cells can increase their adhesion to a matrix is by also sticking to each other. Even if the cells are somewhat loosely attached to the surface, distributing any force among a group pools the attachments of each of the cells and lowers the strain on any one cell. This improves the probability that these cells will remain attached after being subjected to a given force. As E-cadherin was also implicated in a range of other consequences of cancer, its role in these results was assessed with a western blot. Many of the observations from the data correlate with the presence or absence of E-cadherin, and we are able to reverse both the expression and behavior deficits that contributed to the initial problem. In the MCF7 and MDA-MD-231 cells E-

cadherin was (sometimes sharply) increased and restored to a level closer to that of the non-cancerous MCF10A cells.

The interaction of E-cadherin with the actin cytoskeleton contributes to cell-cell adhesion and thus both of these molecules contribute to tumor progression and metastasis.[390] Our investigation suggested that cells on MWNT-collagen substrates are more likely to co-localize actin and E-cadherin and form clusters of several cells, both of which are normal behaviors that suggest an improvement in cell-cell adhesion and organization. Co-localization was more common in clustering cells, an observation that likely reflects the proteins' abilities to execute their intended cell-cell adhesive function. They also seem more content in their locations, staying put instead of migrating. This behavior is reflected in the slower closing rates in the scratch assay.

An interesting question is why the cells might prefer certain concentrations of MWNT in collagen, particularly over other nanoparticles of the same material such as carbon black. This may be because cells prefer binding to fiber-shaped particles,[439] which is a natural extension of cells' preference in binding fibrillar collagen. Cells will also bind to multiple fibers and change their behavior based on the stress that clinging to that fiber arrangement creates.[441, 442] Cells migrate fastest on single fibers, while they migrate the slowest – even slower than when on a flat surface – when settled at the intersection of multiple fibers.[442] This preference echoes the cell niche, where cells prefer a certain topography with physical boundaries.[443, 444] Cells normally receive these physical signals from the extracellular matrix. Only when cells ignore these signals, or they are no longer presented properly, might cancer occur.

Cells will orient themselves based on their niche in the microenvironment, but they can only reach so far.[441] Perhaps the reason MWNT collagen coatings work at specific concentrations is that the randomly distributed particles are far enough away from each other to cause the cells to perceive a niche, but close enough that the cells can reach between them. The TEM images also corroborate this hypothesis, as the MWNT concentrations only become significant once the particles frequently overlap and the significance decreases with much higher

concentrations. This idea reverts to one of the mechanisms of EMT. If a cell exists in a taut configuration, as if it were held up by connections to its neighbors instead of balling up on itself, it might be forced to maintain an epithelial phenotype. The data here suggest that it is possible to interrupt the E-cadherin/actin feedback loop using MWNT to inhibit EMT.

Perhaps even more interestingly, the MWNT-collagen coatings cause a substantially significant increase in autophagy in MDA-MB-231 cells. While the role of autophagy in cancer is incompletely understood, its dual ability to promote or prevent cancer seems to be controlled by what else is happening to the cells. Cells undergoing stress due to severe hypoxia, chemotherapy, or radiation do retreat into autophagy as a protective measure.[406] This is problematic in conventional cancer therapy because autophagy causes senescence (while therapies target proliferative cells) and the cells survive mostly off of their recycled components instead of uptaking toxic molecules designed to attack them. However, our cells were under no such increased stress, and so cells' voluntary retreat from proliferation is a welcome result. The idea of cells fixing their internal damage is also appealing, and while we have not proven that this process is completely reverting cancer cells to their healthy equivalents, our other data suggest that cells might progress somewhat in that direction.

The MWNT-collagen coatings seem to not only stop, but at least partially reverse some of the problems that cause cancer. They decrease the cells' motion, rescue their E-cadherin expression, restore a degree of normal tissue architecture, and encourage protein turnover. Potentially, these coatings could be quite a useful tool for cancer treatment. We envision them as a supplementary treatment after resection of the primary tumor to both fill the tumor void and protect the margins from recurrence. Resection disrupts the tumor area and this process can result in some cancer cells being disturbed but not removed. By interfacing any remaining cancer cells with the MWNT-collagen we believe that we can attenuate further disease resulting from this population. Future *in vivo* work will also investigate the immune response these particles may

generate, such as a foreign body response or neutrophil invasion that may further affect the cancer.

A3.6 Conclusion

This work extends the understanding of the relationship between cells and their microenvironment. We have shown that fiber-like carbon nanotubes, MWNTs, can mimic the natural ECM to encourage cell adhesion and regulation of gene expression. Our data bolster the idea that functional recovery of E-cadherin can mitigate the problematic consequences of its loss that often lead to cancer and the disease's progression. Specifically, we have shown an increase in adhesion and autophagy with an associated increase in E-cadherin expression and decrease in migration. This line of research presents an innovative method of controlling cancer and should be considered for further research to advance it towards clinical utility.

Acknowledgements
Elizabeth Wailes contributed equally to experiments and wrote the manuscript.

REFERENCES

[1] X. Huang*, et al.*, "Plasmonic photothermal therapy (PPTT) using gold nanoparticles," *Lasers Med Sci,* vol. 23, pp. 217-28, Jul 2008.

[2] A. N. Mirza*, et al.*, "Radiofrequency ablation of solid tumors," *Cancer J,* vol. 7, pp. 95-102, Mar-Apr 2001.

[3] S. D. Kim*, et al.*, "Radiofrequency ablation of renal tumors: four-year follow-up results in 47 patients," *Korean J Radiol,* vol. 13, pp. 625-33, Sep 2012.

[4] Q. Lu*, et al.*, "CT-guided percutaneous microwave ablation of pulmonary malignancies: Results in 69 cases," *World J Surg Oncol,* vol. 10, p. 80, 2012.

[5] M. Sato*, et al.*, "Two long-term survivors after microwave coagulation therapy for hepatocellular carcinoma: a case report," *Hepatogastroenterology,* vol. 43, pp. 1035-9, Jul-Aug 1996.

[6] F. W. Kremkau, "Cancer therapy with ultrasound: a historical review," *J Clin Ultrasound,* vol. 7, pp. 287-300, Aug 1979.

[7] G. T. Haar and C. Coussios, "High intensity focused ultrasound: past, present and future," *Int J Hyperthermia,* vol. 23, pp. 85-7, Mar 2007.

[8] W. B. Coley, "The treatment of malignant tumors by repeated inoculations of erysipelas. With a report of ten original cases. 1893," *Clin Orthop Relat Res,* pp. 3-11, Jan 1991.

[9] D. K. Chatterjee*, et al.*, "Nanoparticle-mediated hyperthermia in cancer therapy," *Ther Deliv,* vol. 2, pp. 1001-14, Aug 2011.

[10] B. Hildebrandt*, et al.*, "The cellular and molecular basis of hyperthermia," *Crit Rev Oncol Hematol,* vol. 43, pp. 33-56, Jul 2002.

[11] K. C. Kregel, "Heat shock proteins: modifying factors in physiological stress responses and acquired thermotolerance," *J Appl Physiol,* vol. 92, pp. 2177-86, May 2002.

[12] E. A. Thompson*, et al.*, "Differential response of MCF7, MDA-MB-231, and MCF 10A cells to hyperthermia, silver nanoparticles and silver nanoparticle-induced photothermal therapy," *International Journal of Hyperthermia,* vol. 30, pp. 312-323, 2014.

[13] O. Svelto and D. C. Hanna, *Principles of lasers*, 4th ed. New York: Plenum Press, 1998.

[14] A. E. Siegman, *Lasers*. Mill Valley, Calif.: University Science Books, 1986.

[15] W. T. Silfvast, *Laser fundamentals*. Cambridge, Eng. ; New York, NY, USA: Cambridge University Press, 1996.

[16] J. P. Minton*, et al.*, "An Evaluation of the Physical Response of Malignant Tumor Implants to Pulsed Laser Radiation," *Surg Gynecol Obstet,* vol. 121, pp. 538-44, Sep 1965.

[17] H. G. Journee-de Korver*, et al.*, "Infrared thermotherapy: from laboratory to clinic," *Ophthalmol Clin North Am,* vol. 18, pp. 99-110, viii-ix, Mar 2005.

[18] A. Carpentier*, et al.*, "MR-guided laser-induced thermal therapy (LITT) for recurrent glioblastomas," *Lasers Surg Med,* vol. 44, pp. 361-8, Jul 2012.

[19] Y. Anzai*, et al.*, "Preliminary experience with MR-guided thermal ablation of brain tumors," *AJNR Am J Neuroradiol,* vol. 16, pp. 39-48; discussion 49-52, Jan 1995.

[20] A. Carpentier*, et al.*, "Laser thermal therapy: real-time MRI-guided and computer-controlled procedures for metastatic brain tumors," *Lasers Surg Med,* vol. 43, pp. 943-50, Dec 2011.

[21] A. Carpentier*, et al.*, "Real-time magnetic resonance-guided laser thermal therapy for focal metastatic brain tumors," *Neurosurgery,* vol. 63, pp. ONS21-8; discussion ONS28-9, Jul 2008.

[22] M. Bublik*, et al.*, "Ultrasound-Guided Laser-Induced Thermal Therapy of Malignant Cervical Adenopathy," *The Laryngoscope,* vol. 116, pp. 1507-1511, 2006.
[23] R. Chapman, "New therapeutic technique for treatment of uterine leiomyomas using laser-induced interstitial thermotherapy (LITT) by a minimally invasive method," *Lasers in Surgery and Medicine,* vol. 22, pp. 171-178, 1998.
[24] C. M. Pacella*, et al.*, "Laser Thermal Ablation in the Treatment of Small Hepatocellular Carcinoma: Results in 74 Patients," *Radiology,* vol. 221, pp. 712-720, 2001.
[25] R. R. Anderson and J. A. Parrish, "Selective photothermolysis: precise microsurgery by selective absorption of pulsed radiation," *Science,* vol. 220, pp. 524-7, Apr 29 1983.
[26] W. R. Chen*, et al.*, "Photothermal effects on murine mammary tumors using indocyanine green and an 808-nm diode laser: an in vivo efficacy study," *Cancer Lett,* vol. 98, pp. 169-73, Jan 2 1996.
[27] W. R. Chen*, et al.*, "Chromophore-enhanced in vivo tumor cell destruction using an 808-nm diode laser," *Cancer Lett,* vol. 94, pp. 125-31, Aug 1 1995.
[28] W. R. Chen*, et al.*, "Indocyanine green in-site administration and photothermal destruction of tumor cells using an 808-nm diode laser," *Proceedings of the SPIE - The International Society for Optical Engineering,* vol. 2681 (Laser-Tissue Interaction VII), pp. 94-101, 1996.
[29] R. K. Jain and T. Stylianopoulos, "Delivering nanomedicine to solid tumors," *Nat Rev Clin Oncol,* vol. 7, pp. 653-64, Nov 2010.
[30] K. Cho*, et al.*, "Therapeutic nanoparticles for drug delivery in cancer," *Clin Cancer Res,* vol. 14, pp. 1310-6, Mar 1 2008.
[31] M. F. Tang*, et al.*, "[Recent progress in nanotechnology for cancer therapy]," *Chin J Cancer,* vol. 29, pp. 775-80, Sep 2010.
[32] R. Weissleder, "A clearer vision for in vivo imaging," *Nat Biotechnol,* vol. 19, pp. 316-7, Apr 2001.
[33] S. Shen*, et al.*, "Targeting mesoporous silica-encapsulated gold nanorods for chemo-photothermal therapy with near-infrared radiation," *Biomaterials,* vol. 34, pp. 3150-8, Apr 2013.
[34] F. Ren*, et al.*, "Gold Nanorods Carrying Paclitaxel for Photothermal-Chemotherapy of Cancer," *Bioconjug Chem,* Feb 12 2013.
[35] P. J. Chen*, et al.*, "A novel multifunctional nano-platform with enhanced anti-cancer and photoacoustic imaging modalities using gold-nanorod-filled silica nanobeads," *Chem Commun (Camb),* vol. 49, pp. 892-4, Jan 30 2013.
[36] T. Fernandez Cabada*, et al.*, "Induction of cell death in a glioblastoma line by hyperthermic therapy based on gold nanorods," *Int J Nanomedicine,* vol. 7, pp. 1511-23, 2012.
[37] Z. Zhang*, et al.*, "Mesoporous silica-coated gold nanorods as a light-mediated multifunctional theranostic platform for cancer treatment," *Advanced Materials,* vol. 24, pp. 1418-23, Mar 15 2012.
[38] X. Huang*, et al.*, "Cancer cell imaging and photothermal therapy in the near-infrared region by using gold nanorods," *J Am Chem Soc,* vol. 128, pp. 2115-20, Feb 15 2006.
[39] R. Guo*, et al.*, "Multifunctional nanocarriers for cell imaging, drug delivery, and near-IR photothermal therapy," *Langmuir,* vol. 26, pp. 5428-34, Apr 20 2010.
[40] J. Choi*, et al.*, "Targetable gold nanorods for epithelial cancer therapy guided by near-IR absorption imaging," *Small,* vol. 8, pp. 746-53, Mar 12 2012.
[41] B. Jang*, et al.*, "Gold nanorods for target selective SPECT/CT imaging and photothermal therapy in vivo," *Quant Imaging Med Surg,* vol. 2, pp. 1-11, Mar 2012.

[42] W. S. Kuo*, et al.*, "Gold nanomaterials conjugated with indocyanine green for dual-modality photodynamic and photothermal therapy," *Biomaterials,* vol. 33, pp. 3270-8, Apr 2012.
[43] Y. Akiyama*, et al.*, "Conversion of rod-shaped gold nanoparticles to spherical forms and their effect on biodistribution in tumor-bearing mice," *Nanoscale Research Letters,* vol. 7, p. 565, 2012.
[44] S. Ghosh*, et al.*, "Increased Heating Efficiency and Selective Thermal Ablation of Malignant Tissue with DNA-Encased Multiwalled Carbon Nanotubes," *Acs Nano,* vol. 3, pp. 2667-2673, Sep 2009.
[45] A. Burke*, et al.*, "Long-term survival following a single treatment of kidney tumors with multiwalled carbon nanotubes and near-infrared radiation," *Proceedings of the National Academy of Sciences of the United States of America,* vol. 106, pp. 12897-12902, Aug 4 2009.
[46] N. Khlebtsov and L. Dykman, "Biodistribution and toxicity of engineered gold nanoparticles: a review of in vitro and in vivo studies," *Chem Soc Rev,* vol. 40, pp. 1647-71, Mar 2011.
[47] B. Fadeel and A. E. Garcia-Bennett, "Better safe than sorry: Understanding the toxicological properties of inorganic nanoparticles manufactured for biomedical applications," *Adv Drug Deliv Rev,* vol. 62, pp. 362-74, Mar 8 2010.
[48] A. Kunzmann*, et al.*, "Toxicology of engineered nanomaterials: focus on biocompatibility, biodistribution and biodegradation," *Biochim Biophys Acta,* vol. 1810, pp. 361-73, Mar 2011.
[49] S. T. Yang*, et al.*, "Long-term accumulation and low toxicity of single-walled carbon nanotubes in intravenously exposed mice," *Toxicol Lett,* vol. 181, pp. 182-9, Oct 1 2008.
[50] M. Ema*, et al.*, "Reproductive and developmental toxicity studies of manufactured nanomaterials," *Reprod Toxicol,* vol. 30, pp. 343-52, Nov 2010.
[51] M. J. Rybak-Smith and R. B. Sim, "Complement activation by carbon nanotubes," *Adv Drug Deliv Rev,* vol. 63, pp. 1031-41, Sep 16 2011.
[52] H. J. Johnston*, et al.*, "A review of the in vivo and in vitro toxicity of silver and gold particulates: particle attributes and biological mechanisms responsible for the observed toxicity," *Crit Rev Toxicol,* vol. 40, pp. 328-46, Apr 2010.
[53] G. B. Qu*, et al.*, "The effect of multiwalled carbon nanotube agglomeration on their accumulation in and damage to organs in mice," *Carbon,* vol. 47, pp. 2060-2069, Jul 2009.
[54] S. Link*, et al.*, "Laser photothermal melting and fragmentation of gold nanorods: Energy and laser pulse-width dependence," *Journal of Physical Chemistry A,* vol. 103, pp. 1165-1170, Mar 4 1999.
[55] S. Link*, et al.*, "Laser-induced shape changes of colloidal gold nanorods using femtosecond and nanosecond laser pulses," *Journal of Physical Chemistry B,* vol. 104, pp. 6152-6163, Jul 6 2000.
[56] S. Link*, et al.*, "How does a gold nanorod melt?," *Journal of Physical Chemistry B,* vol. 104, pp. 7867-7870, Aug 24 2000.
[57] P. V. Kamat, "Photophysical, photochemical and photocatalytic aspects of metal nanoparticles," *Journal of Physical Chemistry B,* vol. 106, pp. 7729-7744, Aug 15 2002.
[58] D. Werner and S. Hashimoto, "Controlling the Pulsed-Laser-Induced Size Reduction of Au and Ag Nanoparticles via Changes in the External Pressure, Laser Intensity, and Excitation Wavelength," *Langmuir,* vol. 29, pp. 1295-302, Jan 29 2013.

[59] J. Park*, et al.*, "Two-photon-induced photoluminescence imaging of tumors using near-infrared excited gold nanoshells," *Optics Express,* vol. 16, pp. 1590-9, Feb 4 2008.
[60] L. Feng*, et al.*, "Conjugated polymer nanoparticles: preparation, properties, functionalization and biological applications," *Chem Soc Rev,* vol. 42, pp. 6620-33, Aug 21 2013.
[61] A. J. Heeger, "Semiconducting and Metallic Polymers: The Fourth Generation of Polymeric Materials (Nobel Lecture) Copyright(c) The Nobel Foundation 2001. We thank the Nobel Foundation, Stockholm, for permission to print this lecture," *Angew Chem Int Ed Engl,* vol. 40, pp. 2591-2611, Jul 16 2001.
[62] J. Yang*, et al.*, "Convertible Organic Nanoparticles for Near-Infrared Photothermal Ablation of Cancer Cells," *Angewandte Chemie-International Edition,* vol. 50, pp. 441-444, 2011.
[63] Z. Zha*, et al.*, "Uniform Polypyrrole Nanoparticles with High Photothermal Conversion Efficiency for Photothermal Ablation of Cancer Cells," *Advanced Materials,* Nov 12 2012.
[64] K. Yang*, et al.*, "In Vitro and In Vivo Near-Infrared Photothermal Therapy of Cancer Using Polypyrrole Organic Nanoparticles," *Advanced Materials,* vol. 24, pp. 5586-5592, Nov 2 2012.
[65] M. Chen*, et al.*, "Polypyrrole nanoparticles for high-performance in vivo near-infrared photothermal cancer therapy," *Chem Commun (Camb),* vol. 48, pp. 8934-6, Sep 14 2012.
[66] K. Yang*, et al.*, "In vitro and in vivo near-infrared photothermal therapy of cancer using polypyrrole organic nanoparticles," *Advanced Materials,* vol. 24, pp. 5586-92, Nov 2 2012.
[67] L. Cheng*, et al.*, "Organic Stealth Nanoparticles for Highly Effective in Vivo Near-Infrared Photothermal Therapy of Cancer," *Acs Nano,* vol. 6, pp. 5605-5613, Jun 2012.
[68] C. M. Macneill*, et al.*, "Low Band Gap Donor-Acceptor Conjugated Polymer Nanoparticles and their NIR-mediated Thermal Ablation of Cancer Cells," *Macromol Biosci,* Oct 5 2012.
[69] E. E. Havinga*, et al.*, "A New Class of Small Band-Gap Organic Polymer Conductors," *Polymer Bulletin,* vol. 29, pp. 119-126, Aug 1992.
[70] E. E. Havinga*, et al.*, "Alternate Donor-Acceptor Small-Band-Gap Semiconducting Polymers - Polysquaraines and Polycroconaines," *Synthetic Metals,* vol. 55, pp. 299-306, Mar 15 1993.
[71] L. T. Cheng*, et al.*, "Coupling the Level-Set Method with Molecular Mechanics for Variational Implicit Solvation of Nonpolar Molecules," *Journal of Chemical Theory and Computation,* vol. 5, pp. 257-266, Feb 2009.
[72] S. W. Thomas*, et al.*, "Chemical sensors based on amplifying fluorescent conjugated polymers," *Chemical Reviews,* vol. 107, pp. 1339-1386, Apr 2007.
[73] Y. H. Chan*, et al.*, "Copper(II) and iron(II) ion sensing with semiconducting polymer dots," *Chemical Communications,* vol. 47, pp. 2820-2822, 2011.
[74] M. R. Abidian*, et al.*, "Conducting-polymer nanotubes improve electrical properties, mechanical adhesion, neural attachment, and neurite outgrowth of neural electrodes," *Small,* vol. 6, pp. 421-9, Feb 5 2010.
[75] K. Li*, et al.*, "Generic Strategy of Preparing Fluorescent Conjugated-Polymer-Loaded Poly(DL-lactide-co-Glycolide) Nanoparticles for Targeted Cell Imaging," *Advanced Functional Materials,* vol. 19, pp. 3535-3542, Nov 23 2009.
[76] C. A. Traina*, et al.*, "Design and Synthesis of Monofunctionalized, Water-Soluble Conjugated Polymers for Biosensing and Imaging Applications," *Journal of the American Chemical Society,* vol. 133, pp. 12600-12607, Aug 17 2011.

[77] B. S. Gaylord, *et al.*, "DNA detection using water-soluble conjugated polymers and peptide nucleic acid probes," *Proceedings of the National Academy of Sciences of the United States of America,* vol. 99, pp. 10954-10957, Aug 20 2002.
[78] C. Wu, *et al.*, "Bioconjugation of ultrabright semiconducting polymer dots for specific cellular targeting," *J Am Chem Soc,* vol. 132, pp. 15410-7, Nov 3 2010.
[79] K. Li and B. Liu, "Polymer encapsulated conjugated polymer nanoparticles for fluorescence bioimaging," *Journal of Materials Chemistry,* vol. 22, pp. 1257-1264, 2012.
[80] C. Wu and D. T. Chiu, "Highly fluorescent semiconducting polymer dots for biology and medicine," *Angew Chem Int Ed Engl,* vol. 52, pp. 3086-109, Mar 11 2013.
[81] D. Ding, *et al.*, "Bright far-red/near-infrared conjugated polymer nanoparticles for in vivo bioimaging," *Small,* vol. 9, pp. 3093-102, Sep 23 2013.
[82] C. Wu, *et al.*, "Multicolor conjugated polymer dots for biological fluorescence imaging," *Acs Nano,* vol. 2, pp. 2415-23, Nov 25 2008.
[83] C. Wu, *et al.*, "Preparation and encapsulation of highly fluorescent conjugated polymer nanoparticles," *Langmuir,* vol. 22, pp. 2956-60, Mar 28 2006.
[84] C. F. Wu, *et al.*, "Preparation and encapsulation of highly fluorescent conjugated polymer nanoparticles," *Langmuir,* vol. 22, pp. 2956-2960, Mar 28 2006.
[85] D. Tuncel and H. V. Demir, "Conjugated polymer nanoparticles," *Nanoscale,* vol. 2, pp. 484-94, Apr 2010.
[86] J. Yu, *et al.*, "Nanoscale 3D tracking with conjugated polymer nanoparticles," *J Am Chem Soc,* vol. 131, pp. 18410-4, Dec 30 2009.
[87] J. H. Moon, *et al.*, "Live-cell-permeable poly (p-phenylene ethynylene)," *Angewandte Chemie-International Edition,* vol. 46, pp. 8223-8225, 2007.
[88] C. F. Wu, *et al.*, "Bioconjugation of Ultrabright Semiconducting Polymer Dots for Specific Cellular Targeting," *Journal of the American Chemical Society,* vol. 132, pp. 15410-15417, Nov 3 2010.
[89] S. Kim, *et al.*, "Conjugated polymer nanoparticles for biomedical in vivo imaging," *Chemical Communications,* vol. 46, pp. 1617-1619, 2010.
[90] K. Li, *et al.*, "Conjugated Polymer Based Nanoparticles as Dual-Modal Probes for Targeted In Vivo Fluorescence and Magnetic Resonance Imaging," *Advanced Functional Materials,* vol. 22, pp. 3107-3115, Aug 7 2012.
[91] C. F. Wu, *et al.*, "Design of Highly Emissive Polymer Dot Bioconjugates for In Vivo Tumor Targeting," *Angewandte Chemie-International Edition,* vol. 50, pp. 3430-3434, 2011.
[92] X. H. Gao, *et al.*, "In vivo molecular and cellular imaging with quantum dots," *Current Opinion in Biotechnology,* vol. 16, pp. 63-72, Feb 2005.
[93] T. Jamieson, *et al.*, "Biological applications of quantum dots," *Biomaterials,* vol. 28, pp. 4717-4732, Nov 2007.
[94] L. P. Fernando, *et al.*, "Mechanism of cellular uptake of highly fluorescent conjugated polymer nanoparticles," *Biomacromolecules,* vol. 11, pp. 2675-82, Oct 11 2010.
[95] K. Li and B. Liu, "Polymer-encapsulated organic nanoparticles for fluorescence and photoacoustic imaging," *Chem Soc Rev,* vol. 43, pp. 6570-97, Sep 21 2014.
[96] S. M. Janib, *et al.*, "Imaging and drug delivery using theranostic nanoparticles," *Advanced Drug Delivery Reviews,* vol. 62, pp. 1052-1063, Aug 30 2010.
[97] J. Xie, *et al.*, "Nanoparticle-based theranostic agents," *Advanced Drug Delivery Reviews,* vol. 62, pp. 1064-1079, 2010.
[98] R. Bardhan, *et al.*, "Theranostic nanoshells: from probe design to imaging and treatment of cancer," *Acc Chem Res,* vol. 44, pp. 936-46, Oct 18 2011.

[99] C. M. MacNeill, *et al.*, "Soft Template Synthesis of Donor-Acceptor Conjugated Polymer Nanoparticles: Structural Effects, Stability, and Photothermal Studies," *Journal of Polymer Science Part a-Polymer Chemistry,* vol. 52, pp. 1622-1632, Jun 1 2014.

[100] S. Lal, *et al.*, "Nanoshell-Enabled Photothermal Cancer Therapy: Impending Clinical Impact," *Accounts of Chemical Research,* vol. 41, pp. 1842-1851, Dec 2008.

[101] A. M. Gobin, *et al.*, "Near-infrared resonant nanoshells for combined optical imaging and photothermal cancer therapy," *Nano Letters,* vol. 7, pp. 1929-1934, Jul 2007.

[102] L. R. Hirsch, *et al.*, "Nanoshell-mediated near-infrared thermal therapy of tumors under magnetic resonance guidance," *Proceedings of the National Academy of Sciences of the United States of America,* vol. 100, pp. 13549-13554, Nov 11 2003.

[103] H. C. Huang, *et al.*, "Inorganic nanoparticles for cancer imaging and therapy," *Journal of Controlled Release,* vol. 155, pp. 344-57, Nov 7 2011.

[104] S. J. Son, *et al.*, "Inorganic hollow nanoparticles and nanotubes in nanomedicine Part 2: Imaging, diagnostic, and therapeutic applications," *Drug Discov Today,* vol. 12, pp. 657-63, Aug 2007.

[105] H. K. Moon, *et al.*, "In Vivo Near-Infrared Mediated Tumor Destruction by Photothermal Effect of Carbon Nanotubes," *Acs Nano,* vol. 3, pp. 3707-3713, Nov 2009.

[106] A. Burke, *et al.*, "Long-term survival following a single treatment of kidney tumors with multiwalled carbon nanotubes and near-infrared radiation. ," *Proc Natl Acad Sci,* 2009.

[107] J. T. Robinson, *et al.*, "Ultrasmall Reduced Graphene Oxide with High Near-Infrared Absorbance for Photothermal Therapy," *Journal of the American Chemical Society,* vol. 133, pp. 6825-6831, May 4 2011.

[108] L. Cheng, *et al.*, "Organic stealth nanoparticles for highly effective in vivo near-infrared photothermal therapy of cancer," *Acs Nano,* vol. 6, pp. 5605-13, Jun 26 2012.

[109] J. H. Hou, *et al.*, "Poly [4,4-bis(2-ethylhexyl)cyclopenta [2, 1-b;3,4-b '] dithiophene-2,6-diyl-alt-2,1,3-benzoselenadiazole-4,7-diyl], a New Low Band Gap Polymer in Polymer Solar Cells," *Journal of Physical Chemistry C,* vol. 113, pp. 1601-1605, Jan 29 2009.

[110] Z. Zhu, *et al.*, "Panchromatic conjugated polymers containing alternating donor/acceptor units for photovoltaic applications," *Macromolecules,* vol. 40, pp. 1981-1986, 2007.

[111] I. H. Jung, *et al.*, "Synthesis and Characterization of Cyclopentadithiophene-Based Low Bandgap Copolymers Containing Electron-Deficient Benzoselenadiazole Derivatives for Photovoltaic Devices," *Journal of Polymer Science Part a-Polymer Chemistry,* vol. 48, pp. 1423-1432, 2010.

[112] X. Z. Li, *et al.*, "Synthesis and properties of novel poly(p-phenylenevinylene) copolymers for near-infrared emitting diodes," *European Polymer Journal,* vol. 41, pp. 2923-2933, 2005.

[113] Y. Tsubata, *et al.*, "Single-Component Organic Conductors Based on Neutral Radicals Containing the Pyrazino-Tcnq Skeleton," *Journal of Organic Chemistry,* vol. 57, pp. 6749-6755, 1992.

[114] R. C. Coffin, *et al.*, "Streamlined microwave-assisted preparation of narrow-bandgap conjugated polymers for high-performance bulk heterojunction solar cells," *Nature Chemistry,* vol. 1, pp. 657-661, 2009.

[115] B. White, *et al.*, "Zeta-potential measurements of surfactant-wrapped individual single-walled carbon nanotubes," *Journal of Physical Chemistry C,* vol. 111, pp. 13684-13690, Sep 20 2007.

[116] T. K. Jain, *et al.*, "Iron oxide nanoparticles for sustained delivery of anticancer agents," *Molecular Pharmaceutics,* vol. 2, pp. 194-205, May-Jun 2005.

[117] M. M. Yallapu*, et al.*, "Multi-functional magnetic nanoparticles for magnetic resonance imaging and cancer therapy," *Biomaterials,* vol. 32, pp. 1890-1905, Mar 2011.
[118] J. Hillhouse*, et al.*, "Effect of Seasonal Affective Disorder and Pathological Tanning Motives on Efficacy of an Appearance-Focused Intervention to Prevent Skin Cancer," *Archives of Dermatology,* vol. 146, pp. 485-491, May 2010.
[119] O. M. Merkel*, et al.*, "Nonviral siRNA Delivery to the Lung: Investigation of PEG-PEI Polyplexes and Their In Vivo Performance," *Molecular Pharmaceutics,* vol. 6, pp. 1246-1260, Jul-Aug 2009.
[120] D. Sharma*, et al.*, "Malignant transformation of a pilonidal sinus," *Surgery,* vol. 145, pp. 243-244, Feb 2009.
[121] A. V. Kabanov*, et al.*, "Pluronic((R)) block copolymers for overcoming drug resistance in cancer," *Advanced Drug Delivery Reviews,* vol. 54, pp. 759-779, Sep 13 2002.
[122] J. J. Escobar-Chavez*, et al.*, "Applications of thermoreversible pluronic F-127 gels in pharmaceutical formulations," *Journal of Pharmacy and Pharmaceutical Sciences,* vol. 9, pp. 339-358, Sep-Dec 2006.
[123] A. H. El-Kamel, "In vitro and in vivo evaluation of Pluronic F127-based ocular delivery system for timolol maleate," *International Journal of Pharmaceutics,* vol. 241, pp. 47-55, Jul 8 2002.
[124] M. G. Ewend*, et al.*, "Brain metastases," *Curr Treat Options Oncol,* vol. 2, pp. 537-47, Dec 2001.
[125] X. Cheng and M. C. Hung, "Breast cancer brain metastases," *Cancer Metastasis Rev,* vol. 26, pp. 635-43, Dec 2007.
[126] J. Engel*, et al.*, "Determinants and prognoses of locoregional and distant progression in breast cancer," *Int J Radiat Oncol Biol Phys,* vol. 55, pp. 1186-95, Apr 1 2003.
[127] A. H. Paterson*, et al.*, "Brain metastases in breast cancer patients receiving adjuvant chemotherapy," *Cancer,* vol. 49, pp. 651-4, Feb 15 1982.
[128] C. Lu-Emerson and A. F. Eichler, "Brain metastases," *Continuum (Minneap Minn),* vol. 18, pp. 295-311, Apr 2012.
[129] R. A. Patchell*, et al.*, "A randomized trial of surgery in the treatment of single metastases to the brain," *N Engl J Med,* vol. 322, pp. 494-500, Feb 22 1990.
[130] Y. Cheng*, et al.*, "Blood-Brain Barrier Permeable Gold Nanoparticles: An Efficient Delivery Platform for Enhanced Malignant Glioma Therapy and Imaging," *Small,* vol. 10, pp. 5137-5150, 2014.
[131] M. Tsang*, et al.*, "Effects of increasing carbon nanofiber density in polyurethane composites for inhibiting bladder cancer cell functions," *Tissue Eng Part A,* vol. 17, pp. 1879-89, Jul 2011.
[132] P. Cowin*, et al.*, "Cadherins and catenins in breast cancer," *Curr Opin Cell Biol,* vol. 17, pp. 499-508, Oct 2005.
[133] C. M. Macneill*, et al.*, "Low Band Gap Donor-Acceptor Conjugated Polymer Nanoparticles and their NIR-mediated Thermal Ablation of Cancer Cells," *Macromol Biosci,* vol. 13, pp. 28-34, Jan 2013.
[134] A. Zlotnik*, et al.*, "Homeostatic chemokine receptors and organ-specific metastasis," *Nat Rev Immunol,* vol. 11, pp. 597-606, Sep 2011.
[135] B. Fingleton, "Molecular targets in metastasis: lessons from genomic approaches," *Cancer Genomics Proteomics,* vol. 4, pp. 211-21, May-Jun 2007.
[136] J. M. Wang*, et al.*, "Chemokines and their role in tumor growth and metastasis," *J Immunol Methods,* vol. 220, pp. 1-17, Nov 1 1998.

[137] M. J. Jung*, et al.*, "Upregulation of CXCR4 is functionally crucial for maintenance of stemness in drug-resistant non-small cell lung cancer cells," *Oncogene,* Feb 27 2012.
[138] A. Dubrovska*, et al.*, "CXCR4 expression in prostate cancer progenitor cells," *PLoS One,* vol. 7, p. e31226, 2012.
[139] M. Ehtesham*, et al.*, "CXCR4 mediates the proliferation of glioblastoma progenitor cells," *Cancer Lett,* vol. 274, pp. 305-12, Feb 18 2009.
[140] Y. M. Li*, et al.*, "Upregulation of CXCR4 is essential for HER2-mediated tumor metastasis," *Cancer Cell,* vol. 6, pp. 459-69, Nov 2004.
[141] N. T. Holm*, et al.*, "Elevated levels of chemokine receptor CXCR4 in HER-2 negative breast cancer specimens predict recurrence," *J Surg Res,* vol. 141, pp. 53-9, Jul 2007.
[142] Q. D. Chu*, et al.*, "High chemokine receptor CXCR4 level in triple negative breast cancer specimens predicts poor clinical outcome," *J Surg Res,* vol. 159, pp. 689-95, Apr 2010.
[143] Q. D. Chu*, et al.*, "Chemokine receptor CXCR4 overexpression predicts recurrence for hormone receptor-positive, node-negative breast cancer patients," *Surgery,* vol. 149, pp. 193-9, Feb 2011.
[144] E. Blot*, et al.*, "CXCR4 membrane expression in node-negative breast cancer," *Breast J,* vol. 14, pp. 268-74, May-Jun 2008.
[145] N. Cabioglu*, et al.*, "Expression of growth factor and chemokine receptors: new insights in the biology of inflammatory breast cancer," *Ann Oncol,* vol. 18, pp. 1021-9, Jun 2007.
[146] D. J. Hiller*, et al.*, "CXCR4 as a predictive marker for locally advanced breast cancer post-neoadjuvant therapy," *J Surg Res,* vol. 166, pp. 14-8, Mar 2011.
[147] D. J. Hiller*, et al.*, "Chemokine receptor CXCR4 level in primary tumors independently predicts outcome for patients with locally advanced breast cancer," *Surgery,* vol. 150, pp. 459-65, Sep 2011.
[148] C. Braun and S. Smirnov, "Why is water blue," *J.Chemical Education,* vol. 70, p. 612, 1993.
[149] C. International Agency for Research on, World Health Organization, 150 Cours Albert Thomas, 69372 Lyon CEDEX 08, France2002.
[150] T. Kerner*, et al.*, "Monitoring arterial blood pressure during whole body hyperthermia," *Acta Anaesthesiol Scand,* vol. 46, pp. 561-6, May 2002.
[151] P. Wust*, et al.*, "Hyperthermia in combined treatment of cancer," *Lancet Oncology,* vol. 3, pp. 487-97, Aug 2002.
[152] S. Goff*, et al.*, "Cancer genetics," *European Journal of Cancer Care,* vol. 19, pp. 424-424, Jul 2010.
[153] F. Mohamed*, et al.*, "Thermal enhancement of new chemotherapeutic agents at moderate hyperthermia," *Annals of Surgical Oncology,* vol. 10, pp. 463-468, 2003.
[154] P. H. Sugarbaker*, et al.*, "Update on chemotherapeutic agents utilized for perioperative intraperitoneal chemotherapy," *Oncologist,* vol. 10, pp. 112-122, 2005.
[155] N. G. Portney and M. Ozkan, "Nano-oncology: drug delivery, imaging, and sensing," *Analytical and Bioanalytical Chemistry,* vol. 384, pp. 620-630, 2006.
[156] L. H. Reddy, "Drug delivery to tumours: recent strategies," *Journal of Pharmacy and Pharmacology,* vol. 57, pp. 1231-1242, 2005.
[157] D. B. Shenoy and M. A. Amiji, "Poly(ethylene oxide)-modified poly(epsilon-caprolactone) nanoparticles for targeted delivery of tamoxifen in breast cancer," *International Journal of Pharmaceutics,* vol. 293, pp. 261-270, 2005.
[158] J. K. Robinson*, et al.*, "Skin cancer prevention education for kidney transplant recipients: a systematic evaluation of Internet sites," *Progress in Transplantation,* vol. 20, pp. 344-349, Dec 2010.

[159] G. U. Dachs*, et al.*, "A profile of prognostic and molecular factors in European and Maori breast cancer patients," *BMC Cancer,* vol. 10, Oct 10 2010.
[160] C. L. Marshall*, et al.*, "Establishment of a minimally invasive surgery program Leads to decreased inpatient cost of care in veterans with colon cancer," *American Journal of Surgery,* vol. 200, pp. 632-635, Nov 2010.
[161] B. A. de Valois*, et al.*, "Using Traditional Acupuncture for Breast Cancer-Related Hot Flashes and Night Sweats," *Journal of Alternative and Complementary Medicine,* vol. 16, pp. 1047-1057, Oct 2010.
[162] S. A. Wells*, et al.*, "Vandetanib in Locally Advanced or Metastatic Medullary Thyroid Cancer (Mtc): A Randomized, Double-Blind Phase Iii Trial (Zeta)," *Annals of Oncology,* vol. 21, pp. 315-315, Oct 2010.
[163] S. Link and M. A. El-Sayed, "Shape and size dependence of radiative, non-radiative and photothermal properties of gold nanocrystals," *International Reviews in Physical Chemistry,* vol. 19, pp. 409-453, Jul-Sep 2000.
[164] S. Link and M. A. El-Sayed, "Size and temperature dependence of the plasmon absorption of colloidal gold nanoparticles," *Journal of Physical Chemistry B,* vol. 103, pp. 4212-4217, May 27 1999.
[165] L. R. Hirsch*, et al.*, "Metal nanoshells," *Ann Biomed Eng,* vol. 34, pp. 15-22, Jan 2006.
[166] M. Rycenga*, et al.*, "Controlling the synthesis and assembly of silver nanostructures for plasmonic applications," *Chemical Reviews,* vol. 111, pp. 3669-712, Jun 8 2011.
[167] E. C. Le Ru and P. G. Etchegoin, *Principles of surface-enhanced Raman spectroscopy : and related plasmonic effects*, 1st ed. Amsterdam ; Boston: Elsevier, 2009.
[168] M. Ahamed*, et al.*, "Silver nanoparticle applications and human health," *Clin Chim Acta,* vol. 411, pp. 1841-8, Dec 14 2010.
[169] P. Jena*, et al.*, "Toxicity and antibacterial assessment of chitosan-coated silver nanoparticles on human pathogens and macrophage cells," *Int J Nanomedicine,* vol. 7, pp. 1805-18, 2012.
[170] R. Shukla*, et al.*, "Biocompatibility of gold nanoparticles and their endocytotic fate inside the cellular compartment: a microscopic overview," *Langmuir,* vol. 21, pp. 10644-54, Nov 8 2005.
[171] S. Link*, et al.*, "Simulation of the optical absorption spectra of gold nanorods as a function of their aspect ratio and the effect of the medium dielectric constant," *Journal of Physical Chemistry B,* vol. 103, pp. 3073-3077, Apr 22 1999.
[172] B. Nikoobakht and M. A. El-Sayed, "Preparation and growth mechanism of gold nanorods (NRs) using seed-mediated growth method," *Chemistry of Materials,* vol. 15, pp. 1957-1962, May 20 2003.
[173] X. Jiang*, et al.*, "Thiol-frozen shape evolution of triangular silver nanoplates," *Langmuir,* vol. 23, pp. 2218-23, Feb 13 2007.
[174] C. Loo*, et al.*, "Nanoshell-enabled photonics-based imaging and therapy of cancer," *Technology in Cancer Research & Treatment,* vol. 3, pp. 33-40, Feb 2004.
[175] H. P. Liang*, et al.*, "Gold hollow nanospheres: tunable surface plasmon resonance controlled by interior-cavity sizes," *Journal of Physical Chemistry B,* vol. 109, pp. 7795-800, Apr 28 2005.
[176] Y. Sun*, et al.*, "Synthesis and optical properties of nanorattles and multiple-walled nanoshells/nanotubes made of metal alloys," *J Am Chem Soc,* vol. 126, pp. 9399-406, Aug 4 2004.
[177] J. Y. Chen*, et al.*, "Gold nanocages: Engineering their structure for biomedical applications," *Advanced Materials,* vol. 17, pp. 2255-2261, Sep 16 2005.

[178] J. Chen*, et al.*, "Immuno gold nanocages with tailored optical properties for targeted photothermal destruction of cancer cells," *Nano Lett,* vol. 7, pp. 1318-22, May 2007.
[179] J. Chen*, et al.*, "Optical properties of Pd-Ag and Pt-Ag nanoboxes synthesized via galvanic replacement reactions," *Nano Lett,* vol. 5, pp. 2058-62, Oct 2005.
[180] W. He*, et al.*, "Formation of AgPt alloy nanoislands via chemical etching with tunable optical and catalytic properties," *Langmuir,* vol. 26, pp. 4443-8, Mar 16 2010.
[181] R. G. Sanedrin*, et al.*, "Seed-mediated growth of bimetallic prisms," *Advanced Materials,* vol. 17, pp. 1027-+, Apr 18 2005.
[182] F. Hubenthal*, et al.*, "Optical properties and ultrafast electron dynamics in gold-silver alloy and core-shell nanoparticles," *Applied Physics B-Lasers and Optics,* vol. 93, pp. 39-45, Oct 2008.
[183] Z. Y. Li*, et al.*, "Direct imaging of core-shell structure in silver-gold bimetallic nanoparticles," *Applied Physics Letters,* vol. 87, Dec 12 2005.
[184] Y. W. Cao*, et al.*, "DNA-modified core-shell Ag/Au nanoparticles," *Journal of the American Chemical Society,* vol. 123, pp. 7961-7962, Aug 15 2001.
[185] F. Hubenthal*, et al.*, "Tuning the surface plasmon resonance by preparation of gold-core/silver-shell and alloy nanoparticles," *European Physical Journal D,* vol. 34, pp. 165-168, Jul 2005.
[186] J. P. Abid*, et al.*, "Pure surface plasmon resonance enhancement of the first hyperpolarizability of gold core-silver shell nanoparticles," *Journal of Chemical Physics,* vol. 121, pp. 12577-12582, Dec 22 2004.
[187] P. R. Selvakannan*, et al.*, "Synthesis of aqueous Au core-Ag shell nanoparticles using tyrosine as a pH-dependent reducing agent and assembling phase-transferred silver nanoparticles at the air-water interface," *Langmuir,* vol. 20, pp. 7825-7836, Aug 31 2004.
[188] S. Mandal*, et al.*, "Keggin ions as UV-switchable reducing agents in the synthesis of Au core-Ag shell nanoparticles," *Journal of the American Chemical Society,* vol. 125, pp. 8440-8441, Jul 16 2003.
[189] L. Lu*, et al.*, "Core-shell gold/silver nanoparticles: Synthesis and optical properties," *J Colloid Interface Sci,* vol. 392, pp. 90-5, Feb 15 2013.
[190] K. L. McGilvray*, et al.*, "Photochemical strategies for the seed-mediated growth of gold and gold-silver nanoparticles," *Langmuir,* vol. 28, pp. 16148-55, Nov 20 2012.
[191] L. Chen*, et al.*, "Characterization of Ag/Pt core-shell nanoparticles by UV-vis absorption, resonance light-scattering techniques," *Spectrochimica Acta Part a-Molecular and Biomolecular Spectroscopy,* vol. 68, pp. 484-490, Nov 2007.
[192] N. V. Long*, et al.*, "Synthesis and characterization of Pt-Pd nanoparticles with core-shell morphology: Nucleation and overgrowth of the Pd shells on the as-prepared and defined Pt seeds," *Journal of Alloys and Compounds,* vol. 509, pp. 7702-7709, Jul 21 2011.
[193] H. S. Choi*, et al.*, "Renal clearance of quantum dots," *Nat Biotechnol,* vol. 25, pp. 1165-70, Oct 2007.
[194] A. Pluen*, et al.*, "Role of tumor-host interactions in interstitial diffusion of macromolecules: cranial vs. subcutaneous tumors," *Proc Natl Acad Sci U S A,* vol. 98, pp. 4628-33, Apr 10 2001.
[195] S. Ramanujan*, et al.*, "Diffusion and convection in collagen gels: implications for transport in the tumor interstitium," *Biophys J,* vol. 83, pp. 1650-60, Sep 2002.

[196] J. Rejman, *et al.*, "Size-dependent internalization of particles via the pathways of clathrin- and caveolae-mediated endocytosis," *Biochem J,* vol. 377, pp. 159-69, Jan 1 2004.
[197] W. Jiang, *et al.*, "Nanoparticle-mediated cellular response is size-dependent," *Nat Nanotechnol,* vol. 3, pp. 145-50, Mar 2008.
[198] B. D. Chithrani and W. C. Chan, "Elucidating the mechanism of cellular uptake and removal of protein-coated gold nanoparticles of different sizes and shapes," *Nano Lett,* vol. 7, pp. 1542-50, Jun 2007.
[199] S. Zhang, *et al.*, "Size-Dependent Endocytosis of Nanoparticles," *Advanced Materials,* vol. 21, pp. 419-424, 2009.
[200] Y. Wang, *et al.*, "Evaluating the pharmacokinetics and in vivo cancer targeting capability of Au nanocages by positron emission tomography imaging," *Acs Nano,* vol. 6, pp. 5880-8, Jul 24 2012.
[201] G. Adriani, *et al.*, "The preferential targeting of the diseased microvasculature by disk-like particles," *Biomaterials,* vol. 33, pp. 5504-13, Aug 2012.
[202] Z. G. Yue, *et al.*, "Surface charge affects cellular uptake and intracellular trafficking of chitosan-based nanoparticles," *Biomacromolecules,* vol. 12, pp. 2440-6, Jul 11 2011.
[203] G. Storm, *et al.*, "Surface Modification of Nanoparticles to Oppose Uptake by the Mononuclear Phagocyte System," *Advanced Drug Delivery Reviews,* vol. 17, pp. 31-48, Oct 1995.
[204] A. L. Klibanov, *et al.*, "Amphipathic Polyethyleneglycols Effectively Prolong the Circulation Time of Liposomes," *Febs Letters,* vol. 268, pp. 235-237, Jul 30 1990.
[205] M. E. Akerman, *et al.*, "Nanocrystal targeting in vivo," *Proc Natl Acad Sci U S A,* vol. 99, pp. 12617-21, Oct 1 2002.
[206] X. Chen and H. J. Schluesener, "Nanosilver: a nanoproduct in medical application," *Toxicol Lett,* vol. 176, pp. 1-12, Jan 4 2008.
[207] M. Rai, *et al.*, "Silver nanoparticles as a new generation of antimicrobials," *Biotechnol Adv,* vol. 27, pp. 76-83, Jan-Feb 2009.
[208] G. Sandri, *et al.*, "Wound dressings based on silver sulfadiazine solid lipid nanoparticles for tissue repairing," *Eur J Pharm Biopharm,* Dec 1 2012.
[209] D. Li, *et al.*, "Fabrication of new chitosan-based composite sponge containing silver nanoparticles and its antibacterial properties for wound dressing," *J Nanosci Nanotechnol,* vol. 11, pp. 4733-8, Jun 2011.
[210] L. Huang, *et al.*, "Synergistic combination of chitosan acetate with nanoparticle silver as a topical antimicrobial: efficacy against bacterial burn infections," *Antimicrob Agents Chemother,* vol. 55, pp. 3432-8, Jul 2011.
[211] S. Lu, *et al.*, "Construction, application and biosafety of silver nanocrystalline chitosan wound dressing," *Burns,* vol. 34, pp. 623-8, Aug 2008.
[212] P. Sanpui, *et al.*, "Induction of apoptosis in cancer cells at low silver nanoparticle concentrations using chitosan nanocarrier," *ACS Appl Mater Interfaces,* vol. 3, pp. 218-28, Feb 2011.
[213] S. Gurunathan, *et al.*, "Antiangiogenic properties of silver nanoparticles," *Biomaterials,* vol. 30, pp. 6341-50, Oct 2009.
[214] I. Sur, *et al.*, "Interaction of multi-functional silver nanoparticles with living cells," *Nanotechnology,* vol. 21, p. 175104, Apr 30 2010.
[215] S. C. Boca, *et al.*, "Chitosan-coated triangular silver nanoparticles as a novel class of biocompatible, highly effective photothermal transducers for in vitro cancer cell therapy," *Cancer Letters,* vol. 311, pp. 131-140, Dec 8 2011.

[216] F. Y. Cheng, *et al.*, "Comparative efficiencies of photothermal destruction of malignant cells using antibody-coated silica@Au nanoshells, hollow Au/Ag nanospheres and Au nanorods," *Nanotechnology,* vol. 20, p. 425104, Oct 21 2009.
[217] Y. F. Huang, *et al.*, "Selective photothermal therapy for mixed cancer cells using aptamer-conjugated nanorods," *Langmuir,* vol. 24, pp. 11860-5, Oct 21 2008.
[218] P. Yang, *et al.*, "Synthesis of multifunctional Ag@Au@phenol formaldehyde resin particles loaded with folic acids for photothermal therapy," *Chemistry,* vol. 18, pp. 9294-9, Jul 23 2012.
[219] X. M. Lu, *et al.*, "Fabrication of cubic nanocages and nanoframes by dealloying Au/Ag alloy nanoboxes with an aqueous etchant based on Fe(NO3)(3) or NH4OH," *Nano Letters,* vol. 7, pp. 1764-1769, Jun 2007.
[220] L. Au, *et al.*, "A quantitative study on the photothermal effect of immuno gold nanocages targeted to breast cancer cells," *Acs Nano,* vol. 2, pp. 1645-52, Aug 2008.
[221] J. Chen, *et al.*, "Gold nanocages as photothermal transducers for cancer treatment," *Small,* vol. 6, pp. 811-7, Apr 9 2010.
[222] L. Gao, *et al.*, "Hypocrellin-loaded gold nanocages with high two-photon efficiency for photothermal/photodynamic cancer therapy in vitro," *Acs Nano,* vol. 6, pp. 8030-40, Sep 25 2012.
[223] P. Shi, *et al.*, "pH-responsive NIR enhanced drug release from gold nanocages possesses high potency against cancer cells," *Chem Commun (Camb),* vol. 48, pp. 7640-2, Aug 7 2012.
[224] L. Dykman and N. Khlebtsov, "Gold nanoparticles in biomedical applications: recent advances and perspectives," *Chem Soc Rev,* vol. 41, pp. 2256-82, Mar 21 2012.
[225] L. C. Kennedy, *et al.*, "A new era for cancer treatment: gold-nanoparticle-mediated thermal therapies," *Small,* vol. 7, pp. 169-83, Jan 17 2011.
[226] S. Jain, *et al.*, "Gold nanoparticles as novel agents for cancer therapy," *Br J Radiol,* vol. 85, pp. 101-13, Feb 2012.
[227] M. Hu, *et al.*, "Gold nanostructures: engineering their plasmonic properties for biomedical applications," *Chem Soc Rev,* vol. 35, pp. 1084-94, Nov 2006.
[228] X. Huang, *et al.*, "Comparative study of photothermolysis of cancer cells with nuclear-targeted or cytoplasm-targeted gold nanospheres: continuous wave or pulsed lasers," *J Biomed Opt,* vol. 15, p. 058002, Sep-Oct 2010.
[229] D. K. Kirui, *et al.*, "Targeted near-IR hybrid magnetic nanoparticles for in vivo cancer therapy and imaging," *Nanomedicine,* Dec 6 2012.
[230] X. Qu, *et al.*, "Anti-CD30-targeted gold nanoparticles for photothermal therapy of L-428 Hodgkin's cell," *Int J Nanomedicine,* vol. 7, pp. 6095-103, 2012.
[231] D. K. Kirui, *et al.*, "Gold hybrid nanoparticles for targeted phototherapy and cancer imaging," *Nanotechnology,* vol. 21, p. 105105, Mar 12 2010.
[232] H. Mendoza-Nava, *et al.*, "Laser heating of gold nanospheres functionalized with octreotide: in vitro effect on HeLa cell viability," *Photomedicine and Laser Surgery,* vol. 31, pp. 17-22, Jan 2013.
[233] H. Shen, *et al.*, "Cooperative, nanoparticle-enabled thermal therapy of breast cancer," *Adv Healthc Mater,* vol. 1, pp. 84-9, Jan 11 2012.
[234] R. Fekrazad, *et al.*, "Treatment of oral squamous cell carcinoma using anti-HER2 immunonanoshells," *Int J Nanomedicine,* vol. 6, pp. 2749-55, 2011.
[235] E. S. Day, *et al.*, "Vascular-targeted photothermal therapy of an orthotopic murine glioma model," *Nanomedicine (Lond),* vol. 7, pp. 1133-48, Aug 2012.

[236] M. P. Melancon*, et al.*, "Near-infrared light modulated photothermal effect increases vascular perfusion and enhances polymeric drug delivery," *Journal of Controlled Release,* vol. 156, pp. 265-272, Dec 10 2011.
[237] H. A. Xie*, et al.*, "Integrin alpha(v)beta(3)-targeted gold nanoshells augment tumor vasculature-specific imaging and therapy," *International Journal of Nanomedicine,* vol. 6, pp. 259-269, 2011.
[238] C. Y. Wu*, et al.*, "A gold nanoshell with a silica inner shell synthesized using liposome templates for doxorubicin loading and near-infrared photothermal therapy," *International Journal of Nanomedicine,* vol. 6, 2011.
[239] J. You*, et al.*, "Photothermal-chemotherapy with doxorubicin-loaded hollow gold nanospheres: A platform for near-infrared light-trigged drug release," *Journal of Controlled Release,* vol. 158, pp. 319-28, Mar 10 2012.
[240] W. Lu*, et al.*, "Effects of photoacoustic imaging and photothermal ablation therapy mediated by targeted hollow gold nanospheres in an orthotopic mouse xenograft model of glioma," *Cancer Res,* vol. 71, pp. 6116-21, Oct 1 2011.
[241] W. Lu*, et al.*, "Targeted photothermal ablation of murine melanomas with melanocyte-stimulating hormone analog-conjugated hollow gold nanospheres," *Clin Cancer Res,* vol. 15, pp. 876-86, Feb 1 2009.
[242] J. You*, et al.*, "Exceptionally high payload of doxorubicin in hollow gold nanospheres for near-infrared light-triggered drug release," *Acs Nano,* vol. 4, pp. 1033-41, Feb 23 2010.
[243] J. You*, et al.*, "Effective photothermal chemotherapy using doxorubicin-loaded gold nanospheres that target EphB4 receptors in tumors," *Cancer Res,* vol. 72, pp. 4777-86, Sep 15 2012.
[244] W. I. Choi*, et al.*, "Tumor Regression In Vivo by Photothermal Therapy Based on Gold-Nanorod-Loaded, Functional Nanocarriers," *Acs Nano,* vol. 5, pp. 1995-2003, Mar 2011.
[245] P. S. Kumar*, et al.*, "High-yield synthesis and optical response of gold nanostars," *Nanotechnology,* vol. 19, Jan 9 2008.
[246] J. R. Navarro*, et al.*, "Synthesis of PEGylated gold nanostars and bipyramids for intracellular uptake," *Nanotechnology,* vol. 23, p. 465602, Nov 23 2012.
[247] H. M. Song*, et al.*, "Plasmon-resonant nanoparticles and nanostars with magnetic cores: synthesis and magnetomotive imaging," *Acs Nano,* vol. 4, pp. 5163-73, Sep 28 2010.
[248] S. Wang*, et al.*, "Single Continuous Wave Laser Induced Photodynamic/Plasmonic Photothermal Therapy Using Photosensitizer-Functionalized Gold Nanostars," *Advanced Materials,* Feb 13 2013.
[249] H. Yuan*, et al.*, "TAT peptide-functionalized gold nanostars: enhanced intracellular delivery and efficient NIR photothermal therapy using ultralow irradiance," *J Am Chem Soc,* vol. 134, pp. 11358-61, Jul 18 2012.
[250] H. Yuan*, et al.*, "In vivo particle tracking and photothermal ablation using plasmon-resonant gold nanostars," *Nanomedicine,* vol. 8, pp. 1355-63, Nov 2012.
[251] W. Lu*, et al.*, "Gold nano-popcorn-based targeted diagnosis, nanotherapy treatment, and in situ monitoring of photothermal therapy response of prostate cancer cells using surface-enhanced Raman spectroscopy," *J Am Chem Soc,* vol. 132, pp. 18103-14, Dec 29 2010.
[252] L. Beqa*, et al.*, "Gold nano-popcorn attached SWCNT hybrid nanomaterial for targeted diagnosis and photothermal therapy of human breast cancer cells," *ACS Appl Mater Interfaces,* vol. 3, pp. 3316-24, Sep 2011.
[253] X. Wu*, et al.*, "High-photoluminescence-yield gold nanocubes: for cell imaging and photothermal therapy," *Acs Nano,* vol. 4, pp. 113-20, Jan 26 2010.

[254] B. Pelaz*, et al.*, "Tailoring the synthesis and heating ability of gold nanoprisms for bioapplications," *Langmuir,* vol. 28, pp. 8965-70, Jun 19 2012.
[255] Y. Wang*, et al.*, "Comparison Study of Gold Nanohexapods, Nanorods, and Nanocages for Photothermal Cancer Treatment," *Acs Nano,* Feb 12 2013.
[256] A. Karmi*, et al.*, "Multifunctional nanovehicles for combined 5-fluorouracil and gold nanoparticles based on the nanoprecipitation method," *J Nanosci Nanotechnol,* vol. 11, pp. 4675-83, Jun 2011.
[257] X. Q. Huang*, et al.*, "Freestanding palladium nanosheets with plasmonic and catalytic properties," *Nature Nanotechnology,* vol. 6, pp. 28-32, Jan 2011.
[258] S. H. Tang*, et al.*, "Silica coating improves the efficacy of Pd nanosheets for photothermal therapy of cancer cells using near infrared laser," *Chemical Communications,* vol. 47, pp. 3948-3950, 2011.
[259] X. Q. Huang*, et al.*, "Enhancing the Photothermal Stability of Plasmonic Metal Nanoplates by a Core-Shell Architecture," *Advanced Materials,* vol. 23, pp. 3420-+, Aug 9 2011.
[260] Y. J. Xiong and Y. N. Xia, "Shape-controlled synthesis of metal nanostructures: The case of palladium," *Advanced Materials,* vol. 19, pp. 3385-3391, Oct 19 2007.
[261] C. L. Chen*, et al.*, "Photothermal cancer therapy via femtosecond-laser-excited FePt nanoparticles," *Biomaterials,* vol. 34, pp. 1128-1134, Jan 2013.
[262] C. Lee*, et al.*, "TiO2 Nanotubes as a Therapeutic Agent for Cancer Thermotherapy," *Photochemistry and Photobiology,* vol. 86, pp. 981-989, Jul-Aug 2010.
[263] C. Hong*, et al.*, "Photothermal Therapy Using TiO2 Nanotubes in Combination with Near-Infrared Laser," *Journal of Cancer Therapy,* vol. 1, pp. 52-58, 2010.
[264] J. K. Young*, et al.*, "Tunable nanostructures as photothermal theranostic agents," *Ann Biomed Eng,* vol. 40, pp. 438-59, Feb 2012.
[265] G. P. C. Drummen, "Quantum Dots-From Synthesis to Applications in Biomedicine and Life Sciences," *International Journal of Molecular Sciences,* vol. 11, pp. 154-163, Jan 2010.
[266] M. Varna*, et al.*, "In vivo Distribution of Inorganic Nanoparticles in Preclinical Models," *Journal of Biomaterials and Nanobiotechnology,* vol. 3, pp. 269-279, 2012.
[267] M. Bruchez*, et al.*, "Semiconductor nanocrystals as fluorescent biological labels," *Science,* vol. 281, pp. 2013-2016, Sep 25 1998.
[268] J. Aldana*, et al.*, "Photochemical instability of CdSe nanocrystals coated by hydrophilic thiols," *Journal of the American Chemical Society,* vol. 123, pp. 8844-8850, Sep 12 2001.
[269] B. I. Ipe*, et al.*, "On the generation of free radical species from quantum dots," *Small,* vol. 1, pp. 706-709, Jul 2005.
[270] Y. Q. Wang and L. X. Chen, "Quantum dots, lighting up the research and development of nanomedicine," *Nanomedicine-Nanotechnology Biology and Medicine,* vol. 7, pp. 385-402, Aug 2011.
[271] J. M. Luther*, et al.*, "Localized surface plasmon resonances arising from free carriers in doped quantum dots," *Nature Materials,* vol. 10, pp. 361-366, May 2011.
[272] M. Q. Chu*, et al.*, "The therapeutic efficacy of CdTe and CdSe quantum dots for photothermal cancer therapy," *Biomaterials,* vol. 33, pp. 7071-7083, Oct 2012.
[273] Y. B. Li*, et al.*, "Copper sulfide nanoparticles for photothermal ablation of tumor cells," *Nanomedicine,* vol. 5, pp. 1161-1171, Oct 2010.
[274] A. M. Derfus*, et al.*, "Probing the cytotoxicity of semiconductor quantum dots," *Nano Letters,* vol. 4, pp. 11-18, Jan 2004.

[275] C. M. Hessel*, et al.*, "Copper Selenide Nanocrystals for Photothermal Therapy," *Nano Letters,* vol. 11, pp. 2560-2566, Jun 2011.
[276] M. G. Panthani*, et al.*, "Synthesis of CuInS2, CuInSe2, and Cu(InxGa1-x)Se-2 (CIGS) Nanocrystal "Inks" for Printable Photovoltaics," *Journal of the American Chemical Society,* vol. 130, pp. 16770-16777, Dec 10 2008.
[277] B. Koo*, et al.*, "Synthesis of CuInSe2 Nanocrystals with Trigonal Pyramidal Shape," *Journal of the American Chemical Society,* vol. 131, pp. 3134-+, Mar 11 2009.
[278] M. Zhou*, et al.*, "A Chelator-Free Multifunctional [Cu-64]CuS Nanoparticle Platform for Simultaneous Micro-PET/CT Imaging and Photothermal Ablation Therapy," *Journal of the American Chemical Society,* vol. 132, pp. 15351-15358, Nov 3 2010.
[279] Q. W. Tian*, et al.*, "Hydrophilic Flower-Like CuS Superstructures as an Efficient 980 nm Laser-Driven Photothermal Agent for Ablation of Cancer Cells," *Advanced Materials,* vol. 23, pp. 3542-+, Aug 16 2011.
[280] H. W. Kroto*, et al.*, "C-60 - Buckminsterfullerene," *Nature,* vol. 318, pp. 162-163, 1985.
[281] E. Brown*, et al.*, "Ballistic thermal and electrical conductance measurements on individual multiwall carbon nanotubes," *Applied Physics Letters,* vol. 87, 2005.
[282] M. S. Dresselhaus*, et al.*, "Electronic, thermal and mechanical properties of carbon nanotubes," *Philosophical Transactions of the Royal Society of London Series A-Mathematical Physical and Engineering Sciences,* vol. 362, pp. 2065-2098, 2004.
[283] S. P. Hepplestone*, et al.*, "Size and temperature dependence of the specific heat capacity of carbon nanotubes," *Surface Science,* vol. 600, pp. 3633-3636, 2006.
[284] J. P. Mittal, "Excited-States and Electron-Transfer Reactions of Fullerenes," *Pure and Applied Chemistry,* vol. 67, pp. 103-110, Jan 1995.
[285] P. C. Eklund*, et al.*, "Optical Phonon Modes in Solid and Doped C-60," *Journal of Physics and Chemistry of Solids,* vol. 53, pp. 1391-1413, 1992.
[286] S.Iijima, "Helical Microtubules of Graphitic Carbon," *Nature,* vol. 354, pp. 56-58, 1991.
[287] J. W. Liu*, et al.*, "Temperature and flow rate of NH3 effects on nitrogen content and doping environments of carbon nanotubes grown by injection CVD method," *Journal of Physical Chemistry B,* vol. 109, pp. 15769-15774, 2005.
[288] J. F. Xu*, et al.*, "Optical limiting and enhanced optical nonlinearity in boron-doped carbon nanotubes," *Chemical Physics Letters,* vol. 389, pp. 247-250, 2004.
[289] J. C. Carrero-Sanchez*, et al.*, "Biocompatibility and toxicological studies of carbon nanotubes doped with nitrogen," *Nano Letters,* vol. 6, pp. 1609-1616, 2006.
[290] M. Mahmood*, et al.*, "Synergistic enhancement of cancer therapy using a combination of carbon nanotubes and anti-tumor drug," *Nanomedicine,* vol. 4, pp. 883-893, 2009.
[291] S. M. Bachilo*, et al.*, "Structure-assigned optical spectra of single-walled carbon nanotubes," *Science,* vol. 298, pp. 2361-2366, 2002.
[292] N. Kouklin*, et al.*, "Infrared absorption properties of carbon nanotubes synthesized by chemical vapor deposition," *Applied Physics Letters,* vol. 85, pp. 4463-4465, 2004.
[293] M. J. O'Connell*, et al.*, "Band gap fluorescence from individual single-walled carbon nanotubes," *Science,* vol. 297, pp. 593-596, 2002.
[294] R. Saito*, et al.*, "Optical absorption of graphite and single-wall carbon nanotubes," *Applied Physics a-Materials Science & Processing,* vol. 78, pp. 1099-1105, 2004.
[295] M. S. Dresselhaus and P. C. Eklund, "Phonons in carbon nanotubes," *Advances in Physics,* vol. 49, pp. 705-814, Sep 2000.
[296] S. A. Maksimenko*, et al.*, "Carbon nanotube antenna: Far-field, near-field and thermal-noise properties," *Physica E: Low-dimensional Systems and Nanostructures,* vol. 40, pp. 2360-2364, 2008.

[297] K. Kempa*, et al.*, "Carbon nanotubes as optical antennae," *Advanced Materials,* vol. 19, pp. 421-426, 2007.
[298] P. J. Burke*, et al.*, "Quantitative theory of nanowire and nanotube antenna performance," *Ieee Transactions on Nanotechnology,* vol. 5, pp. 314-334, 2006.
[299] G. W. Hanson, "Fundamental transmitting properties of carbon nanotube antennas," *Ieee Transactions on Antennas and Propagation,* vol. 53, pp. 3426-3435, 2005.
[300] Y. Wang*, et al.*, "Receiving and transmitting light-like radio waves: Antenna effect in arrays of aligned carbon nanotubes," *Applied Physics Letters,* vol. 85, pp. 2607-2609, 2004.
[301] A. Casey*, et al.*, "Interaction of Carbon Nanotubes with Sugar Complexes," *Synthetic Metals,* vol. 153, pp. 357-360, 2005.
[302] N. W. S. Kam*, et al.*, "Carbon nanotubes as multifunctional biological transporters and near-infrared agents for selective cancer cell destruction," *Proceedings of the National Academy of Sciences of the United States of America,* vol. 102, pp. 11600-11605, Aug 16 2005.
[303] V. A. Sinani*, et al.*, "Aqueous dispersions of single-wall and multiwall carbon nanotubes with designed amphiphilic polycations," *Journal of the American Chemical Society,* vol. 127, pp. 3463-3472, 2005.
[304] S. Torti*, et al.*, "Thermal ablation Therapeutics based on CNx Multi-Walled Nanotubes," *International Journal of Nanomedicine,* vol. 2, 2007.
[305] Z. Liu*, et al.*, "Supramolecular chemistry on water-soluble carbon nanotubes for drug loading and delivery," *Acs Nano,* vol. 1, pp. 50-56, Aug 2007.
[306] R. Yang*, et al.*, "Single-walled carbon nanotubes-mediated in vivo and in vitro delivery of siRNA into antigen-presenting cells," *Gene Therapy,* vol. 13, pp. 1714-1723, 2006.
[307] R. P. Feazell*, et al.*, "Soluble single-walled carbon nanotubes as longboat delivery systems for Platinum(IV) anticancer drug design," *Journal of the American Chemical Society,* vol. 129, pp. 8438-+, 2007.
[308] M. Foldvari and M. Bagonluri, "Carbon nanotubes as functional excipients for nanomedicines: I. pharmaceutical properties," *Nanomedicine-Nanotechnology Biology and Medicine,* vol. 4, pp. 173-182, 2008.
[309] M. Foldvari and M. Bagonluri, "Carbon nanotubes as functional excipients for nanomedicines: II. Drug delivery and biocompatibility issues," *Nanomedicine-Nanotechnology Biology and Medicine,* vol. 4, pp. 183-200, 2008.
[310] E. Heister*, et al.*, "Triple functionalisation of single-walled carbon nanotubes with doxorubicin, a monoclonal antibody, and a fluorescent marker for targeted cancer therapy," *Carbon,* vol. 47, pp. 2152-2160, 2009.
[311] H. Huang*, et al.*, "A new family of folate-decorated and carbon nanotube-mediated drug delivery system: synthesis and drug delivery response," *Adv Drug Deliv Rev,* vol. 63, pp. 1332-9, Nov 2011.
[312] R. Krajcik*, et al.*, "Functionalization of carbon nanotubes enables non-covalent binding and intracellular delivery of small interfering RNA for efficient knock-down of genes," *Biochemical and Biophysical Research Communications,* vol. 369, pp. 595-602, 2008.
[313] D. Pantarotto*, et al.*, "Functionalized carbon nanotubes for plasmid DNA gene delivery," *Angewandte Chemie-International Edition,* vol. 43, pp. 5242-5246, 2004.
[314] X. Zhang*, et al.*, "Targeted delivery and controlled release of doxorubicin to cancer cells using modified single wall carbon nanotubes," *Biomaterials,* vol. 30, pp. 6041-7, Oct 2009.

[315] Z. H. Zhang*, et al.*, "Delivery of telomerase reverse transcriptase small interfering RNA in complex with positively charged single-walled carbon nanotubes suppresses tumor growth," *Clinical Cancer Research,* vol. 12, pp. 4933-4939, 2006.
[316] B. Panchapakesan*, et al.*, "Single-Wall Carbon Nanotube Nanobomb Agents for Killing Breast Cancer Cells " *Nanobiotechnology,* vol. 1, pp. 133-140, 2005.
[317] E. Banks*, et al.*, "Is psychological distress in people living with cancer related to the fact of diagnosis, current treatment or level of disability? Findings from a large Australian study," *Medical Journal of Australia,* vol. 193, pp. S62-S67, Sep 6 2010.
[318] X. K. Zhang*, et al.*, "Targeted delivery and controlled release of doxorubicin to cancer cells using modified single wall carbon nanotubes," *Biomaterials,* vol. 30, pp. 6041-6047, 2009.
[319] J. Creaney*, et al.*, "Serum Mesothelin for Early Detection of Asbestos-Induced Cancer Malignant Mesothelioma," *Cancer Epidemiology Biomarkers & Prevention,* vol. 19, pp. 2238-2246, Sep 2010.
[320] J. T. Robinson*, et al.*, "High Performance In Vivo Near-IR (> 1 mu m) Imaging and Photothermal Cancer Therapy with Carbon Nanotubes," *Nano Research,* vol. 3, pp. 779-793, Nov 2010.
[321] S. Joshi*, et al.*, "The Dynamin Inhibitors MiTMAB and OcTMAB Induce Cytokinesis Failure and Inhibit Cell Proliferation in Human Cancer Cells," *Molecular Cancer Therapeutics,* vol. 9, pp. 1995-2006, Jul 2010.
[322] N. H. Levi-Polyachenko*, et al.*, "Rapid Photothermal Intracellular Drug Delivery Using Multiwalled Carbon Nanotubes," *Molecular Pharmaceutics,* vol. 6, pp. 1092-1099, Jul-Aug 2009.
[323] L. W. Zhang and N. A. Monteiro-Riviere, "Lectins modulate multi-walled carbon nanotubes cellular uptake in human epidermal keratinocytes," *Toxicology in Vitro,* vol. In Press, Corrected Proof.
[324] A. A. Shvedova*, et al.*, "Mechanisms of pulmonary toxicity and medical applications of carbon nanotubes: Two faces of Janus?," *Pharmacology & Therapeutics,* vol. 121, pp. 192-204, 2009.
[325] C. Cheng*, et al.*, "Toxicity and imaging of multi-walled carbon nanotubes in human macrophage cells," *Biomaterials,* vol. 30, pp. 4152-4160, 2009.
[326] J. L. Locher*, et al.*, "Disruptions in the organization of meal preparation and consumption among older cancer patients and their family caregivers," *Psycho-Oncology,* vol. 19, pp. 967-974, Sep 2010.
[327] C. J. Balentine*, et al.*, "Obesity Increases Wound Complications in Rectal Cancer Surgery," *Journal of Surgical Research,* vol. 163, pp. 35-39, Sep 2010.
[328] N. C. Tebbutt*, et al.*, "Capecitabine, Bevacizumab, and Mitomycin in First-Line Treatment of Metastatic Colorectal Cancer: Results of the Australasian Gastrointestinal Trials Group Randomized Phase III MAX Study," *Journal of Clinical Oncology,* vol. 28, pp. 3191-3198, Jul 1 2010.
[329] D. Robinson, "Season of cancer diagnosis exerts distinct effects upon short- and long-term survival," *International Journal of Cancer,* vol. 126, pp. 3013-3013, Jun 15 2010.
[330] S. Elliott*, et al.*, "Androgen Deprivation Therapy for Prostate Cancer: Recommendations to Improve Patient and Partner Quality of Life," *Journal of Sexual Medicine,* vol. 7, pp. 2996-3010, Sep 2010.
[331] C. K. Lim*, et al.*, "Phthalocyanine-aggregated polymeric nanoparticles as tumor-homing near-infrared absorbers for photothermal therapy of cancer," *Theranostics,* vol. 2, pp. 871-9, 2012.

[332] C. S. Jin, *et al.*, "Ablation of Hypoxic Tumors with Dose-Equivalent Photothermal, but Not Photodynamic, Therapy Using a Nanostructured Porphyrin Assembly," *Acs Nano,* Feb 12 2013.
[333] A. Yuan, *et al.*, "Application of near-infrared dyes for tumor imaging, photothermal, and photodynamic therapies," *Journal of Pharmaceutical Sciences,* vol. 102, pp. 6-28, Jan 2013.
[334] S. Mordon, *et al.*, "Indocyanine green: Physicochemical factors affecting its fluorescence in vivo," *Microvascular Research,* vol. 55, pp. 146-152, Mar 1998.
[335] V. L. Dzurinko, *et al.*, "Intravenous and indocyanine green angiography," *Optometry,* vol. 75, pp. 743-55, Dec 2004.
[336] T. Desmettre, *et al.*, "Fluorescence properties and metabolic features of indocyanine green (ICG) as related to angiography," *Surv Ophthalmol,* vol. 45, pp. 15-27, Jul-Aug 2000.
[337] X. Zheng, *et al.*, "Enhanced tumor treatment using biofunctional indocyanine green-containing nanostructure by intratumoral or intravenous injection," *Mol Pharm,* vol. 9, pp. 514-22, Mar 5 2012.
[338] W. R. Chen, *et al.*, "Chromophore-enhanced laser-tumor tissue photothermal interaction using an 808-nm diode laser," *Cancer Lett,* vol. 88, pp. 15-9, Jan 6 1995.
[339] S. Yoneya, *et al.*, "Binding properties of indocyanine green in human blood," *Investigative Ophthalmology & Visual Science,* vol. 39, pp. 1286-1290, Jun 1998.
[340] V. Saxena, *et al.*, "Degradation kinetics of indocyanine green in aqueous solution," *Journal of Pharmaceutical Sciences,* vol. 92, pp. 2090-2097, Oct 2003.
[341] M. L. J. Landsman, *et al.*, "Light-Absorbing Properties, Stability, and Spectral Stabilization of Indocyanine Green," *Journal of Applied Physiology,* vol. 40, pp. 575-583, 1976.
[342] G. Patonay, *et al.*, "Noncovalent labeling of biomolecules with red and near-infrared dyes," *Molecules,* vol. 9, pp. 40-49, Mar 2004.
[343] G. R. Cherrick, *et al.*, "Indocyanine green: observations on its physical properties, plasma decay, and hepatic extraction," *J Clin Invest,* vol. 39, pp. 592-600, Apr 1960.
[344] V. Saxena, *et al.*, "Enhanced photo-stability, thermal-stability and aqueous-stability of indocyanine green in polymeric nanoparticulate systems," *J Photochem Photobiol B,* vol. 74, pp. 29-38, Mar 19 2004.
[345] R. H. Patel, *et al.*, "Multifunctionality of indocyanine green-loaded biodegradable nanoparticles for enhanced optical imaging and hyperthermia intervention of cancer," *J Biomed Opt,* vol. 17, p. 046003, Apr 2012.
[346] M. A. Yaseen, *et al.*, "Laser-induced heating of dextran-coated mesocapsules containing indocyanine green," *Biotechnol Prog,* vol. 23, pp. 1431-40, Nov-Dec 2007.
[347] J. Yu, *et al.*, "Synthesis of near-infrared-absorbing nanoparticle-assembled capsules," *Chemistry of Materials,* vol. 19, pp. 1277-1284, Mar 20 2007.
[348] J. Yu, *et al.*, "Self-Assembly Synthesis, Tumor Cell Targeting, and Photothermal Capabilities of Antibody-Coated Indocyanine Green Nanocapsules," *Journal of the American Chemical Society,* vol. 132, pp. 1929-1938, Feb 17 2010.
[349] X. Zheng, *et al.*, "Indocyanine green-containing nanostructure as near infrared dual-functional targeting probes for optical imaging and photothermal therapy," *Mol Pharm,* vol. 8, pp. 447-56, Apr 4 2011.
[350] C. Zhang, *et al.*, "Sentinel lymph node mapping by a near-infrared fluorescent heptamethine dye," *Biomaterials,* vol. 31, pp. 1911-1917, Mar 2010.

[351] C. Zhang, *et al.*, "A near-infrared fluorescent heptamethine indocyanine dye with preferential tumor accumulation for in vivo imaging," *Biomaterials,* vol. 31, pp. 6612-6617, Sep 2010.
[352] C. L. Peng, *et al.*, "Multimodal Image-Guided Photothermal Therapy Mediated by Re-188-Labeled Micelles Containing a Cyanine-Type Photosensitizer," *Acs Nano,* vol. 5, pp. 5594-5607, Jul 2011.
[353] L. G. Gutwein, *et al.*, "Fractionated photothermal antitumor therapy with multidye nanoparticles," *Int J Nanomedicine,* vol. 7, pp. 351-7, 2012.
[354] J. F. Lovell, *et al.*, "Enzymatic regioselection for the synthesis and biodegradation of porphysome nanovesicles," *Angew Chem Int Ed Engl,* vol. 51, pp. 2429-33, Mar 5 2012.
[355] J. F. Lovell, *et al.*, "Porphysome nanovesicles generated by porphyrin bilayers for use as multimodal biophotonic contrast agents," *Nature Materials,* vol. 10, pp. 324-32, Apr 2011.
[356] Y. Liu, *et al.*, "Dopamine-Melanin Colloidal Nanospheres: An Efficient Near-Infrared Photothermal Therapeutic Agent for In Vivo Cancer Therapy," *Advanced Materials,* Dec 21 2012.
[357] M. A. Franco-Molina, *et al.*, "Antitumor activity of colloidal silver on MCF-7 human breast cancer cells," *Journal of Experimental & Clinical Cancer Research,* vol. 29, Nov 2010.
[358] M. Park, *et al.*, "The effect of particle size on the cytotoxicity, inflammation, developmental toxicity and genotoxicity of silver nanoparticles," *Biomaterials,* vol. 32, pp. 9810-9817, Dec 2011.
[359] K. K. Y. Wong, *et al.*, "Further Evidence of the Anti-inflammatory Effects of Silver Nanoparticles," *Chemmedchem,* vol. 4, pp. 1129-1135, Jul 2009.
[360] C. P. Lin, et.al., "Reactive Oxidizing Species Produced near the Plasma Membrane Induce Apoptosis in Bovine Aorta Endothelial Cells," *Experimental Cell Research,* vol. 259, p. 351, 2000.
[361] X. W. Chen and O. Inganas, "Three-step redox in polythiophenes: Evidence from electrochemistry at an ultramicroelectrode," *Journal of Physical Chemistry,* vol. 100, pp. 15202-15206, Sep 12 1996.
[362] B. Di, *et al.*, "Electroluminescence enhancement in polymer light-emitting diodes through inelastic scattering of oppositely charged bipolarons," *Journal of Physical Chemistry B,* vol. 115, pp. 9339-44, Aug 4 2011.
[363] "American Cancer Society. Cancer Facts and Figures 2011," 2011.
[364] A. Bianco, *et al.*, "Applications of carbon nanotubes in drug delivery," *Curr Opin Chem Biol,* vol. 9, pp. 674-9, Dec 2005.
[365] A. Bianco and M. Prato, "Can carbon nanotubes be considered useful tools for biological applications?," *Advanced Materials,* vol. 15, pp. 1765-1768, Oct 16 2003.
[366] Z. A. Liu, *et al.*, "Single-walled carbon nanotubes in biomedical imaging," *Journal of Materials Chemistry,* vol. 21, pp. 586-598, 2011.
[367] H. Ali-Boucetta, *et al.*, "Multiwalled carbon nanotube-doxorubicin supramolecular complexes for cancer therapeutics," *Chemical Communications,* pp. 459-461, 2008.
[368] S. V. Torti, *et al.*, "Thermal ablation therapeutics based on CN(x) multi-walled nanotubes," *Int J Nanomedicine,* vol. 2, pp. 707-14, 2007.
[369] Z. Liu, *et al.*, "Drug delivery with carbon nanotubes for in vivo cancer treatment," *Cancer Research,* vol. 68, pp. 6652-6660, Aug 15 2008.

[370] R. Marches*, et al.*, "Specific thermal ablation of tumor cells using single-walled carbon nanotubes targeted by covalently-coupled monoclonal antibodies," *International Journal of Cancer,* vol. 125, pp. 2970-2977, Dec 15 2009.
[371] R. B. Li*, et al.*, "P-Glycoprotein Antibody Functionalized Carbon Nanotube Overcomes the Multidrug Resistance of Human Leukemia Cells," *Acs Nano,* vol. 4, pp. 1399-1408, Mar 2010.
[372] J. F. Ross*, et al.*, "Differential Regulation of Folate Receptor Isoforms in Normal and Malignant-Tissues in-Vivo and in Established Cell-Lines - Physiological and Clinical Implications," *Cancer,* vol. 73, pp. 2432-2443, May 1 1994.
[373] H. Huang*, et al.*, "A new family of folate-decorated and carbon nanotube-mediated drug delivery system: Synthesis and drug delivery response," *Advanced Drug Delivery Reviews,* vol. 63, pp. 1332-1339, Nov 2011.
[374] N. W. S. Kam and H. J. Dai, "Carbon nanotubes as intracellular protein transporters: Generality and biological functionality," *Journal of the American Chemical Society,* vol. 127, pp. 6021-6026, 2005.
[375] Z. Sideratou*, et al.*, "Synthesis and characterization of multifunctional hyperbranched polyesters as prospective contrast agents for targeted MRI," *Bioorganic & Medicinal Chemistry Letters,* vol. 20, pp. 4177-4181, Jul 15 2010.
[376] S. Dhar*, et al.*, "Targeted single-wall carbon nanotube-mediated Pt(IV) prodrug delivery using folate as a homing device," *Journal of the American Chemical Society,* vol. 130, pp. 11467-11476, Aug 27 2008.
[377] K. J. Livak and T. D. Schmittgen, "Analysis of relative gene expression data using real-time quantitative PCR and the 2(-Delta Delta C(T)) Method," *Methods,* vol. 25, pp. 402-8, Dec 2001.
[378] J. S. Yuan*, et al.*, "Statistical analysis of real-time PCR data," *BMC Bioinformatics,* vol. 7, p. 85, 2006.
[379] S. Wang and P. S. Low, "Folate-mediated targeting of antineoplastic drags, imaging agents, and nucleic acids to cancer cells," *Journal of Controlled Release,* vol. 53, pp. 39-48, Apr 30 1998.
[380] A. R. Vortherms*, et al.*, "Synthesis, characterization, and in vitro assay of folic acid conjugates of 3'-azido-3'-deoxythymidine (AZT): toward targeted AZT based anticancer therapeutics," *Nucleosides Nucleotides Nucleic Acids,* vol. 27, pp. 173-85, Feb 2008.
[381] I. D. Rosca*, et al.*, "Oxidation of multiwalled carbon nanotubes by nitric acid," *Carbon,* vol. 43, pp. 3124-3131, Dec 2005.
[382] S. Mohapatra*, et al.*, "Synthesis of highly stable folic acid conjugated magnetite nanoparticles for targeting cancer cells," *Nanotechnology,* vol. 18, Sep 26 2007.
[383] S. Osswald*, et al.*, "Elimination of D-band in Raman spectra of double-wall carbon nanotubes by oxidation," *Chemical Physics Letters,* vol. 402, pp. 422-427, Feb 4 2005.
[384] J. Zhu*, et al.*, "Improving the dispersion and integration of single-walled carbon nanotubes in epoxy composites through functionalization," *Nano Letters,* vol. 3, pp. 1107-1113, Aug 2003.
[385] J. L. Bahr and J. M. Tour, "Covalent chemistry of single-wall carbon nanotubes," *Journal of Materials Chemistry,* vol. 12, pp. 1952-1958, 2002.
[386] C. Velasco-Santos*, et al.*, "Chemical functionalization of carbon nanotubes through an organosilane," *Nanotechnology,* vol. 13, pp. 495-498, Aug 2002.
[387] S. S. Yu*, et al.*, "Size- and charge-dependent non-specific uptake of PEGylated nanoparticles by macrophages," *Int J Nanomedicine,* vol. 7, pp. 799-813, 2012.
[388] American Cancer Society, "Cancer Facts and Figures," 2014.

[389] D. Hanahan and R. A. Weinberg, "Hallmarks of cancer: the next generation," *Cell,* vol. 144, pp. 646-74, Mar 4 2011.
[390] R. B. Hazan and L. Norton, "The epidermal growth factor receptor modulates the interaction of E-cadherin with the actin cytoskeleton," *J Biol Chem,* vol. 273, pp. 9078-84, Apr 10 1998.
[391] D. L. Rimm*, et al.*, "Reduced alpha-catenin and E-cadherin expression in breast cancer," *Lab Invest,* vol. 72, pp. 506-12, May 1995.
[392] L. Fan*, et al.*, "Loss of E-cadherin promotes prostate cancer metastasis via upregulation of metastasis-associated gene 1 expression," *Oncol Lett,* vol. 4, pp. 1225-1233, Dec 2012.
[393] S. Kispert*, et al.*, "Cigarette smoke increases PAF accumulation, cell motility and EMT in triple negative breast cancer cells," in *Experimental Biology*, San Diego, CA, 2014.
[394] H. L. Chua*, et al.*, "NF-kappaB represses E-cadherin expression and enhances epithelial to mesenchymal transition of mammary epithelial cells: potential involvement of ZEB-1 and ZEB-2," *Oncogene,* vol. 26, pp. 711-24, Feb 1 2007.
[395] E. Fransvea*, et al.*, "Blocking transforming growth factor-beta up-regulates E-cadherin and reduces migration and invasion of hepatocellular carcinoma cells," *Hepatology,* vol. 47, pp. 1557-66, May 2008.
[396] U. Valcourt*, et al.*, "TGF-beta and the Smad signaling pathway support transcriptomic reprogramming during epithelial-mesenchymal cell transition," *Mol Biol Cell,* vol. 16, pp. 1987-2002, Apr 2005.
[397] L. Seguin*, et al.*, "An integrin beta3-KRAS-RalB complex drives tumour stemness and resistance to EGFR inhibition," *Nat Cell Biol,* vol. 16, pp. 457-68, May 2014.
[398] Y. H. Soung*, et al.*, "Crosstalk between integrin and receptor tyrosine kinase signaling in breast carcinoma progression," *BMB Rep,* vol. 43, pp. 311-8, May 2010.
[399] D. Cheresh, "Tumor progression induced by integrin αvβ3 mediated anchorage-dependent and -independent signaling " in *Experimental Biology*, San Diego, CA, 2014.
[400] J. S. King*, et al.*, "The induction of autophagy by mechanical stress," *Autophagy,* vol. 7, pp. 1490-9, Dec 2011.
[401] P. O. Seglen*, et al.*, "Sequestration assays for mammalian autophagy," *Methods Enzymol,* vol. 452, pp. 63-83, 2009.
[402] J. Kopitz*, et al.*, "Nonselective autophagy of cytosolic enzymes by isolated rat hepatocytes," *J Cell Biol,* vol. 111, pp. 941-53, Sep 1990.
[403] B. W. Katona*, et al.*, "EZH2 inhibition enhances the efficacy of an EGFR inhibitor in suppressing colon cancer cells," *Cancer Biol Ther,* vol. 15, pp. 1677-87, Dec 2 2014.
[404] H. Wu*, et al.*, "Autophagic responses to hypoxia and anticancer therapy in head and neck cancer," *Pathol Res Pract,* Nov 25 2014.
[405] J. S. Carew*, et al.*, "Autophagy as a target for cancer therapy: new developments," *Cancer Manag Res,* vol. 4, pp. 357-65, 2012.
[406] E. L. Eskelinen, "The dual role of autophagy in cancer," *Curr Opin Pharmacol,* vol. 11, pp. 294-300, Aug 2011.
[407] E. White and R. S. DiPaola, "The double-edged sword of autophagy modulation in cancer," *Clin Cancer Res,* vol. 15, pp. 5308-16, Sep 1 2009.
[408] M. Yilmaz and G. Christofori, "EMT, the cytoskeleton, and cancer cell invasion," *Cancer Metastasis Rev,* vol. 28, pp. 15-33, Jun 2009.
[409] A. Jeanes*, et al.*, "Cadherins and cancer: how does cadherin dysfunction promote tumor progression?," *Oncogene,* vol. 27, pp. 6920-9, Nov 24 2008.

[410] M. V. Fournier*, et al.*, "Interaction of E-cadherin and PTEN regulates morphogenesis and growth arrest in human mammary epithelial cells," *Cancer Res,* vol. 69, pp. 4545-52, May 15 2009.
[411] M. Bissell, "Experiments that point to a new understanding of cancer," in *TED Talk*, 2012.
[412] G. Venugopalan*, et al.*, "Externally applied forces can phenotypically revert malignant breast epithelial structures," in *American Society for Cell Biology*, San Francisco, CA, 2012.
[413] E. Alpaslan and T. J. Webster, "Nanotechnology and picotechnology to increase tissue growth: a summary of in vivo studies," *Int J Nanomedicine,* vol. 9 Suppl 1, pp. 7-12, 2014.
[414] J. Holy*, et al.*, "Adhesion, proliferation and differentiation of pluripotent stem cells on multi-walled carbon nanotubes," *IET Nanobiotechnol,* vol. 5, pp. 41-6, Jun 2011.
[415] J. Meng*, et al.*, "Enhancement of nanofibrous scaffold of multiwalled carbon nanotubes/polyurethane composite to the fibroblasts growth and biosynthesis," *J Biomed Mater Res A,* vol. 88, pp. 105-16, Jan 2009.
[416] M. Schurmann*, et al.*, "Interaction of adult human neural crest-derived stem cells with a nanoporous titanium surface is sufficient to induce their osteogenic differentiation," *Stem Cell Res,* vol. 13, pp. 98-110, May 9 2014.
[417] K. Memarzadeh*, et al.*, "Nanoparticulate zinc oxide as a coating material for orthopaedic and dental implants," *J Biomed Mater Res A,* May 26 2014.
[418] H. Tiainen*, et al.*, "Ultra-porous titanium oxide scaffold with high compressive strength," *J Mater Sci Mater Med,* vol. 21, pp. 2783-92, Oct 2010.
[419] F. M. Tonelli*, et al.*, "Carbon nanotube interaction with extracellular matrix proteins producing scaffolds for tissue engineering," *Int J Nanomedicine,* vol. 7, pp. 4511-29, 2012.
[420] S. Ni*, et al.*, "A mechanism for the enhanced attachment and proliferation of fibroblasts on anodized 316L stainless steel with nano-pit arrays," *J Biomed Mater Res B Appl Biomater,* pp. 1-7, Mar 8 2014.
[421] M. A. Shokrgozar*, et al.*, "Fabrication of porous chitosan/poly(vinyl alcohol) reinforced single-walled carbon nanotube nanocomposites for neural tissue engineering," *J Biomed Nanotechnol,* vol. 7, pp. 276-84, Apr 2011.
[422] J. T. Connelly, "Terminal differentiation of human epidermal stem cells on micro-patterned substrates," *Methods Mol Biol,* vol. 916, pp. 15-22, 2012.
[423] M. W. Tibbit*, et al.*, "Controlled two-photon photodegradation of PEG hydrogels to study and manipulate subcellular interactions on soft materials," *Soft Matter,* vol. 6, pp. 5100-5108, 2010.
[424] L. MacQueen*, et al.*, "Mesenchymal stem cell mechanobiology and emerging experimental platforms," *J R Soc Interface,* vol. 10, p. 20130179, Jul 6 2013.
[425] M. A. Bray*, et al.*, "Nuclear morphology and deformation in engineered cardiac myocytes and tissues," *Biomaterials,* vol. 31, pp. 5143-50, Jul 2010.
[426] J. Liu*, et al.*, "Control of neuronal network organization by chemical surface functionalization of multi-walled carbon nanotube arrays," *Nanotechnology,* vol. 22, p. 195101, May 13 2011.
[427] R. A. MacDonald*, et al.*, "Collagen-carbon nanotube composite materials as scaffolds in tissue engineering," *J Biomed Mater Res A,* vol. 74, pp. 489-96, Sep 1 2005.
[428] M. P. Jagtoyen, J; Rantell, T; Derbyshire, F., "Porosity of Carbon Nanotubes," *Adsorpt Sci and Technol,* vol. 17, pp. 289-93, 2000.

[429] A. S. Raut*, et al.*, "Effect of porosity variation on the electrochemical behavior of vertically aligned multi-walled carbon nanotubes," *Electrochem commun,* vol. 19, pp. 138-141, Jun 1 2012.
[430] Y. Sudaryanto*, et al.*, "High surface area activated carbon prepared from cassava peel by chemical activation," *Bioresour Technol,* vol. 97, pp. 734-9, Mar 2006.
[431] G. Cellot*, et al.*, "Carbon nanotube scaffolds tune synaptic strength in cultured neural circuits: novel frontiers in nanomaterial-tissue interactions," *J Neurosci,* vol. 31, pp. 12945-53, Sep 7 2011.
[432] T. Akasaka*, et al.*, "Adhesion of human osteoblast-like cells (Saos-2) to carbon nanotube sheets," *Biomed Mater Eng,* vol. 19, pp. 147-53, 2009.
[433] M. F. Riaz, A; Amin, G; Alvi, NH; Nur, O; Willander, M, "Buckling and elastic stability of vertical ZnO nanotubes and nanorods," *J Appl Phys,* vol. 106, pp. 121-127, 2009.
[434] L. M. Gilbertson*, et al.*, "Toward tailored functional design of multi-walled carbon nanotubes (MWNTs): electrochemical and antimicrobial activity enhancement via oxidation and selective reduction," *Environ Sci Technol,* vol. 48, pp. 5938-45, May 20 2014.
[435] C. D. Reyes and A. J. Garcia, "A centrifugation cell adhesion assay for high-throughput screening of biomaterial surfaces," *J Biomed Mater Res A,* vol. 67, pp. 328-33, Oct 1 2003.
[436] L. C. Bui*, et al.*, "Nedd9/Hef1/Cas-L mediates the effects of environmental pollutants on cell migration and plasticity," *Oncogene,* vol. 28, pp. 3642-51, Oct 15 2009.
[437] Y. L. Chao*, et al.*, "Breast carcinoma cells re-express E-cadherin during mesenchymal to epithelial reverting transition," *Mol Cancer,* vol. 9, p. 179, 2010.
[438] U. Cavallaro and G. Christofori, "Cell adhesion and signalling by cadherins and Ig-CAMs in cancer," *Nat Rev Cancer,* vol. 4, pp. 118-32, Feb 2004.
[439] E. Hirata*, et al.*, "Development of a 3D collagen scaffold coated with multiwalled carbon nanotubes," *J Biomed Mater Res B Appl Biomater,* vol. 90, pp. 629-34, Aug 2009.
[440] Y. Cao*, et al.*, "Preparation and characterization of grafted collagen-multiwalled carbon nanotubes composites," *J Nanosci Nanotechnol,* vol. 7, pp. 447-51, Feb 2007.
[441] P. Sharma*, et al.*, "The mechanistic influence of aligned nanofibers on cell shape, migration and blebbing dynamics of glioma cells," *Integr Biol (Camb),* vol. 5, pp. 1036-44, Aug 2013.
[442] K. Sheets*, et al.*, "Shape-dependent cell migration and focal adhesion organization on suspended and aligned nanofiber scaffolds," *Acta Biomater,* vol. 9, pp. 7169-77, Jul 2013.
[443] L. Li and T. Xie, "Stem cell niche: structure and function," *Annu Rev Cell Dev Biol,* vol. 21, pp. 605-31, 2005.
[444] M. P. Lutolf and J. A. Hubbell, "Synthetic biomaterials as instructive extracellular microenvironments for morphogenesis in tissue engineering," *Nat Biotechnol,* vol. 23, pp. 47-55, Jan 2005.

CURRICULUM VITAE

EDUCATION

May 2015 PhD Biomedical Engineering (Cell & Tissue track)
Virginia Tech-Wake Forest School of Biomedical Engineering and Sciences

May 2010 B.S. Bioengineering (Biomaterials concentration), magna cum laud
Clemson University, Clemson, SC 29634

EXPERIENCE

Wake Forest University

PhD Student

Advisor: Dr. Levi-Polyachenko **Aug 2010 – May 2015**

Synthesized and characterized novel nanomaterials from donor-acceptor conjugated polymers to both detect cancer with near infrared fluoresence and treat cancer with near infrared photothermal therapy. I have worked frequently with TEM, confocal microscope, fluorescent microscopes, ultraviolet/visible spectrophotometer, fluorescence spectrophotometer, 800 nm laser diode, 808 nm laser diode, 1064 nm Nd:YAG laser, and zetasizer. I am adept in aseptic cell culture technique and have worked with over 15 different immortalized cell lines, and am proficient with MTS assays, BCA assays, clonogenic assays, and western blot. Additionally I have written IACUC protocols and worked with both subcutaneous flank and mammary fat pad tumor models in Balb/c mice and have utilized IVIS to monitor tumor growth with bioluminescence.

Clemson University

Undergraduate Researcher

Advisor: Dr. Alexis **Aug 2009-July 2010**

Conducted research to characterize ligand targeted polymeric nanoparticles. Optimized ligand conjugation and performed *in vitro* work to determine effect of ligand targeting on uptake of fluorescent polymeric nanoparticles into various types of cancerous and non-cancerous cells.

South Carolina Research Authority

Intern **May 2009-July 2010**

Assisted with documentation required for closing out government contracts. Additionally worked in the lab fabricating composite materials and prosthetic sockets.

Robert Bosch Corporation

Engineering Intern **Summer 2008**

Worked in the quality control materials lab in the Charleston plant. Operated FTIR, SEM, metallograph, GDOES, optical microscopes, and hardness testers, as well as prepared samples via cutting, mounting, polishing, and etching.

Medical University of SC

Undergraduate Researcher

Advisor Dr. Ramamurthi **Summer 2007**

Conducted research studies to determine the effect of nicotine on the proliferation of endothelial cells. Test results were the control experiment for endothelial cells differentiated from adult stem cells also treated with nicotine.

PATENTS

- N. Levi, C. MacNeill, D. Carroll, E. Graham "Low Band Gap Conjugated Polymeric Compositions And Applications Thereof," PCT/US13/36451
- L. Argenta, N. Levi, E. Wailes, M. Morykwas, M. McGee, W. Wagner, E. Graham "Methods and Compositions for Inhibiting Fibrosis and/or Fibrotic Scar Contracture," PCT/US2014/032673
- N. Levi, L. Argenta, C. MacNeill, E. Graham "Composite PolyDOTS and Applications Thereof," provisional patent applied for 4/10/2014

PROFESSIONAL ACTIVITIES

Journal Reviews

Peer reviewer for *Journal of Nanoparticle Research*

Professional Membership

2013 - present Society of Thermal Medicine

2010 - present Biomedical Engineering Society

Awards and Honors

2014	Gold Medal, Student in Basic Research, Wake Forest Division of Surgical Sciences Research Day
2013	Travel Award for BMES Meeting in Seattle, WA
2006-2010	Clemson University Trustee Scholarship, $1,000 annually
2006-2010	Robert Bosch Scholarship, $2,000 annually
2006-2010	Palmetto Fellows Scholar, $10,000 annually
2006-2010	Clemson University President's and Dean's List

SCIENTIFIC OUTREACH

Scientific Presentation

"Science Day" at Central Middle School – Spring 2013

"Women Leaders in STEM" at Hanes Magnet Middle School – Spring 2013

"STEM Night" at Hanes Magnet Middle School – Spring 2013

Science Fair Judge

Science Fair Judge at Sherwood Elementary – Fall 2013 and 2014

District Science Fair Judge (Highschool Biology) – Spring 2013

Science Fair Judge at Whitaker Elementary – Spring 2012

FIRST LEGO League

Mentor to Walkertown Middle School – Fall 2012 and 2013

PUBLICATIONS

Peer-Reviewed Articles

1. **Elizabeth G. Graham**, Elizabeth Wailes, Nicole H. Levi-Polyachenko "Effect of Multi-Walled Carbon Nanotubes on Breast Cancer Cell Adhesion" *Journal of Biomedical Nanotechnology* (accepted)

2. Edreca A. Thompson, **Elizabeth G. Graham**, Christopher M. MacNeill, Michelle Young, George Donati, Elizabeth M. Wailes, Bradley T. Jones, Nicole H. Levi-Polyachenko "Differential Response of Breast Cancer Cells to Silver Nanoparticles and Photothermal Ablation*" International Journal of Hyperthermia*, 2014 Aug;30(5):312-23. doi: 10.3109/02656736.2014.936051.

3. Christopher M. MacNeill, **Elizabeth G. Graham**, Nicole H. Levi-Polyachenko "Soft Template Synthesis of Donor–Acceptor Conjugated Polymer Nanoparticles: Structural Effects, Stability, and Photothermal Studies" *Journal of Polymer Science Part A*, Volume 52, Issue 11, April 2014, pp. 1622-1632. doi 10.1002/pola.27176

4. **Elizabeth G. Graham**, Christopher M. MacNeill, Nicole H. Levi-Polyachenko "Quantifying Folic Acid Functionalized Multi-Walled Carbon Nanotubes Bound to Colorectal Cancer Cells for Improved Photothermal Ablation" *Journal of Nanoparticle Research* (2013) 15: 1649-1657. doi 10.1007/s11051-013-1649-7.

Review Articles

1. **Elizabeth G. Graham**, Christopher M. MacNeill, Nicole H. Levi-Polyachenko "Comparative Review of Metal, Carbon, and Polymer Nanoparticles for Infrared Photothermal Therapies" *Nano LIFE* 03, 1330002 (2013) doi 10.1142/S1793984413300021

Book Chapters

1. Thomas Moore, **Elizabeth Graham**, Brandon Mattix, Frank Alexis "Nanoparticles to Cross Biological Barriers", *Biomaterials in Science: An Integrated Clinical and Engineering Approach.* Boca Raton: CRC Press, 2012.

PRESENTATIONS

2015 Oral Presentation at VT-WF SBES 14th Annual Graduate Student Research Symposium. "Polymer Dynamic Organic Theranostic Spheres (PolyDOTS) for Photothermal Ablation and Fluorescent Imaging of Breast Cancer *In Vitro* and *In Vivo*"

2015 Oral Presentation at Society of Thermal Medicine's 32nd Annual Meeting. "Theranostic Polymer Nanoparticles for Photothermal Ablation and Fluorescent Imaging of Breast Cancer *In Vitro* and *In Vivo*"

2014 Poster Presentation at WF Division of Surgical Sciences 22nd Annual Resident and Fellows' Research Day. "Development and Characterization of Polymer Dynamic Organic Theranostic Spheres (Poly-DOTS) for Treatment of Brain Metastasis of Breast Cancer *In Vitro*"

2014 Poster Presentation at VT-WF SBES 13th Annual Graduate Student Research Symposium. "Development and Characterization of Polymer Dynamic Organic Theranostic Spheres (Poly-DOTS) for Treatment of Brain Metastasis of Breast Cancer *In Vitro*"

2014 Oral Presentation at Society of Thermal Medicine's 31st Annual Meeting. "CXCR4 Targeted Polymer Nanoparticles for Enhanced Photothermal Ablation of the Brain Metastasis of Breast Cancer *In Vitro*"

2013 Poster Presentation at the Annual Meeting of Biomedical Engineering Society. "Effect of Multi-Walled Carbon Nanotubes on Breast Cancer Cell Adhesion"

2013 Poster Presentation at Poster Presentation at WF Division of Surgical Sciences 21st Annual Resident and Fellows' Research Day. "Effect of Multi-Walled Carbon Nanotubes on Breast Cancer Cell Adhesion"

2013 Poster Presentation at VT-WF SBES 12th Annual Graduate Student Research Symposium. "Effect of Multi-Walled Carbon Nanotubes on Breast Cancer Cell Adhesion"

2013 Oral Presentation at Society of Thermal Medicine's 30th Annual Meeting. "Targeted Thermal Ablation of Colorectal Cancer Cells *In Vitro* Using Folic Acid-Functionalized Multi-Walled Carbon Nanotubes"

2012 Poster Presentation at WF Division of Surgical Sciences 20th Annual Resident and Fellows' Research Day. "Targeted Thermal Ablation of Colorectal Cancer Cells *In Vitro* Using Folic Acid-Functionalized Multi-Walled Carbon Nanotubes"

2012 Poster Presentation at the Annual Meeting of Biomedical Engineering Society. "Targeted Thermal Ablation of Colorectal Cancer Cells *In Vitro* Using Folic Acid-Functionalized Multi-Walled Carbon Nanotubes"

2012 Poster Presentation at VT-WF SBES 11th Annual Graduate Student Research Symposium. "Targeted Thermal Ablation of Colorectal Cancer Cells *In Vitro* Using Folic Acid-Functionalized Multi-Walled Carbon Nanotubes"

2012 Poster Presentation at WFU 12th Annual Graduate Student and Postdoctoral Research Day. "Targeted Thermal Ablation of Colorectal Cancer Cells *In Vitro* Using Folic Acid-Functionalized Multi-Walled Carbon Nanotubes"

STUDENTS MENTORED and TEACHING EXPERIENCE

2014 – present Helped to advise junior graduate student

Ms. Eleanor McCabe. Project Title: "Folic acid functionalized polymer nanoparticles for targeted photothermal therapy of colorectal cancer"

2014 - present Helped to advise undergraduate researcher

Ms. Taylor Ibelli. Project Title: "Photothermal ablation of streptococcus pyogenes using fluorescent bio-polymer nanoparticles"

Summer 2013 Helped to advise medical student summer researcher

Mr. Brad Terry. Project Title: "Intraperitoneal perfusion of MWNT-FA in murine model of peritoneal metastasis of colorectal cancer"

2007 - 2008 Supplemental Instructor for Calculus II at Clemson University